

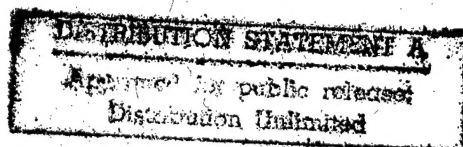


STANFORD UNIVERSITY

Fourier Optics and Optical Diagnostics Laboratory

Diffraction Properties of Volume and Layered Photorefractive Gratings with Application to Holographic Storage

A DISSERTATION SUBMITTED TO THE
DEPARTMENT OF APPLIED PHYSICS
STANFORD UNIVERSITY



ONR Seattle

APR 28 1993

Raymond De Vré
June 1996

19981030 002

DIFFRACTION PROPERTIES OF VOLUME AND
LAYERED PHOTOREFRACTIVE GRATINGS WITH
APPLICATION TO HOLOGRAPHIC STORAGE

A DISSERTATION
SUBMITTED TO THE DEPARTMENT OF APPLIED PHYSICS
AND THE COMMITTEE ON GRADUATE STUDIES
OF STANFORD UNIVERSITY
IN PARTIAL FULFILLMENT OF THE REQUIREMENTS
FOR THE DEGREE OF
DOCTOR OF PHILOSOPHY

Raymond De Vré

June 1996

© Copyright by Raymond De Vré 1996
All Rights Reserved

I certify that I have read this dissertation and that in my opinion it is fully adequate, in scope and quality, as a dissertation for the degree of Doctor of Philosophy.

Lambertus Hesselink
(Principal Advisor)

I certify that I have read this dissertation and that in my opinion it is fully adequate, in scope and quality, as a dissertation for the degree of Doctor of Philosophy.

Walter A. Harrison

I certify that I have read this dissertation and that in my opinion it is fully adequate, in scope and quality, as a dissertation for the degree of Doctor of Philosophy.

Gordon S. Kino

Approved for the University Committee on Graduate Studies:

Dean of Graduate Studies

Abstract

In the past few years there has been growing interest in photorefractive crystals because their unique optical properties make them excellent recording media for holograms. To record a hologram two beams, a reference beam and an information-carrying signal beam, are incident on the crystal. These two beams create an interference pattern that induces, through the photorefractive effect, a spatially-variant index of refraction. When a readout beam properly illuminates this recorded hologram, part of the incident light is diffracted such that, ideally, the diffracted beam is a perfect reconstruction of the original signal beam. The illumination condition that yields the optimum diffraction efficiency is called the Bragg condition. As soon as one moves away from the Bragg condition, for example, by changing the angle or the wavelength of the readout beam, by modifying the index of refraction of the crystal, or by inducing strains inside the crystal, the diffraction efficiency drops to almost zero. All these changes can formally be described by a single parameter ξ , known as the Bragg detuning parameter, such that, in most practical situations, the diffraction efficiency is proportional to $(\sin \xi / \xi)^2$ where $\xi = 0$ if the Bragg condition is satisfied. This selectivity behavior is the most important property of thick holograms and is the main reason why these photorefractive gratings are used in multiplexed holographic data storage and wavelength filtering.

In the first part of this thesis, we review the fundamental principles and the basic physics of holography and of the photorefractive effect. In the second part of the thesis, we develop a general formalism to study Bragg detuning effects that takes into account electric field effects, temperature effects, polarization effects as well as changes in readout angle and wavelength. We then use this formalism to

study diffraction and Bragg detuning effects as they pertain to holographic data storage in photorefractive crystals. We analyze more specifically the consequences of Bragg detuning on the retrieval of image-bearing holograms because it is shown that detuning leads to image distortion. Transfer functions are introduced to quantify these distortions and to analyze two aspects of holographic data storage in which Bragg detuning occurs. The first one deals with thermal fixing, in which temperature changes are applied to photorefractive crystals as a way to fix the information recorded inside these crystals. The second one deals with electric fields applied to crystals as a way to enhance and control diffraction efficiencies. Finally in the third part of the thesis, we study theoretically the diffraction properties of photorefractive stratified volume holographic optical elements and analyze their use in the context of dynamic wavelength filtering.

Acknowledgments

I would first like to thank my advisor, Prof. Lambertus Hesselink, for his generous support over the many years I have spent in his research group at Stanford University. I would also like to thank all the former and current students of the group with whom I enjoyed working and from whom I learned a lot about photorefractives. I want to extend special thanks to the following doctoral and post-doctoral students for their contribution to the work presented in this thesis and for their expertise from which I benefited a lot: Jeffrey P. Wilde, Muthu Jeganathan, John F. Heanue, and Korhan Gürkan. I have also greatly profited from exchange and help from Matt C. Bashaw, Stephen L. Smith, Yuval Levy, Raj Batra, and Thierry Delmarcelle. I am very grateful to Paula Perron and Lylian Sequeira for helping me with administrative problems.

I also want to express my deepest gratitude to Ms. Albert Jadot who funded my first year at Stanford University through the Belgian American Educational Foundation.

Finally, I would like to thank the faculty, the staff, and the students of the Music department for welcoming me into their department. Their encouragement has allowed me to continue my musical education and to actively perform in piano recitals and chamber music concerts while pursuing my research.

This research has been partially supported by the Advanced Research Projects Agency (ARPA) through the Center for Nonlinear Optical Materials (CNOM), the Photorefractive Information Systems Materials (PRISM) consortium, and the Holographic Data Storage Systems (HDSS) consortium.

Contents

Abstract	iv
Acknowledgments	vi
1 Introduction	1
1.1 Motivation	1
1.2 Organization and Summary of the Thesis	3
I FUNDAMENTAL PRINCIPLES	7
2 Holography	9
2.1 Introduction	9
2.1.1 Recording	9
2.1.2 Recording Medium	10
2.1.3 Reconstruction	11
2.2 Coupled-Wave Equations	14
2.3 Diffraction Efficiency	17
2.3.1 Transmission Geometry	18
2.3.2 Reflection Geometry	20
3 The Photorefractive Effect	24
3.1 Introduction	24
3.2 Band Transport Model	25
3.3 Space-Charge Field	31

3.3.1	Amplitude of the Space-Charge Field	33
3.3.2	Phase of the Space-Charge Field	36
3.3.3	Time Constants	38
3.3.4	Electron-Hole Competition	39
3.4	Index Grating Modulation	40

II BRAGG DETUNING ISSUES IN PHOTOREFRACTIVE CRYSTALS **45**

4	Recording of a Photorefractive Hologram	47
4.1	Introduction	47
4.2	Coupled-Wave Equations	48
4.3	Analytical Solutions	53
4.3.1	Transmission Geometry	53
4.3.2	Reflection Geometry	54
4.4	Index Grating	57
4.4.1	Transmission Geometry	57
4.4.2	Reflection Geometry	61
4.5	Conclusions	63
5	Readout of a Photorefractive Hologram	65
5.1	Introduction	65
5.2	Coupled-Wave Equations	66
5.3	Analytical Solutions	68
5.3.1	Bragg Selectivity	68
5.3.2	Maximum Diffraction Efficiency	73
5.4	Conclusions	78
6	Bragg Detuning Effects	79
6.1	Introduction	79
6.2	Angle, Wavelength and Index Changes	80
6.3	Crystal Expansion	86

6.3.1	Thermal Expansion	88
6.3.2	Piezoelectric Expansion	89
6.4	Bragg Detuning Parameter	89
6.5	Phase Coupling Effect	93
6.6	Experiments	94
6.6.1	Introduction	94
6.6.2	Phase Coupling Effect	96
6.6.3	Electro-Optic Effect	100
6.6.4	Phase Coupling and Electro-Optic Effects	105
6.6.5	Polarization Effect	107
6.6.6	Temperature Effect	108
6.7	Conclusions	109
7	Image-Bearing Holograms	111
7.1	Introduction	111
7.2	Holographic Data Storage	112
7.3	Image-Bearing Holograms	114
7.3.1	Transfer Function	115
7.4	Thermal Fixing in Holographic Data Storage	117
7.4.1	Thermal Fixing	117
7.4.2	Transfer Function	117
7.4.3	Discussions	119
7.4.4	Experimental Results	127
7.4.5	Conclusions	130
7.5	ECD Effect in Holographic Data Storage	132
7.5.1	Introduction	132
7.5.2	Electric Field Enhancement	133
7.5.3	Transfer Function	135
7.5.4	Experimental Results	137
7.6	Conclusions	141
7.7	Appendix to Chapter 7	142

III DIFFRACTION ANALYSIS OF STRUCTURES OF GRATINGS

145

8 Structures of Thin Gratings

147

8.1 Introduction 147

8.2 Analytical Analysis 149

8.2.1 General Configuration 149

8.2.2 Thin Hologram Condition 153

8.2.3 Propagation of the Readout Field 153

8.2.4 Diffraction Efficiency 154

8.2.5 Limit for an Infinite Number of Holograms 157

8.2.6 Non-Photorefractive Films 162

8.3 Holographic Multiplexing 163

8.4 Phase Multiplexing 164

8.4.1 Optimum Case 165

8.4.2 Photorefractive Case 168

8.5 Conclusions 169

9 Structures of Thick Gratings

172

9.1 Introduction 172

9.2 Transmission Geometry 174

9.2.1 Layer Matrices 175

9.2.2 Closed-Form Solutions 178

9.3 Reflection Geometry 183

9.3.1 Layer Matrices 185

9.3.2 Closed-Form Solutions 188

9.4 Dynamic Multiple-Wavelength Filter 191

9.5 Conclusions 198

10 Conclusions and Future Research

199

A List of Publications

202

A.1 Papers 202

A.2 Presentations	203
Bibliography	204

List of Tables

3.1	Characteristic fields.	29
3.2	Characteristic rates.	30
3.3	Characteristic lengths.	30
3.4	General constants and SBN:60 characteristic parameters.	33
3.5	Electro-optic coefficients for SBN:60 and SBN:75	41
4.1	Values of the physical parameters for a Ce-doped SBN:60 crystal . . .	54
7.1	Parameters for the photorefractive crystals Ce-SBN:75 and LiNbO ₃ .	118
7.2	Ferroelectric photorefractive materials having phase transition temperatures within 100 °C of room temperature	133
8.1	Maximum first-order diffraction efficiency as a function of N and corresponding grating strength.	163
8.2	Phase pattern $\phi_{j,k}$ across the structure for the optimum case and chosen intensities A_k^2 of each hologram.	167
8.3	Field pattern $E_{0,j,k}$ across the structure for the photorefractive case and chosen intensities A_k^2 of each hologram	170

List of Figures

2.1	Recording of a hologram	10
2.2	Wavefront reconstruction	12
2.3	Wave vectors in a k -space representation	16
2.4	Transmission and reflection geometries	19
2.5	Transmission holograms: normalized diffraction efficiency	21
2.6	Reflection holograms: normalized diffraction efficiency	22
2.7	Perpendicular geometry	23
3.1	Photoexcitation of charge carriers in the band transport model	26
3.2	Formation of the index grating through the photorefractive effect . .	27
3.3	Dispersion relation of the amplitude of the space-charge field \mathcal{E}_{SC} for different values of the acceptor concentration	34
3.4	Dispersion relation of the amplitude of the space-charge field \mathcal{E}_{SC} for different values of the applied field	35
3.5	Variation of the amplitude of the space-charge field \mathcal{E}_{SC} as a function of applied electric field for different grating spacings	36
3.6	Debye screening length as a function of acceptor concentration	37
3.7	Dispersion relation of the phase of the space-charge field for different values of the applied field	37
3.8	Variation of the photorefractive phase shift as a function of applied electric field for different grating spacings	38
3.9	Index ellipsoid	43
4.1	Recording configurations	52

4.2	Intensity of the reference and the signal beams as they propagate through the crystal (transmission geometry)	55
4.3	Intensity of the reference and the signal beams as they propagate through the crystal (reflection geometry)	56
4.4	Transmission geometry: grating amplitude $m(z)$ and grating phase $\psi(z)$ as a function of distance inside the crystal for different applied fields	58
4.5	Density plot of an index grating in the transmission geometry for two values of the pump-to-probe ratio	60
4.6	Reflection geometry: grating amplitude $m(z)$ and grating phase $\psi(z)$ as a function of distance inside the crystal for different applied fields .	61
4.7	Reflection geometry: grating amplitude $m(z)$ as a function of pump-to-probe ratio and distance inside the crystal for two values of the acceptor concentration	63
5.1	Index modulation depth $m(z)$ and corresponding selectivity behavior in the transmission geometry	72
5.2	Index modulation depth $m(z)$ and corresponding selectivity behavior in the reflection geometry	74
5.3	Theoretical maximum diffraction efficiency as a function of applied field in the transmission geometry	76
5.4	Experimental maximum diffraction efficiency as a function of applied field in the transmission geometry	77
5.5	Theoretical maximum diffraction efficiency as a function of pump-to-probe ratio in the reflection geometry	77
6.1	Crystal orientation with respect to the propagation axis assuming a uniaxial crystal	84
6.2	Anisotropic expansion of the grating spacing inside the crystal	87
6.3	Angular bandwidth as a function of reference beam angle	92
6.4	Wavelength bandwidth as a function of reference beam angle	92
6.5	Experimental setup	95

6.6	Experimental and theoretical diffraction efficiencies as a function of ξ for holograms recorded at five different applied fields	98
6.7	Experimental data points and theoretical fit of the angular detuning $\Delta\hat{\theta}_p$ as a function of applied field	99
6.8	Experimental diffraction efficiencies as a function of ξ for holograms recorded at five different applied fields (large pump-to-probe ratio) . .	100
6.9	Angular selectivity of a grating written at symmetric incidence and read at five different applied fields	103
6.10	Angular selectivity of a grating written at asymmetric incidence and read at five different applied fields	104
6.11	Electro-optic coefficient as a function of field for a Ce-doped SBN:75 crystal	104
6.12	Three-dimensional representation of the Bragg detuning parameter as a function of E_{0R} and $\hat{\theta}_s$ in an asymmetric transmission geometry . .	106
6.13	Normalized diffraction efficiency of a grating written with extraordinary polarization and read with ordinary polarization	108
6.14	Measured angular detuning yielding a value for the birefringence of a SBN:60 crystal	109
7.1	Representation of a typical holographic data storage setup	113
7.2	k -space representation of the retrieval of an image-bearing hologram under a modified Bragg condition	116
7.3	Transfer function in the perpendicular geometry using LiNbO ₃ for a $\Delta T = -150^\circ\text{C}$	120
7.4	Phase of the complex transfer function in the perpendicular geometry using LiNbO ₃ for a $\Delta T = -150^\circ\text{C}$	121
7.5	Field of view as a function of temperature in the perpendicular geometry using LiNbO ₃	122
7.6	Angular detuning and wavelength detuning as a function of temperature using LiNbO ₃	122

7.7	Relative angular shift of the diffracted beam as a function of θ_s for a $\Delta T = -150^\circ\text{C}$	123
7.8	Relative detuning changes as a function of θ_r in the perpendicular geometry for a $\Delta T = -150^\circ\text{C}$	124
7.9	Field of view as a function of θ_r in the three recording geometries for a $\Delta T = -150^\circ\text{C}$	126
7.10	Field of view as a function of the number of SLM pixels that are fully reconstructed for three different focal lengths f	127
7.11	Circular aperture recorded in LiNbO_3 using the perpendicular geometry: (a) shows the thermally fixed image using the low-high-low process, (b)-(f) show the fixed images using the high-low process	128
7.12	Transfer function corresponding to the experimental images ($\Delta T = -115^\circ\text{C}$)	129
7.13	Angular selectivity: theoretical curve corresponding to $l = 1\text{ cm}$, and experimental curves corresponding to the unfixed grating, the fixed grating (low-high-low), and the fixed grating (high-low)	130
7.14	Transfer function as a function of signal beam angular extent at four different applied fields (asymmetric configuration)	136
7.15	Transfer function as a function of signal beam angular extent at four different applied fields (symmetric configuration)	137
7.16	Diffraction efficiency of five angularly multiplexed planar holograms recorded in a Ce-SBN:75 at $T = 60^\circ\text{C}$ and read with three different applied fields	138
7.17	Distribution of the diffraction efficiencies of one hundred angularly multiplexed planar holograms recorded in Ce-SBN:75 at $T = 60^\circ\text{C}$ and read with an applied field of 4 kV/cm	139
7.18	Air Force resolution test target stored in a Ce-doped SBN:75 crystal and reconstructed using the ECD effect	140
8.1	General configuration of a SVHOE in the writing and the reading geometries	150

8.2	<i>k</i> -vector diagram of the writing, the reading, and the diffracted wave vectors	157
8.3	Comparison between a SVHOE and a Fabry-Perot etalon	158
8.4	Diffraction efficiency as a function of the Bragg detuning parameter for SVHOE's of different number <i>N</i> of thin films and for the equivalent thick grating	161
8.5	General concept of phase multiplexing in a SVHOE	166
8.6	Normalized diffraction efficiencies of seven holograms recorded in a SVHOE of seven films: optimum case	168
8.7	Normalized diffraction efficiencies of four holograms recorded in a SVHOE of seven films: photorefractive case	170
9.1	<i>k</i> -vector diagram in the transmission geometry	175
9.2	SVHOE of thick gratings in the transmission geometry	176
9.3	Normalized diffraction efficiency as a function of Bragg detuning parameter for a SVHOE of <i>N</i> identical grating layers in the transmission geometry	182
9.4	Normalized diffraction efficiency as a function of Bragg detuning parameter for a SVHOE of <i>N</i> identical grating layers in the transmission geometry (constant total length <i>L</i>)	183
9.5	<i>k</i> -vector diagram in the reflection geometry	184
9.6	SVHOE of thick gratings in the reflection geometry	186
9.7	Illustration of the phase shift that arises between the beams $\sigma^{(k)}$ in the reflection geometry as a result of the propagation in the buffer layers	191
9.8	Wavelength shift of the maximum diffraction efficiency as a function of buffer layer thickness for a photorefractive SVHOE in the reflection geometry	192
9.9	Schematic representation of a dynamic multiple-wavelength filter, with the photorefractive layers, the buffer layers, and the transparent electrodes	193
9.10	Wavelength response of a two-layer SVHOE system	195

9.11 Output spectral distribution of a dynamic multiple-wavelength filter . 197

Chapter 1

Introduction

1.1 Motivation

The main goal of the research presented in this dissertation is to study the diffraction properties of layered and volume photorefractive gratings in the context of holographic storage and optical signal processing. The major application of interest in this research is volume holography in which a photorefractive crystal acts as the recording medium. The fundamental property of a volume hologram is that it has a finite bandwidth within which it can be retrieved, meaning that the hologram must be illuminated in a precise way in order for it to be able to diffract part of the incident readout light. For example, if the angle of incidence of the readout beam varies, a diffracted signal will exist only when the readout beam angle lies within a finite given angular bandwidth. This bandwidth is inversely proportional to the thickness of the recording medium. Therefore the longer the crystal, the more selective is the hologram.

This selectivity behavior of volume holograms is the fundamental property behind the two applications that are treated in this dissertation. The first one is multiplexing, in which several holograms can be stored in a single crystal because of the finite bandwidth of each individual hologram. Typically the holograms are stored at different reference beam angles or wavelengths such that the diffraction efficiency of each hologram is maximum where the diffraction efficiency of all the other holograms is

minimum. The second application is wavelength filtering, in which the crystal acts as a narrow-band filter on a broad-band input signal. With a crystal of 1 cm, a spectral bandwidth as low as 10 pm can be easily achieved.

In the context of holographic data storage, one of the problems that we have sought to analyze in depth is the distortion that arises because of Bragg detuning changes, i.e., because of changes in the crystal properties that are due to electric fields or temperature changes applied to the crystal and that occur during the recording/readout cycle.

Holographic data storage using photorefractive crystals is a very promising technology to achieve high capacity data storage with fast data transfer rates and short access times. However in a real holographic data storage system, many problems occur that tend to degrade the overall performance of the system, characterized by its signal-to-noise ratio, its maximum capacity, its reconstruction fidelity, its physical size, etc. Currently a lot of attention and research is being devoted to the study of the impact of imperfect crystals, of imperfect optical components, of misalignment, and of noise on the performance of a holographic data storage system. These problems can be roughly defined as materials and systems problems. However, very little work is being done on a comprehensive study of Bragg detuning effects and on the distortions that these effects may induce in a storage device. These problems can typically be classified as physical-optics problems. The first part of this thesis deals with these problems, first by developing a general Bragg detuning formalism, and second by defining, computing, and measuring Bragg detuning-based transfer functions that quantify the distortions that occur through Bragg detuning effects in a holographic data storage system. To illustrate these phenomena, we consider two aspects of holographic storage, one being related to thermal fixing and the other one being related to the electrically controlled diffraction effect.

In the second part of this thesis, we analyze the properties of structures of photorefractive films, also known as photorefractive stratified volume holographic optical elements. These devices are receiving a lot of attention currently because they offer several advantages over bulk crystals. First, for many photorefractive materials, growing films is easier and cheaper than growing bulk crystals. Second, each film and

each layer of the structure can be seen as independent degrees of freedom. Therefore, because of their increased number of degrees of freedom they offer opportunities for novel applications in the fields of optical communication and beam steering, to mention a few. One can also envision building devices in which different physical mechanisms, like transport and the electro-optic effect, are physically separated (e.g., composite and engineered materials) to obtain new materials with enhanced properties and improved performance. In this context, we have come up with a new application of photorefractive stratified volume holographic optical elements that consists of a dynamic multiple-wavelength filter that could have potentially useful applications in the field of wavelength division multiplexing.

1.2 Organization and Summary of the Thesis

In Part I we first review the principle and the general theory of volume holography (Chapter 2) and then describe the basic physical process underlying the photorefractive effect (Chapter 3). In Part II we describe several issues that are specifically related to photorefractive gratings and to their diffraction and Bragg selectivity properties. In Chapter 4, we combine volume holography and photorefractive theory to study grating formation in a typical photorefractive crystal. We show that under certain conditions, the recorded photorefractive grating has a nonuniform amplitude and phase upon reaching steady-state, despite the fact that the grating is originally written by two plane waves. One effect that is especially examined is the fringe bending effect, where the fringes of the grating tilt while the recording process takes place. We also show how amplitude coupling between the two writing beams significantly reduces the thickness of the index grating inside the crystal. In Chapter 5, we study the diffraction properties of these nonuniform gratings. We show that there is a simple Fourier transform relationship between the selectivity behavior of the diffracted intensity and the shape of the grating inside the crystal. We study, for example, how amplitude coupling creates a phenomenon of apodization by suppressing the side lobes present in the diffraction efficiency of a typical uniform grating. Chapter 6 is devoted to an experimental and theoretical study of the different mechanisms that

affect the Bragg condition in photorefractive crystals like strontium barium niobate (SBN) and lithium niobate (LiNbO_3). We start by developing a general formalism to study Bragg detuning effects and then concentrate on the following most important effects: fringe bending effects; electro-optic effects; temperature effects; and polarization effects. We show how careful measurements of angular selectivities and of shifts in the Bragg condition can yield valuable information on some of the crystal parameters, like the electro-optic coefficients and the birefringence. In practice, especially in holographic data storage, image-bearing holograms are stored in photorefractive crystals. With images, Bragg detuning changes have the added effect of inducing deformation when the stored image-bearing holograms are retrieved. In Chapter 7, Bragg detuning effects are investigated as a source of image distortion. Transfer functions are defined, computed and experimentally measured to quantify these distortions. Two cases of interest that correspond to two different aspects of holographic data storage are examined:

- the first case deals with thermal fixing in a digital holographic data storage system, in which a change of temperature is applied to the crystal to achieve fixing of the information inside the recording medium. The fixing of information stored in photorefractive crystals can be achieved by heating the crystal either during or after the recording process. We analyze these two methods to achieve fixing: the first method, in which there is a temperature difference between recording and readout, is called the high-low process, and the second method, in which no net temperature difference is present between recording and readout, is called the low-high-low process. We specifically consider the trade-offs regarding image deformation and diffraction efficiency between these two fixing methods in the different typical recording geometries.

- the second case deals with the electrically controlled diffraction effect, in which an electric field is applied to the photorefractive crystal upon readout to control and enhance the diffraction efficiency of the image-bearing holograms. We experimentally show that electrically controlled diffraction can be successfully implemented in a holographic data storage system by storing and retrieving with an applied field of a few kiloVolts per centimeter multiple planar holograms recorded using angular multiplexing. We were also able to record high-resolution image-bearing holograms and

to retrieve them without image-field loss, despite the presence of an applied electric field.

In Part III of the dissertation, we study the properties of stratified volume holographic optical elements. In Chapter 8, we analyze the diffraction properties of layered structures of thin photorefractive gratings and in Chapter 9, we extend this study to include the diffraction properties of layered structures of thick photorefractive gratings. We develop an exhaustive analytical formalism to study these two types of devices and derive simple closed-form solutions for their first-order diffraction efficiency that match the numerical and experimental results that have recently been published in the literature. Finally, using these results, we propose a novel optical device, a dynamic multiple-wavelength filter, and study the properties of such a device in the context of wavelength division multiplexing.

Part I

FUNDAMENTAL PRINCIPLES

Chapter 2

Holography

2.1 Introduction

In 1948, D. Gabor [1] proposed a new imaging process that he called wavefront reconstruction and that is now known as holography. In this process, a coherent reference wave (usually a plane wave) interferes with the light scattered or diffracted from an object so that both amplitude and phase information are encoded in a recording medium. Using a suitable readout scheme, it is then possible to reconstruct the original object from the recorded interference pattern.

2.1.1 Recording

Consider a signal (object) wavefront given by

$$A_s(\vec{r}) = |A_s(\vec{r})| \exp[-i\phi_s(\vec{r})] \quad (2.1)$$

and a reference wavefront that has a constant amplitude

$$A_r(\vec{r}) = |A_r| \exp[-i\phi_r(\vec{r})] \quad (2.2)$$

When the two waves interfere coherently inside the recording medium as shown on Fig. 2.1, the light intensity recorded is given by

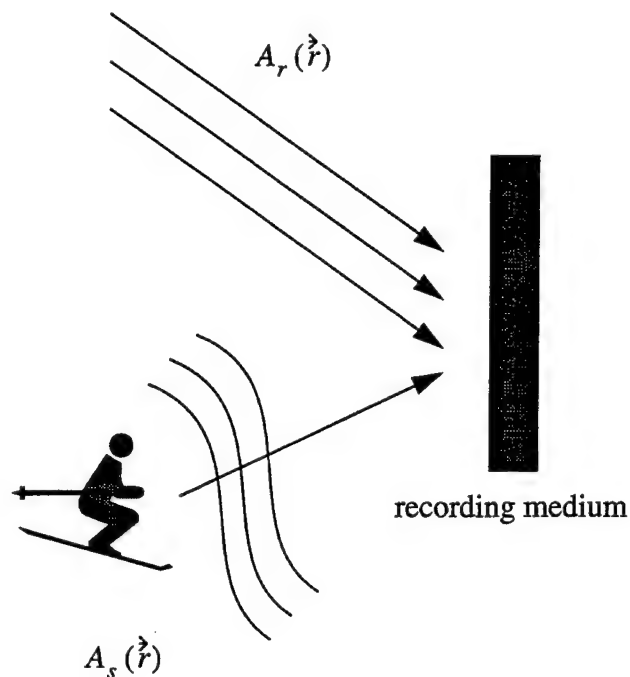


Figure 2.1: Recording of a hologram.

$$\begin{aligned}
 I(\vec{r}) &= |A_s(\vec{r}) + A_r(\vec{r})|^2 \\
 &= |A_s(\vec{r})|^2 + |A_r|^2 + 2|A_s(\vec{r})||A_r| \cos[\phi_r(\vec{r}) - \phi_s(\vec{r})]
 \end{aligned} \tag{2.3}$$

This expression shows that information on the intensity and the phase of the incident object are recorded onto the medium. Once exposed to $I(\vec{r})$, the medium is called a hologram or equivalently a grating.

2.1.2 Recording Medium

We assume that the response of the recording medium is linear for the range of intensities used. The amplitude transmittance [2] of the recording medium after exposure is then given by

$$t(\vec{r}) = t_b + \beta[|A_s(\vec{r})|^2 + A_s(\vec{r})A_r^*(\vec{r}) + A_s^*(\vec{r})A_r(\vec{r})] \tag{2.4}$$

where t_b is a uniform bias transmittance due to the constant reference wave and β is a constant depending on the medium used and on the level of exposure.

2.1.3 Reconstruction

If a recording medium with the transmittance $t(\vec{r})$ is then illuminated on one side by a coherent readout wave $A_p(\vec{r})$, the wave emerging on the other side of the recording medium is given by

$$\begin{aligned} A_p(\vec{r})t(\vec{r}) = & t_b A_p(\vec{r}) + \beta A_p |A_s(\vec{r})|^2 + \beta A_s(\vec{r}) A_p(\vec{r}) A_r^*(\vec{r}) \\ & + \beta A_s^*(\vec{r}) A_p(\vec{r}) A_r(\vec{r}) \end{aligned} \quad (2.5)$$

If the readout wave is identical to the reference wave, the original wavefront, $A_s(\vec{r})$, can be exactly reconstructed [third term of Eq. (2.5)] and a virtual image of the original object is generated [Fig. 2.2(a)]. If the readout wave is the conjugate of the reference wave, the conjugate of the original wavefront, $A_s^*(\vec{r})$, can be exactly reconstructed [fourth term of Eq. (2.5)] and a real image of the original object is generated [Fig. 2.2(b)]. In the case considered here the recording medium has a linear response and generates only an amplitude grating, and there is only one order of diffraction. More generally, a planar thin grating is described by an arbitrary function $t(\vec{r})$. For a real $t(\vec{r})$, an amplitude grating is obtained and for an imaginary $t(\vec{r})$ acting only on the phase of the light wave penetrating the grating, a phase grating is obtained. Generally, the transmittance $t(\vec{r})$ is a complex function and a mixed amplitude and phase grating is present. In this case more than one order of diffraction will emerge from the grating.

If the reference and the signal waves are two plane waves, the wavefronts are given by

$$\begin{aligned} A_s(\vec{r}) &= |A_s| \exp(-i\vec{k}_s \cdot \vec{r}) \\ A_r(\vec{r}) &= |A_r| \exp(-i\vec{k}_r \cdot \vec{r}) \end{aligned} \quad (2.6)$$

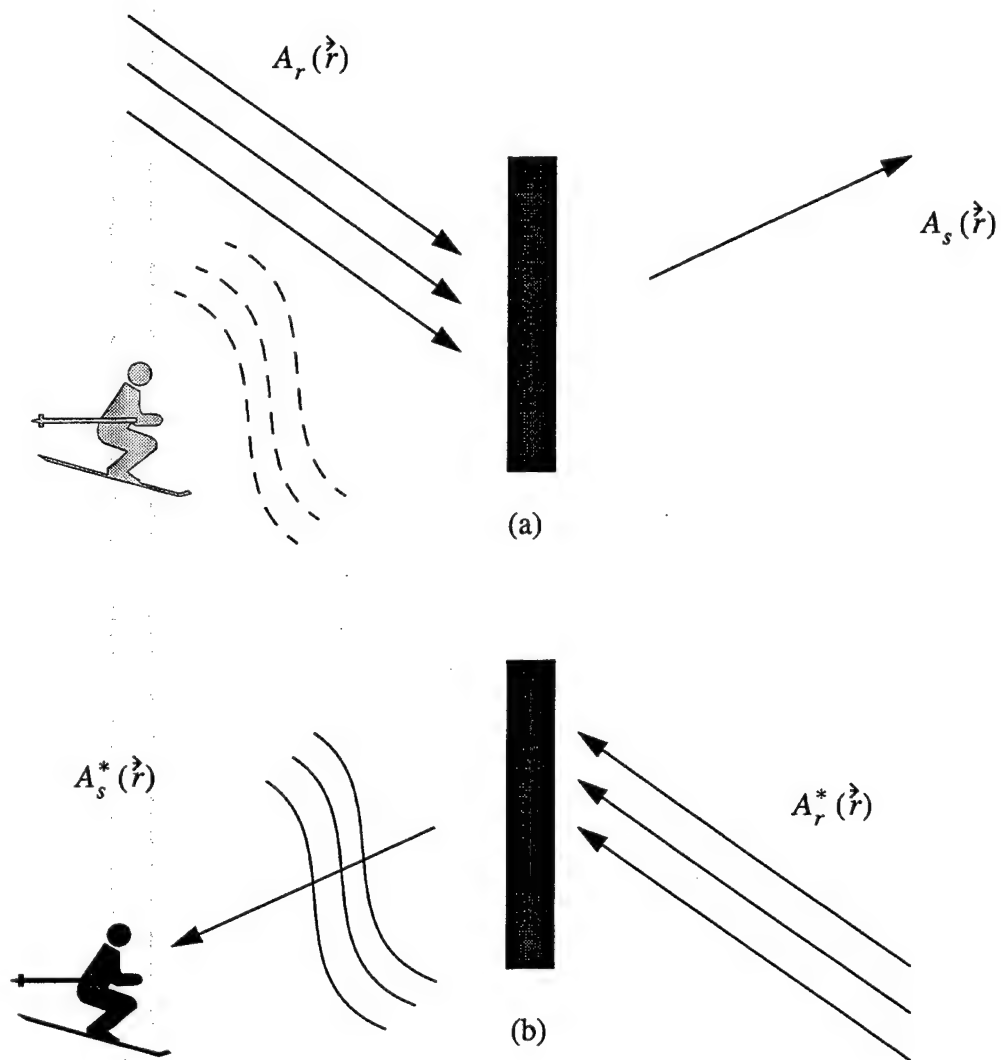


Figure 2.2: Wavefront reconstruction: (a) virtual image, (b) real image.

where \vec{k}_s and \vec{k}_r are the wave vectors of the signal and the reference beams, respectively. The intensity recorded inside the medium is given by

$$\begin{aligned} I(\vec{r}) &= |A_s|^2 + |A_r|^2 + 2|A_r||A_s| \cos[(\vec{k}_s - \vec{k}_r) \cdot \vec{r}] \\ &= I_0(1 + m \cos[(\vec{k}_s - \vec{k}_r) \cdot \vec{r}]) \end{aligned} \quad (2.7)$$

where $I_0 = I_r + I_s$ is the total intensity and $m = 2\sqrt{I_r I_s}/I_0$ is the modulation depth. At this point it is useful to define a grating vector \vec{K} defining the interference pattern being recorded,

$$\vec{K} = \vec{k}_s - \vec{k}_r \quad (2.8)$$

The vector \vec{K} has a magnitude equal to $2\pi/\Lambda$ where Λ is, by definition, the grating period.

Holograms behave differently depending on the relationship between the period Λ and the thickness of the recording medium l . Two categories are commonly defined, thick grating and thin grating. To differentiate between the two categories, a quality factor Q is defined as [3]

$$Q = \frac{2\pi\lambda_0 l}{\bar{n}\Lambda^2} \quad (2.9)$$

where λ_0 is the vacuum wavelength and \bar{n} is the index of refraction of the recording medium. By definition, if $Q \geq 2\pi$, the grating is considered *thick* and if $Q \leq 2\pi$, the grating is considered *thin*. The description of holography done so far in terms of a transmittance $t(\vec{r})$ is only valid for thin holograms. In the next section we consider in more detail the properties of gratings recorded in a thick medium. We analyze more specifically the case of thick phase gratings in which the incident intensity $I(\vec{r})$ modulates the index of refraction of the medium because, as shown in Chapter 3, this is the case relevant to photorefractive materials.

2.2 Coupled-Wave Equations

In this section, we review the results of Kogelnik's coupled-wave analysis of the diffraction of light by a thick uniform phase grating [4]. Consider a thick medium (e.g., a photorefractive crystal) containing a uniform phase grating described by a modulated index of refraction $n(\vec{r})$, the modulation being given by

$$\Delta n(\vec{r}) = \Delta n \cos(\vec{K} \cdot \vec{r} + \phi), \quad (2.10)$$

where Δn is the grating amplitude, ϕ is the grating phase, and \vec{K} is the grating vector. In photorefractive materials, as we shall show in Chapter 3, Δn and ϕ are directly related to the space-charge field that arises from charge redistribution during recording [5]. Consider the following electric field, consisting of a readout wave incident on the grating (a_ρ) and a diffracted wave emerging from the grating (a_σ),

$$E(\vec{r}) = a_\rho(z) \exp(-i\vec{k}_\rho \cdot \vec{r}) + a_\sigma(z) \exp(-i\vec{k}_\sigma \cdot \vec{r}) \quad (2.11)$$

where \vec{k}_ρ and \vec{k}_σ are the wave vectors of the readout beam and the diffracted beam, respectively. These two beams interact with the grating inside the crystal in such a way that the momentum-conservation relation, $k_{\sigma\perp} = k_{\rho\perp} + K_\perp$, is satisfied [6]; \perp denotes the vector component perpendicular to the propagation axis (the z axis) in the plane of incidence. This relation holds true because it is implicitly assumed that the crystal has infinite dimension in the direction perpendicular to the propagation axis. Figure 2.3 represents these different vectors in a k -space diagram.

To derive the coupled equations that describe the interaction between these two waves, it is necessary to solve the wave equation

$$\nabla^2 E(\vec{r}) + k^2(\vec{r})E(\vec{r}) = 0 \quad (2.12)$$

where, neglecting loss,

$$\begin{aligned} k^2(\vec{r}) &= \left[\frac{2\pi(\bar{n} + \Delta n(\vec{r}))}{\lambda_o} \right]^2 \\ &= k_o^2 + 4k_o \frac{\pi}{\lambda_o} \Delta n(\vec{r}) \end{aligned} \quad (2.13)$$

because the index modulation is assumed to be small compared with the bulk index of refraction \bar{n} . $k_o = 2\pi\bar{n}/\lambda_o$ is the amplitude of the wave vector inside the crystal.

Assuming the slowly varying envelope approximation, the following system of equations is derived from the wave equation [Eq. (2.12)],

$$\begin{aligned}\cos\theta_\rho \frac{da_\rho}{dz} &= -i\kappa \exp\left[i\left(\phi + \frac{2\xi z}{l}\right)\right] a_\sigma \\ \cos\theta_\sigma \frac{da_\sigma}{dz} &= -i\kappa \exp\left[-i\left(\phi + \frac{2\xi z}{l}\right)\right] a_\rho\end{aligned}\quad (2.14)$$

where l is the crystal length,

$$\xi = \frac{l}{2}\Delta k_z = \frac{l}{2}(k_{\rho z} + K_z - k_{\sigma z}) \quad (2.15)$$

is the Bragg detuning parameter,

$$\kappa = \frac{\pi\Delta n}{\lambda_o} \quad (2.16)$$

is the coupling constant, λ_o is the readout wavelength outside the medium ($\lambda = \lambda_o/\bar{n}$ is the wavelength inside the medium), and θ_ρ , θ_σ are the angles that the reading beam and the diffracted beam make with the z axis, respectively (see Fig. 2.3). The Bragg condition is satisfied when, by definition, $\xi = 0$, i.e., when the vectorial identity $\vec{k}_\sigma = \vec{k}_\rho + \vec{K}$ is satisfied. A full description of the Bragg detuning parameter ξ is found in Chapter 6. With the change of variables

$$\begin{aligned}A_\sigma &= a_\sigma \exp\left[i\frac{2\xi z}{l}\right] \\ A_\rho &= a_\rho\end{aligned}\quad (2.17)$$

the coupled-wave equations [Eq. (2.14)] reduce to the system

$$\begin{aligned}\cos\theta_\rho \frac{dA_\rho}{dz} &= -i\kappa \exp(i\phi) A_\sigma \\ \cos\theta_\sigma \left(\frac{dA_\sigma}{dz} - i\frac{2\xi}{l} A_\sigma\right) &= -i\kappa \exp(-i\phi) A_\rho\end{aligned}\quad (2.18)$$

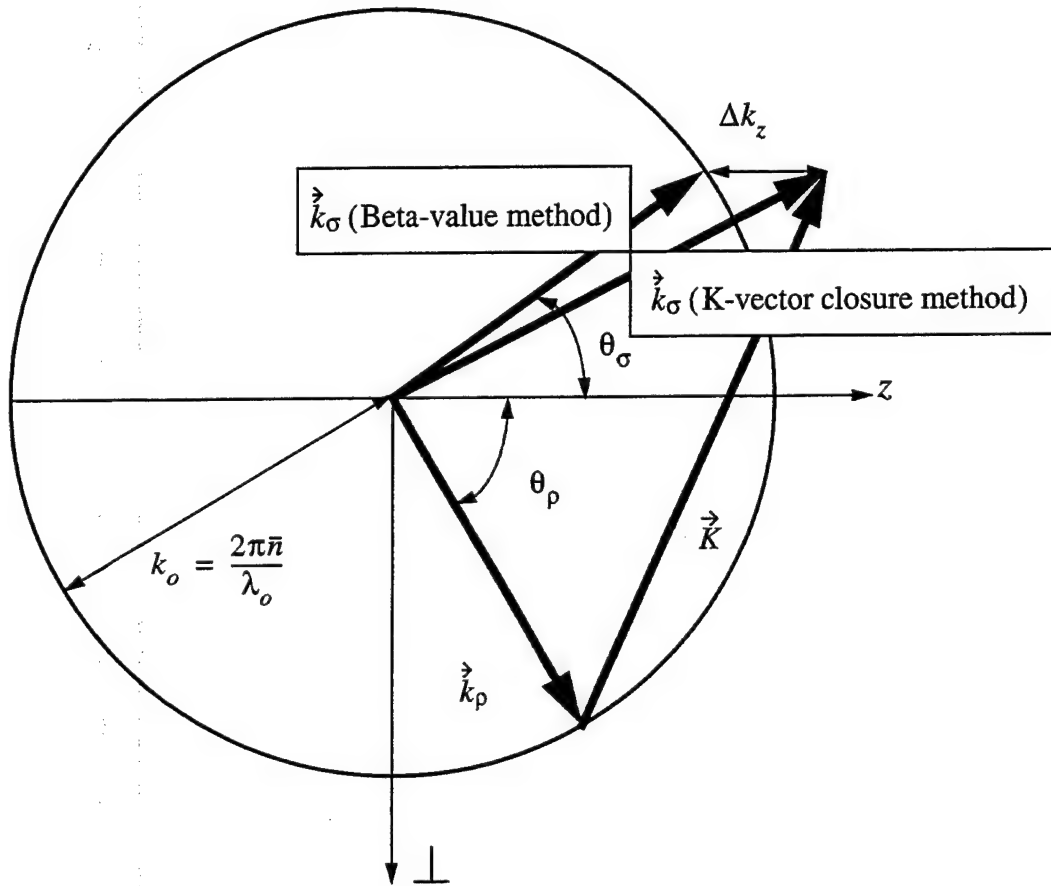


Figure 2.3: k -space representation of the readout wave vector (\vec{k}_ρ), the diffracted wave vector (\vec{k}_σ) (for the Beta-value method and for the K -vector closure method), the grating vector (\vec{K}), and the vector mismatch ($\Delta k_z = k_{\rho z} + K_z - k_{\sigma z} = 2\xi/l$).

This method to solve the diffraction problem is known as the Beta-value method. In this case, the amplitude of the diffracted wave vector \vec{k}_σ remains constant for all off-Bragg readout ($|\vec{k}_\sigma| = k_o$) and the Bragg detuning parameter is defined as the wave vector mismatch along the propagation direction. Therefore

$$k_{\sigma z} = \sqrt{k_o^2 - (k_{\rho\perp} + K_\perp)^2} \quad (2.19)$$

There exists another method known as the K -vector closure method (that Kogelnik uses in Ref. [4]) in which the wavelength of the diffracted light changes as the readout beam moves off-Bragg. In this method the relation

$$\vec{k}_\sigma = \vec{k}_\rho + \vec{K} \quad (2.20)$$

holds true at all time and the Bragg detuning parameter ξ is defined as

$$\xi = -\frac{l}{2 \cos \theta_\sigma} \frac{k_o^2 - |\vec{k}_\sigma|^2}{2k_o^2} \quad (2.21)$$

The Bragg condition is still satisfied when $\xi = 0$, i.e., when the amplitude of the diffracted wave vector is equal to k_o , the amplitude of the readout wave vector. It can be shown [6] that to first order these two methods are equivalent and that the two definitions of the Bragg detuning parameter [Eqs. (2.15) and (2.21)] are the same.

2.3 Diffraction Efficiency

The set of coupled-wave equations [Eq. (2.18)] defining the diffraction problem is a linear system of equations that can be solved assuming the following forms for the readout wave $A_\rho(z)$ and the diffracted wave $A_\sigma(z)$:

$$\begin{aligned} A_\rho(z) &= r_1 \exp(\gamma_1 z) + r_2 \exp(\gamma_2 z) \\ A_\sigma(z) &= s_1 \exp(\gamma_1 z) + s_2 \exp(\gamma_2 z) \end{aligned} \quad (2.22)$$

and with the appropriate boundary conditions. Two geometries are considered, as shown in Fig. 2.4, the transmission geometry in which the two beams are copropagating and the reflection geometry in which the two beams are counterpropagating.

The six coefficients γ_1 , γ_2 , r_1 , s_1 , r_2 , and s_2 are determined by inserting these two functional forms into the two coupled-wave equations defined by Eq. (2.18) and by using the boundary conditions.

2.3.1 Transmission Geometry

For arbitrary boundary conditions at the front face of the crystal ($z = 0$), the solutions to the coupled-wave equations [Eq. (2.18)] at the exit face of the crystal ($z = l$) are expressed in the following way,

$$\begin{pmatrix} A_\rho(l) \\ A_\sigma(l) \end{pmatrix} = M^{tr}(l) \begin{pmatrix} A_\rho(0) \\ A_\sigma(0) \end{pmatrix} \quad (2.23)$$

where $M^{tr}(l)$ is the matrix that describes the diffraction from a uniform grating of length l in the transmission geometry. The matrix is given by

$$M^{tr}(l) = \exp(i\xi) \times \begin{pmatrix} -i\xi \frac{\sin \sqrt{\xi^2 + \nu^2}}{\sqrt{\xi^2 + \nu^2}} + \cos \sqrt{\xi^2 + \nu^2} & -i\nu \sqrt{\frac{\cos \theta_\sigma}{\cos \theta_\rho}} \exp(i\phi) \frac{\sin \sqrt{\xi^2 + \nu^2}}{\sqrt{\xi^2 + \nu^2}} \\ -i\nu \sqrt{\frac{\cos \theta_\rho}{\cos \theta_\sigma}} \exp(-i\phi) \frac{\sin \sqrt{\xi^2 + \nu^2}}{\sqrt{\xi^2 + \nu^2}} & i\xi \frac{\sin \sqrt{\xi^2 + \nu^2}}{\sqrt{\xi^2 + \nu^2}} + \cos \sqrt{\xi^2 + \nu^2} \end{pmatrix} \quad (2.24)$$

where

$$\nu = \frac{\kappa l}{\sqrt{\cos \theta_\rho \cos \theta_\sigma}} \quad (2.25)$$

is called the grating strength. For the boundary conditions associated with the usual diffraction problem, the diffracted signal is equal to zero at the front-face of the crystal, $A_\sigma(0) = 0$. In this case, neglecting Fresnel losses, the diffraction efficiency is defined as

$$\eta = \frac{\cos \theta_\sigma}{\cos \theta_\rho} \left| \frac{A_\sigma(l)}{A_\rho(0)} \right|^2 \quad (2.26)$$

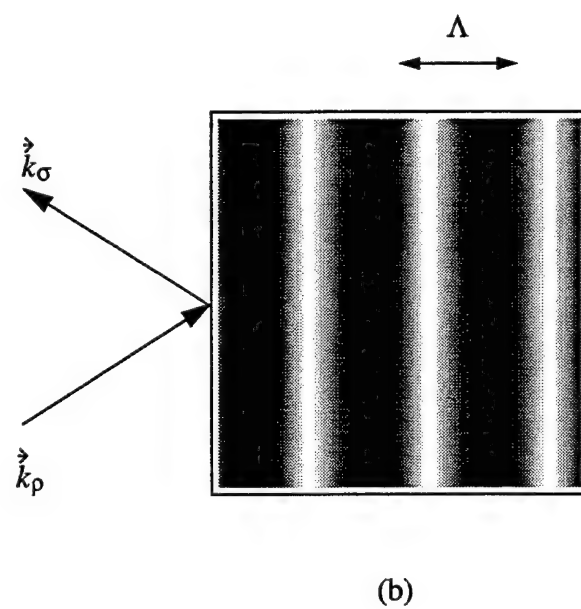
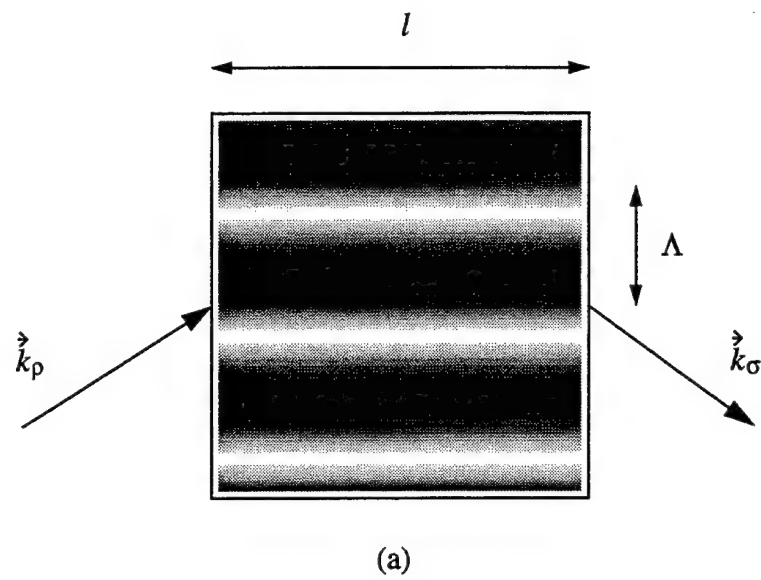


Figure 2.4: (a) Transmission geometry, (b) reflection geometry.

From Eq. (2.24), the diffraction efficiency η is given by

$$\eta = \frac{\sin^2 \sqrt{\xi^2 + \nu^2}}{1 + \frac{\xi^2}{\nu^2}} \quad (2.27)$$

Figure 2.5 shows the diffraction efficiency, normalized to unity, illustrating the Bragg selectivity response in three different cases, corresponding to the following values for the grating strength ν : $\pi/8$, $\pi/2$, and $3\pi/4$. Two special cases are of interest. The first case corresponds to Bragg-matched readout for which the diffraction efficiency is given by

$$\eta = \sin^2 \nu \quad (2.28)$$

and the second case corresponds to a weak grating for which the grating strength ν is small compared to the Bragg detuning parameter ξ and for which the diffraction efficiency reduces to

$$\eta = \nu^2 \text{sinc}^2 \xi \quad (2.29)$$

From this expression one can define a bandwidth determined by the distance between two successive zeros of the diffraction function, i.e., by $\Delta\xi = \pi$. The Bragg selectivity is defined as the inverse of the bandwidth $\Delta\xi$.

2.3.2 Reflection Geometry

For arbitrary boundary conditions given by $A_\rho(0)$ and $A_\sigma(l)$, the solutions to the coupled-wave equations [Eq. (2.18)] are expressed in the following way,

$$\begin{pmatrix} A_\rho(l) \\ A_\sigma(0) \end{pmatrix} = M^{re}(l) \begin{pmatrix} A_\rho(0) \\ A_\sigma(l) \end{pmatrix} \quad (2.30)$$

where $M^{re}(l)$ is the matrix that describes the diffraction from a uniform grating of length l in the reflection geometry. The matrix is given by

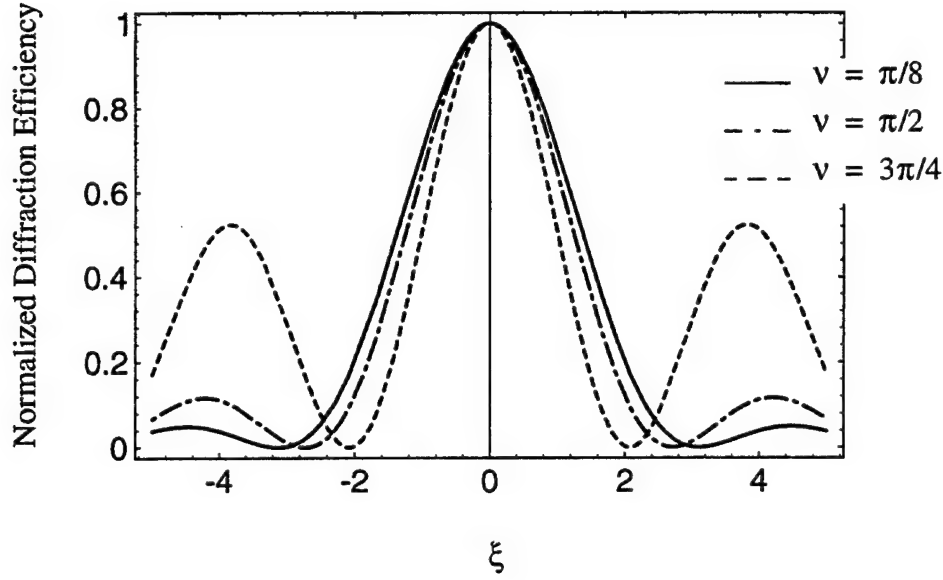


Figure 2.5: Transmission holograms: Normalized diffraction efficiency showing the Bragg selectivity response at three different values of the grating strength ν .

$$M^{re}(l) = \frac{1}{\sqrt{\nu^2 - \xi^2} \cosh \sqrt{\nu^2 - \xi^2} + i\xi \sinh \sqrt{\nu^2 - \xi^2}} \times \begin{pmatrix} \exp(i\xi)\sqrt{\nu^2 - \xi^2} & i\nu\sqrt{\frac{-\cos\theta_\sigma}{\cos\theta_\rho}} e^{i\phi} \sinh \sqrt{\nu^2 - \xi^2} \\ i\nu\sqrt{\frac{-\cos\theta_\rho}{\cos\theta_\sigma}} e^{-i\phi} \sinh \sqrt{\nu^2 - \xi^2} & \exp(-i\xi)\sqrt{\nu^2 - \xi^2} \end{pmatrix} \quad (2.31)$$

where, taking into account that in this geometry $\cos\theta_\rho$ and $\cos\theta_\sigma$ have opposite signs,

$$\nu = \frac{\kappa l}{\sqrt{-\cos\theta_\rho \cos\theta_\sigma}} \quad (2.32)$$

is the grating strength. For the boundary conditions associated with the usual diffraction problem, the diffracted signal is equal to zero at the back-face of the crystal, $A_\sigma(l) = 0$. In this case, neglecting Fresnel losses, the diffraction efficiency of the grating is defined as

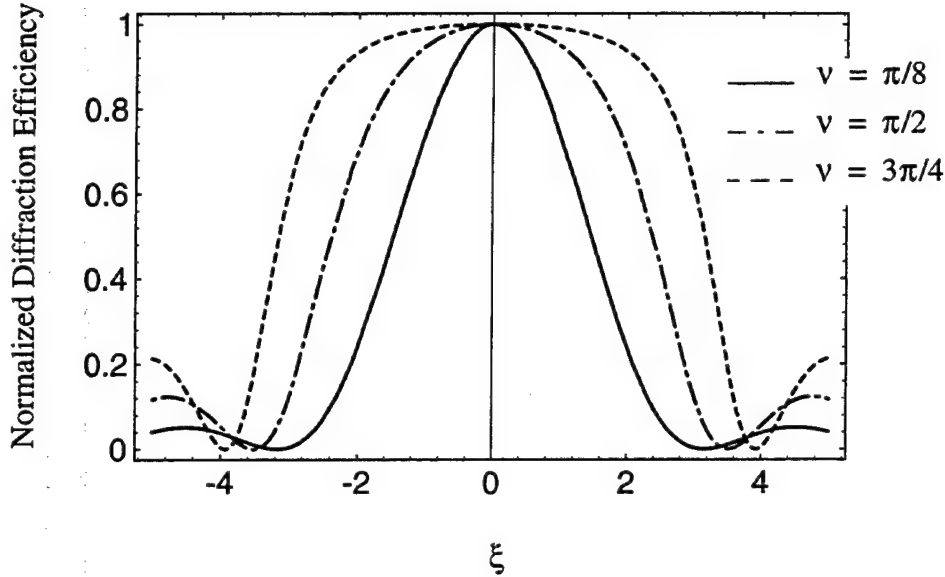


Figure 2.6: Reflection holograms: Normalized diffraction efficiency showing the Bragg selectivity response at three different values of the grating strength ν .

$$\eta = -\frac{\cos \theta_\sigma}{\cos \theta_\rho} \left| \frac{A_\sigma(0)}{A_\rho(0)} \right|^2 \quad (2.33)$$

From Eq. (2.31), the diffraction efficiency η is given by

$$\eta = \frac{\sinh^2 \sqrt{\nu^2 - \xi^2}}{1 - \frac{\xi^2}{\nu^2} + \sinh^2 \sqrt{\nu^2 - \xi^2}} \quad (2.34)$$

Figure 2.6 shows the normalized diffraction efficiency illustrating the Bragg selectivity response in three different cases corresponding to the following values for the grating strength ν : $\pi/8$, $\pi/2$, and $3\pi/4$. For Bragg-matched readout, the efficiency is given by

$$\eta = \tanh^2 \nu \quad (2.35)$$

If the grating strength ν is small compared to the Bragg detuning parameter ξ , the diffraction efficiency reduces to

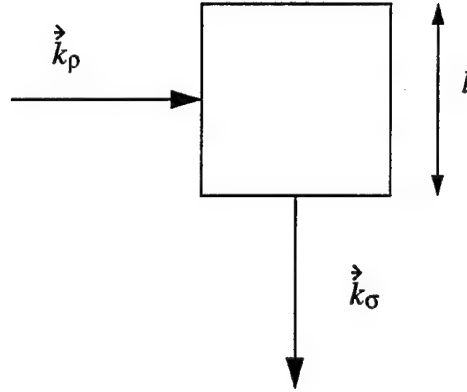


Figure 2.7: Perpendicular geometry.

$$\eta = \nu^2 \text{sinc}^2 \xi \quad (2.36)$$

So far we have introduced the transmission and the reflection geometries. A third geometry is commonly used in photorefractive holography: the perpendicular geometry (also known as the 90 degrees geometry) in which the angle between the readout and the diffracted beam is approximately equal to 90 degrees, as illustrated in Fig. 2.7. This geometry is much more complex to treat rigorously because the wave vectors are not collinear and the signal and reference beams are incident on the crystal on perpendicular surfaces. Therefore, a full two-dimensional coupled-wave analysis is required to analyze this problem exactly [7]. However, it can be shown that if the following assumptions are met (as it is usually the case in practice), the diffraction efficiency in the 90 degrees geometry reduces to the small grating strength result of the transmission geometry, i.e., $\eta = \nu^2 \text{sinc}^2 \xi$: (i) during recording, the intensity of the signal wave A_s is significantly less than the intensity of the reference beam A_r (leading to $m = 2\sqrt{I_s/I_r} \ll 1$); (ii) the readout wave doesn't get depleted during reconstruction. Under these assumptions, the readout wave acts as a source and full coupled-wave analysis is not required.

Chapter 3

The Photorefractive Effect

3.1 Introduction

About thirty years ago it was discovered that an intense laser beam focused on a LiNbO_3 crystal induces a change of the index of refraction of the crystal [8]. The index inhomogeneity distorted the wavefront of the beam that went through the crystal and was therefore referred to as *laser damage*. Since the damage was reversible (by heating up the crystal), the term *photorefractive* was adopted to describe the phenomenon. This term was chosen because the observed phenomenon was analogous to the then-already well-known photochromic effect [9], which describes light-induced absorption changes.

The most common model that describes the photorefractive process is known as the *band transport model*. This model assumes that photoexcited electrons (or holes) are ejected from filled donor (or acceptor) sites into the conduction (or valence) band as shown in Fig. 3.1. In LiNbO_3 the main donor/acceptor centers consist of Fe impurities ($\text{Fe}^{2+}/\text{Fe}^{3+}$) and in SBN, they consist of Ce impurities. In many cases, defects and other various impurities can also introduce intermediate levels in the band gap that act as donor/acceptor levels. Once excited, the charge-carriers migrate to the dark regions inside the crystal before recombining into empty traps. The resulting charge separation induces a space-charge field which then modulates the index of refraction through the electro-optic effect. This model was first developed

by Kukhtarev *et al.* in 1976 [5] [10]. The photorefractive effect is now widely studied and has been the subject of many review articles, among others by Glass [11], Hall *et al.* [12] and Hesselink and Bashaw [13]. Many photorefractive applications are also being developed in such fields as holographic data storage, optical processing and computing, wavefront reconstruction, soliton propagation, etc. An extensive description of different photorefractive applications can be found in Refs. [14] and [15].

Applications based on photorefractive media are quite diverse, but broadly speaking they can be classified into two different categories: (i) those that utilize beam fanning, a form of scattering, in a high-gain crystal (e.g., self- and mutually-pumped phase conjugation [16], novelty filtering [17], and optical limiting [18]), and (ii) those involving conventional holographic storage [19] (e.g., mass data storage and optical interconnections) or real-time holographic image processing [20] (e.g., image correlation, edge enhancement, and mask defect detection [21]) in which beam fanning and other sources of noise scattering act to degrade device performance. From a materials perspective, the ferroelectric class of photorefractive crystals (e.g., LiNbO_3 , SBN, BaTiO_4) finds significant use in both of these categories, while the sillenite (e.g., BSO, BGO) and semiconductor photorefractives (e.g., photorefractive multiple quantum wells) tend to be better suited to the latter case, predominantly for real-time image processing applications. Recently, some polymers that have a strong photorefractive effect have also been discovered [22].

3.2 Band Transport Model

In this section, we outline the basic equations that describe the band transport model, assuming a single charge carrier with a single level. We then derive the solutions for the space-charge field assuming small intensity modulation depths as described in Ref. [10]. Figure 3.1 represents the energy level model for the photorefractive effect in which a single set of recombination centers gives rise to either electrons in the conduction band or holes in the valence band. Thus the material contains localized energy levels of the same species of concentration N . Levels occupied by electrons

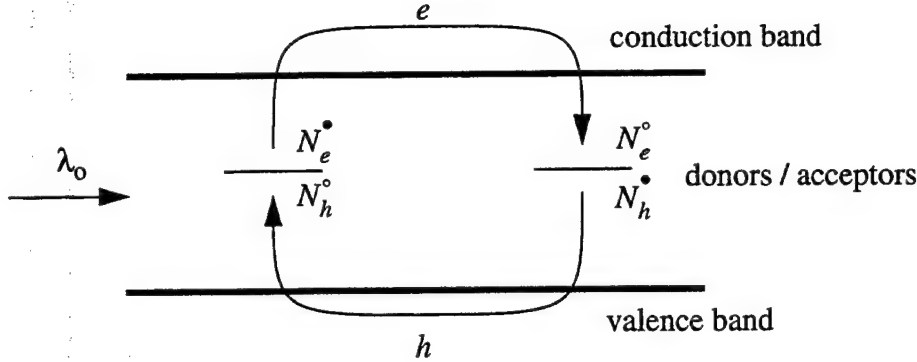


Figure 3.1: Band transport model: photoexcitation of charge carriers.

have a concentration of N^{\bullet} , and levels empty of electrons have a concentration of N° . This notation allows us to describe electron and hole transport in a uniform way. For example, if N is the concentration of electron donors, then $N^{\circ} = N^{+}$ and $N^{\bullet} = N - N^{+}$. For hole transport, $N^{\circ} = N^{-}$. Photorefractive recording is then induced by illuminating the crystal with a spatially variant intensity pattern $I(\vec{r})$ that causes photoexcitation from the occupied donor sites. The charge carriers drift and diffuse and finally get retrapped in unoccupied levels to give rise to a spatially variant space-charge. This space-charge gives rise to an electric space-charge field through Maxwell's equations, which then modulates the index of refraction of the material through the electro-optic effect. The successive steps of this process are depicted in Fig. 3.2.

The mathematical treatment is based on the following set of equations, assuming that the electron is the charge carrier,

$$\frac{\partial N^{\circ}}{\partial t} = (s_e I + \beta_e) N^{\bullet} - \gamma_e n N^{\circ} \quad \text{rate equation} \quad (3.1)$$

$$\vec{\nabla} \cdot \vec{E} = \frac{e}{\epsilon \epsilon_0} [(N^{\circ} - N_0^{\circ}) - n] \quad \text{Poisson's equation} \quad (3.2)$$

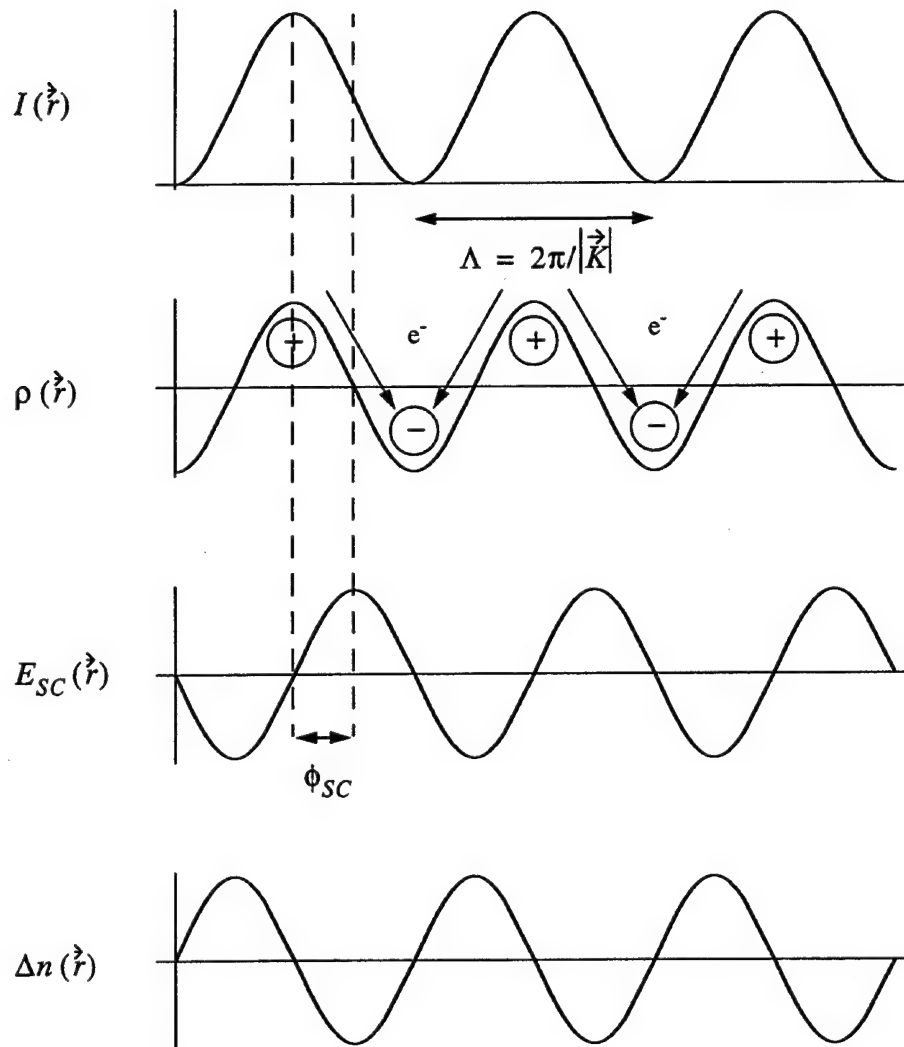


Figure 3.2: Steps explaining the formation of an index grating: formation of the space-charge through drift and diffusion that induces a space-charge field through Poisson's equation, that then creates an index grating through the electro-optic effect.

$$\vec{j}_e = e\mu_e n \vec{E} + k_B T \mu_e \vec{\nabla} n \quad \text{current equation} \quad (3.3)$$

$$\frac{\partial n}{\partial t} = (s_e I + \beta_e) N^\bullet - \gamma_e n N^\circ + \frac{1}{e} \vec{\nabla} \cdot \vec{j}_e \quad \text{continuity equation} \quad (3.4)$$

where s_e is the electron photoionization cross-section, β_e is the electron thermal ionization coefficient, γ_e is the electron recombination coefficient, n is the free electron density, I is the light intensity, ϵ is the relative permittivity, ϵ_0 is the vacuum permittivity, N_0° represents the equilibrium concentration of empty centers in the absence of illumination, k_B is the Boltzmann constant, T is the temperature, and μ_e is the free electron mobility. These equations assume that there is no photovoltaic effect, but we shall show later how the photovoltaic effect can be introduced as a pseudo-applied electric field to the crystal.

As we saw in the previous chapter, the light intensity incident on the crystal is given by

$$I(\vec{r}) = I_0(1 + m \cos \vec{K} \cdot \vec{r}) \quad (3.5)$$

where $I_0 = I_r + I_s$ is the total intensity,

$$m = 2 \frac{\sqrt{I_r I_s}}{I_0} \quad (3.6)$$

is the modulation depth and I_r and I_s are the reference beam and the signal beam intensities, respectively. The modulation depth m is assumed to be much smaller than unity so that the different physical quantities introduced in the model equations can be described by their zero- and first-order Fourier components:

$$\begin{aligned} n(\vec{r}, t) &= n_0(t) + \Re [n_1(t) e^{i\vec{K} \cdot \vec{r}}] \\ N^\circ(\vec{r}, t) &= N_0^\circ(t) + \Re [N_1^\circ(t) e^{i\vec{K} \cdot \vec{r}}] \\ E(\vec{r}, t) &= E_0(t) + \Re [E_1(t) e^{i\vec{K} \cdot \vec{r}}] \end{aligned} \quad (3.7)$$

where $n_1(t)$, $N_1^\circ(t)$, and $E_1(t)$ are complex quantities containing amplitude and phase

Symbol	Definition	Expression
E_0	Applied field	E_0
E_D	Diffusion field	$k_B T \vec{K} / e$
E_Q	Saturation field	$e N_0^\circ (N - N_0^\circ) / (\epsilon \epsilon_0 \vec{K} N)$

Table 3.1: Characteristic fields.

information. The following approximations are assumed in order to solve the band transport equations:

- We assume that at room temperature the dark conductivity is much smaller than the photo-induced conductivity (i.e., we assume that the centers are deep). We can therefore neglect thermal ionization and take $\beta_e = 0$. For shallow levels, thermal ionization cannot be neglected.
- We assume that the free-carrier concentration n is small compared to N^\bullet and N° (small-carrier-concentration approximation), and n can therefore be neglected in Eq. (3.2).
- We assume that upon illumination, the free electron density n quickly reaches a steady-state value n_0 , and consider that

$$\frac{\partial n_0(t)}{\partial t} = 0 \quad (3.8)$$

n_0 is given by

$$n_0 = \frac{s_e I_0}{\gamma_e} \frac{N - N_0^\circ}{N_0^\circ} \quad (3.9)$$

Before writing the solutions to Eqs. (3.1), (3.2), (3.3), and (3.4), it is useful to define several characteristic parameters shown in Tables 3.1, 3.2, and 3.3.

Symbol	Definition	Expression
Γ_{die}	Dielectric relaxation rate	$e\mu_e n_0 / (\epsilon\epsilon_0)$
Γ_{Ie}	Photoionization + ion-recombination rates	$s_e I_0 + \gamma_e n_0$
Γ_{Re}	Electron recombination rate	$\gamma_e N_0^\circ$
Γ_{Ee}	Carrier drift rate	$\mu_e \vec{K} E_0$
Γ_{De}	Carrier diffusion rate	$\mu_e \vec{K} E_D$

Table 3.2: Characteristic rates.

Symbol	Definition	Expression
l_D	Debye screening length	$\sqrt{\epsilon\epsilon_0 k_B T N / [e^2 N_0^\circ (N - N_0^\circ)]}$
l_E	Applied field screening length	$\epsilon\epsilon_0 E_0 N / [e N_0^\circ (N - N_0^\circ)]$
r_{De}	Free-electron diffusion length	$\sqrt{\mu_e k_B T / (e \Gamma_{Re})}$
r_{Ee}	Free-electron drift length	$\mu_e E_0 / \Gamma_{Re}$

Table 3.3: Characteristic lengths.

3.3 Space-Charge Field

By using these definitions and by inserting Eq. (3.7) into Eqs. (3.1), (3.2), (3.3), and (3.4), the following rate equation is derived for the fundamental of the space-charge field E_1 ,

$$\frac{1}{\Gamma_{die}} \left(1 + \frac{\Gamma_{De}}{\Gamma_{Re}} - i \frac{\Gamma_{Ee}}{\Gamma_{Re}} \right) \frac{\partial E_1}{\partial t} = -m(E_0 + iE_D) - E_1 \left(1 + \frac{E_D}{E_Q} - i \frac{E_0}{E_Q} \right) \quad (3.10)$$

which can be simplified to

$$\frac{1}{\Gamma_e} \frac{\partial E_1}{\partial t} = E_{SC} - E_1 \quad (3.11)$$

where

$$E_{SC} = -m \frac{E_0 + iE_D}{1 + \frac{E_D}{E_Q} - i \frac{E_0}{E_Q}} \quad (3.12)$$

is the complex space-charge field and

$$\Gamma_e = \Gamma_{die} \frac{1 + \frac{E_D}{E_Q} - i \frac{E_0}{E_Q}}{1 + \frac{\Gamma_{De}}{\Gamma_{Re}} - i \frac{\Gamma_{Ee}}{\Gamma_{Re}}} \quad (3.13)$$

is the complex exponential response rate. The solutions to Eq. (3.11) are, for grating formation,

$$E_1 = E_{SC} [1 - \exp(-\Gamma_e t)] \quad (3.14)$$

and for grating erasure,

$$E_1 = E_{SC} \exp(-\Gamma_e t) \quad (3.15)$$

The complex space-charge field $E_{SC} = |E_{SC}| \exp(i\phi_{SC})$ can be decomposed into amplitude and phase such that

$$\phi_{SC} = -\arctan \frac{E_D}{E_0} \left(1 + \frac{E_D}{E_Q} + \frac{E_0^2}{E_D E_Q} \right)$$

$$|E_{SC}| = m \sqrt{\frac{E_0^2 + E_D^2}{\left(1 + \frac{E_D}{E_Q}\right)^2 + \left(\frac{E_0}{E_Q}\right)^2}} \quad (3.16)$$

The photorefractive phase shift ϕ_{SC} is a very important parameter that appears in photorefractive theory and is a direct manifestation of the non-local properties of the photorefractive effect. As we shall show in subsequent chapters this phase shift, representing the phase difference between the illumination pattern and the index grating, is responsible for many peculiar photorefractive effects such as wave-mixing and beam coupling. We introduce here a useful quantity, $\mathcal{E}_{SC} = |E_{SC}|/m$, that represents the normalized space-charge field, i.e., the space-charge field up to the modulation depth m . This quantity is also called the saturated space-charge field.

The solutions expressed by Eq. (3.16) are rigorously only valid for small m . It is however possible to show that these solutions remain valid to a good approximation up to $m = 0.8$. Above $m = 0.8$, either higher Fourier orders need to be considered or the system of equations must be solved numerically [23]. The figures in the following sections show how the amplitude and the phase of the space-charge field vary as a function of the following three parameters, the applied field E_0 , the acceptor concentration N_0° , and the magnitude of the grating vector $|\vec{K}| = 2\pi/\Lambda$, directly related to the grating spacing Λ .

Photovoltaic Effect

It has been observed that in certain photorefractive crystals like LiNbO_3 a photocurrent can be produced without an applied voltage. This effect is called the photovoltaic effect [11]. It is due to unidirectional transport of free carriers along the polar axis of the crystal. A reasonable interpretation of the effect can be given in terms of asymmetric charge transfer from the absorbing impurity to the neighboring host ions during excitation: the photocarrier is excited with preferred momentum in one direction along the polar axis. Note that the measured current or voltage does not depend on the electrode material or on the illumination on the electrodes. The magnitude of this current (if due to electron transport) can be characterized by the equation

Parameter	Value
ϵ_0	$8.85 \cdot 10^{-12} \text{ F/m}$
e	$1.6 \cdot 10^{-19} \text{ C}$
k_B	$1.38 \cdot 10^{-23} \text{ J/K}$
T	300 K
λ_o	514 nm
N	10^{25} m^{-3}
ϵ	880
\bar{n}	2.3

Table 3.4: General constants and SBN:60 characteristic parameters.

$$\vec{j}_e^{ph} = \kappa_e s_e N^* I \vec{c} \quad (3.17)$$

that consists of an additional term to be added to Eq. (3.3) and where κ_e is known as the Glass photovoltaic constant for electrons and \vec{c} is a unit vector along the c axis of the crystal. The relation defining the photovoltaic current [Eq. (3.17)] is valid only for short electron transport lengths where the electron transport length is defined as the mean distance the electrons travel before randomization of the velocity. The equation shows that a pseudo electric field generated along the c axis can be defined to describe the same photovoltaic effect,

$$\vec{E}_0^{ph} = \frac{\kappa_e s_e N^* I}{e \mu_e n} \vec{c} \quad (3.18)$$

The high photovoltaic effect observed in LiNbO₃ (fields up to 100 kV/cm in an open circuit configuration) is mainly due to the low mobility μ_e of the excited carriers, leading to a large value for E_0^{ph} .

3.3.1 Amplitude of the Space-Charge Field

Figure 3.3 shows the dispersion of the normalized space-charge field \mathcal{E}_{SC} as a function of the magnitude of the grating vector $|\vec{K}|$ in SBN:60 for different values of the acceptor concentration N_0^o . Figure 3.4 shows the dispersion of the normalized space-charge field \mathcal{E}_{SC} as a function of the magnitude of the grating vector $|\vec{K}|$ in SBN:60

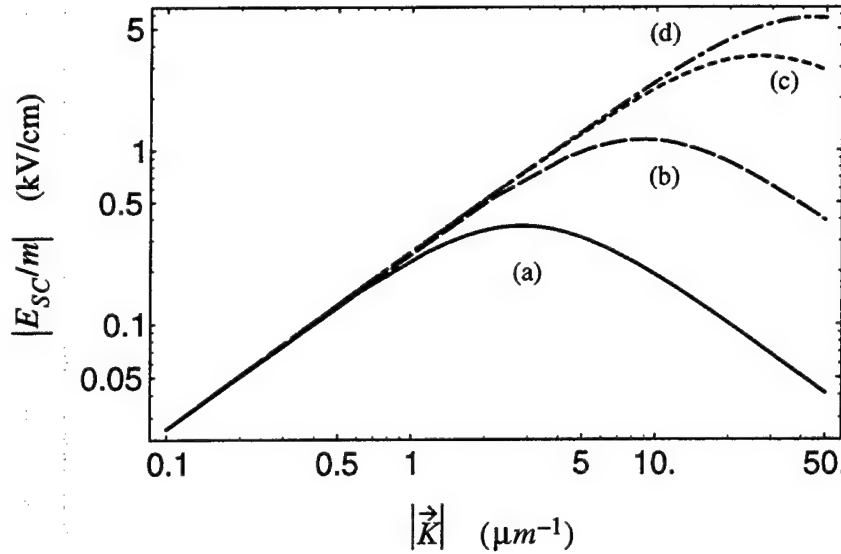


Figure 3.3: Dispersion relation of the amplitude of the space-charge field in SBN:60 for different values of the acceptor concentration at $E_0 = 0$ kV/cm: $N_0^o =$ (a) 10^{22}m^{-3} , (b) 10^{23}m^{-3} , (c) 10^{24}m^{-3} , (d) $0.5 \cdot 10^{25}\text{m}^{-3}$.

for different values of the applied field E_0 . The values for the different parameters relevant to SBN:60 are given in Table 3.4.

In the absence of an applied field, the amplitude of the space-charge field is maximum when the diffusion field is equal to the saturation field, which occurs when the magnitude of the grating vector is equal to the inverse of the Debye screening length, i.e.,

$$|\vec{K}| = \frac{1}{l_D} \quad \text{or} \quad \Lambda = 2\pi l_D \quad (3.19)$$

For grating spacings smaller than $2\pi l_D$, the saturation field E_Q is smaller than the diffusion field E_D and the amplitude of the space-charge field E_{SC} is equal to the saturation field if $E_0 = 0$. This limit is called the saturation limit because the recording process is dominated by strong diffusion which drives the space-charge field to saturation because the actual number of photorefractive trapping sites is finite. This also explains why in this regime an applied field E_0 does not affect the space-charge field. As the number of sites N_0^o increases, the saturation field increases accordingly, to reach a maximum when $N_0^o = N/2$, i.e., when the number of filled

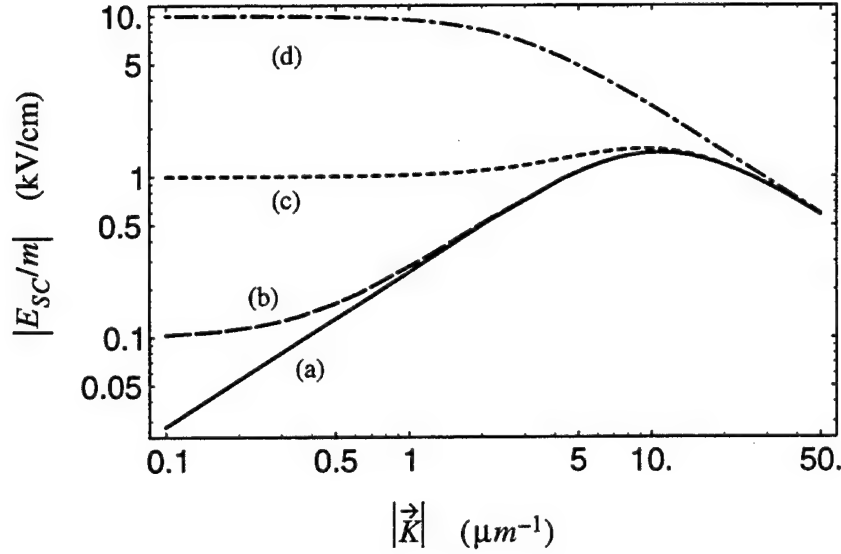


Figure 3.4: Dispersion relation of the amplitude of the space-charge field in SBN:60 for different values of the applied field at $N_0^o = 1.5 \cdot 10^{23} \text{m}^{-3}$:

$E_0 =$ (a) 0.01 kV/cm, (b) 0.1 kV/cm, (c) 1 kV/cm, (d) 10 kV/cm.

traps equal the number of empty traps, $N_0^o = N_0^*$.

For grating spacings larger than $2\pi l_D$, the diffusion field E_D is smaller than the saturation field E_Q . In the absence of an applied field, the amplitude of the space-charge field \mathcal{E}_{SC} is equal to the diffusion field E_D . If a field E_0 is applied to the crystal, three regimes have to be distinguished:

- $E_0 < E_D$, $\mathcal{E}_{SC} = E_D$
- $E_D < E_0 < E_Q$, $\mathcal{E}_{SC} = E_0$
- $E_Q < E_0$, $\mathcal{E}_{SC} = E_Q$

These three regimes are illustrated in Fig. 3.5 [curves (a), (b), and (c)] that shows the variation of the amplitude of the space-charge field \mathcal{E}_{SC} in SBN:60 as a function of the applied electric field E_0 for large grating spacings. As the applied field increases, first the charge carriers move in such a way that they screen the electric field and the space-charge field is equal to the applied field. Finally at very high applied fields, as all the trapping sites are occupied, one reaches saturation and the space-charge field is equal to the saturation field.

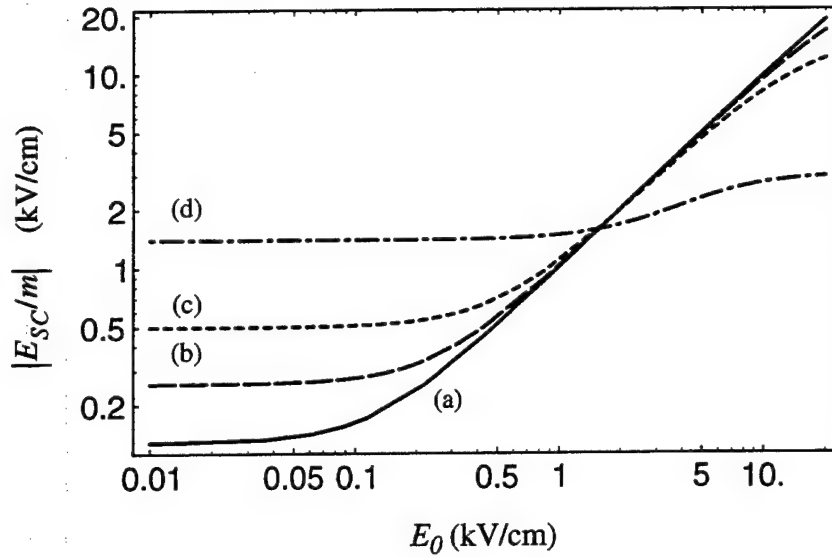


Figure 3.5: Variation of the amplitude of the space-charge field in SBN:60 as a function of applied electric field for different grating spacings at $N_0^o = 1.5 \cdot 10^{23} \text{ m}^{-3}$:

(a) $|\vec{K}| = 0.5 \mu\text{m}^{-1}$ ($\Lambda = 12 \mu\text{m}$), (b) $|\vec{K}| = 1 \mu\text{m}^{-1}$ ($\Lambda = 6 \mu\text{m}$), (c) $|\vec{K}| = 2 \mu\text{m}^{-1}$ ($\Lambda = 3 \mu\text{m}$), (d) $|\vec{K}| = 10 \mu\text{m}^{-1}$ ($\Lambda = 0.6 \mu\text{m}$).

This discussion shows the importance of the Debye screening length l_D because in the absence of an applied field, the space-charge field is maximum at this point. As we shall show in the next chapters, the diffraction efficiency of a photorefractive grating is directly related to \mathcal{E}_{SC} . In many applications, it is desirable to maximize the diffraction efficiency, i.e., the space-charge field. One way of achieving this goal is to operate the crystal around the Debye screening length that is essentially a function of the acceptor concentration N_0^o . Figure 3.6 represents $2\pi l_D$ as a function of N_0^o in SBN:60 and shows how, by changing the trap concentration, it is possible to change the range of grating spacings where the space-charge field and ultimately the diffraction efficiency are maximum.

3.3.2 Phase of the Space-Charge Field

In the absence of an applied field, the photorefractive process is dominated by diffusion and the photorefractive phase shift is always equal to $\pi/2$ regardless of the value of

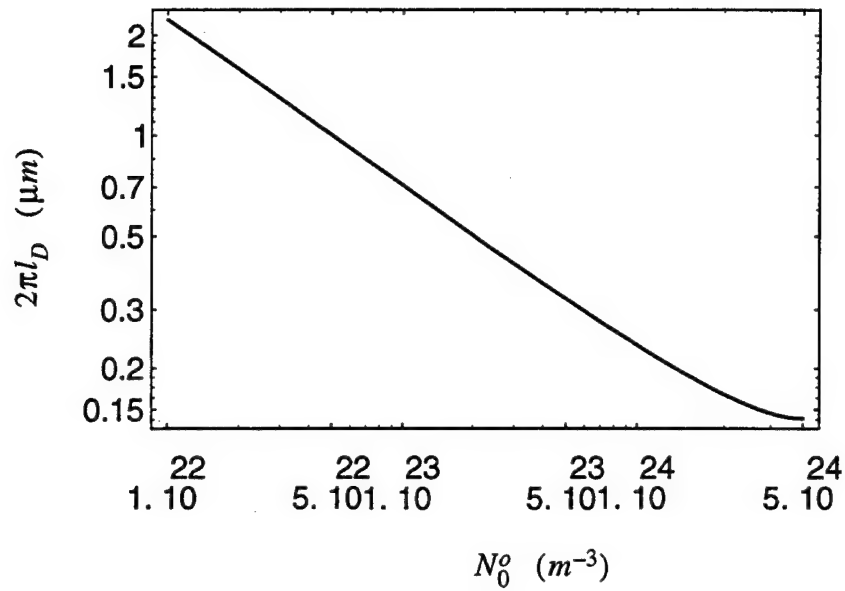


Figure 3.6: Debye screening length l_D (in micrometers) as a function of the acceptor concentration N_0^o in SBN:60.

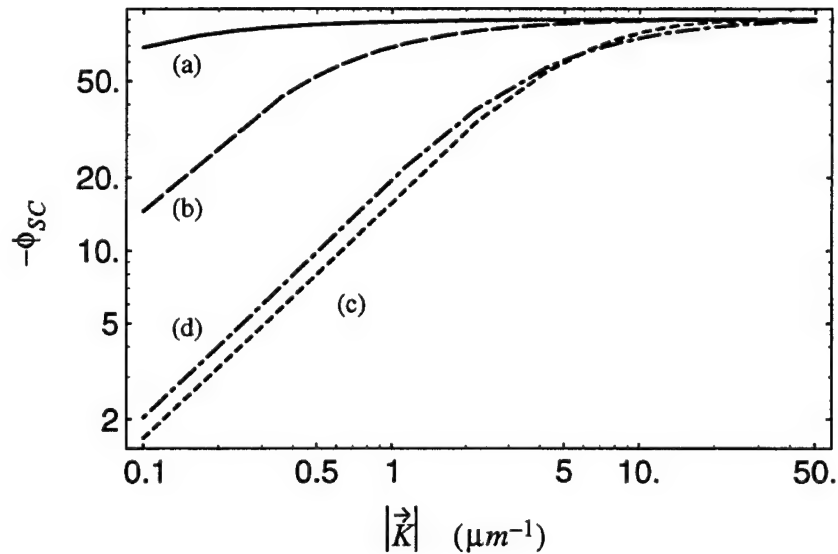


Figure 3.7: Dispersion relation of the phase of the space-charge field (in degrees) in SBN:60 for different values of the applied field at $N_0^o = 1.5 \cdot 10^{23} \text{ m}^{-3}$: $E_0 =$ (a) 0.01 kV/cm, (b) 0.1 kV/cm, (c) 1 kV/cm, (d) 10 kV/cm.

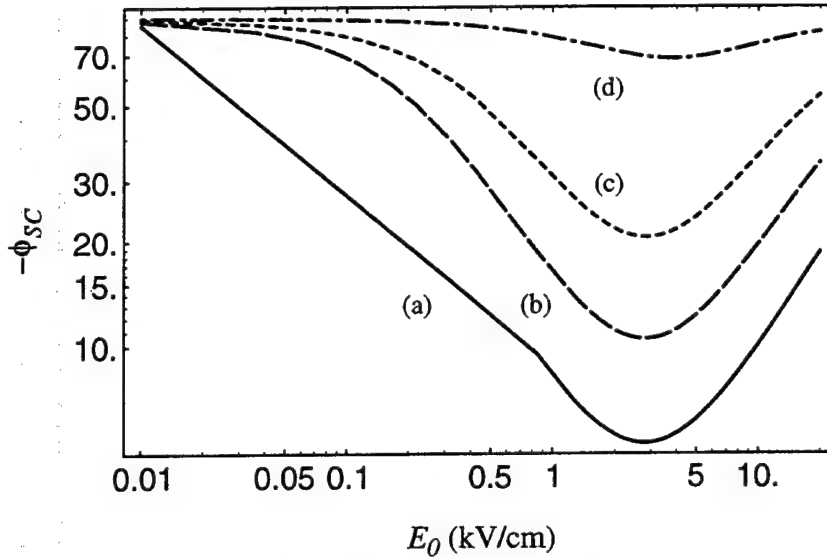


Figure 3.8: Variation of the photorefractive phase shift (in degrees) in SBN:60 as a function of applied electric field for different grating spacings at $N_0^o = 1.5 \cdot 10^{23} \text{m}^{-3}$: (a) $|\vec{K}| = 0.5 \mu\text{m}^{-1}$ ($\Lambda = 12 \mu\text{m}$), (b) $|\vec{K}| = 1 \mu\text{m}^{-1}$ ($\Lambda = 6 \mu\text{m}$), (c) $|\vec{K}| = 2 \mu\text{m}^{-1}$ ($\Lambda = 3 \mu\text{m}$), (d) $|\vec{K}| = 10 \mu\text{m}^{-1}$ ($\Lambda = 0.6 \mu\text{m}$).

the grating period and the value of the acceptor concentration. In the presence of an applied field, the phase shift can take values between 0 and $-\pi/2$ as illustrated in Fig. 3.7. If the applied field is very small, the phase shift ϕ_{SC} remains close to the value of $-\pi/2$ for all grating spacings. If the value of the electric field is high compared with the diffusion field but smaller than the saturation field, the phase shift is close to zero at large grating spacings because $\mathcal{E}_{SC} = E_0$. For an applied field larger than the saturation field at large grating spacings or for all values of the applied field at small grating spacings, $\mathcal{E}_{SC} = E_Q$, and the photorefractive phase shift is close to $-\pi/2$. Figure 3.8 shows the variation of the photorefractive phase shift as a function of the applied electric field E_0 , leading to the same conclusions.

3.3.3 Time Constants

The time evolution of the space-charge field is determined by the function $\exp(-\Gamma_e t)$. The exponential response rate Γ_e is a complex function that contains a real part $1/\tau_e$

(τ_e is the photorefractive time constant) and an imaginary part ω_e , the photorefractive frequency, $\Gamma_e = (1/\tau_e) + i\omega_e$:

$$\begin{aligned}\tau_e &= \frac{1}{\Gamma_{die}} \frac{(1 + |\vec{K}|^2 r_{De}^2)^2 + |\vec{K}|^2 r_{Ee}^2}{(1 + |\vec{K}|^2 l_D^2)(1 + |\vec{K}|^2 r_{De}^2) + |\vec{K}|^2 l_{Ee} r_{Ee}} \\ \omega_e &= \Gamma_{die} \frac{|\vec{K}| r_{Ee} - |\vec{K}| l_E}{(1 + |\vec{K}|^2 r_{De}^2)^2 + |\vec{K}|^2 r_{Ee}^2}\end{aligned}\quad (3.20)$$

These equations show that the response rate is proportional to the incident intensity through Γ_{die} . This explains how prolonged readout can be achieved using a low-intensity readout beam because the erasure time is larger in this case. It can be shown [13] that the dispersion relation of the response rate is flat at constant acceptor concentration. In the presence of an applied field E_0 , the imaginary part ω_e is non-zero. In this case the growth of the space-charge field during recording can be represented by damped oscillations. We will not analyze in more detail the time constants and the temporal behavior of the space-charge field because the work described in this thesis considers only the recording process once it has reached steady-state or the readout process when the grating is considered fixed (non-destructive readout). For a detailed analysis of transient and dynamic effects in photorefractive materials, the reader can refer to Ref. [23].

3.3.4 Electron-Hole Competition

So far we have concentrated solely on electron transport. If we include hole transport that occurs when electrons are excited from the valence band to unoccupied levels, the space-charge field that takes into account both types of transport can be written as [24]

$$E_{SC}^{e-h} = \frac{\Gamma_e E_{SC} + \Gamma_h E_{SC}^*}{\Gamma_e + \Gamma_h} \quad (3.21)$$

where E_{SC} is the space-charge field given by Eq. (3.12), E_{SC}^* is the complex conjugate of E_{SC} , and Γ_h is the response rate for holes. In the diffusion regime, Eq. (3.21) simplifies to

$$E_{SC}^{e-h} = \zeta(K)E_{SC} \quad (3.22)$$

where $\zeta(K)$ is the electron-hole competition factor [25] given by

$$\zeta(K) = \frac{\Gamma_e - \Gamma_h}{\Gamma_e + \Gamma_h} \quad (3.23)$$

In general $\zeta(K)$ is a function of the grating spacing and is positive when electron transport dominates and negative when hole transport dominates inside the photorefractive material.

3.4 Index Grating Modulation

The presence of a space-charge field creates an index grating through the electro-optic effect. Most of the ferroelectric-photorefractive crystals that are of interest in this research are anisotropic crystals that are characterized by their unperturbed impermeability tensor [26]:

$$\beta_{ij}^0 = \left(\frac{1}{\varepsilon} \right)_{ij}^0 \quad (3.24)$$

We will only consider uniaxial crystals for which

$$\beta_{ij}^0 = \begin{pmatrix} \frac{1}{n_o^2} & 0 & 0 \\ 0 & \frac{1}{n_o^2} & 0 \\ 0 & 0 & \frac{1}{n_e^2} \end{pmatrix} \quad (3.25)$$

where n_o and n_e represent the ordinary and the extraordinary index of refraction along the two principal axes of the crystal, the a axis and the c axis, respectively. When an electric field \vec{E} is present inside the crystal (it can be an externally applied field E_0 or an internal field like the space-charge field E_{SC} or the photovoltaic field E_0^{ph}), it modifies the impermeability tensor according to

$$\beta_{ij} = \beta_{ij}^0 + \sum_{k=1,2,3} r_{ijk} E_k \quad (3.26)$$

	SBN:60	SBN:75
r_{13}	47	67
r_{33}	235	1340
r_{42}		42

Table 3.5: Electro-optic coefficients in pm/V for SBN:60 and SBN:75.

where r_{ijk} is, by definition, the electro-optic tensor of the crystal and E_k ($k = 1, 2, 3$) are the components of the electric field inside the crystal, in this case the components of the space-charge field along the three principal axes of the crystal. As an example, we consider the case of SBN, a crystal that belongs to the symmetry class $4mm$ and for which the electro-optic tensor is given by (in reduced notation)

$$r_{ijk} \equiv \begin{pmatrix} 0 & 0 & r_{13} \\ 0 & 0 & r_{13} \\ 0 & 0 & r_{33} \\ 0 & r_{42} & 0 \\ r_{42} & 0 & 0 \\ 0 & 0 & 0 \end{pmatrix} \quad (3.27)$$

Table 3.5 [26][27] gives typical values for the electro-optic coefficients at room temperature for SBN:60 and SBN:75. In the presence of a field, the indices of refraction along the three crystal orientations (n_x , n_y and n_z) are determined by

$$\begin{pmatrix} \frac{1}{n_x^2} & 0 & 0 \\ 0 & \frac{1}{n_y^2} & 0 \\ 0 & 0 & \frac{1}{n_z^2} \end{pmatrix} = \begin{pmatrix} \frac{1}{n_o^2} + r_{13}E_z & 0 & r_{42}E_x \\ 0 & \frac{1}{n_o^2} + r_{13}E_z & r_{42}E_y \\ r_{42}E_x & r_{42}E_y & \frac{1}{n_e^2} + r_{33}E_z \end{pmatrix} \quad (3.28)$$

If the electric field is applied along the z axis only the crystal remains uniaxial and the new indices of refraction are given by

$$\begin{aligned} n_x &= n_y = n_o - 1/2r_{13}n_o^3E_z \\ n_z &= n_e - 1/2r_{33}n_e^3E_z \end{aligned} \quad (3.29)$$

In practice the space-charge field is aligned along the c axis of the crystal if the recording configuration is such that the grating vector is parallel to the c axis ($E_z = E_{SC}$). Therefore Eq. (3.29) defines how the space-charge field generates an index grating by creating spatially variant ordinary and extraordinary indices of refraction. The index ellipsoid shown in Fig. 3.9 represents the index of refraction seen by a beam incident on the crystal at an angle φ . If light with ordinary polarization is incident on the crystal, since the crystal remains uniaxial, the index change seen by the beam is equal to

$$\Delta n_o(\vec{r}) = -1/2r_{13}n_o^3|E_{SC}|\cos(\vec{K} \cdot \vec{r} + \phi_{SC}) \quad (3.30)$$

regardless of the angle φ . If light with extraordinary polarization is incident on the crystal, the index change seen by the beam coming at an angle φ is given by $\Delta n_e(\varphi, \vec{r})$, determined by solving

$$\frac{1}{[n_e(\varphi) + \Delta n_e(\varphi, \vec{r})]^2} = \frac{\sin^2 \varphi}{[n_o + \Delta n_o(\vec{r})]^2} + \frac{\cos^2 \varphi}{[n_e + \Delta n_e(\vec{r})]^2} \quad (3.31)$$

where $\Delta n_e(\vec{r}) = -1/2r_{33}n_e^3|E_{SC}|\cos(\vec{K} \cdot \vec{r} + \phi_{SC})$ and

$$\frac{1}{n_e^2(\varphi)} = \frac{\sin^2 \varphi}{n_o^2} + \frac{\cos^2 \varphi}{n_e^2} \quad (3.32)$$

For small $\Delta n_o(\vec{r})$ and $\Delta n_e(\vec{r})$ compared with n_o and n_e ,

$$\Delta n_e(\varphi, \vec{r}) = \sin^2 \varphi \Delta n_o(\vec{r}) + \cos^2 \varphi \Delta n_e(\vec{r}) \quad (3.33)$$

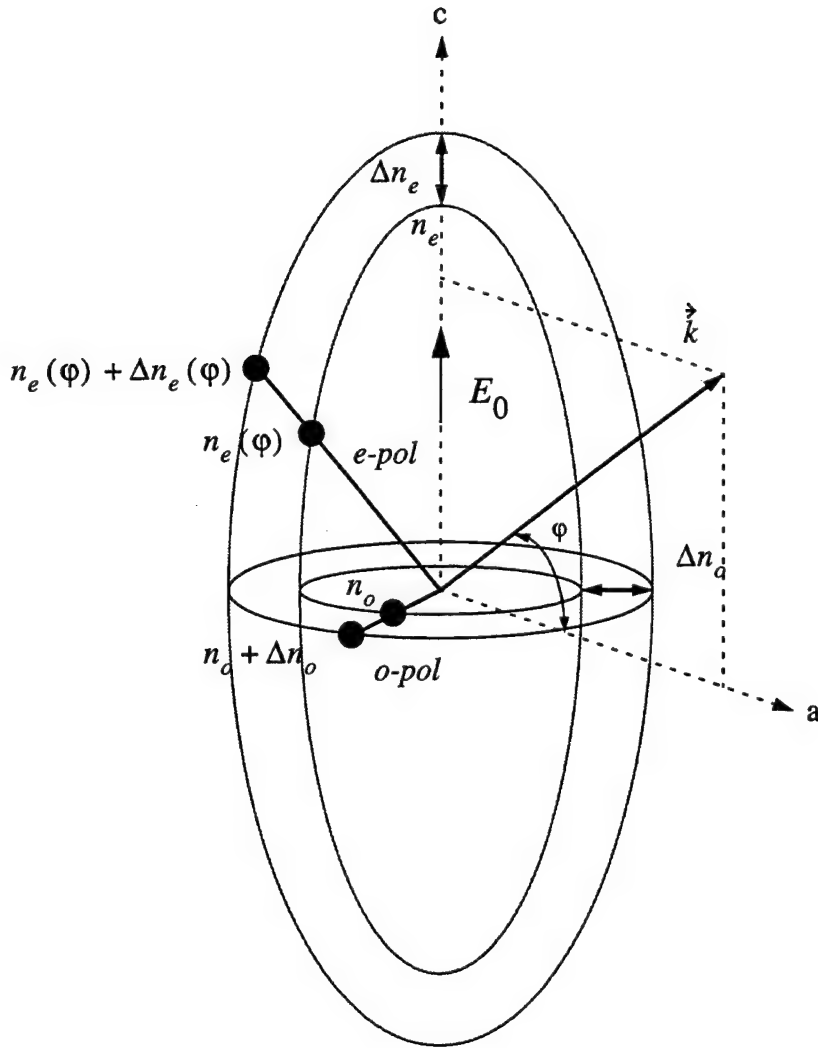


Figure 3.9: Variation of the index ellipsoid along the principal axes of the crystal under an electric field, assuming that it is applied along the c axis.

Part II

BRAGG DETUNING ISSUES IN PHOTOREFRACTIVE CRYSTALS

Chapter 4

Recording of a Photorefractive Hologram

4.1 Introduction

In this chapter we describe the grating formation in a typical photorefractive crystal. This requires us to reconsider the coupled-wave theory developed in Chapter 2 for the derivation of the diffraction properties of uniform gratings to take into account the photorefractive process described in Chapter 3, because the photorefractive effect strongly affects the recording of a hologram in a photorefractive crystal. We shall show in the following sections of this chapter that as a result of the nature of the photorefractive process, the recorded grating is nonuniform in amplitude as well as in phase. The mathematical treatment draws heavily on the two-wave mixing theory developed by P. Yeh in Refs. [15] and [28].

Two-wave mixing is a physical process that takes advantage of the nonlinear response of some materials to the illumination of electromagnetic radiation. For example, the illumination from two writing beams, a signal and a reference beam, results in the formation of an interference pattern that creates an index grating as we described in the previous chapter. While the two writing beams are incident on the crystal, they interact with the grating they are forming and they scatter continuously from it. This results in a situation where one beam scatters into the other and vice-versa.

Such scattering explains the energy exchange and wave-mixing observed in photorefractive materials. In developing the model for two-wave mixing, we assume that all the beams have the same frequency (degenerate wave-mixing) so that a stationary pattern is established inside the crystal. We only consider the steady-state response of the photorefractive medium and neglect transients.

4.2 Coupled-Wave Equations

We examine the writing of a photorefractive hologram by linearly polarized plane waves (extraordinary polarization or ordinary polarization). As stated in Chapter 3, we consider only the case in which the electric field is aligned along the c axis of the crystal to take advantage of the high electro-optic coefficients in this configuration in crystals such as SBN (r_{13} and r_{33} instead of r_{42}) and therefore maximize the diffraction efficiency. Consider the following writing field incident upon the crystal; the field consists of a reference wave and a signal wave:

$$\vec{E}^W(\vec{r}) = A_r(z) \exp(-i\vec{k}_r \cdot \vec{r})\hat{e}_r + A_s(z) \exp(-i\vec{k}_s \cdot \vec{r})\hat{e}_s \quad (4.1)$$

where A_r , A_s are the complex field amplitudes of the reference and the signal waves, respectively. In the case of photorefractive materials, the amplitudes of the two writing beams are functions of the propagation distance z because the medium interacts and modifies the beams inside the crystal as the recording process reaches steady-state. As we show in the rest of this chapter, this results in the formation of a grating inside the crystal that is nonuniform in amplitude and in phase. In Chapter 2, we developed Kogelnik's diffraction theory of uniform gratings (see Fig. 2.4). However, to analyze the diffraction properties of photorefractive gratings, it is necessary to extend Kogelnik's theory to account for gratings that have nonuniform amplitude and phase. This description is done in the next chapter, Chapter 5. \vec{k}_r and \vec{k}_s are the wave vectors of the two writing beams and \hat{e}_r and \hat{e}_s are the unit vectors along the polarization directions. These two waves write a grating in the photorefractive crystal whose initial grating vector is given by

$$\vec{K} = \vec{k}_s - \vec{k}_r \quad (4.2)$$

The intensity incident on the crystal is given by

$$I(z) = [|A_r(z)|^2 + |A_s(z)|^2] \left\{ 1 + \Re \left[\frac{2A_r(z)A_s^*(z)(\hat{e}_r \cdot \hat{e}_s)}{|A_r(z)|^2 + |A_s(z)|^2} e^{i\vec{K} \cdot \vec{r}} \right] \right\} \quad (4.3)$$

As we explained in Chapter 3, such an interference pattern gives rise to an index grating with amplitude

$$\Delta n(\vec{r}) = \Re \left[\frac{n_1}{2} e^{i\phi_{SC}} \frac{2A_r A_s^*}{|A_r|^2 + |A_s|^2} e^{i\vec{K} \cdot \vec{r}} \right] \quad (4.4)$$

where

$$n_1 = -\bar{n}^3 r_{eff} \zeta(K) (\hat{e}_r \cdot \hat{e}_s) \mathcal{E}_{SC} \quad (4.5)$$

and $\mathcal{E}_{SC} = |E_{SC}|/m$ is the intensity-independent normalized space-charge field; ϕ_{SC} is the photorefractive phase shift; r_{eff} is the effective electro-optic coefficient which is a function of the writing geometry, the crystal geometry and the polarization of the light [26]; and $\zeta(K)$ [Eq. (3.23)] is the electron-hole competition factor.

To study grating formation in the crystal, it is necessary to solve the wave equation for the electric field given by Eq. (4.1),

$$\nabla^2 \vec{E}^W(\vec{r}) + k^2(\vec{r}) \vec{E}^W(\vec{r}) = 0 \quad (4.6)$$

where

$$k^2(\vec{r}) = k_o^2 - i\alpha k_o + 4k_o \frac{\pi}{\lambda_o} \Delta n(\vec{r}) \quad (4.7)$$

$k_o = 2\pi\bar{n}/\lambda_o$ is the propagation constant inside the crystal; α is the intensity absorption coefficient; \mathcal{E}_{SC} and ϕ_{SC} are assumed to be given by the standard band transport model for the photorefractive effect as described in the previous chapter [Eq. (3.12)];

$$\mathcal{E}_{SC} \exp(i\phi_{SC}) = -\frac{E_Q(E_{0W} + iE_D)}{E_Q + E_D - iE_{0W}} \quad (4.8)$$

E_{0W} is the electric field applied during writing; E_D is the diffusion field; and E_Q is the saturation field. In the absence of a field, the phase shift is constant and equal to $\pi/2$, but in the presence of an applied field it can take any value between 0 and π , depending on the value and orientation of the field.

By solving the wave equation [Eq. (4.6)], assuming the slowly varying envelope approximation, we derive the following set of equations to describe the steady-state variation inside the crystal of the complex amplitudes of the reference and the signal waves:

$$\begin{aligned}\cos \theta_r \frac{dA_r}{dz} &= -i\kappa \exp(i\phi_{SC}) \frac{|A_s|^2 A_r}{|A_s|^2 + |A_r|^2} - \frac{\alpha}{2} A_r \\ \cos \theta_s \frac{dA_s}{dz} &= -i\kappa \exp(-i\phi_{SC}) \frac{|A_r|^2 A_s}{|A_s|^2 + |A_r|^2} - \frac{\alpha}{2} A_s\end{aligned}\quad (4.9)$$

where θ_r and θ_s are the angles (inside the crystal) that the respective wave vectors \vec{k}_r and \vec{k}_s make with the z axis (the propagation axis), and κ is the coupling constant given by

$$\kappa = \frac{\pi n_1}{\lambda_0} \quad (4.10)$$

Decomposing the complex amplitudes into intensity and phase,

$$\begin{aligned}A_r(z) &= \sqrt{I_r(z)} e^{i\psi_r(z)} \\ A_s(z) &= \sqrt{I_s(z)} e^{i\psi_s(z)}\end{aligned}\quad (4.11)$$

we obtain a set of real equations describing the steady-state variations of the intensity and the phase of both the reference and the signal beams:

$$\begin{aligned}\cos \theta_r \frac{dI_r}{dz} &= 2\kappa \sin \phi_{SC} \frac{I_s I_r}{I_s + I_r} - \alpha I_r \\ \cos \theta_s \frac{dI_s}{dz} &= -2\kappa \sin \phi_{SC} \frac{I_r I_s}{I_s + I_r} - \alpha I_s \\ \cos \theta_r \frac{d\psi_r}{dz} &= -\kappa \cos \phi_{SC} \frac{I_s}{I_s + I_r} \\ \cos \theta_s \frac{d\psi_s}{dz} &= -\kappa \cos \phi_{SC} \frac{I_r}{I_s + I_r}\end{aligned}\quad (4.12)$$

The first two equations describe amplitude coupling that is related to the energy exchange process between the writing beams. The last two equations describe phase coupling that takes place only when a field is applied to the photorefractive crystal during the recording of a hologram ($\cos \phi_{SC} \neq 0$). In the absence of an electric field (i.e., $E_{0W} = 0$, $\phi_{SC} = -\pi/2$, the diffusion-dominated case) the phases of the two beams remain constant within the crystal. In the perfectly drift-dominated case (i.e., $\sin \phi_{SC} = 0$) the amplitudes of the two beams remain constant inside the crystal, and only phase coupling affects grating formation. The rest of this chapter is devoted to the study of the effects of amplitude and phase coupling on grating formation.

The two usual recording geometries are considered: the transmission geometry in which the two writing beams are copropagating, and the reflection geometry in which the two beams are counterpropagating. We explained in Chapter 2 under which general assumptions the perpendicular geometry reduces to the transmission geometry. Figure 4.1 shows a diagram representing the two recording geometries with the orientations of the c axis, the applied electric field E_0 , and the grating vector \vec{K} . In the transmission-geometry case the boundary conditions for Eq. (4.9) are $A_r(0)$ and $A_s(0)$. Note also that $\cos \theta_r$ and $\cos \theta_s$ have the same sign. In the reflection-geometry case the boundary conditions are $A_r(0)$ and $A_s(l)$, where l is the crystal length. In this case $\cos \theta_r$ and $\cos \theta_s$ have opposite signs.

Once the writing process has reached steady state, the following index function is present in the crystal

$$n(\vec{r}) = \bar{n} + \frac{n_1}{2} \frac{2\sqrt{I_r(z)I_s(z)}}{I_r(z) + I_s(z)} \cos [\vec{K}^{PC}(z) \cdot \vec{r} + \phi_{SC}] \quad (4.13)$$

Initially the grating vector is constant (\vec{K}), but after the process reaches steady state the grating vector is given by

$$\vec{K}^{PC}(z) = \vec{K}_\perp + \left[\frac{\psi(z)}{z} + K_z \right] \hat{e}_z \quad (4.14)$$

where \vec{K}_\perp and K_z are the perpendicular and the longitudinal components of \vec{K} , respectively, and $\psi(z)$ is the phase difference between the reference and the signal waves:

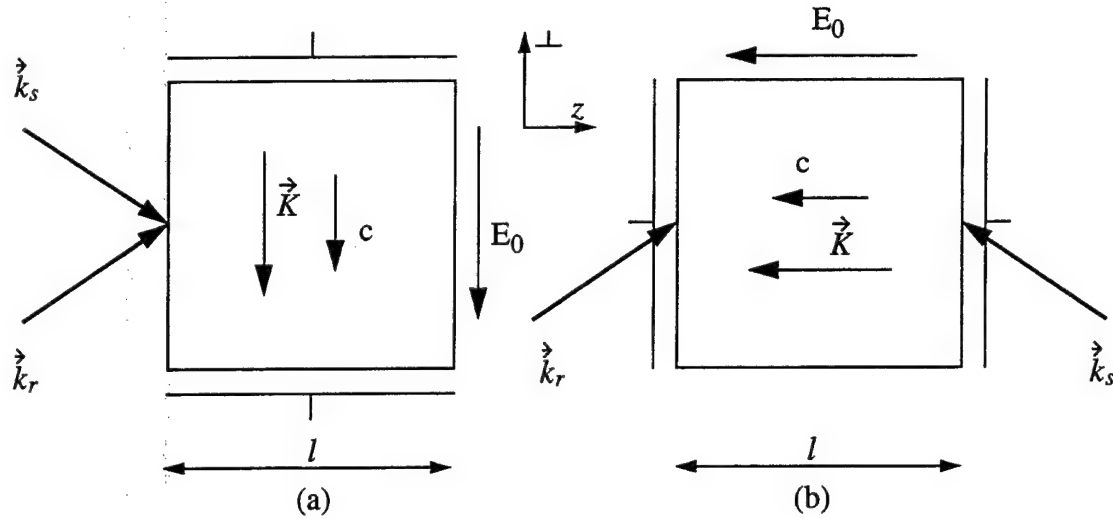


Figure 4.1: Recording configurations: (a) transmission geometry, (b) reflection geometry.

$$\psi(z) = \psi_r(z) - \psi_s(z) \quad (4.15)$$

Because of amplitude coupling and phase coupling, neither the amplitude nor the phase of the grating are uniform in the z direction. Phase coupling affects only the longitudinal component of the grating vector and leaves the transverse component unchanged. It is important to stress here that because of phase coupling, which is present when an electric field is applied to the crystal during recording, the grating vector changes during writing and becomes spatially nonuniform, in spite of the fact that the grating is initially written with two plane waves.

In the transmission geometry the grating is typically written such that $|\vec{K}_\perp| \gg |K_z|$. Therefore phase coupling tends primarily to affect the orientation of the grating vector. In the transmission geometry this effect is referred to as the *fringe bending effect*. $\psi(z)$ can be considered to be the function describing the shape that the fringes take inside the crystal. In the reflection geometry, typically $|\vec{K}_\perp| \ll |K_z|$. Therefore phase coupling tends primarily to affect the magnitude of the grating vector, i.e., the grating spacing. We shall show, however, that in practice, phase coupling is always

negligible in the reflection geometry.

4.3 Analytical Solutions

In this section we specifically consider the symmetric configuration, in which the signal beam and the reference beam make equal angles (in magnitude) with the z axis:

$$|\cos \theta_r| = |\cos \theta_s| = \cos \theta \quad (4.16)$$

In this case the set of equations describing amplitude and phase coupling [Eq. (4.12)] can be solved analytically for the two types of geometries considered. For simplicity the following two parameters are introduced [15]:

$$\begin{aligned} \gamma &= -\frac{2\kappa}{\cos \theta} \sin \phi_{SC} \\ \beta &= \frac{\kappa}{\cos \theta} \cos \phi_{SC} \end{aligned} \quad (4.17)$$

For consistency we assume that the electron-hole competition factor, the orientation of the c axis, and the electric field are such that by convention the sign of γ is positive. The analytical solutions can be found by integrating Eq. (4.12) as described in Ref. [15], where without loss of generality we can choose $\psi(0)$ equal to 0.

4.3.1 Transmission Geometry

In the transmission geometry, the solutions to Eq. (4.12) are [15]:

$$\begin{aligned} I_r(z) &= I_r(0) \frac{1 + r_{pp}^{-1}}{1 + r_{pp}^{-1} \exp(\gamma z)} e^{-\alpha z / \cos \theta} \\ I_s(z) &= I_s(0) \frac{1 + r_{pp}}{1 + r_{pp} \exp(-\gamma z)} e^{-\alpha z / \cos \theta} \\ \psi(z) &= -\frac{\beta}{\gamma} \ln \frac{[r_{pp} + \exp(\gamma z)][1 + r_{pp} \exp(-\gamma z)]}{(1 + r_{pp})^2} \end{aligned} \quad (4.18)$$

Parameter	Value
N	10^{25} m^{-3}
N_0^o	$1.5 \cdot 10^{23} \text{ m}^{-3}$
$r_{eff}\zeta(K)$ (e-pol)	125 pm/V
$r_{eff}\zeta(K)$ (o-pol)	25 pm/V
l	2.5 mm
\bar{n}	2.3

Table 4.1: Values of the physical parameters for a Ce-doped SBN:60 photorefractive crystal.

where r_{pp} is the beam ratio,

$$r_{pp} = \frac{I_r(0)}{I_s(0)} \quad (4.19)$$

Since $\gamma > 0$, the signal beam is the beam that becomes amplified in the crystal at the expense of the reference beam; i.e., the signal beam can be referred to as the probe beam, the reference beam as the pump beam, and r_{pp} as the pump-to-probe ratio. Figure 4.2 shows the intensity of the reference and the signal beams as they propagate through the crystal for two values of the applied field, 0 and 5 kV/cm and for a pump-to-probe ratio $r_{pp} = 100$. A grating spacing of $2 \mu\text{m}$, a crystal length of 2.5 mm, and extraordinarily polarized light are considered for this example. Figure 4.2 shows that for large gain coefficients γ , complete energy transfer can occur from the pump beam to the probe beam. For ordinary polarization, the constant γ is about 5 to 10 times smaller than for extraordinary polarization, and thus much less energy will be exchanged from pump to probe. The numerical values used in all the following figures of this chapter are given in Table 4.1 and correspond to a Ce-doped SBN:60 crystal.

4.3.2 Reflection Geometry

In the reflection geometry the system of equations [Eq. (4.12)] admits of an exact solution only for zero loss ($\alpha = 0$). But in the presence of loss, provided that $\alpha \ll \gamma$,

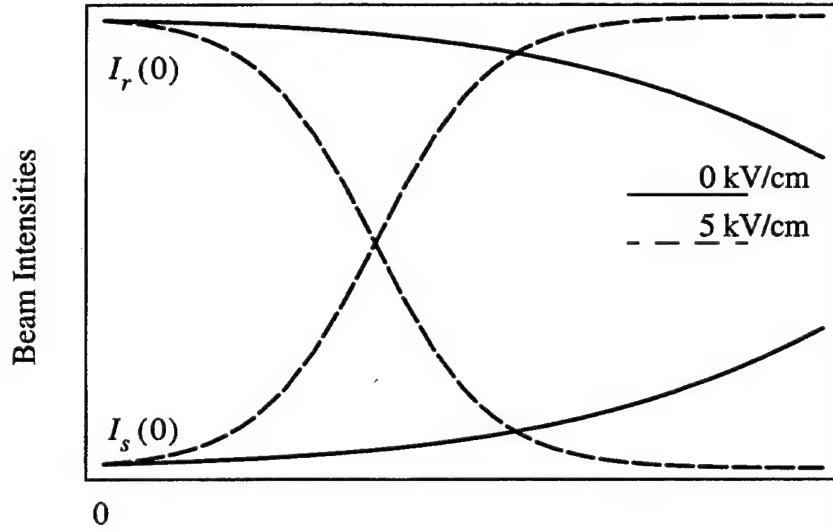


Figure 4.2: Intensity of the reference and the signal beams as they propagate (transmission geometry) through the crystal for two values of the applied field: $E_{0W} = 0$ and 5 kV/cm ($r_{pp} = 100$, $\Lambda = 2 \mu\text{m}$, and $l = 2.5 \text{ mm}$).

a good approximation to the exact solution is given by [15]:

$$\begin{aligned} I_r(z) &= \left[-C + \sqrt{C^2 + B \exp(-\gamma z)} \right] e^{-\alpha z / \cos \theta} \\ I_s(z) &= \left[C + \sqrt{C^2 + B \exp(-\gamma z)} \right] e^{\alpha(z-l) / \cos \theta} \\ \psi(z) &= -\beta z \end{aligned} \quad (4.20)$$

where

$$\begin{aligned} B &= I_r(0)I_s(l) \frac{I_r(0) + I_s(l)}{I_s(l) + I_r(0) \exp(-\gamma l)} \\ C &= \frac{1}{2} \frac{I_s^2(l) - I_r^2(0) \exp(-\gamma l)}{I_s(l) + I_r(0) \exp(-\gamma l)} \end{aligned} \quad (4.21)$$

In this geometry too the signal beam is amplified and the reference beam is depleted. A pump-to-probe ratio r_{pp} can therefore be defined as

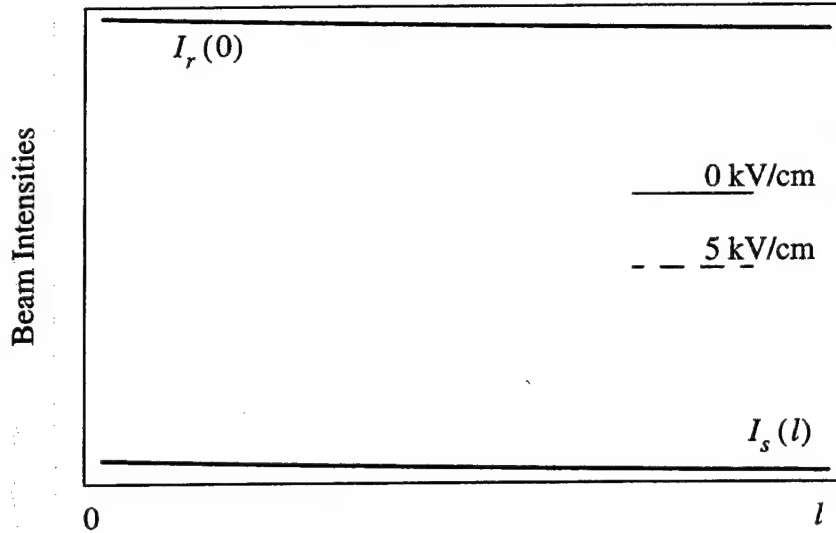


Figure 4.3: Intensity of the reference and the signal beams as they propagate (reflection geometry) through the crystal for two values of the applied field: $E_{0W} = 0$ and 5 kV/cm ($r_{pp} = 100$, $\Lambda = 0.1 \text{ } \mu\text{m}$, and $l = 2.5 \text{ mm}$).

$$r_{pp} = \frac{I_r(0)}{I_s(l)} \quad (4.22)$$

Figure 4.3 shows the intensity of the reference and the signal beams as they propagate through the crystal for two values of the applied field E_{0W} and for a grating spacing of $0.1 \text{ } \mu\text{m}$ and a pump-to-probe ratio of 100. In this case, because the grating spacing is small, the applied field does not modify the space-charge field and therefore does not increase the gain coefficient γ contrary to the transmission-geometry case (Fig. 4.2). In addition, because of the orientation of the c axis that is parallel to the propagation axis, the light incident on the crystal has ordinary polarization, which further reduces the amplitude of the constant γ , which explains why, in this geometry, the energy exchange between the two beams is incomplete.

4.4 Index Grating

It is interesting to study the dependence inside the crystal of the phase $\psi(z)$ and of the amplitude of the grating $n(\vec{r})$ [Eq. (4.13)]. A normalized grating amplitude $m(z)$, i.e., the modulation depth, can be defined as

$$m(z) = \frac{2\sqrt{I_r(z)I_s(z)}}{I_r(z) + I_s(z)} \quad (4.23)$$

4.4.1 Transmission Geometry

In the transmission geometry the modulation depth $m(z)$ and the phase $\psi(z)$ take simple analytical forms:

$$\begin{aligned} m(z) &= \operatorname{sech}\left(\frac{\gamma z - \ln r_{pp}}{2}\right) \\ \psi(z) &= 2\frac{\beta}{\gamma} \ln m(z) + \text{constant} \end{aligned} \quad (4.24)$$

Figure 4.4 shows the dependence of $\psi(z)$ and $m(z)$ inside an SBN:60 crystal ($l = 2.5$ mm) for a grating written with extraordinarily polarized light, for different applied fields (E_{0W}), for two pump-to-probe ratios ($r_{pp} = 100$ and $r_{pp} = 1/100$), and for a grating spacing of $5 \mu\text{m}$.

In the transmission geometry, the space charge field is strongly affected by the applied electric field because the grating spacing $\Lambda = 5 \mu\text{m}$ is much larger than the Debye grating spacing ($= 2\pi l_D = 0.7 \mu\text{m}$ at $N_0^\circ = 1.5 \cdot 10^{23} \text{ m}^{-3}$). Therefore the field significantly affects the coupling constants γ and β and the behavior of the modulation depth $m(z)$ and of the phase $\psi(z)$, as is shown in Fig. 4.4. The figure shows, for example, the increase in phase shift that is due to stronger phase coupling at high applied fields. It also shows how the field reduces the effective thickness of the grating inside the crystal owing to stronger amplitude coupling. The beam ratio r_{pp} has a strong influence, too; for values of r_{pp} larger than one, the modulation initially increases and possibly reaches unity at some point inside the crystal. For these values of r_{pp} the phase is a nonlinear function of the distance inside the crystal.

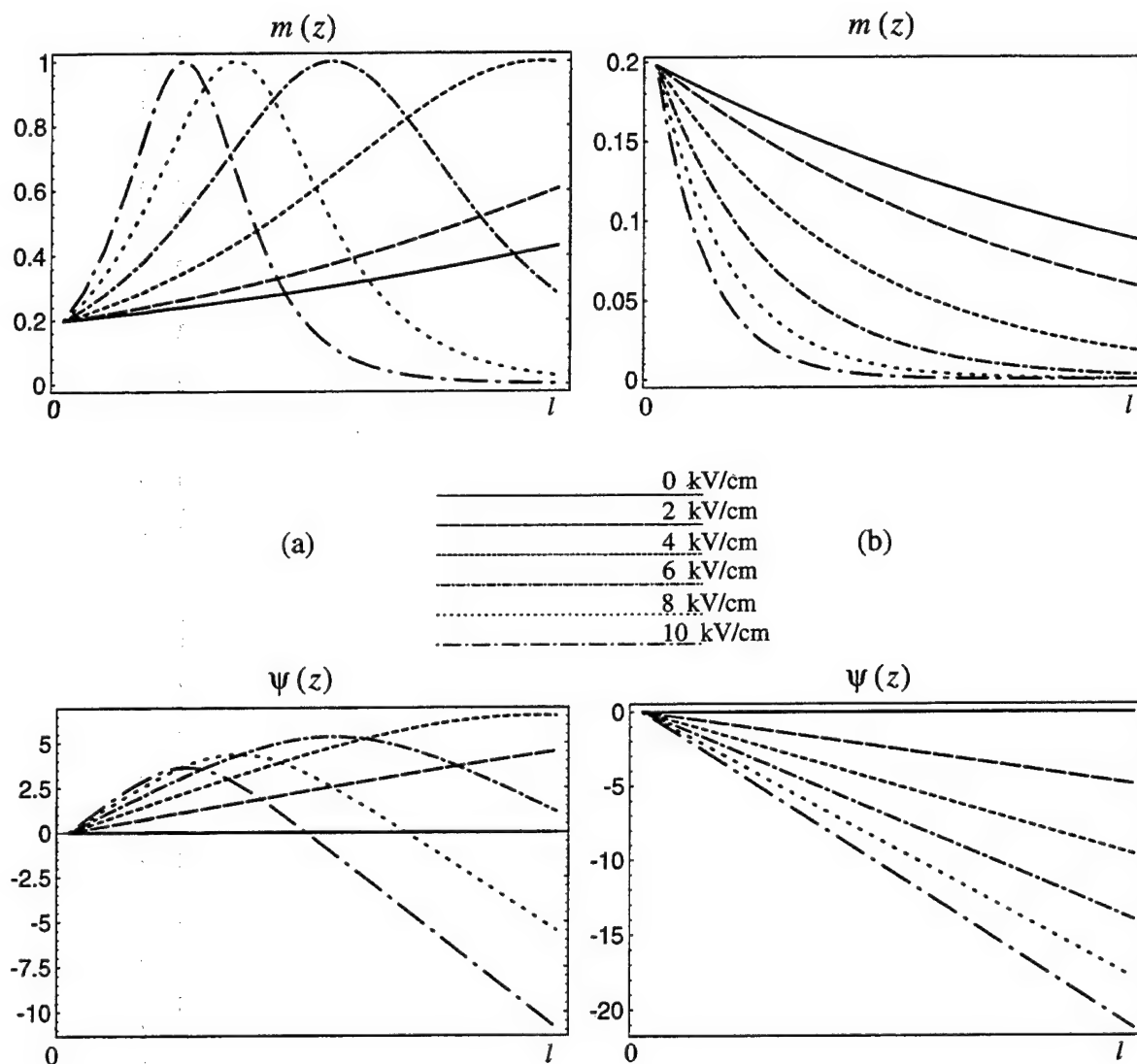


Figure 4.4: Transmission geometry: grating amplitude $m(z)$ and grating phase $\psi(z)$ as a function of distance inside a SBN:60 crystal for 6 different fields (from 0 to 10 kV/cm). (a) $r_{pp} = 100$ and (b) $r_{pp} = 1/100$ ($\Lambda = 5 \mu\text{m}$, $l = 2.5 \text{ mm}$).

For values of r_{pp} much smaller than one the modulation $m(z)$ always decreases with the propagation distance, and to a good approximation $\psi(z)$ is a linear function of z :

$$\begin{aligned} m(z) &= 2\sqrt{r_{pp}} \exp\left(-\frac{\gamma z}{2}\right) \\ \psi(z) &= -\beta z \end{aligned} \quad (4.25)$$

These two limiting cases are illustrated with r_{pp} taken equal to 1/100 and 100/1 in Fig. 4.4. Another special case of interest is the drift-dominated case, attained when $\gamma = 0$. In this case

$$\begin{aligned} m(z) &= \frac{2\sqrt{r_{pp}}}{1 + r_{pp}} \\ \lim_{\gamma \rightarrow 0} \psi(z) &= -\beta z \frac{1 - r_{pp}}{1 + r_{pp}} \end{aligned} \quad (4.26)$$

Note also that the loss does not have any effect on the transmission geometry, as it cancels out in the expression for the modulation and does not appear in the phase coupling equations. For gratings written with ordinarily polarized light, the coupling is much weaker (because r_{13} is used instead of r_{33} for r_{eff}), and the fringe bending effect will be accordingly reduced because of a reduction in the magnitude of the constants γ and β .

Another way to represent the index grating is by a density plot where the contrast between the dark and the bright regions is proportional to the amplitude of the grating. Figures 4.5(a) and 4.5(b) represent the gratings as described by Figs. 4.4(a) and 4.4(b) for an applied field of 10 kV/cm. It clearly illustrates the concept of fringe bending. For small pump-to-probe ratios, as we said earlier, the fringe bending is linear and the final grating recorded in the crystal is the initial grating defined by the grating vector \vec{K} rotated by an amount β . For large pump-to-probe ratios, the resulting grating can be viewed as a spatial distribution of grating vectors along the crystal length defined by $\vec{K}^{PC}(z)$.

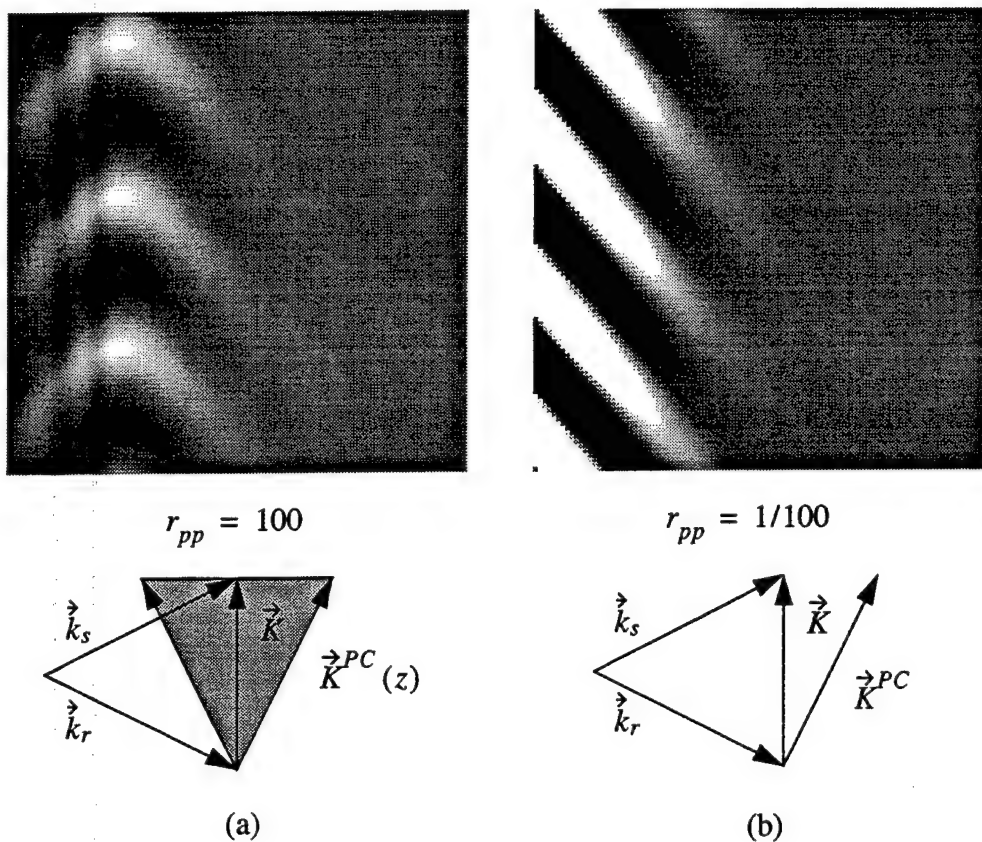


Figure 4.5: Density plot of an index grating in the transmission geometry: (a) $r_{pp} = 100$, (b) $r_{pp} = 1/100$ ($\Lambda = 5 \mu\text{m}$, $l = 2.5 \text{ mm}$, $E_{0W} = 10 \text{ kV/cm}$). The horizontal axis represents the propagation axis (0 to l) and the vertical axis represents the transverse axis inside the crystal (0 to three times Λ).

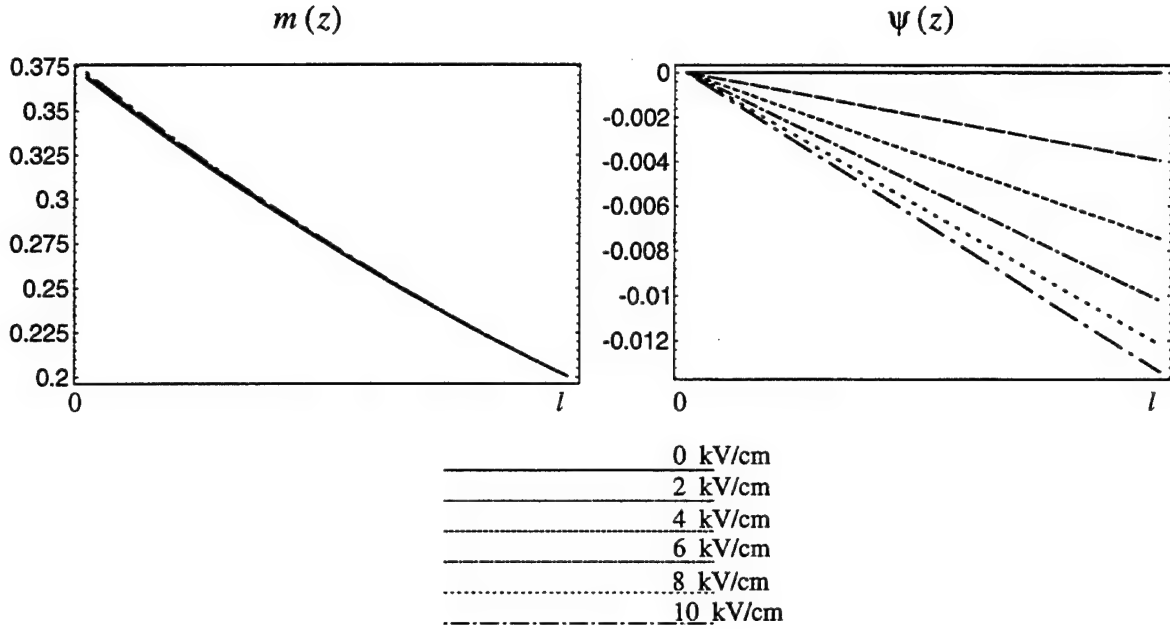


Figure 4.6: Reflection geometry: grating amplitude $m(z)$ and grating phase $\psi(z)$ as a function of distance inside a SBN:60 crystal for 6 different fields (from 0 to 10 kV/cm) ($r_{pp} = 100$, $\Lambda = 0.1 \mu\text{m}$, $l = 2.5 \text{ mm}$).

4.4.2 Reflection Geometry

In the reflection geometry, the modulation depth $m(z)$ and the phase $\psi(z)$ take the following analytical forms:

$$\begin{aligned}
 m(z) &= \frac{1}{\sqrt{2}} \exp\left(\frac{\ln \frac{B}{C^2} - \gamma z}{4}\right) \sqrt{\text{sech}\left(\frac{\ln \frac{B}{C^2} - \gamma z}{2}\right)} \\
 \psi(z) &= -\beta z
 \end{aligned} \tag{4.27}$$

where B and C are given by Eq. (4.21). Figure 4.6 represents one example of index amplitude $m(z)$ and phase $\psi(z)$ inside the crystal in the reflection geometry. The grating spacing is taken equal to $\Lambda = 0.1 \mu\text{m}$ with ordinary polarization and a pump-to-probe ratio $r_{pp} = 100$. In the reflection geometry and for the crystal described in Table 4.1, the applied electric field has little effect on phase coupling and amplitude coupling. Indeed, because the grating spacing ($\Lambda = 0.1 \mu\text{m}$) is smaller than the Debye

grating spacing, the space-charge field is essentially limited by the saturation field and is not affected by the applied field. Therefore the value of the photorefractive phase shift remains close to $-\pi/2$, keeping the constant β small. Figure 4.6 shows how small the phase shift $\psi(z)$ is and how little the modulation $m(z)$ is affected by the applied electric field compared with the transmission-geometry case. Provided that $\alpha \ll \gamma$, loss does not significantly change the modulation inside the crystal.

In the reflection geometry the sinusoidally varying term of the index grating goes as

$$\sin \left[\left(\frac{2\pi}{\Lambda} - \beta \right) z \right] \quad (4.28)$$

$2\pi/\Lambda$ is typically of the order of 10^7 m^{-1} in the reflection geometry. A maximum value for β can be estimated using

$$\beta^{max} = \left| \frac{\pi n_1^{max}}{\lambda_o} \right| \ll |\vec{K}| \quad (4.29)$$

Even considering a big index change of $n_1^{max} = 10^{-2}$, it gives a maximum value for $\beta^{max} = 10^5 \text{ m}^{-1}$. Equation (4.29) shows that in the reflection geometry, regardless of the value of the acceptor concentration and of the applied field, phase coupling is negligible and is not going to affect the grating spacing Λ .

It can be seen from Eq. (4.21) that $C = 0$ when

$$\ln r_{pp} = \frac{\gamma l}{2} \quad (4.30)$$

In this case, $I_r(z) = I_s(z)$ at all points inside the crystal and the modulation is uniformly equal to unity inside the crystal. In the reflection geometry it is therefore possible to get a perfectly uniform index grating despite amplitude coupling by appropriately choosing the pump-to-probe ratio such that Eq. (4.30) is satisfied. Figure 4.7 represents the modulation $m(z)$ as a function of z and r_{pp} for two values of the acceptor concentration N_o° . In case (a), the value of the Debye screening length is such that amplitude coupling is very weak. As seen by Eq. (4.30), this situation leads to a constant index grating inside the crystal ($m = 1$) for a ratio $r_{pp} \approx 1$. In case (b), that corresponds to a much higher acceptor concentration, the Debye screening length

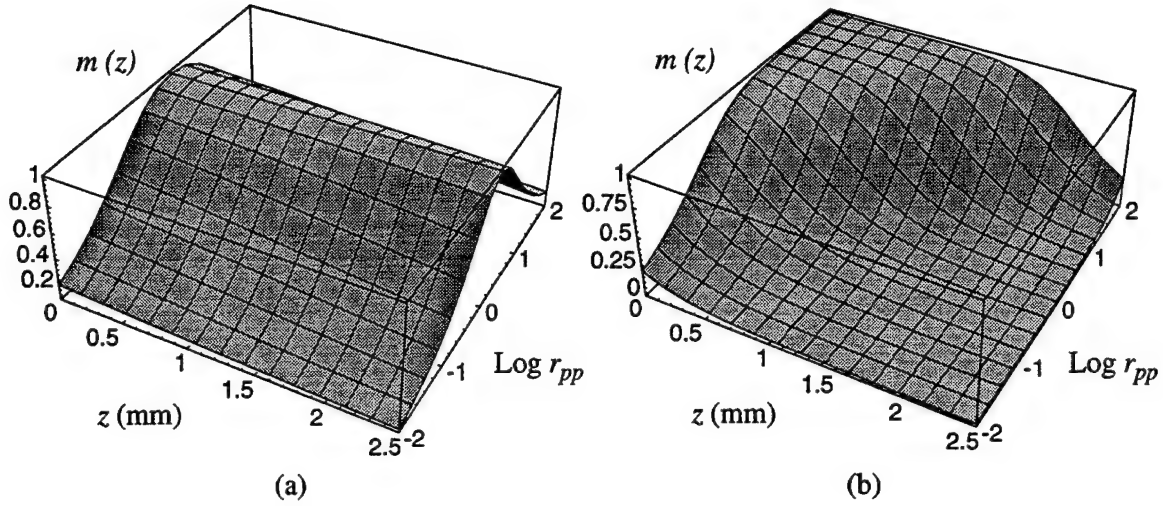


Figure 4.7: Representation of the modulation depth $m(z)$ as a function of pump-to-probe ratio r_{pp} and length z inside the crystal (SBN:60) for two values of the acceptor concentration: (a) $N_0 = 1.5 \cdot 10^{23} \text{ m}^{-3}$, (b) $N_0 = 0.5 \cdot 10^{25} \text{ m}^{-3}$ ($\Lambda = 0.1 \text{ } \mu\text{m}$, $E_{0W} = 0 \text{ kV/cm}$)

is in the same range as the grating spacing (see Fig. 3.6). In this case, amplitude coupling is much stronger, as illustrated in Fig. 4.7(b). In the case of strong coupling the effective thickness of the grating inside the crystal can be significantly reduced, as it is also the case in the transmission geometry.

4.5 Conclusions

In this chapter we have analyzed the formation of gratings in photorefractive crystals in the transmission and in the reflection geometries. We have shown that because of the nonlinear nature of the photorefractive effect there is amplitude and phase coupling between the recording beams during grating formation. These two forms of coupling lead to the formation of gratings that have nonuniform amplitude and nonuniform phase, which results in fringe bending. We have studied and analyzed the influence of several factors that play an important role during grating formation,

i.e., the grating spacing Λ , the applied electric field E_0 , the acceptor concentration N_0^o , and the pump-to-probe ratio r_{pp} .

In the next chapter we shall study the diffraction properties of such nonuniform gratings (shown in Figs. 4.5 and 4.7) and show how the selectivity behavior of their diffraction efficiency is related to the shape of the grating inside the crystal.

Chapter 5

Readout of a Photorefractive Hologram

5.1 Introduction

In this chapter we describe the diffraction properties of the photorefractive gratings whose formation has been described in Chapter 4. We describe more specifically the selectivity properties of these gratings, i.e., the behavior of the diffraction efficiency away from the Bragg condition $\xi = 0$. In Chapter 2, we derived the diffraction efficiency and analyzed the selectivity behavior of uniform gratings. This behavior is compared in this chapter with the selectivity of gratings that are nonuniform in amplitude as well as in phase. In Chapter 6, we will then analyze the different factors that modify the Bragg condition in photorefractive crystals, i.e., the different processes by which the Bragg detuning parameter and the Bragg condition can be altered (the Bragg condition being defined as the point where the diffraction efficiency is maximum). It is important to analyze these two factors, the Bragg condition and the selectivity, because they are important parameters to consider in holographic storage for example. Indeed, the Bragg condition determines where the information is recorded in a crystal and the selectivity is directly related to the maximum capacity that can be stored in that crystal.

In analyzing the diffraction properties of photorefractive gratings, we concentrate

on the nondestructive readout properties. Nondestructive readout assumes that either the photorefractive grating is fixed and is not erased by the readout process, or that the readout process is done at a low enough intensity so that the grating persists long enough and is not substantially erased during the readout process. As we saw in Chapter 3, the erasure time constant is directly proportional to the light intensity, therefore at weak intensity nondestructive readout can be achieved over reasonably long readout times.

In Chapter 4 we showed how an applied field, the acceptor concentration, the grating spacing and the recording geometry can significantly modify the grating shape inside the grating. In this chapter we show how these different parameters affect diffraction efficiency.

5.2 Coupled-Wave Equations

In this section we derive the coupled-wave equations describing the readout process, assuming a nondestructive readout process. We show that the equations are formally identical to the equations derived in Chapter 2 for a uniform grating, except that a nonuniform grating amplitude as well as a nonuniform Bragg detuning parameter have to be introduced.

We examine the diffraction properties of the recorded nonuniform grating when a field E_{0R} is applied to the crystal during readout. The field applied during readout need not be the same as the field applied during writing, but this difference will affect the Bragg detuning parameter as discussed in the next chapter, Chapter 6. The approach used here is similar to the one used by Kubota [29] to solve the problem of bending of interference fringes inside a hologram owing to a pre-stress in photographic emulsions.

The sum of the reading (ρ) and diffracted (σ) fields during the readout process is given by, similar to Eq. (2.11),

$$E^R(\vec{r}) = a_\rho(z) \exp(-i\vec{k}_\rho \cdot \vec{r}) + a_\sigma(z) \exp(-i\vec{k}_\sigma \cdot \vec{r}) \quad (5.1)$$

where a_ρ and a_σ are the complex field amplitudes and \vec{k}_ρ and \vec{k}_σ are the corresponding

wave vectors. On readout, momentum conservation implies that

$$\vec{k}_{\sigma\perp} = \vec{k}_{\rho\perp} + \vec{K}_{\perp} \quad (5.2)$$

By inserting Eq. (5.1) into the standard wave equation, neglecting loss, considering the slowly varying envelope approximation, and assuming that the modulation of the index of refraction is given by Eq. (4.13),

$$\Delta n(\vec{r}) = \frac{n_1}{2} m(z) \cos [\vec{K} \cdot \vec{r} + \phi_{SC} + \psi(z)] \quad (5.3)$$

we derive the following coupled equations to describe the amplitudes of the reading and the diffracted waves:

$$\begin{aligned} \cos \theta_{\rho} \frac{da_{\rho}}{dz} &= -i\kappa(z) \exp(i\phi_{SC}) a_{\sigma} \exp[i\chi(z)z] \\ \cos \theta_{\sigma} \frac{da_{\sigma}}{dz} &= -i\kappa(z) \exp(-i\phi_{SC}) a_{\rho} \exp[-i\chi(z)z] \end{aligned} \quad (5.4)$$

where the function $\chi(z)$ and the coupling function $\kappa(z)$ are given by

$$\chi(z) = k_{\rho z} - k_{\sigma z} + \frac{\psi(z)}{z} + K_z \quad (5.5)$$

$$\kappa(z) = \frac{\pi}{\lambda_o} \frac{n_1}{2} m(z) \quad (5.6)$$

and θ_{ρ} and θ_{σ} are the angles inside the crystal that the reading and the diffracted wave vectors make with the z axis, respectively. $m(z) = 2\sqrt{I_r(z)I_s(z)}/[I_r(z) + I_s(z)]$ is the modulation depth and $\psi(z) = \psi_r(z) - \psi_s(z)$ is the grating phase as defined in Chapter 4. For the transmission geometry, $m(z)$ and $\psi(z)$ are found with Eq. (4.18), and for the reflection geometry, they are found with Eq. (4.20).

With the change of variables

$$\begin{aligned} A_{\rho}(z) &= a_{\rho}(z) \\ A_{\sigma}(z) &= a_{\sigma}(z) \exp[i\chi(z)z] \end{aligned} \quad (5.7)$$

the system of equations [Eq. (5.4)] can be simplified to yield

$$\begin{aligned} \cos \theta_\rho \frac{dA_\rho}{dz} &= -i\kappa(z) \exp(i\phi_{SC}) A_\sigma \\ \cos \theta_\sigma \left(\frac{dA_\sigma}{dz} - i \frac{\tilde{\xi}(z)}{l} A_\sigma \right) &= -i\kappa(z) \exp(-i\phi_{SC}) A_\rho \end{aligned} \quad (5.8)$$

where

$$\tilde{\xi}(z) = 2\xi + l \frac{d\psi(z)}{dz} \quad (5.9)$$

is the generalized nonuniform Bragg detuning parameter. ξ is the Bragg detuning parameter in the absence of phase coupling and is given by

$$\xi = \frac{l}{2} (k_{\rho z} - k_{\sigma z} + K_z) \quad (5.10)$$

The coupled-wave equations written this way for a nonuniform grating [Eq. (5.8)] are then completely analogous to the coupled-wave equations for a uniform grating as derived in Chapter 2, Eq. (2.18), except for a coupling constant and a Bragg detuning parameter that are now functions of the propagation distance z . The boundary conditions for Eq. (5.8) are, for the transmission geometry, $A_\sigma(0) = 0$ and $A_\rho(0) = \text{constant}$, and, for the reflection geometry, $A_\sigma(l) = 0$ and $A_\rho(0) = \text{constant}$. In some specific cases, the system of coupled-equations describing the readout process can be solved to yield simple analytical solutions.

5.3 Analytical Solutions

5.3.1 Bragg Selectivity

If the coupling is weak, i.e., if the amplitude of the reading beam $a_\rho(z)$ is approximately constant throughout the crystal (the undepleted pump approximation), we can find a closed-form solution for the diffracted wave, valid in both geometries, by directly integrating Eq. (5.4):

$$a_\sigma(\xi) = -ia_\rho(0) \frac{\exp(-i\phi_{SC})}{\cos \theta_\sigma} \int_0^l \kappa(z) \exp[-i\psi(z)] \exp\left(-i2\xi \frac{z}{l}\right) dz \quad (5.11)$$

Note that Eq. (5.11) will be rederived in Chapter 8 using a completely different approach.

Uniform Grating

In the absence of phase and amplitude coupling, i.e., $\psi(z) = \psi(0)$ and $\kappa(z) = \kappa(0)$, the set of equations [Eq. (5.8)] reduces to the well-known equations of Kogelnik's theory [4], and the diffraction efficiency of the weak grating can directly be derived from Eq. (5.11), by noting that

$$\int_0^l \exp\left(-i2\xi \frac{z}{l}\right) dz = le^{-i\xi \frac{\sin \xi}{\xi}} \quad (5.12)$$

Therefore,

$$\eta(\xi) = \frac{|a_\sigma(\xi)|^2}{|a_\rho(0)|^2} = \left(\frac{\pi n_1 m(0) l}{2\lambda_o \cos \theta_\sigma} \right)^2 \text{sinc}^2 \xi \quad (5.13)$$

This equation is the same as the expression derived in Chapter 2 for the diffraction efficiency of a weak grating,

$$\eta = \nu^2 \text{sinc}^2 \xi \quad (5.14)$$

that is valid in all three geometries, the transmission, the reflection and the perpendicular geometry.

Nonuniform Grating

Equation (5.11) is also interesting because it shows how the off-Bragg behavior of a thick nonuniform grating is directly related to the Fourier transform of the complex index envelope $\Delta n(z)$, given by

$$\Delta n(z) = \frac{n_1}{2} m(z) \exp[-i\psi(z)] \quad (5.15)$$

When multiplied by a rect function corresponding to the crystal boundaries, it represents the index grating inside the crystal. According to [30], the Fourier transform $F(v)$ of a function $f(u)$ is defined as

$$F(v) = \int_{-\infty}^{\infty} f(u) e^{-i2\pi uv} du \quad (5.16)$$

This integral, which is a function of v , may be written as $F(v) = \mathcal{F}_v[f(u)]$. The formula exhibiting the reversibility of the Fourier transform is

$$f(u) = \int_{-\infty}^{\infty} F(v) e^{i2\pi uv} dv \quad (5.17)$$

The diffracted signal is then given by, noting that $u = z/l$ and $v = \xi/\pi$

$$a_\sigma(\xi) = -ia_\rho(0) \frac{\pi l \exp(-i\phi_{SC})}{\lambda_o \cos \theta_\sigma} \mathcal{F}_{\frac{\xi}{\pi}} \left[\text{rect} \left(\frac{z}{l} - \frac{1}{2} \right) \Delta n(z) \right] \quad (5.18)$$

In other words, in the undepleted pump approximation the efficiency is determined by the convolution of a sinc function (representing the crystal boundaries) and of the Fourier transform of the complex index envelope:

$$\begin{aligned} \eta(\xi) &\propto \left| \mathcal{F}_{\frac{\xi}{\pi}} \left[\Delta n(z) \text{rect} \left(\frac{z}{l} - \frac{1}{2} \right) \right] \right|^2 \\ &\propto \left| \mathcal{F}_{\frac{\xi}{\pi}} [\Delta n(z)] * \text{sinc} \xi \exp(-i\xi) \right|^2 \end{aligned} \quad (5.19)$$

When an electric field is applied to the crystal during writing, under certain conditions, as shown in Fig. 4.4, the grating amplitude $m(z)$ goes from an almost constant value inside the crystal (at 0 kV/cm) to a full sech(z) (at 10 kV/cm). Relation (5.19) shows that in this case, the shape of the selectivity curve $\eta(\xi)$ will substantially depart from the typical $\text{sinc}^2 \xi$ shape because of the convolution with the Fourier transform of the index envelope. Strong amplitude coupling essentially smoothes the tail of the selectivity curve by suppressing the side lobes, i.e., it creates a phenomenon of *apodization*. This also demonstrates the relationship as conjugate coordinates between the propagation parameter (z/l) and the Bragg detuning parameter (ξ/π).

An important case of interest is when the function $\psi(z)$ is a linear function of z :

$$\psi(z) = \omega z \quad (5.20)$$

where ω is some arbitrary constant coefficient. In this case, the diffraction efficiency is given by

$$\eta(\xi) \propto \left| \mathcal{F}_{\xi + \frac{l\omega}{2\pi}} \left[m(z) \text{rect} \left(\frac{z}{l} - \frac{1}{2} \right) \right] \right|^2 \quad (5.21)$$

Therefore the diffraction efficiency is simply translated along the ξ axis by an amount $l\omega/2$ and the selectivity shape depends only on the Fourier transform of the modulation depth $m(z)$. This case is important because $\psi(z)$ is a linear function of z in the following three cases: in the reflection geometry [Eq. (4.20)], in the transmission geometry for small pump-to-probe ratios [Eq. (4.25)], and in the transmission geometry for $\gamma = 0$ [Eq. (4.26)]. In this last case, the amplitude of the grating is constant, too (because there is no amplitude coupling): in the perfectly drift-dominated case (i.e., $\gamma = 0$), $\kappa(z) = \text{constant}$ and from Eq. (4.26), $\xi(z)$ is given by

$$\tilde{\xi}(z) = 2\xi - l\beta \frac{1 - r_{pp}}{1 + r_{pp}} \quad (5.22)$$

In this case, the solutions to Eq. (5.8) reduce to Kogelnik's solutions [4] for a uniform grating with a constant detuning parameter.

Discussions

Figure 5.1 shows the modulation depth $m(z)$ and the corresponding selectivity behavior of the diffraction efficiency in the transmission geometry for a pump-to-probe ratio $r_{pp} = 1/100$, a grating spacing $\Lambda = 5 \mu\text{m}$ and an acceptor concentration $N_0^\circ = 1.5 \cdot 10^{23} \text{ m}^{-3}$ (for the same SBN:60 crystal used in Chapter 4, $l = 2.5 \text{ mm}$ and $N = 10^{25} \text{ m}^{-3}$). The four figures correspond to four different applied fields, 0, 3, 6, and 9 kV/cm. In this case, the selectivity behavior is just the Fourier transform of the function $m(z)$ inside the crystal. However, due to phase coupling, there is a rotation of the fringes of the grating that translates itself onto a translation of the diffraction efficiency along the ξ axis. The maximum diffraction efficiency is around 10 to 12 %, which shows that the Fourier transform approximation is valid in this case.

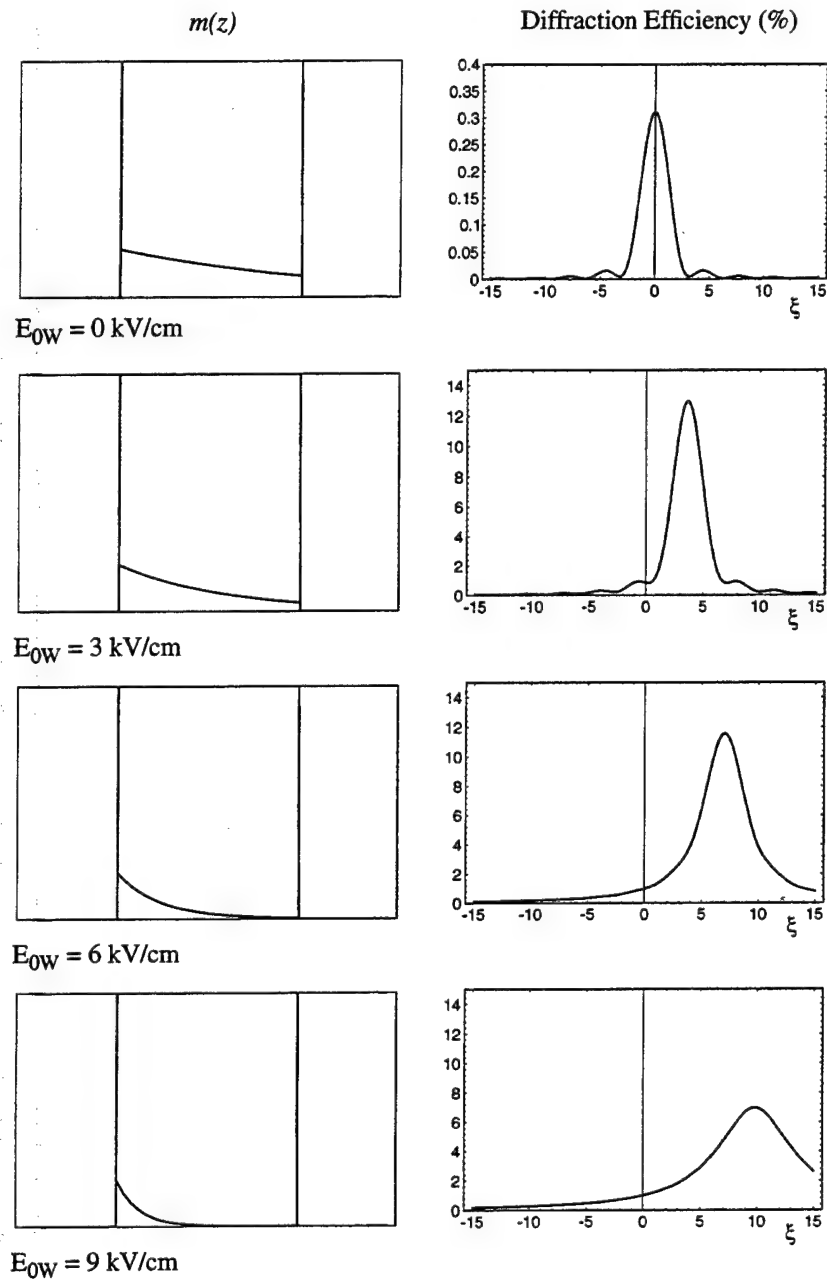


Figure 5.1: Index modulation depth $m(z)$ and corresponding selectivity behavior in the transmission geometry ($r_{pp} = 1/100$, $\Lambda = 5 \mu\text{m}$, $N_0^\circ = 1.5 \cdot 10^{23} \text{ m}^{-3}$, $l = 2.5 \text{ mm}$ and $N = 10^{25} \text{ m}^{-3}$ for a SBN:60 crystal). The boxes on the left-hand figures represent the crystal boundaries and are normalized to unity.

Figure 5.2 shows the index modulation depth $m(z)$ and the corresponding selectivity behavior in the reflection geometry at no applied field, for a grating spacing $\Lambda = 0.1 \mu\text{m}$ and an acceptor concentration $N_0^o = 2 \cdot 10^{24} \text{ m}^{-3}$. The two figures correspond to two pump-to-probe ratios r_{pp} , 1/100 and 100. In this case, too, the selectivity behavior is just the Fourier transform on the function $m(z)$ inside the crystal. In the reflection geometry phase coupling is negligible, as mentioned in Chapter 4, regardless of the value of N_0^o and indeed no significant translation of the diffraction efficiency along the ξ axis is observed.

5.3.2 Maximum Diffraction Efficiency

If $\tilde{\xi}(z)$ is taken equal to zero in Eq. (5.8) and the symmetric configuration is considered ($\cos \theta_p = \cos \theta$), a general analytical solution valid for any given $\kappa(z)$ can be found. Hong and Saxena [31] derived the solutions for the specific case when $m(z)$ is given by Eq. (4.24). More generally, for any $m(z)$, the solution for the diffraction efficiency η can be written as follows:

For the transmission geometry,

$$\eta = \sin^2 \left(\frac{\pi n_1}{2\lambda_o \cos \theta} \int_0^l m(z) dz \right) \quad (5.23)$$

When $m(z)$ is given by Eq. (4.24),

$$m(z) = \text{sech} \left(\frac{\gamma z - \ln r_{pp}}{2} \right) \quad (5.24)$$

the diffraction efficiency [Eq. (5.23)] can be written as

$$\eta = \sin^2 \left[\frac{1}{\sin \phi_{SC}} \arctan \left(\tanh \frac{\gamma z - \ln r_{pp}}{4} \right) + \frac{1}{\sin \phi_{SC}} \arctan \left(\tanh \frac{\ln r_{pp}}{4} \right) \right] \quad (5.25)$$

For the reflection geometry,

$$\eta = \tanh^2 \left(\frac{\pi n_1}{2\lambda_o \cos \theta} \int_0^l m(z) dz \right) \quad (5.26)$$

when $m(z)$ is given by Eq. (4.27),

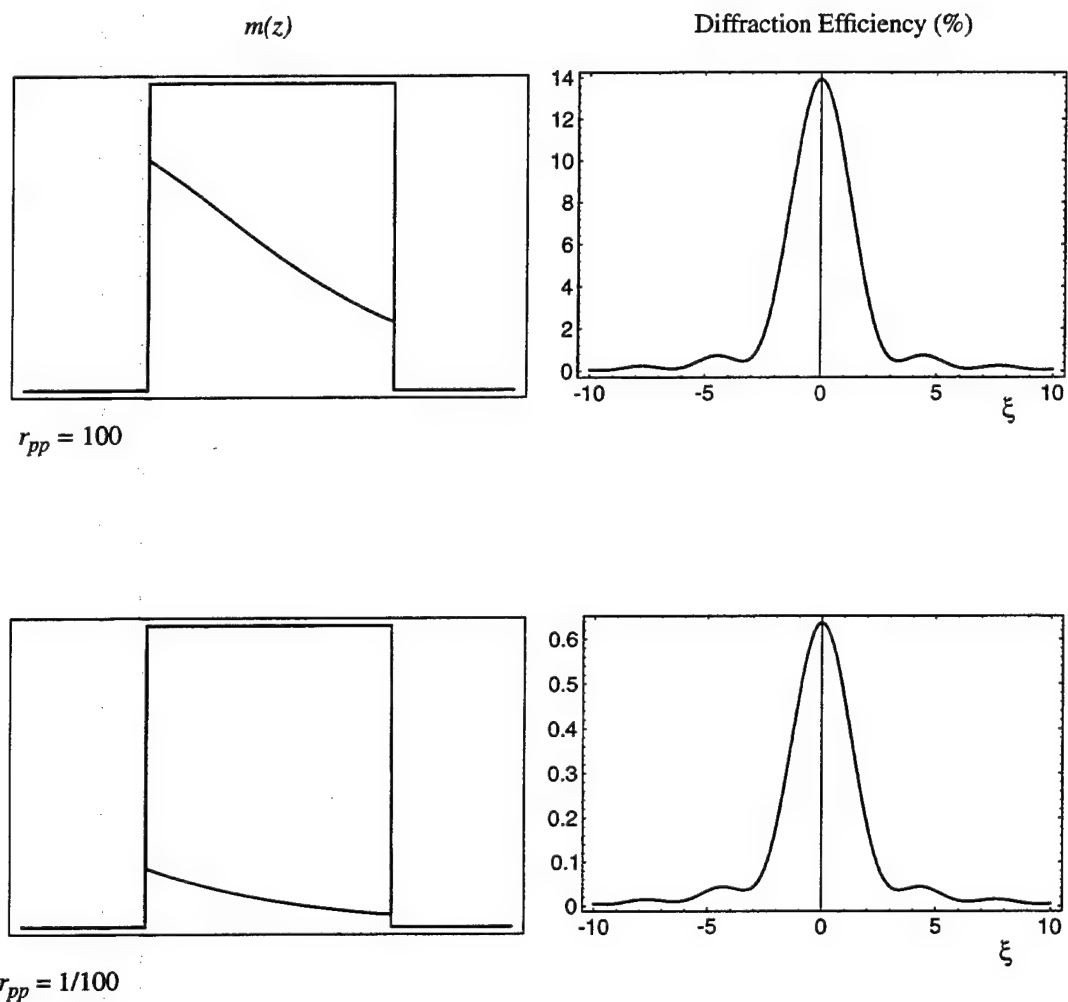


Figure 5.2: Index modulation depth $m(z)$ and corresponding selectivity behavior in the reflection geometry at no applied field ($\Lambda = 0.1 \mu\text{m}$, $N_0^o = 2 \cdot 10^{24} \text{ m}^{-3}$, $l = 2.5 \text{ mm}$ and $N = 10^{25} \text{ m}^{-3}$ for a SBN:60 crystal).

$$m(z) = \frac{1}{\sqrt{1 + \exp\left(\gamma z - \ln \frac{B}{C^2}\right)}} \quad (5.27)$$

the diffraction efficiency [Eq. (5.26)] can be written as

$$\eta = \tanh^2 \left[\frac{2}{\sin \phi_{SC}} \mathcal{G} \left(\sqrt{1 + \frac{C^2}{B}} \right) + \frac{2}{\sin \phi_{SC}} \mathcal{G} \left(\sqrt{1 + \exp\left(\gamma l - \ln \frac{B}{C^2}\right)} \right) \right] \quad (5.28)$$

where

$$\mathcal{G}(x) = \frac{1}{2} \ln \left| \frac{1+x}{1-x} \right| \quad (5.29)$$

Equations (5.23) and (5.26) can be considered as expressions representing the maximum diffraction efficiency because they correspond to zero Bragg detuning [$\tilde{\xi}(z) = 0$]. In the case of uniform gratings, they reduce to the equations derived in Chapter 2,

$$\begin{aligned} \eta &= \sin^2 \nu \quad (\text{transmission}) \\ \eta &= \tanh^2 \nu \quad (\text{reflection}) \end{aligned} \quad (5.30)$$

Figure 5.3 shows the maximum diffraction efficiency (for three different grating spacings Λ) as a function of applied field (E_{0W}) in the transmission geometry ($r_{pp} = 1/100$). It shows that after some point the maximum diffraction efficiency starts to decrease with field. This is due to stronger amplitude coupling between the writing beams, causing the amplitude of the index grating to be significant only at $z = 0$, i.e., near the entrance face of the crystal: amplitude coupling decreases the effective thickness of the index envelope. At high applied fields this thickness decrease dominates the increase in space-charge field amplitude in such a way that the net diffraction efficiency decreases.

Figure 5.4 shows experimental measurements of the maximum diffraction efficiency as a function of applied field (E_{0W}) in the transmission geometry ($r_{pp} = 1/100$ and $\Lambda = 5 \mu\text{m}$). It shows good qualitative agreement with the theoretical curves of Fig. 5.3 (the experimental setup will be further discussed in Chapter 6). Several points need

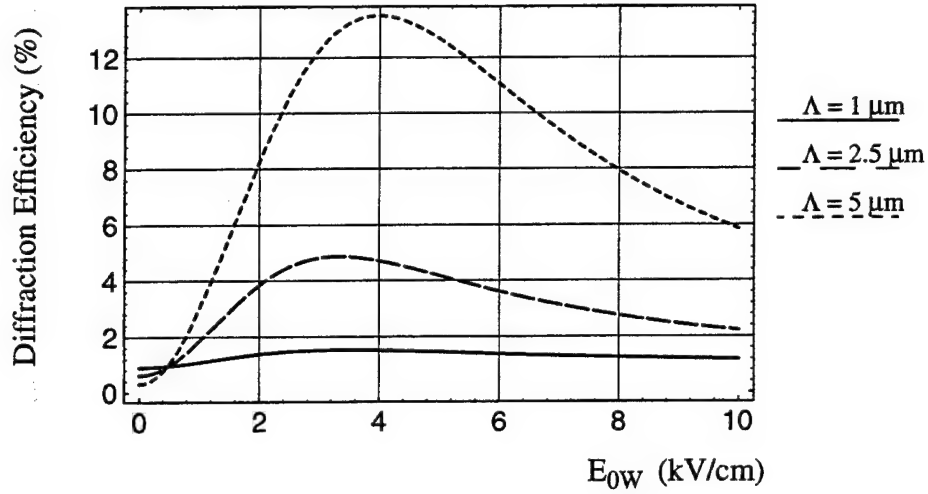


Figure 5.3: Maximum diffraction efficiency as a function of applied field (E_{0W}) for three grating spacings, Λ ($1 \mu\text{m}$, $2.5 \mu\text{m}$ and $5 \mu\text{m}$) (transmission geometry and $r_{pp} = 1/100$).

to be emphasized though: (i) it is difficult to measure absolute efficiencies, as shown on Fig. 5.4 in which two sets of identical experiments are represented. Measurements are often unpredictable because the crystal is not uniform and the results depend on the location used inside the crystal to record the holograms; (ii) at high applied fields, the gain being very high, it induces strong beam fanning that also tends to deplete the diffracted signal. Figure 5.5 shows the maximum diffraction efficiency (for four different acceptor concentrations N_0^o) as a function of pump-to-probe ratio r_{pp} , in the reflection geometry, and at no applied field. It shows that there is a point where the diffraction efficiency is maximum. This point, which is a function of the acceptor concentration, is directly related to the value of the pump-to-probe ratio for which the grating, in the reflection geometry, is uniform. We showed in Chapter 4 [Eq. (4.30)] that when

$$\ln r_{pp} = \frac{\gamma l}{2} \quad (5.31)$$

the modulation depth inside the crystal is uniformly equal to unity inside the crystal.

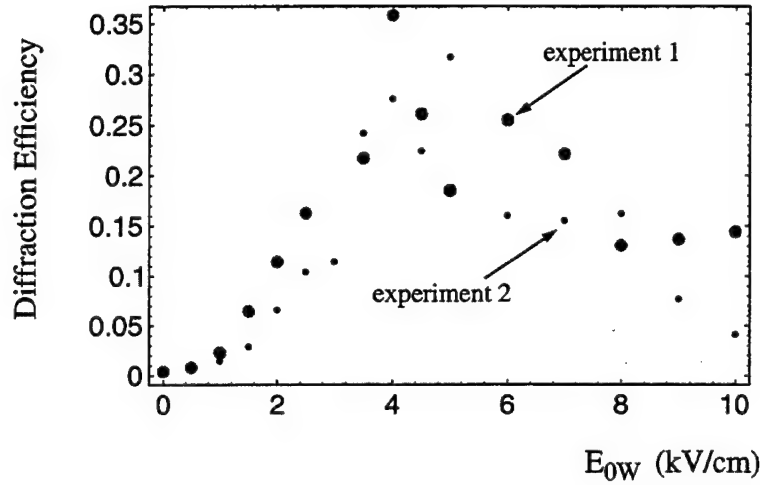


Figure 5.4: Experimental maximum diffraction efficiency as a function of applied field (E_{0W}) for a grating spacing $\Lambda = 5 \mu\text{m}$ (transmission geometry and $r_{pp} = 1/100$).

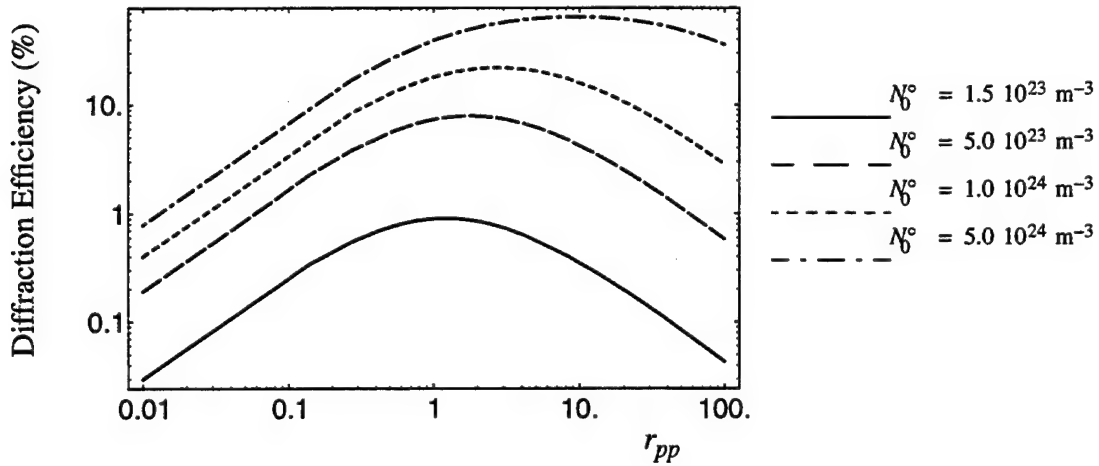


Figure 5.5: Maximum diffraction efficiency as a function of pump-to-probe ratio (r_{pp}) for four acceptor concentrations N_0^o at $\Lambda = 0.1 \mu\text{m}$ (reflection geometry and $E_{0W} = 0$ kV/cm).

This point is also the point where the diffraction efficiency is maximum. At small acceptor concentrations, the parameter γ is small and the diffraction efficiency is maximum for a pump-to-probe ratio close to one.

5.4 Conclusions

In this chapter we have solved the coupled-wave equations describing the readout process for fixed nonuniform gratings. We have derived analytical solutions for the diffraction efficiency in the undepleted pump approximation as well as in the case of zero Bragg detuning $\tilde{\xi}(z) = 0$. The most important conclusion is that a phenomenon of apodization is observed in the diffraction efficiency because the photorefractive grating is nonuniform: the side lobes of the selectivity behavior that are normally observed in the case of uniform gratings disappear when the grating is nonuniform.

In the transmission geometry, in order to solve the complete problem, i.e., with a depleted pump, a general modulation depth $m(z)$, and a general phase $\psi(z)$, to the best of our knowledge, it is necessary to solve the set of equations numerically as no analytical solution could be found. The reflection geometry is easier to treat because $\tilde{\xi}(z)$ is a constant. Hofmeister *et al.* [32] were able to derive a general analytical solution in this case using hypergeometric functions.

In the next chapter we will concentrate on the Bragg condition, i.e., the point where the diffraction efficiency is maximum. We already showed how phase coupling in the transmission geometry induces a shift of the selectivity curve along the Bragg detuning axis due to fringe bending. In the next chapter we will consider other effects that can also contribute to a change in the Bragg condition. Finally we will show a series of experimental results confirming the theory developed in this chapter and in Chapter 6.

Chapter 6

Bragg Detuning Effects

6.1 Introduction

In this chapter, we study in detail the different mechanisms that affect Bragg detuning and that are usually encountered in applications making use of photorefractive crystals. When a grating is recorded in a photorefractive crystal, the Bragg condition is satisfied when, by definition, the expression $\tilde{\xi}(z)$ is identically equal to zero. Physically, it means that the Bragg condition is satisfied when, for example, the reading configuration is identical to the recording configuration and no fringe bending takes place. However in many practical instances, the recording and the readout configurations are different because of changes in external conditions. As we shall show, this situation induces a shift of the diffraction efficiency along the Bragg detuning axis. These changes can, for example, be due to variations in the angle or the wavelength of the readout beam relative to the position or wavelength of the reference beam. A change in Bragg condition can also be due to variations in the index of refraction of the crystal or to an expansion or a dilatation of the crystal. In the former case, it modifies the wavelength of light inside the crystal and in the latter case it affects the grating spacing inside the crystal. Such effects can be induced by electric fields applied to the photorefractive crystal, by polarization changes or by temperature changes. It is thus important to start by analyzing the Bragg detuning parameter separately to determine exactly by how much the diffraction efficiency is detuned for

a given change in external conditions.

We start from the general expression for the Bragg detuning parameter derived in Chapter 5,

$$\tilde{\xi}(z) = 2\xi + \xi_{PC}(z) \quad (6.1)$$

where

$$\xi = \frac{l}{2}(k_{\rho z} - k_{\sigma z} + K_z) = \xi^{\Delta n} + \xi^{\Delta \Lambda} \quad (6.2)$$

and

$$\xi_{PC}(z) = l \frac{d\psi(z)}{dz} \quad (6.3)$$

By definition $\xi^{\Delta n}$ encompasses the terms that depend on changes in angle and wavelength of the readout beam and the terms that depend on changes in index of refraction of the crystal. $\xi^{\Delta \Lambda}$ encompasses the terms that account for the crystal expansion (or dilatation). From these definitions we derive, in the rest of this chapter, an explicit and comprehensive analytical expression for the Bragg detuning parameter $\tilde{\xi}$, assuming a first-order calculation. We then show experimental results of Bragg detuning measurements in strontium barium niobate (SBN) and fit the results to the general theory. We first show results from measurements of Bragg detuning due to fringe bending and phase coupling when an electric field is applied to a SBN:60 crystal during recording. We then show how the electro-optic effect induces Bragg detuning in SBN:75 and deduce values for the electro-optic coefficient of the crystal. Finally, we show how the measurement of Bragg detuning at different polarizations yields a value for the birefringence of SBN:60.

6.2 Angle, Wavelength and Index Changes

In this section, we analyze how the Bragg detuning parameter (denoted by $\xi^{\Delta n}$ in this case) is affected by changes in the angle and the wavelength of the readout beam and

by changes in the bulk index of refraction \bar{n} of the crystal. $\xi^{\Delta n}$ is given by Eq. (6.2), otherwise written as

$$\xi^{\Delta n} = \frac{l}{2}(k_{\rho z} - k_{\sigma z} - k_{rz} + k_{sz}) \quad (6.4)$$

If λ_o is the wavelength during writing and $\lambda_o + \Delta\lambda_o$ is the wavelength during readout ($\Delta\lambda_o$ is a variable describing to first order the wavelength detuning of the readout beam), the different components of the four wave vectors are given by

$$\begin{aligned} k_{\rho z} &= \frac{2\pi}{\lambda_o + \Delta\lambda_o} n_\rho \cos \theta_\rho & k_{\rho \perp} &= \frac{2\pi}{\lambda_o + \Delta\lambda_o} n_\rho \sin \theta_\rho \\ k_{\sigma z} &= \frac{2\pi}{\lambda_o + \Delta\lambda_o} n_\sigma \cos \theta_\sigma & k_{\sigma \perp} &= \frac{2\pi}{\lambda_o + \Delta\lambda_o} n_\sigma \sin \theta_\sigma \end{aligned} \quad (6.5)$$

$$k_{rz} = \frac{2\pi}{\lambda_o} n_r \cos \theta_r \quad k_{r \perp} = \frac{2\pi}{\lambda_o} n_r \sin \theta_r$$

$$k_{sz} = \frac{2\pi}{\lambda_o} n_s \cos \theta_s \quad k_{s \perp} = \frac{2\pi}{\lambda_o} n_s \sin \theta_s$$

where n_i ($i = r, s, \rho, \sigma$) is the index seen by the respective beam. Because of the anisotropy of the crystal, the different beams do not necessarily see the same index of refraction. We define

$$\begin{aligned} \theta_\rho &= \theta_r + \Delta\theta_\rho \\ \theta_\sigma &= \theta_s + \Delta\theta_\sigma \end{aligned} \quad (6.6)$$

where $\Delta\theta_\rho$ is a variable describing to first order the angular detuning of the readout beam. $\Delta\theta_\sigma$ describes the angular shift of the diffracted beam and can be determined directly from the momentum-conservation relation, $k_{\sigma \perp} = k_{\rho \perp} + K_\perp$,

$$\frac{n_\sigma}{\lambda_o + \Delta\lambda_o} \sin \theta_\sigma = \frac{n_\rho}{\lambda_o + \Delta\lambda_o} \sin \theta_\rho + \frac{n_s}{\lambda_o} \sin \theta_s - \frac{n_r}{\lambda_o} \sin \theta_r \quad (6.7)$$

that simplifies to

$$n_\sigma(\sin \theta_s + \Delta\theta_\sigma \cos \theta_s) = n_\rho(\sin \theta_r + \Delta\theta_\rho \cos \theta_r) + (n_s \sin \theta_s - n_r \sin \theta_r) \left(1 + \frac{\Delta\lambda_o}{\lambda_o}\right) \quad (6.8)$$

by keeping only the first-order terms in $\Delta\theta_\rho$, $\Delta\theta_\sigma$, and $\Delta\lambda_o$. We assume that there is no first-order change in the index of refraction as a function of angle (this is the case in uniaxial crystals, as explained later), i.e.,

$$n_\sigma = n_\sigma(\theta_\sigma) = n_\sigma(\theta_s + \Delta\theta_\sigma) = n_\sigma(\theta_s) \quad (6.9)$$

The difference between n_r and n_s is assumed to be a first-order quantity, as well as the differences

$$\begin{aligned} \Delta n_\rho &= n_\rho - n_r \\ \Delta n_\sigma &= n_\sigma - n_s \end{aligned} \quad (6.10)$$

In this case we can define an average bulk index of refraction \bar{n} , and the angular shift of the diffracted beam can be expressed as

$$\Delta\theta_\sigma = \frac{1}{\cos\theta_s} \left[\left(\frac{\Delta n_\rho}{\bar{n}} - \frac{\Delta\lambda_o}{\lambda_o} \right) \sin\theta_r - \left(\frac{\Delta n_\sigma}{\bar{n}} - \frac{\Delta\lambda_o}{\lambda_o} \right) \sin\theta_s + \Delta\theta_\rho \cos\theta_r \right] \quad (6.11)$$

By using Eq. (6.11) and Eq. (6.5) in the definition of the Bragg detuning parameter [(Eq. (6.4))] and by considering only the first-order terms in $\Delta\theta_\rho$, Δn_σ , Δn_ρ , and $\Delta\lambda_o$, we can express $\xi^{\Delta n}$ as

$$\xi^{\Delta n} = \frac{\pi \bar{n} l}{\lambda_o \cos\theta_s} \left[\left(\frac{\Delta n_\rho}{\bar{n}} - \frac{\Delta\lambda_o}{\lambda_o} \right) \cos(\theta_r - \theta_s) - \left(\frac{\Delta n_\sigma}{\bar{n}} - \frac{\Delta\lambda_o}{\lambda_o} \right) - \Delta\theta_\rho \sin(\theta_r - \theta_s) \right] \quad (6.12)$$

This expression is valid in all three writing geometries. The angular detuning $\Delta\theta_\rho$ is taken inside the crystal. There are thus two contributions to this angular detuning: one is due to the outside physical rotation of the readout beam and one is due to the change in index of refraction Δn_ρ , which also creates a rotation of the readout beam inside the crystal because of Snell's law, even if the beam is not physically rotated outside the crystal.

In the transmission and the reflection geometry, if the angles outside the crystal are denoted by a hat, $\hat{\theta}$, one can write

$$\sin \hat{\theta}_\rho = n_\rho \sin \theta_\rho \quad (6.13)$$

$$\sin \hat{\theta}_r + \Delta \hat{\theta}_\rho \cos \hat{\theta}_r = n_\rho (\sin \theta_r + \Delta \theta_\rho \cos \theta_r) \quad (6.14)$$

where $\Delta \hat{\theta}_\rho = \hat{\theta}_\rho - \hat{\theta}_r$ is the amount by which the readout beam is physically rotated outside the crystal relative to the position of the reference beam. Since $n_\rho(\theta_\rho) = n_\rho(\theta_r)$ and $\sin \hat{\theta}_r = n_r \sin \theta_r$,

$$\Delta \theta_\rho = \frac{\Delta \hat{\theta}_\rho \cos \hat{\theta}_r}{\bar{n} \cos \theta_r} - \frac{\Delta n_\rho}{\bar{n}} \tan \theta_r \quad (6.15)$$

Similarly, in the perpendicular geometry, because the reference beam is incident on a perpendicular surface of the crystal and all the angles are measured with respect to the z axis,

$$\cos \hat{\theta}_\rho = n_\rho \cos \theta_\rho \quad (6.16)$$

$$\cos \hat{\theta}_r - \Delta \hat{\theta}_\rho \sin \hat{\theta}_r = n_\rho (\cos \theta_r - \Delta \theta_\rho \sin \theta_r) \quad (6.17)$$

Since $n_\rho(\theta_\rho) = n_\rho(\theta_r)$ and $\cos \hat{\theta}_r = n_r \cos \theta_r$,

$$\Delta \theta_\rho = \frac{\Delta \hat{\theta}_\rho \sin \hat{\theta}_r}{\bar{n} \sin \theta_r} + \frac{\Delta n_\rho}{\bar{n}} \cot \theta_r \quad (6.18)$$

If the angle and the wavelength of the readout beam remain unchanged and if the contribution from the index change is assumed isotropic, $\Delta n_\rho = \Delta n_\sigma = \Delta n$, the Bragg detuning parameter is given by

$$\xi^{\Delta n} = \frac{\pi \Delta n l \cos \theta_s - \cos \theta_r}{\lambda_o \cos \theta_s \cos \theta_r} \quad (6.19)$$

in the transmission and in the reflection geometries, and by

$$\xi^{\Delta n} = \frac{\pi \Delta n l \sin \theta_s - \sin \theta_r}{\lambda_o \cos \theta_s \sin \theta_r} \quad (6.20)$$

in the perpendicular geometry. Equation (6.19) is important because it demonstrates that by just using the symmetric configuration in the transmission geometry, it is possible to cancel out the contribution due to an isotropic index change in the expression for the Bragg detuning parameter.

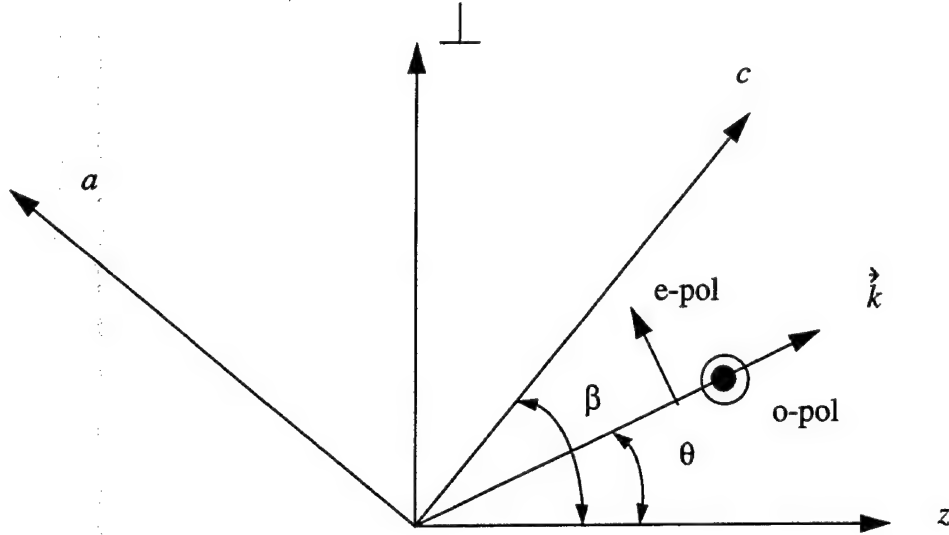


Figure 6.1: Crystal orientation with respect to the propagation axis. $\beta = 0^\circ$ for the reflection geometry, $\beta = 45^\circ$ for the perpendicular geometry, and $\beta = 90^\circ$ for the transmission geometry.

Uniaxial crystals

In this subsection we compute the index changes that occur in crystals that typically are used for photorefractive applications: uniaxial crystals like SBN and LiNbO₃. We consider the geometry shown in Fig. 6.1 with the c axis in the plane of incidence. In-plane polarization corresponds to extraordinary polarization and out-of-plane polarization corresponds to ordinary polarization. For ordinary polarization the light sees an isotropic material, and the changes in index of refraction are thus isotropic. For an extraordinarily polarized beam incident at an angle θ , the index of refraction is determined by solving

$$\frac{1}{n_e^2(\theta)} = \frac{\sin^2(\theta - \beta)}{n_e^2} + \frac{\cos^2(\theta - \beta)}{n_o^2} \quad (6.21)$$

where β is the angle that the c axis makes with the propagation axis z , and n_o is the ordinary and n_e is the extraordinary index of refraction. The angle β is chosen such that the grating vector \vec{K} is parallel to the c axis to maximize the diffraction efficiency. During readout, assuming that the crystal remains uniaxial (this is rigorously true

only if the space-charge field and the applied electric field are aligned along the c axis of the crystal), the two principal indices of refraction, n_o and n_e , change to

$$\begin{aligned} n_o &\rightarrow n_o + \Delta n_o \\ n_e &\rightarrow n_e + \Delta n_e \end{aligned} \quad (6.22)$$

As a result of thermal and electric field effects,

$$\begin{aligned} \Delta n_o &= -\frac{1}{2}r_{13}n_o^3\Delta E_0 + \frac{\partial n_o}{\partial T}\Delta T \\ \Delta n_e &= -\frac{1}{2}r_{33}n_e^3\Delta E_0 + \frac{\partial n_e}{\partial T}\Delta T \end{aligned} \quad (6.23)$$

where ΔE_0 and ΔT are variations in applied field and temperature between the readout and the recording configurations, r_{13} and r_{33} are the electro-optic coefficients and $\partial n_o/\partial T$ and $\partial n_e/\partial T$ are the index coefficients for thermal change. The new index of refraction is then given by

$$\frac{1}{[n_e(\theta) + \Delta n_e(\theta)]^2} = \frac{\sin^2(\theta - \beta)}{(n_e + \Delta n_e)^2} + \frac{\cos^2(\theta - \beta)}{(n_o + \Delta n_o)^2} \quad (6.24)$$

To first order in Δn_e and Δn_o , $\Delta n_e(\theta)$ is given by

$$\Delta n_e(\theta) = \sin^2(\theta - \beta)\Delta n_e + \cos^2(\theta - \beta)\Delta n_o \quad (6.25)$$

It can be shown that there is no index change to first order as a result of a first-order change in angle, i.e., if $\theta = \bar{\theta} + \Delta\theta$, $n_e(\theta) = n_e(\bar{\theta})$ if $\Delta\theta$ is a first-order quantity. In the rest of this chapter we assume that the same polarization is used for the readout, the diffracted, and the writing beams. Therefore if ordinary polarization is used, $\Delta n_\rho = \Delta n_\sigma = \Delta n_o$, and if extraordinary polarization is used, $\Delta n_\rho = \Delta n_e(\theta_r)$ and $\Delta n_\sigma = \Delta n_e(\theta_s)$. In the transmission geometry ($\beta = \pi/2$), it is most often the case that the angles of incidence (θ_r, θ_s) inside the crystal are small. Since furthermore in most of the crystals $r_{13} \ll r_{33}$, to a good approximation, Eq. (6.25) simplifies to

$$\Delta n_e(\theta) \approx \Delta n_e \quad (6.26)$$

and the crystal can be considered as an isotropic medium regarding index of refraction changes, even for extraordinarily polarized light. The general formulation for the Bragg detuning parameter [Eq. (6.12)] is also valid to describe anisotropic diffraction where the readout beam and the diffracted beam have different polarization states [33].

6.3 Crystal Expansion

If the crystal itself expands or contracts after recording, it leads to a change in the length of the grating spacing. The related change in grating vector then induces a change in the Bragg detuning parameter (denoted by $\xi^{\Delta\Lambda}$ in this case). Starting from Eq. (6.2),

$$\xi^{\Delta\Lambda} = \frac{l}{2}(k_{\rho z} + K_z^d - \sqrt{k^2 - (k_{\rho\perp} + K_{\perp}^d)^2}) \quad (6.27)$$

where

$$\begin{aligned} \vec{k}_{\rho} &= \vec{k}_r \\ k^2 &= |\vec{k}_r|^2 \\ \vec{K}^d &= \vec{K} + \Delta\vec{K} \end{aligned} \quad (6.28)$$

where \vec{K} is the initial grating vector and \vec{K}^d is the grating vector after deformation. Therefore

$$\xi^{\Delta\Lambda} = \frac{l}{2} \left[k_{sz} + \Delta K_z - \sqrt{k^2 - (k_{s\perp} + \Delta K_{\perp})^2} \right] \quad (6.29)$$

which, to first order in ΔK_z and ΔK_{\perp} , reduces to

$$\xi^{\Delta\Lambda} = \frac{l}{2} (\Delta K_z + \tan \theta_s \Delta K_{\perp}) \quad (6.30)$$

In practice, the known quantities are the strains along the two principal axes, $\epsilon_c = \Delta\Lambda_c/\Lambda_c$ and $\epsilon_a = \Delta\Lambda_a/\Lambda_a$, where Λ_c and Λ_a are the projections of the grating spacing

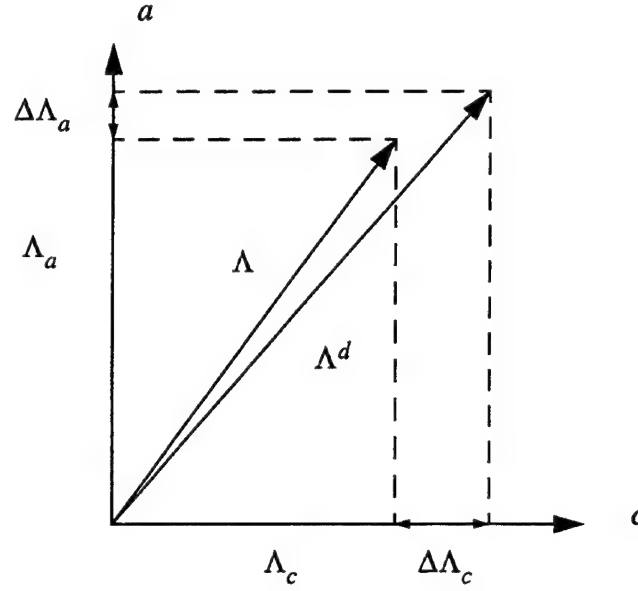


Figure 6.2: Anisotropic expansion of the grating spacing inside the crystal: deformations along the principal axes of the crystal ($\Lambda = 2\pi/|\vec{K}|$ and $\Lambda^d = 2\pi/|\vec{K}^d|$).

$\Lambda = 2\pi/|\vec{K}|$ along the c and a axes, respectively (Fig. 6.2). We then need to relate these known strains to the changes in grating vector ΔK_z and ΔK_\perp . We have

$$\begin{aligned} K_c &= \vec{K} \cdot \hat{e}_c = 2\pi \frac{\Lambda_c}{\Lambda_a^2 + \Lambda_c^2} \\ K_a &= \vec{K} \cdot \hat{e}_a = 2\pi \frac{\Lambda_a}{\Lambda_a^2 + \Lambda_c^2} \end{aligned} \quad (6.31)$$

By differentiating Eq. (6.31) we get that

$$\begin{aligned} \frac{\Delta K_c}{K_c} &= \frac{K_a^2 - K_c^2}{\vec{K}^2} \frac{\Delta \Lambda_c}{\Lambda_c} - 2 \frac{K_a^2}{\vec{K}^2} \frac{\Delta \Lambda_a}{\Lambda_a} \\ \frac{\Delta K_a}{K_a} &= \frac{K_c^2 - K_a^2}{\vec{K}^2} \frac{\Delta \Lambda_a}{\Lambda_a} - 2 \frac{K_c^2}{\vec{K}^2} \frac{\Delta \Lambda_c}{\Lambda_c} \end{aligned} \quad (6.32)$$

From the definition of the grating vector \vec{K} we have that

$$\begin{aligned} K_c &= \frac{2\pi\bar{n}}{\lambda_o} [\cos(\theta_s - \beta) - \cos(\theta_r - \beta)] \\ K_a &= \frac{2\pi\bar{n}}{\lambda_o} [\sin(\theta_s - \beta) - \sin(\theta_r - \beta)] \end{aligned} \quad (6.33)$$

We also have that

$$\begin{aligned}\Delta K_z &= \Delta K_c \cos \beta - \Delta K_a \sin \beta \\ \Delta K_\perp &= \Delta K_c \sin \beta + \Delta K_a \cos \beta\end{aligned}\quad (6.34)$$

By use of Eqs. (6.32), (6.33) and (6.34) in the expression for $\xi^{\Delta\Lambda}$ [Eq. (6.30)], it is possible to relate the detuning parameter to the strains $\Delta\Lambda_c/\Lambda_c$ and $\Delta\Lambda_a/\Lambda_a$:

$$\begin{aligned}\xi^{\Delta\Lambda} = \frac{l}{2 \cos \theta_s} &\left\{ \cos(\theta_s - \beta) \frac{K_c}{\bar{K}^2} \left[(K_a^2 - K_c^2) \frac{\Delta\Lambda_c}{\Lambda_c} - 2K_a^2 \frac{\Delta\Lambda_a}{\Lambda_a} \right] + \right. \\ &\left. \sin(\theta_s - \beta) \frac{K_a}{\bar{K}^2} \left[(K_c^2 - K_a^2) \frac{\Delta\Lambda_a}{\Lambda_a} - 2K_c^2 \frac{\Delta\Lambda_c}{\Lambda_c} \right] \right\}\end{aligned}\quad (6.35)$$

which can be simplified to yield

$$\begin{aligned}\xi^{\Delta\Lambda} = \frac{\pi l \bar{n}}{\lambda_o \cos \theta_s} &\left\{ [\cos(\theta_r - \theta_s) - 1] \left[\frac{\Delta\Lambda_c}{\Lambda_c} \cos^2(\theta_r - \beta) + \frac{\Delta\Lambda_a}{\Lambda_a} \sin^2(\theta_r - \beta) \right] - \right. \\ &\left. \sin(\theta_r - \theta_s) \left(\frac{\Delta\Lambda_a}{\Lambda_a} - \frac{\Delta\Lambda_c}{\Lambda_c} \right) \sin(\theta_r - \beta) \cos(\theta_r - \beta) \right\}\end{aligned}\quad (6.36)$$

We consider two types of crystal expansion; one is due to thermal changes and the other one is due to electric fields. In the rest of this chapter and in Chapter 7 we show under which circumstances these two effects are either important or negligible.

6.3.1 Thermal Expansion

When a crystal is heated, it expands according to [34]

$$\epsilon_{ij} = \alpha_{ij} T \quad (6.37)$$

where the thermal expansion coefficient α is a second-rank tensor that relates temperature (T) to strain (ϵ), another second-rank tensor. For uniaxial crystals, there are only two nonzero coefficients, $\alpha_{11} = \alpha_{22} = \alpha_a$ and $\alpha_{33} = \alpha_c$, along the two principal axes of the crystal. This leads to

$$\begin{aligned}\epsilon_c &= \epsilon_{33} = \frac{\Delta\Lambda_c}{\Lambda_c} = \alpha_c \Delta T \\ \epsilon_a &= \epsilon_{11} = \frac{\Delta\Lambda_a}{\Lambda_a} = \alpha_a \Delta T\end{aligned}\quad (6.38)$$

where ΔT is the change in temperature between writing and readout. The following convention is adopted for the sign of α : if $\alpha > 0$, the crystal expands when it is heated ($\Delta T \geq 0$).

6.3.2 Piezoelectric Expansion

An electric field \vec{E}_0 applied to a photorefractive crystal induces expansion (strain) inside the crystal through the piezoelectric effect

$$\epsilon_{ij} = \sum_j d_{ijk} E_{0k} \quad (6.39)$$

where d_{ijk} is the piezoelectric tensor [27]. For uniaxial crystals and an electric field E_0 applied along the c axis, the only piezoelectric coefficients (in reduced notation) relevant to the expansion of the crystal are d_{13} and d_{33} :

$$\begin{aligned}\epsilon_c &= \frac{\Delta\Lambda_c}{\Lambda_c} = d_{33} \Delta E_0 \\ \epsilon_a &= \frac{\Delta\Lambda_a}{\Lambda_a} = d_{13} \Delta E_0\end{aligned}\quad (6.40)$$

where $\Delta E_0 = E_{0W} - E_{0R}$ is the change in applied field between writing and readout.

6.4 Bragg Detuning Parameter

The complete Bragg detuning parameter ξ can then be written as the sum of the two contributions,

$$\xi = \xi^{\Delta n} + \xi^{\Delta \Lambda} \quad (6.41)$$

Therefore,

$$\xi = \frac{\pi l \bar{n}}{\lambda_o \cos \theta_s} \left\{ \frac{\Delta n_\rho - \Delta n_\sigma}{\bar{n}} + \left[\epsilon_c \cos^2(\theta_r - \beta) + \epsilon_a \sin^2(\theta_r - \beta) + \frac{\Delta n_\rho}{\bar{n}} - \frac{\Delta \lambda_o}{\lambda_o} \right] [\cos(\theta_r - \theta_s) - 1] - \left[\Delta \theta_\rho(\Delta \hat{\theta}_\rho, \Delta n_\rho) + (\epsilon_a - \epsilon_c) \sin(\theta_r - \beta) \cos(\theta_r - \beta) \right] \sin(\theta_r - \theta_s) \right\} \quad (6.42)$$

If extraordinarily polarized light is considered, Eq. (6.42) can be written as

$$\xi = \frac{\pi l \bar{n}}{\lambda_o \cos \theta_s} \left\{ \frac{\Delta n_e - \Delta n_o}{\bar{n}} \sin(\theta_r - \theta_s) \sin(\theta_r + \theta_s - 2\beta) + \left[\left(\epsilon_c + \frac{\Delta n_o}{\bar{n}} \right) \cos^2(\theta_r - \beta) + \left(\epsilon_a + \frac{\Delta n_e}{\bar{n}} \right) \sin^2(\theta_r - \beta) - \frac{\Delta \lambda_o}{\lambda_o} \right] [\cos(\theta_r - \theta_s) - 1] - \left[\Delta \theta_\rho(\Delta \hat{\theta}_\rho, \Delta n_o, \Delta n_e) + (\epsilon_a - \epsilon_c) \sin(\theta_r - \beta) \cos(\theta_r - \beta) \right] \sin(\theta_r - \theta_s) \right\} \quad (6.43)$$

If ordinarily polarized light is used, Eq. (6.42) simplifies to

$$\xi = \frac{\pi l \bar{n}}{\lambda_o \cos \theta_s} \left\{ \left[\epsilon_c \cos^2(\theta_r - \beta) + \epsilon_a \sin^2(\theta_r - \beta) + \frac{\Delta n_o}{\bar{n}} - \frac{\Delta \lambda_o}{\lambda_o} \right] [\cos(\theta_r - \theta_s) - 1] - \left[\Delta \theta_\rho(\Delta \hat{\theta}_\rho, \Delta n_o) + (\epsilon_a - \epsilon_c) \sin(\theta_r - \beta) \cos(\theta_r - \beta) \right] \sin(\theta_r - \theta_s) \right\} \quad (6.44)$$

Equation (6.42) shows how external variations between the readout and the recording configurations induce changes in the Bragg condition. Therefore, by measuring Bragg condition changes, it is possible to measure variations in the crystal properties and determine some of the crystal parameters (e.g., electro-optic coefficient, birefringence, etc.), as shown in the experiments described in the next sections. By further examining the diffraction efficiency away from the Bragg condition and measuring the selectivity behavior, it is also possible to obtain information on the index grating modulation depth and on the interaction length inside the crystal [35], as mentioned in the previous chapter.

Equation (6.42) consists of a sum of three terms, the terms proportional to $(\Delta n_\rho - \Delta n_\sigma)$ and $(\epsilon_a - \epsilon_c)$ being direct manifestations of the anisotropy of the crystal. If the crystal were perfectly isotropic, the physical meaning of the second term is that both index change and crystal expansion could be viewed as equivalent wavelength changes $[\Delta\Lambda/\Lambda + \Delta n/\bar{n} \equiv (\Delta\lambda/\lambda)_{\text{equi}}]$. Therefore a shift in the readout wavelength is sufficient to compensate for these effects and the shift is the same regardless of the value of the signal beam angle θ_s . The third term means that the anisotropic part of the crystal expansion can be viewed as an equivalent angular detuning of the readout beam. This contribution can therefore be compensated by a change in readout angle. The anisotropy of the index of refraction introduces an additional term (the first one) that cannot be compensated directly by an angle or a wavelength change.

Important concepts to analyze from these expressions for the Bragg detuning parameter are the angular selectivity and the wavelength selectivity of a planar grating. By definition the angular (wavelength) selectivity is given by the inverse of the angular (wavelength) bandwidth defined in Chapter 2. In terms of ξ , the bandwidth is given by $\Delta\xi^{(bw)} = \pi$. Translated into angle and wavelength, the bandwidths are given by

$$\begin{aligned}\Delta\theta^{(bw)} &= \left| \frac{\lambda_o \cos \theta_s}{\bar{n}l \sin(\theta_s - \theta_r)} \right| \\ \frac{\Delta\lambda_o^{(bw)}}{\lambda_o} &= \left| \frac{\lambda_o \cos \theta_s}{\bar{n}l \cos(\theta_r - \theta_s) - 1} \right|\end{aligned}\quad (6.45)$$

Figures 6.3 and 6.4 give these bandwidths as a function of the reference beam angle θ_r for a given signal beam angle $\theta_s = 0$. The figures show that the perpendicular geometry offers the largest angular selectivity and that the reflection geometry offers the largest wavelength selectivity. These selectivity properties are one of the main reasons the perpendicular geometry is chosen for holographic data storage using angular multiplexing, and the reflection geometry is chosen for holographic data storage using wavelength multiplexing. In addition, scatter noise is minimized in the perpendicular geometry.

When an image-bearing hologram is recorded in a photorefractive crystal, it can

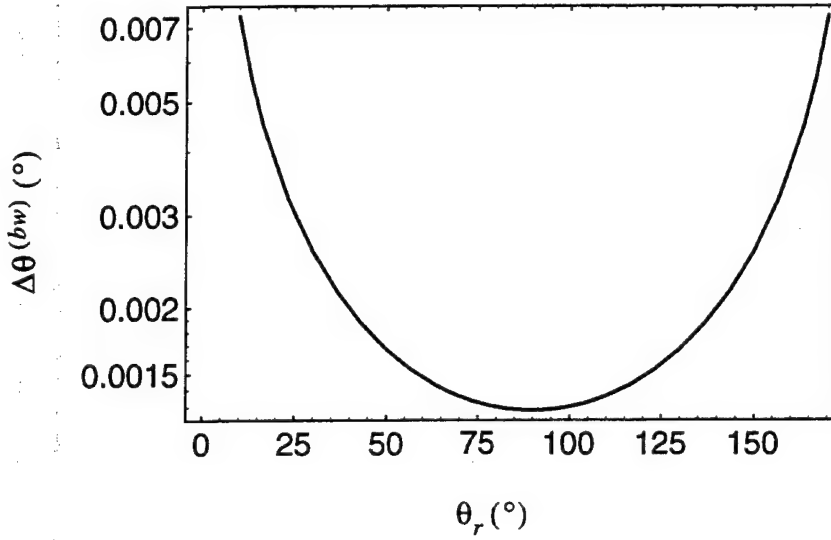


Figure 6.3: Angular bandwidth $\Delta\theta^{(bw)}$ as a function of reference beam angle θ_r for a crystal length $l = 1$ cm ($\lambda_o = 514$ nm, $\bar{n} = 2.3$).

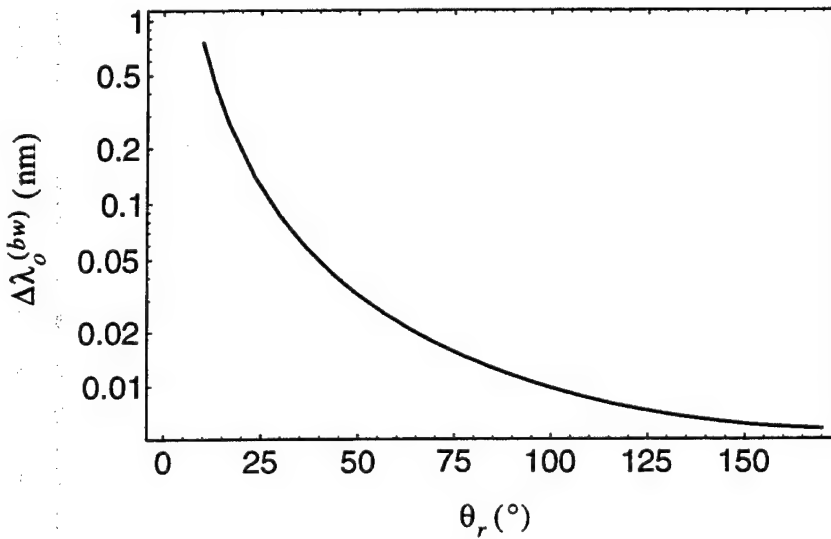


Figure 6.4: Wavelength bandwidth $\Delta\lambda_o^{(bw)}$ as a function of reference beam angle θ_r for a crystal length $l = 1$ cm ($\lambda_o = 514$ nm, $\bar{n} = 2.3$).

be viewed as a collection of plane waves incident on the crystal at different angles θ_s , all of these waves being recorded with a single reference plane wave at θ_r . Equation (6.42) gives the Bragg detuning as seen by each of the components θ_s . For perfect reconstruction of the whole image during readout, it is necessary to satisfy the relation $\xi(\theta_s) = 0$ for all θ_s contained within the image bandwidth. The two variables at our disposal that can be controlled to satisfy $\xi(\theta_s) = 0$ are $\Delta\lambda_o/\lambda_o$ and $\Delta\hat{\theta}_p$. By examining Eq. (6.42), one can see that if there is no index anisotropy, the first term in Eq. (6.42) cancels out, and reconstruction over the whole image bandwidth can be done by adjusting simultaneously $\Delta\lambda_o/\lambda_o$ and $\Delta\hat{\theta}_p$, despite the anisotropy of the crystal expansion. In the next chapter, we will examine in more detail the reconstruction of image-bearing holograms under a modified Bragg condition and define transfer functions to quantify the distortion that occurs during readout.

6.5 Phase Coupling Effect

From Eqs. (4.18) and (4.20), the following expressions can be derived for the phase coupling component of the Bragg detuning parameter in the transmission geometry (ξ_{PC}^T) and in the reflection geometry (ξ_{PC}^R), respectively:

$$\begin{aligned}\xi_{PC}^T(z) &= -l\beta \tanh \frac{\gamma z - \ln r_{pp}}{2} \\ \xi_{PC}^R(z) &= -l\beta\end{aligned}\tag{6.46}$$

Some special cases of Bragg shifting in LiNbO₃ induced by phase coupling due to the photovoltaic effect have been analyzed by Heaton *et al.* [36] and demonstrated by Tao *et al.* [37] [38].

In the transmission geometry, strong nonlinear coupling occurs at large applied fields. As shown in Fig. 4.4, this coupling induces strong nonlinear variations in the modulation and in the phase of the index grating inside the crystal. For large pump-to-probe ratios ($r_{pp} \gg 1$), the Bragg detuning parameter $\xi_{PC}^T(z)$ is a nonlinear function of z . In this case the concept of a Bragg condition is actually lost: $\tilde{\xi}(z) = 0$ cannot be satisfied at all points inside the crystal because the grating consists of a

spatial distribution of grating vectors inside the crystal. This means that a hologram recorded under these conditions can no longer be retrieved with optimum efficiency. For small values of r_{pp} ($r_{pp} \ll 1$), the Bragg detuning parameter is approximately constant ($\xi_{PC}^T \approx -l\beta$), implying that in this case, phase coupling simply shifts the diffraction efficiency along the Bragg detuning axis and that the concept of a Bragg condition remains meaningful.

In the reflection geometry, the Bragg detuning component due to phase coupling ξ_{PC}^R is constant regardless of the value of the pump-to-probe ratio. Like in the previous case ($r_{pp} \ll 1$ in the transmission geometry), phase coupling simply shifts the Bragg selectivity curve along the Bragg detuning axis. However, we showed in Chapter 4 that in the reflection geometry, phase coupling is always negligible, mainly because of the necessary use of ordinary polarization and of small grating spacings. Therefore, in the reflection geometry, Bragg detuning due to phase coupling will in general not be observed. The same conclusion holds for the perpendicular geometry as well.

Figures 4.4 (transmission geometry) and 4.6 (reflection geometry) show that amplitude coupling tends to reduce the effective thickness of the index grating inside the crystal. Because the readout beam sees an effectively thinner grating, the Bragg selectivity of the resulting hologram will decrease. We already showed (Fig. 5.3) how this decrease in effective thickness also influences the maximum diffraction efficiency.

6.6 Experiments

6.6.1 Introduction

We performed several experiments to measure the Bragg detuning and the diffraction efficiency of holograms written and/or retrieved in the presence of an applied field. We used only the transmission geometry because the properties of our photorefractive crystals (Ce-doped SBN:60 and Ce-doped SBN:75) are such that their optimum response (Debye screening length) lies within the large grating spacing domain ($\sim 1 \mu\text{m}$). Figure 6.5 is a diagram of the experimental setup. It consists of a simple holographic arrangement in which a single laser beam originating from an argon-ion

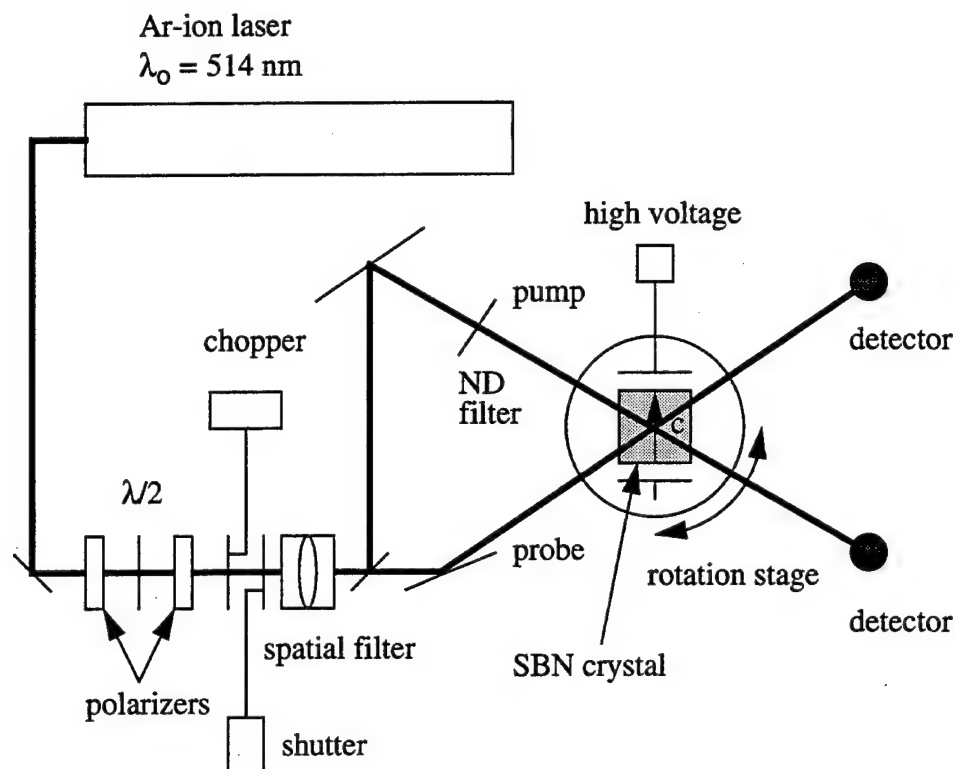


Figure 6.5: Experimental setup: ND, neutral density filter; $\lambda/2$, half-wave plate.

laser is split into two branches of equal optical length, one branch being the reference beam, the other one being the signal beam. The crystal is mounted on a rotation stage to facilitate the measurement of the diffraction efficiency as a function of the incidence angle of the readout beam.

To measure ξ_{PC}^T it is necessary to apply a field during recording to yield phase coupling between the writing beams. $\xi^{\Delta n}$ can be measured using the electro-optic effect, by recording with no field to avoid phase coupling and applying a field during readout. A weak readout beam is necessary for nondestructive readout and to avoid beam fanning. With the SBN:60 crystal used in the transmission geometry, the electro-optic effect is too weak to permit observation of a substantial Bragg detuning $\xi^{\Delta n}$ that can be measured accurately. Therefore, to illustrate the Bragg detuning due to the electro-optic effect, experiments are performed in Ce-doped SBN:75, which has a much more pronounced electro-optic effect. At room temperature SBN:75 is quite close to the ferroelectric phase transition and therefore exhibits also a nonlinear

electro-optic effect. This experiment will thus also confirm the nonlinear behavior that is characteristic of photorefractive crystals operating near the phase transition [39]. Finally, to illustrate Eq. (6.42) with SBN:60, a grating is written with extraordinary polarization and read with ordinary polarization. The birefringence Δn_b is large enough to observe and measure accurately a detuning.

6.6.2 Phase Coupling Effect

We already showed in Chapter 5, using a simple Fourier transform argument, how phase coupling shifts the Bragg condition. The purpose of this experiment is then to measure the phase coupling component of the Bragg detuning parameter and to fit the results to the theoretical model to obtain valuable information on some of the crystal parameters. The symmetric geometry is used to cancel out the electro-optic component of the Bragg detuning parameter. The grating ($\Lambda = 5 \mu\text{m}$) is written with extraordinarily polarized light ($\lambda_o = 514 \text{ nm}$) in a Ce-doped (0.05 mol%) SBN:60 crystal with the field applied along the c axis. The crystal is completely illuminated to minimize screening fields. The hologram is written to steady state with an exposure of 0.28 J/cm^2 ($I = 56 \text{ mW/cm}^2$ for 5 secs). Readout is then performed with one of the original writing beams sufficiently reduced in intensity so as not significantly to erase the written hologram. With a grating spacing Λ of $5 \mu\text{m}$ and a field E_{0W} of 10 kV/cm ($l = 2.67 \text{ mm}$), it can easily be shown that the contribution from the piezoelectric effect is at least more than one order of magnitude smaller than the observed detuning due to fringe bending (we use $d_{33} = 80 \text{ pm/V}$ which is a typical value for SBN:60 [27]). This confirms that in this case, the piezoelectric component is negligible. Since, in addition, fringe bending is not affected by the nondestructive readout process, it is not necessary to apply a field during the diffraction efficiency and the Bragg detuning measurements. This also allows us to minimize beam fanning.

The first set of experiments is conducted with a pump-to-probe ratio $r_{pp} = 1/100$. For this small value of r_{pp} , the phase of the grating varies linearly inside the crystal, $\psi(z) \approx -\beta z$ [Eq. (6.46) and Fig. 4.5(b)]. The Bragg condition, defined as the condition for which the diffraction efficiency is maximum, is then given by

$$\xi^{[\eta^{max}]} = -\frac{l}{2} \frac{d\psi}{dz} = \frac{l\kappa}{2} \cos \phi_{SC} \quad (6.47)$$

and is different for holograms recorded at different fields, since ϕ_{SC} and κ depend on E_{0W} .

The dotted curves of Fig. 6.6 show the experimental diffraction efficiencies, with the peak efficiency normalized to unity, as a function of the angular detuning $\Delta\hat{\theta}_\rho$ [translated into the Bragg detuning parameter $\xi = \pi l \sin(\theta_r - \theta_s) \Delta\hat{\theta}_\rho / (\lambda_o \cos \theta_s)$] for five planar gratings recorded at five different electric fields. The solid curves show the corresponding theoretical diffraction efficiencies that we obtained by numerically solving the coupled-wave equations for the readout process, as described in Chapter 5.

Figure 6.6 shows good agreement between theory and experiment. The discrepancy at zero field is due to the background noise, as the efficiency is very small. The asymmetry observed at high fields appears to be due to beam fanning and scattering from striations in the crystal. At high electric fields, owing to stronger energy transfer, the magnitude of the grating is significant only near the entrance face of the crystal as mentioned in Chapter 4. Therefore the reading beam sees a thinner grating, which explains why the width of the diffraction peak increases with the applied field: if amplitude coupling takes place in a long crystal, it is no longer the crystal length l but the width of the grating amplitude (proportional to $1/\gamma$) that determines the Bragg selectivity of the grating. Figure 6.6 also clearly illustrates the phenomenon of apodization, since at high applied fields, the side lobes have completely disappeared.

Figure 6.7 shows the experimental data points and the theoretical fit for the angular detuning $\Delta\hat{\theta}_\rho$ of the maximum diffraction efficiency determined from Eq. (6.47), as a function of the applied field E_{0W} (note that because the angles of incidence are small, one can take $\Delta\hat{\theta}_\rho = \bar{n}\Delta\theta_\rho$):

$$\Delta\hat{\theta}_\rho(E_{0W}) = \kappa \cos \phi_{SC} \frac{\bar{n}\Lambda}{2\pi} \quad (6.48)$$

from which $r_{eff}\zeta(K)$ and E_Q are inferred: $r_{eff}\zeta(K) = 125 \text{ pm/V}$ and $E_Q = 22 \text{ kV/cm}$ at $\Lambda = 5 \text{ }\mu\text{m}$. This yields a value for $N_0^o = 1.5 \cdot 10^{23} \text{ m}^{-3}$. An independent measurement of the electro-optic coefficient r_c of the crystal,

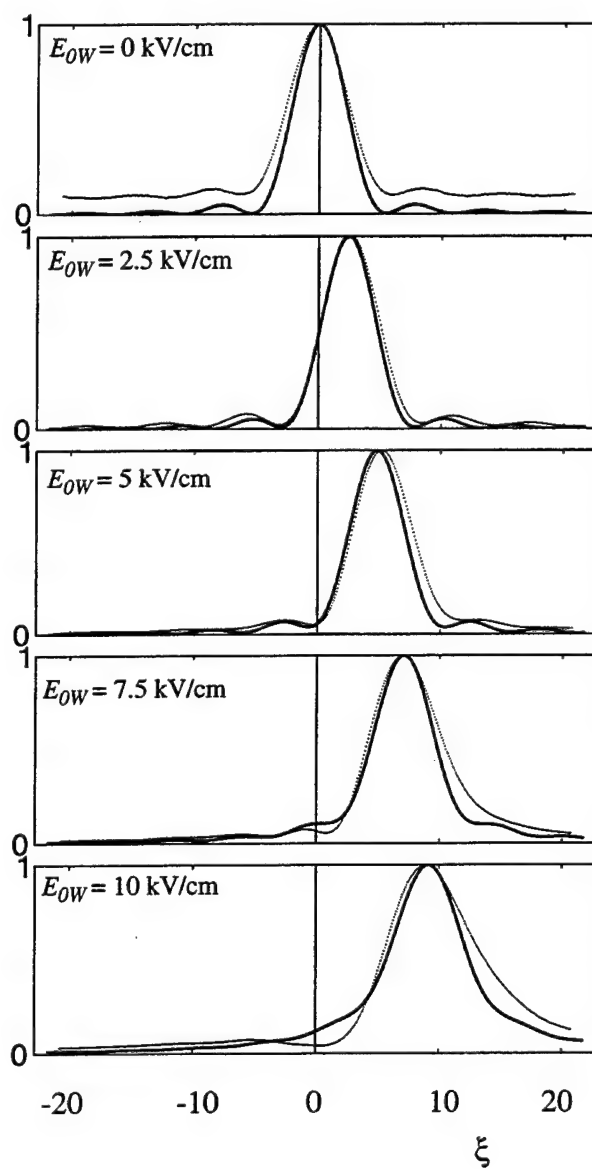


Figure 6.6: Experimental (dotted curves) and theoretical (solid curves) diffraction efficiencies as a function of the Bragg detuning parameter ξ for holograms recorded at five different applied fields E_{OW} in SBN:60 ($r_{pp} = 1/100$, $\Lambda = 5 \mu\text{m}$).

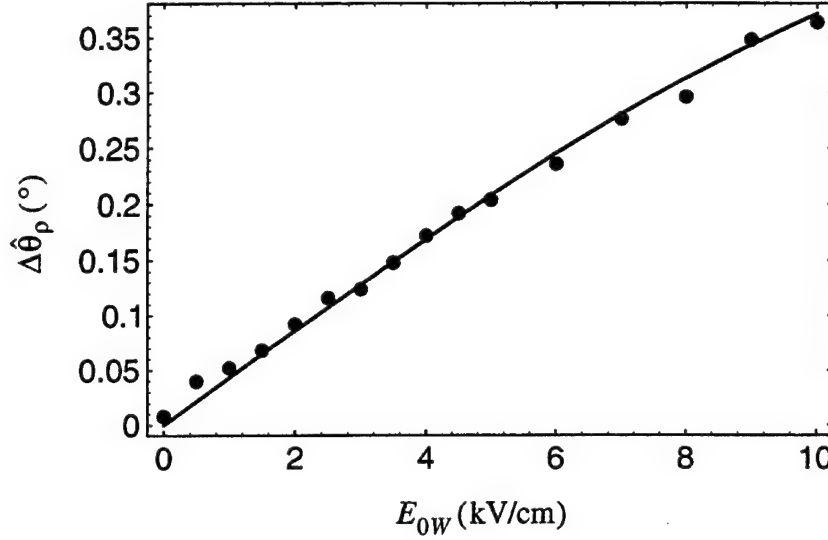


Figure 6.7: Experimental data points and theoretical fit of the angular detuning $\Delta\hat{\theta}_\rho$ (in degrees) as a function of the applied field E_{0W} (in kV/cm) ($r_{pp} = 1/100$, $\Lambda = 5 \mu\text{m}$)

$$r_c = r_{33} - \frac{n_o^3}{n_e^3} r_{13} \quad (6.49)$$

yields a value of 180 pm/V, which is consistent with other experimental values found in the literature and the value of $r_{eff}\zeta(K)$ measured above, considering that typical values for $\zeta(K)$ in SBN:60 vary from 0.6 to 1.0 [25].

The second set of experiments is conducted with a beam ratio $r_{pp} = 100$. With a large value of r_{pp} it is possible to get a fringe shape having both a negative and a positive slope [Fig. 4.5(a)] which creates a strong asymmetry in the diffraction efficiency. This also results in an important broadening of the main diffraction peak and in the appearance of a double peak in the selectivity curve, as shown in the experimental plots of Fig. 6.8. In this case, particularly for large grating spacings, the linearization of the band transport model is no longer valid, as the modulation depth inside the crystal approaches unity. It becomes difficult to fit the diffraction efficiencies to the theory because the selectivity is extremely sensitive to small changes in the nonuniform index amplitude and in the phase inside the crystal. Nevertheless, it

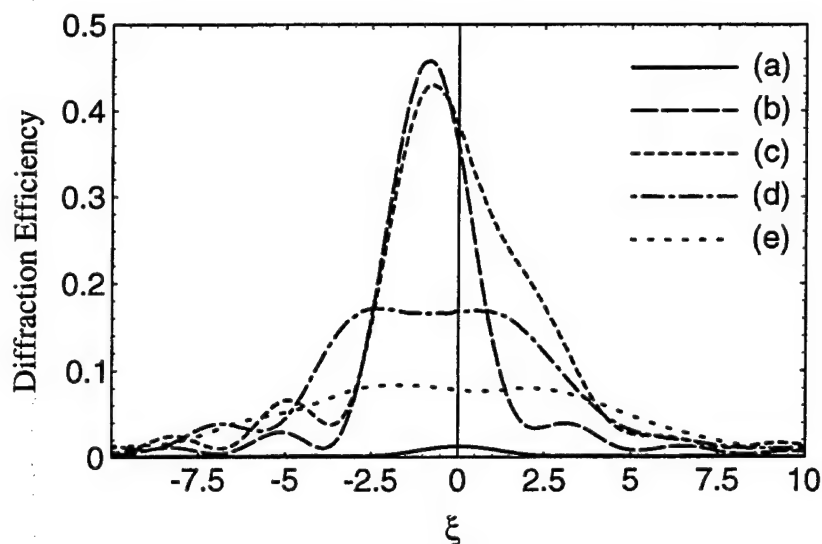


Figure 6.8: Experimental diffraction efficiencies as a function of the Bragg detuning parameter ξ for holograms recorded in SBN:60 at five different applied fields: (a) 0, (b) 2.5, (c) 5, (d) 7.5, and (e) 10 kV/cm ($r_{pp} = 100$, $\Lambda = 5 \mu\text{m}$).

is important to note that wave mixing alters considerably the Bragg condition and the selectivity of holograms; this can be of significant importance for image amplification and may pose upper limits on data storage.

6.6.3 Electro-Optic Effect

Equations

If there are no changes in the angle and the wavelength of the readout beam and if an isotropic index change $\Delta n_p = \Delta n_s = \Delta n$ is considered, the Bragg detuning parameter in the transmission and reflection geometry is given by Eq. (6.19):

$$\xi^{\Delta n} = \frac{\pi \Delta n l}{\lambda_o} \left(\frac{\cos \theta_s - \cos \theta_r}{\cos \theta_s \cos \theta_r} \right) \quad (6.50)$$

Because the angles of incidence are small (the beams are almost at normal incidence on the crystal), this expression can be written to a good approximation using Snell's law as

$$\begin{aligned}
\xi^{\Delta n} &= \frac{\pi \Delta n l}{\lambda_o} \left(\frac{\sin^2 \hat{\theta}_r - \sin^2 \hat{\theta}_s}{2\bar{n}^2} \right) \quad \text{transmission geometry} \\
\xi^{\Delta n} &= \frac{\pi \Delta n l}{\lambda_o} \left[2 + \frac{1}{2\bar{n}^2} (\sin^2 \hat{\theta}_r + \sin^2 \hat{\theta}_s) \right] \quad \text{reflection geometry} \quad (6.51)
\end{aligned}$$

The index change Δn comes from the fact that the bulk index seen by the writing and the readout waves is different. For example in an uniaxial crystal, Δn can take the following forms (again assuming small incidence angles inside the crystal):

$$\begin{aligned}
\Delta n_{e-pol} &= -\frac{1}{2} n_e^3 [r_{33}(E_{0W})E_{0W} - r_{33}(E_{0R})E_{0R}] \\
\Delta n_{o-pol} &= -\frac{1}{2} n_o^3 [r_{13}(E_{0W})E_{0W} - r_{13}(E_{0R})E_{0R}] \\
\Delta n_b &= n_e - n_o \quad (6.52)
\end{aligned}$$

for gratings written and read with extraordinary polarization and in the presence of an applied field (Δn_{e-pol}), for gratings written and read with ordinary polarization and in the presence of an applied field (Δn_{o-pol}), and for gratings written with one polarization and read with the other polarization in the absence of a field (Δn_b). In Eq. (6.52) r_{ij} is the low-frequency unclamped electro-optic coefficient defined by [40]

$$r_{lk}(E_0) = \hat{r}_{lk}(E_0) + \sum_m p_{lm}(E_0)d_{mk}(E_0) \quad (6.53)$$

where \hat{r}_{ij} is the high-frequency clamped electro-optic tensor that includes the nonlinear terms responsible for such effects as electrically controlled diffraction (ECD) [39], p_{ij} is the elasto-optic tensor, and d_{ij} is the piezoelectric tensor. It is important to note that the full expression for r_{ij} , as given in Eq. (6.53), must be considered when one is properly accounting for the electro-optic effects described here. Detailed and interesting discussions on the differences between clamped (strain-free) and unclamped (stress-free) electro-optic coefficients as well as their influence on the photorefractive effect through a uniform or nonuniform field can be found in Refs. [41] and [42].

In the transmission geometry, even if the fields applied during writing and readout are different, the Bragg detuning parameter cancels out in the symmetric configuration ($\hat{\theta}_r = -\hat{\theta}_s$). Note also that in this case, the detuning parameter is much larger

for extraordinarily polarized light than for ordinarily polarized light. In the reflection geometry, regardless of the recording configuration, there is a detuning as soon as the fields applied during recording and readout are different. Note also that in absolute value [Eq. (6.51)], for the same field difference, the detuning is much larger in the reflection geometry than it is in the transmission geometry. The former is thus a more favorable geometry for the field multiplexing technique [43]. Note also that in the reflection geometry, the piezoelectric contribution can usually not be neglected.

Electro-Optic Coefficient of SBN:75

The goal of this experiment is to measure the electro-optic component of the Bragg detuning parameter in a Ce-doped (0.015 wt %) SBN:75 crystal ($l = 5$ mm) and deduce from the experiment values for the electro-optic coefficient of that crystal. The grating is written with extraordinary polarization ($\lambda_o = 514$ nm) with a total exposure of 0.19 J/cm² ($I = 37.5$ mW/cm² for 5 secs) and is subsequently read with a weak-intensity beam while an electric field is applied to the crystal. To avoid phase coupling no field is applied to the crystal during the recording process.

Figures 6.9 and 6.10 show the angular selectivity of gratings written in the symmetric configuration and the asymmetric configuration, respectively, and then read in the presence of an applied field (E_{OR}) (the diffraction efficiency at zero applied field is normalized to one). The five curves in each figure correspond to five different applied fields, from 0 kV/cm to 4 kV/cm. In the symmetric configuration, no significant detuning is observed. Indeed in this configuration there is no contribution from the electro-optic effect as shown by Eq. (6.51). The only contribution that could induce Bragg detuning would be from the piezoelectric effect. Figure 6.9 confirms (as indicated earlier) that in the transmission geometry the piezoelectric contribution to the detuning is negligible in SBN. Figure 6.10 shows the angular selectivity of a grating written in the asymmetric configuration at approximately the same grating spacing ($\Lambda = 0.6$ μ m). This figure shows a strong detuning arising from the electro-optic effect. The figure also clearly illustrates the electrically controlled diffraction (ECD) phenomenon: applying an electric field after writing the grating enhances the

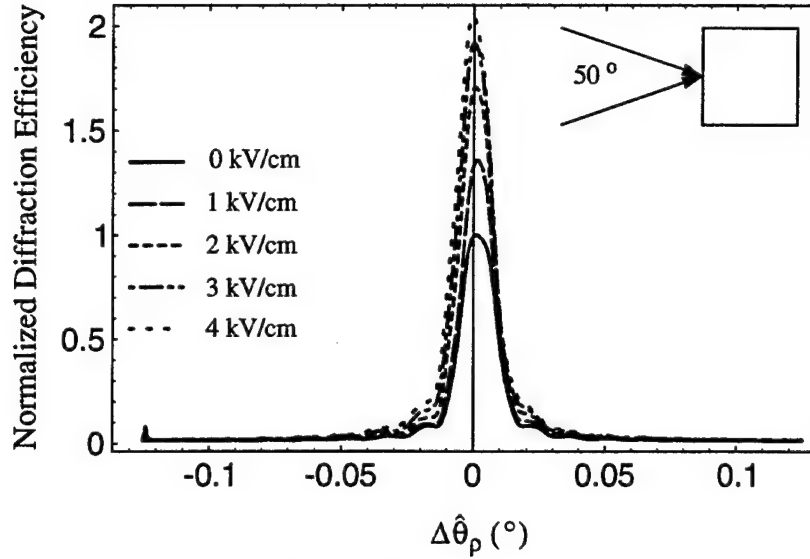


Figure 6.9: Angular selectivity of a grating written at symmetric incidence in SBN:75 and then read at five different applied fields E_{0R} equal to 0-4 kV/cm ($\Lambda = 0.6 \mu\text{m}$, $\hat{\theta}_r = -\hat{\theta}_s = 25^\circ$).

diffraction efficiency of that grating. At room temperature in this crystal the increase is approximately a factor of two. Closer to the ferroelectric transition, i.e., at higher temperatures, the increase is much more pronounced, as is observed in Ref. [39] (as much as one or even two orders of magnitude). The ECD effect will be further discussed in the next chapter in the context of holographic data storage. By taking Bragg detuning measurements at different grating spacings and different applied fields, it is possible to estimate the value of the electro-optic coefficient $r_{33}(E)$ by use of Eq. (6.51)

$$\xi = -\frac{2\pi l n_e}{\lambda_o} \sin^2 \hat{\theta}_s r_{33}(E_{0R}) E_{0R} \quad (6.54)$$

Figure 6.11 shows the general behavior of r_{33} as a function of field at three different grating spacings. The behavior and the values agree well with the observed behavior mentioned in Ref. [44] and is characteristic of photorefractive crystals operating near the ferroelectric phase transition.

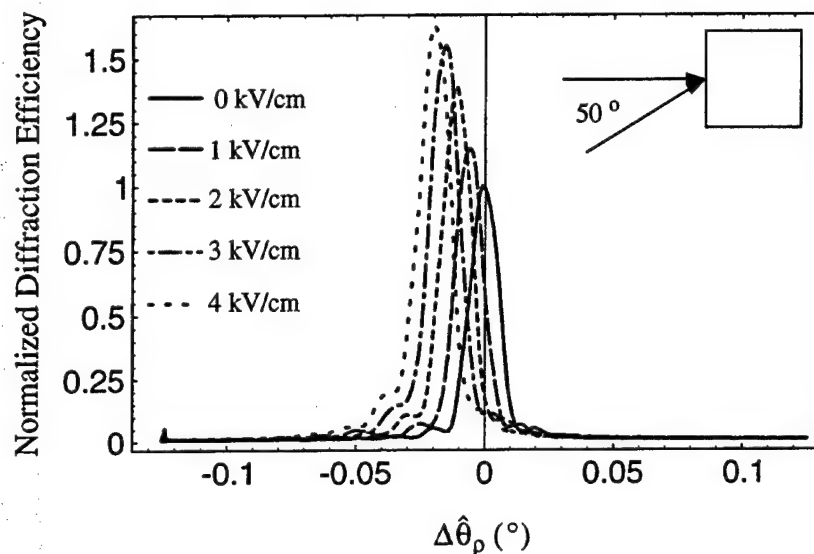


Figure 6.10: Angular selectivity of a grating written at asymmetric incidence in SBN:75 and then read at five different applied fields E_{0R} equal to 0-4 kV/cm ($\Lambda = 0.6 \mu\text{m}$, $\hat{\theta}_r = 0^\circ$, $\hat{\theta}_s = 50^\circ$).

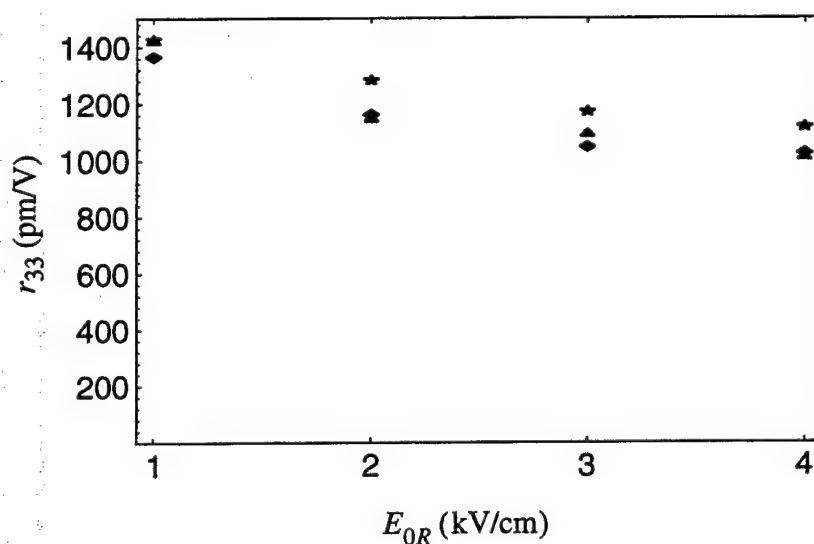


Figure 6.11: Electro-optic coefficient r_{33} as a function of the field E_{0R} for Ce-doped SBN:75 (★ $\Lambda = 0.6 \mu\text{m}$; △ $\Lambda = 0.75 \mu\text{m}$; ◇ $\Lambda = 1 \mu\text{m}$).

6.6.4 Phase Coupling and Electro-Optic Effects

In the absence of phase coupling [$\xi_{PC}(z) = 0$] and with no external change in the readout beam [$\Delta\hat{\theta}_\rho = \Delta\lambda_o = 0$], if a field E_{0W} is applied during the recording of a hologram in a general writing configuration, then the same field needs to be applied during readout to satisfy the Bragg condition, $\tilde{\xi} = 0$, thereby retrieving the stored hologram with maximum efficiency. This is the basic principle of the field multiplexing technique introduced by Stepanov *et al.* [43] and further developed by Kewitsch *et al.* [45].

In the presence of a linear detuning that is due to phase coupling (as it is the case in the transmission geometry for small pump-to-probe ratios $r_{pp} \ll 1$; in the perfectly drift-dominated case $\gamma = 0$; or in the reflection geometry), it is still possible to retrieve the hologram with maximum efficiency, but it is necessary either to apply a different field during readout than during writing or to adjust the angle ($\Delta\hat{\theta}_\rho$) or the wavelength ($\Delta\lambda_o$) of the reading wave to compensate for the phase-coupling component. If the phase-coupling component is small, one can reconstruct the hologram by simply changing the field during readout.

For large grating spacings in the transmission geometry, because of strong phase coupling, the fringe-bending effect can be so large that it becomes impossible for one to retrieve the image by simply applying a different electric field. It is then necessary to fulfill the Bragg condition by adjusting $\Delta\hat{\theta}_\rho$ or $\Delta\lambda_o$. Figure 6.12 shows a three-dimensional representation of the Bragg detuning parameter $\tilde{\xi}$ in the transmission geometry for SBN:60 as a function of E_{0R} and $\hat{\theta}_s$, taking $\hat{\theta}_r = 0$, a writing field $E_{0W} = 5$ kV/cm, a pump-to-probe ratio $r_{pp} \ll 1$, and extraordinary polarization. In this case Eq. (6.1) simplifies to

$$\tilde{\xi} = \frac{\pi l}{2\lambda_o} n_e \sin^2 \hat{\theta}_s r_{33} (E_{0W} - E_{0R}) - l\beta \quad (6.55)$$

The highlighted curve (intersection of the plane with the shaded contour) represents the Bragg condition $\tilde{\xi} = 0$. It shows how the fringe-bending effect can be compensated by application of a field that is different during readout than during writing. Figure 6.12 also shows that for large grating spacings (small $\hat{\theta}_s$), the Bragg detuning parameter cannot be compensated by adjustment of only the field during readout. In

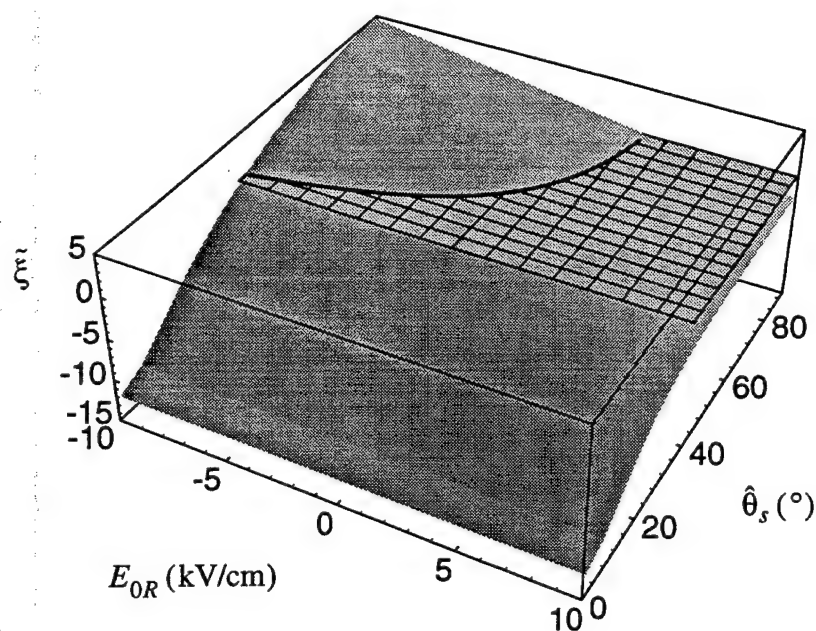


Figure 6.12: Three-dimensional representation of the Bragg detuning parameter ξ as a function of E_{0R} and $\hat{\theta}_s$ in an asymmetric transmission geometry, showing the simultaneous influence of the phase coupling component and the electro-optic component in SBN:60 ($r_{pp} \ll 1$, $\hat{\theta}_r = 0$, $E_{0W} = 5$ kV/cm). The plane (solid grid) represents $\xi = 0$.

this case it is necessary to either change the angle or the wavelength of the incoming readout beam.

6.6.5 Polarization Effect

Our goal in this experiment is to measure the detuning that is due to the birefringence of a Ce-doped SBN:60 crystal. We exemplify Eq. (6.51) by writing a grating with extraordinarily polarized light and by reading it with ordinarily polarized light at low intensity. The grating is written with an asymmetric configuration, i.e., with the reference beam coming at normal incidence ($\hat{\theta}_r = 0$) and the signal beam coming at an angle $\hat{\theta}_s$. The intensities of the two writing beams are both equal to 29 mW/cm². In this case assuming small incidence angles, we have that

$$\begin{aligned} n_s &= n_r = n_e \\ n_\sigma &= n_\rho = n_o \end{aligned} \quad (6.56)$$

and the Bragg detuning parameter reduces to

$$\xi = \frac{\pi l \bar{n}}{\lambda_o \cos \theta_s} \left\{ \frac{\Delta n_b}{\bar{n}} [\cos(\theta_r - \theta_s) - 1] - \frac{\Delta \hat{\theta}_\rho}{\bar{n}} \sin(\theta_r - \theta_s) \right\} \quad (6.57)$$

No electric field is applied to the crystal during writing or readout. Figure 6.13 shows the angular selectivity of a grating written with the reference beam coming at normal incidence and the signal beam coming at an angle $\hat{\theta}_s$ of 40°. The main diffraction peak corresponds to ordinary polarization readout, and the small peak at 0° corresponds to Bragg-matched readout, because a small amount of extraordinary polarization is still present in the readout beam. From data at different signal-beam angles $\hat{\theta}_s$, the birefringence determined from Eq. (6.57),

$$|\Delta n_b| = \left| \Delta \hat{\theta}_{pol} \frac{\sin \theta_s}{\cos \theta_s - 1} \right| \quad (6.58)$$

can be estimated. $\Delta \hat{\theta}_{pol}$ is the observed angular detuning (angle taken outside the crystal) of the main diffraction peak, i.e., $\Delta \hat{\theta}_\rho$ when $\xi = 0$. Figure 6.14 shows the measured angular detuning $\Delta \hat{\theta}_{pol}$ as a function of the parameter X ,

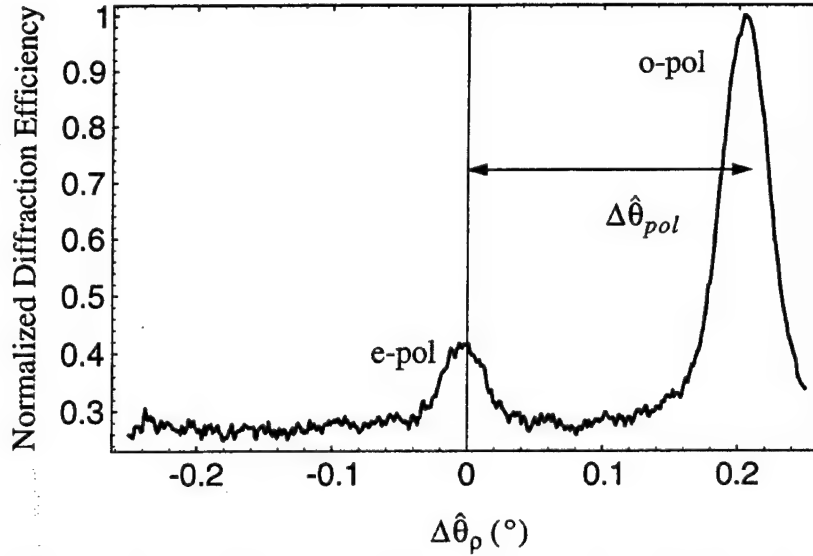


Figure 6.13: Normalized diffraction efficiency of a grating written with extraordinary polarization and read with ordinary polarization in SBN:60 ($\Lambda = 0.75 \mu\text{m}$).

$$X = \frac{\cos \theta_s - 1}{\sin \theta_s} \left(\frac{180}{\pi} \right) \quad (6.59)$$

for five data points at $\hat{\theta}_s = 0^\circ, 20^\circ, 30^\circ, 40^\circ$ and 50° . The angular coefficient of the linear fit is then a direct measure of the birefringence and yields $|\Delta n_b| = 0.027$. This value agrees well with other published values for the birefringence of bulk SBN:60 [46].

6.6.6 Temperature Effect

Under the assumptions used in this chapter, the Bragg detuning parameter varies linearly with a change of temperature, the proportionality coefficient being determined from the recording geometry and the parameters α_a , α_c , $\partial n_o / \partial T$, and $\partial n_e / \partial T$. We will discuss in more detail in the next chapter the consequence of Bragg detuning due to thermal changes when we analyze the effects of thermally fixing information in a holographic data storage system.

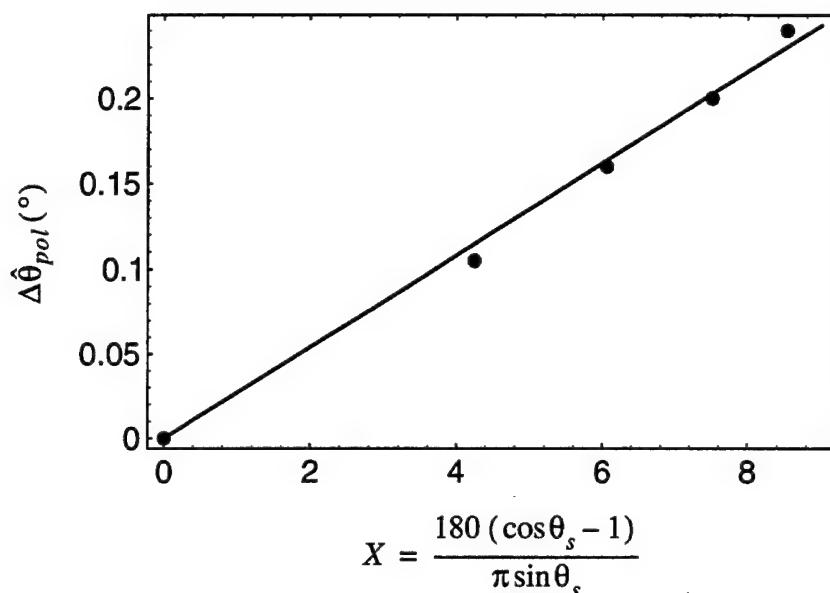


Figure 6.14: Measured angular detuning in degrees ($\Delta\hat{\theta}_{pol}$) as a function of the parameter X . The angular coefficient of the linear fit yields $|\Delta n_b| = 0.027$.

6.7 Conclusions

In this chapter we have studied how different mechanisms affect the Bragg condition in photorefractive crystals. We have concentrated on the effects that induce variations in the index of refraction of the crystal and that change the grating vector inside the medium. These variations can be due to change of polarization, change of wavelength, change of temperature or change of applied fields. Using a plane wave approach, we first derived an analytical expression for the Bragg detuning parameter, taking into account all these different mechanisms and the fact that the crystal is anisotropic. We then showed how careful measurements of Bragg detuning can yield valuable information on several of the crystal parameters like the acceptor concentration, the electro-optic coefficient and the birefringence.

In practice though, most often image-bearing holograms are stored in photorefractive crystals and not simple plane waves. Nevertheless, the theory developed in this chapter is useful to solve the problems that arise when image-bearing holograms are recorded. In general, when image-bearing holograms are reconstructed under a

different Bragg condition, the images cannot be fully and perfectly reconstructed because of some deformation that occurs upon readout, as we shall show in the next chapter. We will show that, using the results of this chapter, transfer functions can be defined to quantify these distortions and we will also propose methods to compensate for these distortions.

Chapter 7

Image-Bearing Holograms

7.1 Introduction

In this chapter we examine the case of image-bearing volume holograms and the problems that arise when the conditions under which they are retrieved are different from the recording conditions. The case of image-bearing holograms is especially important in holographic data storage applications. We start this chapter by a brief review of holographic data storage and then analyze the theory underlying the retrieval of images when Bragg conditions change. We show that it is useful to define transfer functions, whose expressions derive directly from the results presented in Chapter 6. We consider two practical examples of holographic data storage applications in which a change of Bragg condition cannot be avoided. The first one corresponds to the typical setup for a digital data storage system in which thermal fixing is used to fix the information inside the crystal. The second one corresponds to a transmission geometry configuration in which holograms are stored in a SBN:75 crystal operating near the phase transition and an electric field is applied to the crystal to dynamically control the diffraction efficiency of the image-bearing holograms.

7.2 Holographic Data Storage

As we said in the first chapter, many applications in optical storage and optical processing make use of photorefractive materials. In this section we focus on the use of photorefractive materials for volume holographic data storage. This encompasses applications in which either a few holograms, each having a large diffraction efficiency, or a large number of holograms, each having a small share of the available dynamic range, are to be recorded in a given volume of material. Ferroelectric-photorefractive materials tend to be highly polarizable (as characterized by large dielectric and electro-optic effects) and, when suitably doped, they generally provide large dynamic ranges with correspondingly high storage capacities. Accessing the full storage capacity, though, requires that all sources of noise scattering be kept to an absolute minimum in order to provide the best possible signal-to-noise ratio (SNR) during readout [7]. An estimate of this total capacity can be done by use of an exhaustive analysis that considers the interactions and trade-offs between signal-to-noise ratio, cross talk, and capacity issues [7] [47].

The storage of multiplexed volume holograms in photorefractive media, particularly for data storage applications, has recently become a topic of renewed interest. Angular multiplexing [48] [49] is widely used because it is the easiest to implement experimentally. Up to 10,000 holograms [49] have been stored using this method, in which each image is stored at a given angle for the reference beam. Phase encoding is a variant of angular multiplexing, in which each image is recorded with a different phase code, the different codes being orthogonal to each other [50] [51]. This method has the advantage of having no moving parts. Wavelength multiplexing [52] [53] in which each hologram is stored at a different reference wave wavelength can also be used. In photorefractive media possessing a sufficiently large electro-optic and piezoelectric effect, an applied electric field can directly be used for multiplexing, as first demonstrated in LiNbO_3 by Stepanov *et al.* [43] and most recently by Kewitsh *et al.* [45]. In this case, the bulk refractive index, and hence the Bragg condition, is controlled by the electric field. There also exist other exotic multiplexing techniques to store multiple holograms in a single volume, like the mosaic multiplexing [54] and

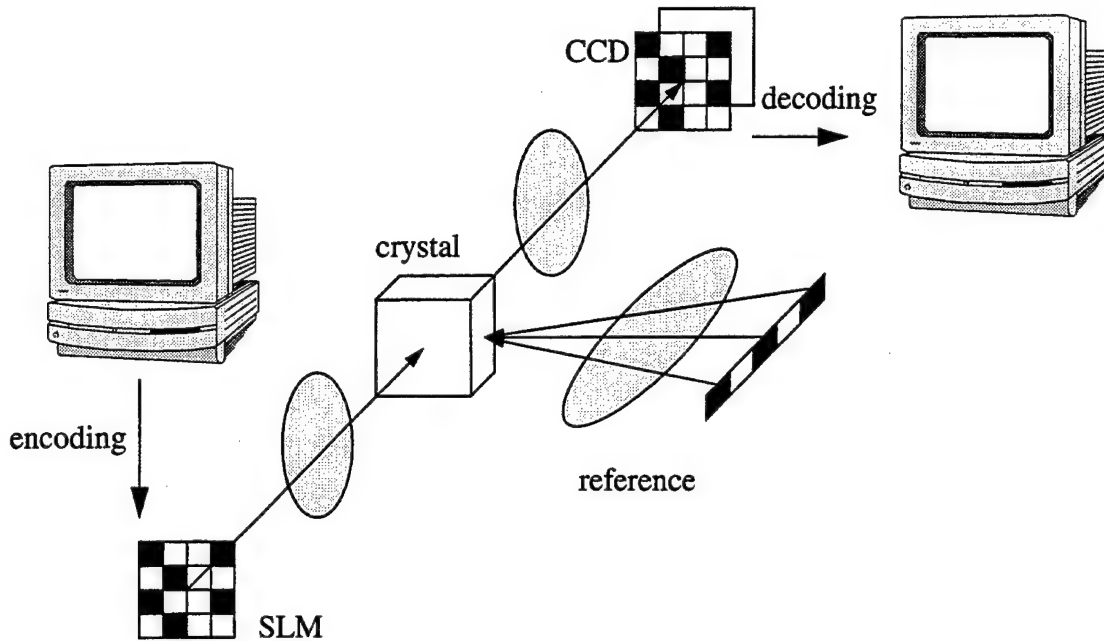


Figure 7.1: Representation of a typical setup for holographic data storage.

the fractal multiplexing [49] techniques developed at the California Institute of Technology. All these schemes take advantage of the large Bragg selectivity of volume holograms to store large numbers of holograms in a single crystal.

These different data storage techniques offer various advantages and disadvantages, as explained and described in the references that have been mentioned. However they all have the same generic setup like the one shown in Fig. 7.1. It consists of a computer feeding the digital information onto a spatial-light-modulator (SLM) that usually modulates the amplitude of the signal wave. This information is recorded inside the crystal with the use of a reference beam. During retrieval, the readout beam, at the appropriate Bragg condition, is diffracted out of the crystal and the diffracted signal is then captured by a charge-coupled-display (CCD) array before the information is fed back to the computer for further treatment. The multiplexing techniques mentioned above deal with the different possible ways the reference beam can be used to record the information and then to retrieve the signal at the correct Bragg condition.

7.3 Image-Bearing Holograms

We start by examining the case of image-bearing volume holograms and the problems that arise when they are retrieved under different Bragg conditions. An image can always be decomposed into a set of angular components, and each component can then be viewed as a plane wave incident on the crystal at a different angle θ_s . The set of angles θ_s that forms the image is called the signal beam angular extent.

When the Fourier transform of the input image is stored in the crystal, the signal beam angular extent represents the field of view, i.e., the lateral extent of the image. In the two-dimensional representation considered here, the lateral extent is measured in the plane of incidence and in a direction perpendicular to the propagation axis. In this case each point or pixel on the input image corresponds to a plane wave propagating at a given angle θ_s . If the crystal acts as a filter and limits the signal beam angular extent to some finite quantity, it puts an upper limit on the size of an input image such that the whole signal is reconstructed during readout. When an imaging system is used, the components of the angular spectrum represent the different spatial frequencies contained in the image. In this case a crystal that limits the signal beam angular extent imposes a limit on the spatial resolution of the images that can be stored in the crystal. The relationship between the signal beam angular extent and either the lateral size or the resolution of the input image is determined by the F number of the optical system used in the setup.

The consequences of changes in the Bragg condition during the readout process on the reconstruction quality is an important problem to analyze, because it is a problem that occurs in many applications that make use of image-bearing holograms. For example, the most promising method for fixing information in a holographic data storage system is currently thermal fixing [55], but as we shall show in the next section, this can lead to situations where image-bearing holograms are recorded and retrieved at different temperatures. An applied electric field might also be used during readout, for example, in a system that uses the electrically controlled diffraction effect [39], to enhance and dynamically control diffraction efficiencies. However a readout electric field different from the writing electric field will also induce a change in the Bragg

condition through the electro-optic and piezoelectric effects. Anisotropic diffraction at various wavelengths [33] is used to achieve nondestructive readout, but it also modifies the Bragg condition through polarization and wavelength changes.

A change in Bragg condition during the readout of an image-bearing hologram has two consequences, as illustrated in Fig. 7.2 : first, the readout beam needs to be adjusted (by changing $\Delta\lambda_o$ and/or $\Delta\hat{\theta}_p$) to achieve optimum diffraction efficiency, and second, in the most general case, only a single angular component of the image (θ_s^0) can be made to be exactly Bragg matched. Therefore, because only one of the image angular components is exactly Bragg matched, it is necessary to examine by how much the readout process under a different Bragg condition induces distortion in the reconstructed signal. This is done by decomposing the stored input image into its angular spectrum and by determining the amplitude of each diffracted plane wave component. One can define a transfer function, $H(\theta_s)$, relating the input angular spectrum, $\mathcal{A}_p(\theta_s)$ to the diffracted angular spectrum, $\mathcal{A}_r(\theta_s)$, such that $\mathcal{A}_r(\theta_s) = H(\theta_s)\mathcal{A}_p(\theta_s)$ where θ_s represents the signal beam angular extent [56].

7.3.1 Transfer Function

To compute $H(\theta_s)$, we assume that the input signal has a narrow bandwidth so as to neglect the dispersion of the photorefractive response and the modulation due to the obliquity factor. We further assume that the efficiencies are small so as to neglect the intermodulation gratings. In this case, the complex transfer function, based solely on Bragg detuning effects, is given by [57][58][59]

$$H(\theta_s) = \exp[-i\xi^0(\theta_s)] \frac{\sin \xi^0(\theta_s)}{\xi^0(\theta_s)} \quad (7.1)$$

where $\xi^0(\theta_s)$ is the detuning seen by the component at θ_s , assuming that the component at θ_s^0 is Bragg matched [i.e., $\xi(\theta_s^0) = 0$]. We consider three different cases, corresponding to the three different ways to satisfy the relation $\xi(\theta_s^0) = 0$, using the variables $\Delta\hat{\theta}_p$ and $\Delta\lambda_o$: case (i), by changing only the angle $\hat{\theta}_p$ of the readout beam, which is the easiest to implement experimentally if angular multiplexing is used; case (ii), by changing only the wavelength λ_o of the readout beam, which can

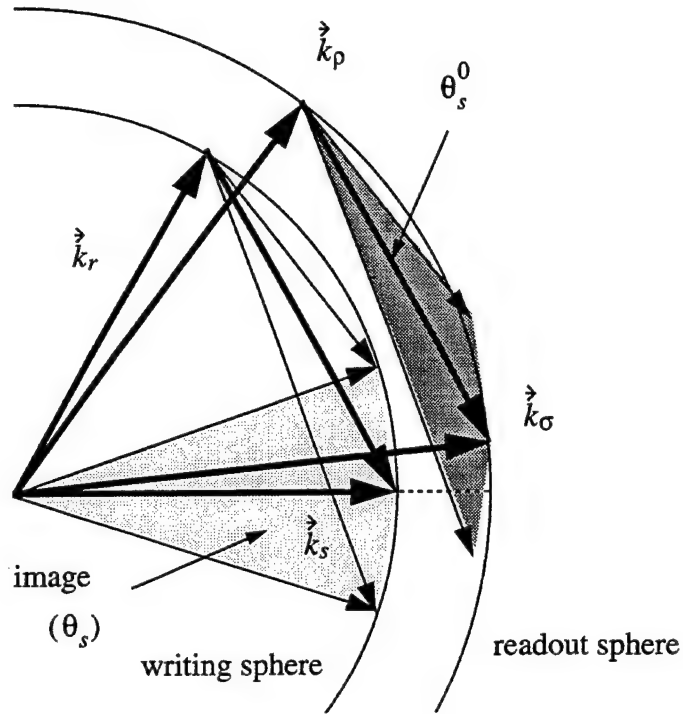


Figure 7.2: k -space representation of an image-bearing hologram when a change of Bragg condition occurs during readout.

be implemented easily if wavelength multiplexing is used; and case (iii), by changing simultaneously the angle $\hat{\theta}_p$ and the wavelength λ_o of the readout beam. In the last case, because both variables are modified, one more degree of freedom exists for us to try to improve the transfer function. Therefore, in addition to $\xi(\theta_s^0) = 0$, one can also impose $d\xi(\theta_s)/d\theta_s = 0$ at $\theta_s = \theta_s^0$ to improve the flatness of the transfer function around the component θ_s^0 and to get better reconstruction quality. From Eq. (6.42) it is possible to compute explicitly the parameter $\xi^0(\theta_s)$ and hence the transfer function $H(\theta_s)$ as well as the detunings $\Delta\hat{\theta}_p$ and $\Delta\lambda_o$ necessary to satisfy $\xi(\theta_s^0) = 0$ in these three different cases. The general analytical expressions are given in an appendix to this chapter. As we shall show in the following examples, these three cases lead to very different transfer functions and to different image quality on reconstruction.

7.4 Thermal Fixing in Holographic Data Storage

7.4.1 Thermal Fixing

The basic idea underlying the thermal fixing process is to generate an ionic grating that matches and compensates the original space-charge pattern of trapped electronic charges and that is not erasable optically [60]. This ionic grating can be generated by heating the crystal either after (low-high-low process) or during (high-low process) the storage process. The crystal is then cooled down and exposed to uniform light to erase the electronic contribution to the grating and reveal the then-fixed ionic grating. Theories have been proposed recently to explain in detail the physical mechanisms and the dynamics of thermal fixing [61] [62]. If the storage and the ionic compensation take place at the same time at an elevated temperature, the ionic grating is not bounded by a pre-existing electronic grating, and after the revealing process this high-low method in general generates higher diffraction efficiencies than does the low-high-low method [63] [64]. Large diffraction efficiencies are highly desirable in a holographic data storage system because higher capacity can be achieved for the same signal-to-noise ratio [7]. Unfortunately, this temperature difference between readout and writing induces strains and index changes inside the crystal that then affect the Bragg condition, as shown by Eq. (6.42). Using this technique, Staebler *et al.* [65] were, however, able to store, fix, and retrieve multiple image-bearing holograms angularly multiplexed in LiNbO_3 in the transmission geometry.

7.4.2 Transfer Function

In this example we consider a typical digital holographic data storage system [19], using the perpendicular geometry ($\theta_r = -90^\circ$) to angularly multiplex images in a LiNbO_3 crystal, with ordinarily polarized light ($\lambda_o = 514 \text{ nm}$), the c axis at 45° , no applied field, and an assumed temperature difference $\Delta T = -150^\circ\text{C}$ necessary to achieve fixing (high-low method). This ΔT induces a change in the index of refraction and a change in the grating spacing owing to thermal expansion. Typical values for the different crystal parameters are given in Table 7.1, the values for LiNbO_3 coming

Parameters	LiNbO ₃	SBN:75
l	1 cm	1 cm
λ_o	514 nm	514 nm
\bar{n}	2.21	2.3
α_a	$14 \cdot 10^{-6}$ 1/K	-
α_c	$4 \cdot 10^{-6}$ 1/K	-
$\partial n_o / \partial T$	$5.9 \cdot 10^{-6}$ 1/K	-
$\partial n_e / \partial T$	$6.4 \cdot 10^{-6}$ 1/K	-
r_{13}	10 pm/V	67 pm/V
r_{33}	30 pm/V	1340 pm/V
d_{13}	2 pm/V	25 pm/V
d_{33}	8 pm/V	80 pm/V

Table 7.1: Parameters for the photorefractive crystals Ce-SBN:75 and LiNbO₃.

from Ref. [66].

We assume the image to be normally incident on the crystal and take $\theta_s^0 = 0$, which corresponds to the dc component of the angular spectrum. Since for data storage, the Fourier transform of the input image is usually stored in the crystal, the signal beam angular extent θ_s , representing the field of view, is a measure of the lateral dimension of the input object that is stored in the crystal and, by extension, of the number of pixels on the input spatial light modulator. This number will determine the page capacity and ultimately the total capacity of a holographic data storage system. Under these conditions the different transfer functions given in the appendix at the end of this chapter can be simplified to yield (taking into account that the angle θ_s is small, typically a few degrees):

case (i)

$$\xi^0(\theta_s) = -\frac{\pi l \bar{n} \Delta T}{\lambda_o} \left(\frac{1}{\bar{n}} \frac{\partial n_o}{\partial T} + \frac{\alpha_c + \alpha_a}{2} \right) \theta_s \quad (7.2)$$

$$\Delta \hat{\theta}_\rho = \bar{n} \left(\frac{1}{\bar{n}} \frac{\partial n_o}{\partial T} + \alpha_c \right) \Delta T \quad (7.3)$$

case (ii)

$$\xi^0(\theta_s) = -\frac{\pi l \bar{n} \Delta T}{\lambda_o} \left(\frac{\alpha_a - \alpha_c}{2} \right) \theta_s \quad (7.4)$$

$$\frac{\Delta \lambda_o}{\lambda_o} = \left(\frac{1}{\bar{n}} \frac{\partial n_o}{\partial T} + \alpha_c \right) \Delta T \quad (7.5)$$

case (iii)

$$\xi^0(\theta_s) = 0 \quad (7.6)$$

$$\frac{\Delta \lambda_o}{\lambda_o} = \left(\frac{1}{\bar{n}} \frac{\partial n_o}{\partial T} + \frac{\alpha_c + \alpha_a}{2} \right) \Delta T \quad (7.7)$$

$$\Delta \hat{\theta}_\rho = \bar{n} \left(\frac{\alpha_c - \alpha_a}{2} \right) \Delta T \quad (7.8)$$

7.4.3 Discussions

Figure 7.3 represents the square of the amplitude of the transfer function, $|H(\theta_s)|^2$, [Eq. (7.1)] as a function of θ_s (measured in degrees inside the crystal). The solid curve corresponds to case (i) ($\Delta \hat{\theta}_\rho$), the dashed curve to case (ii) ($\Delta \lambda_o$), and the dotted line to case (iii) ($\Delta \hat{\theta}_\rho$ and $\Delta \lambda_o$). By changing $\Delta \hat{\theta}_\rho$ only, the reconstructed bandwidth is limited to a full width of $\sim 1.5^\circ$. The distortion is due to the factor $(1/\bar{n})\partial n_o/\partial T + 1/2(\alpha_c + \alpha_a)$, where thermal expansion is the dominant factor. By changing $\Delta \lambda_o$ only, one can achieve reconstruction over a larger signal bandwidth because distortion depends only on the difference $\alpha_a - \alpha_c$, i.e., the anisotropic part of thermal expansion. When $\theta_r = -90^\circ$, anisotropy is the sole cause for image distortion and reconstruction over the whole angular spectrum is possible if the crystal is isotropic ($\alpha_a = \alpha_c$). By optimizing the wavelength and the angle of the readout beam simultaneously, one can achieve reconstruction (to first order in $\Delta \hat{\theta}_\rho$ and $\Delta \lambda_o$) over the whole signal bandwidth, despite the crystal anisotropy. Figure 7.4 represents the Bragg detuning parameter $\xi^0(\theta_s)$, i.e., the phase of the transfer function, as a function of θ_s , for the same three different cases.

From such a transfer function we define a field of view, corresponding to the angle between its (-1) and (+1) zeros. Figure 7.5 shows the field of view (FOV) expressed

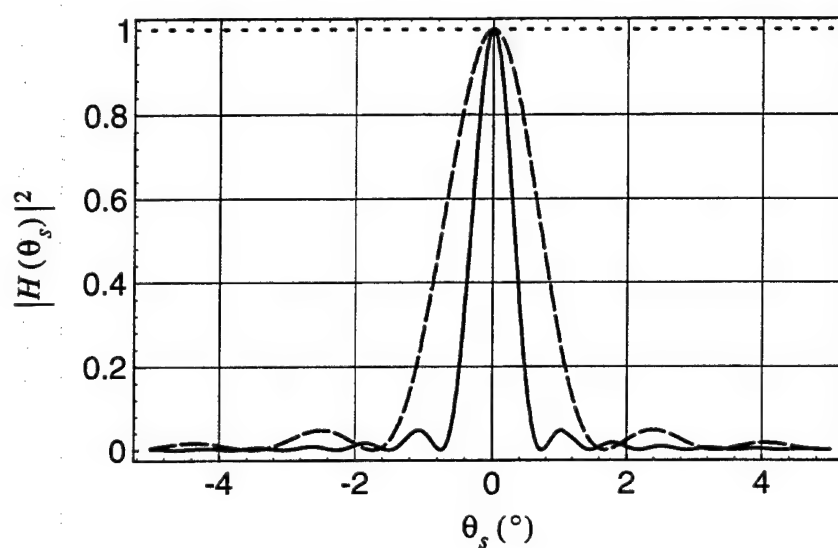


Figure 7.3: Transfer function in the perpendicular geometry with use of LiNbO_3 for a $\Delta T = -150^\circ\text{C}$. The solid curve represents the case in which only the angle of the readout beam is adjusted [case (i)], the dashed curve represents the case in which only the wavelength of the readout beam is adjusted [case (ii)], and the dotted line represents the case in which both the angle and the wavelength are simultaneously adjusted [case (iii)].

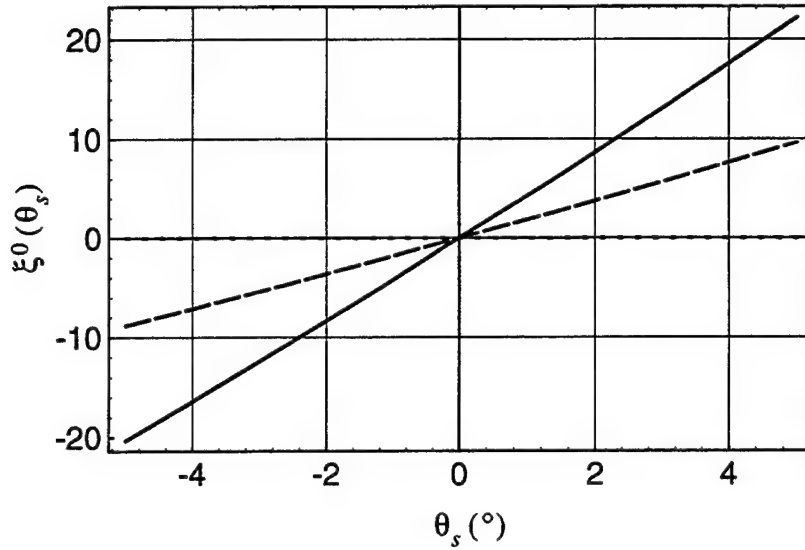


Figure 7.4: Bragg detuning parameter (phase of the complex transfer function) in the perpendicular geometry with use of LiNbO_3 for a $\Delta T = -150^\circ\text{C}$. Solid curve: case (i); dashed curve: case (ii); and dotted line: case (iii).

in degrees as a function of temperature for case (i) (solid curve) and case (ii) (dashed curve). The third case, case (iii), is not represented since in this case the full field of view is reconstructed, as shown by the flat transfer function of Fig. 7.3. Figure 7.5 shows that the field of view increases with decreasing temperature changes. Therefore, if a given temperature change is required for fixing to be achieved and if, for example, angular multiplexing is used with no tunable laser source, Bragg detuning sets an upper limit on the reconstructed field of view, hence on the size of the input image (number of pixels).

Figures 7.6(a) and (b) compare the different detunings that are required to Bragg match the dc component of the angular spectrum of the image, i.e., to impose $\xi(\theta_s^0) = 0$, as a function of temperature. Figure 7.6(a) compares the angular detuning of case (i) [Eq. (7.3)] with case (iii) [Eq. (7.8)]. Figure 7.6(b) compares the wavelength detuning of case (ii) [Eq. (7.5)] with case (iii) [Eq. (7.7)]. In particular, the wavelength detuning necessary to Bragg match the dc component of the image (at 100°C , $\Delta\lambda_0 \approx 0.5 \text{ nm}$) [in case (ii) or case (iii)] is shown to be much larger than the wavelength bandwidth of the grating itself (that is of the order of 0.01 nm).

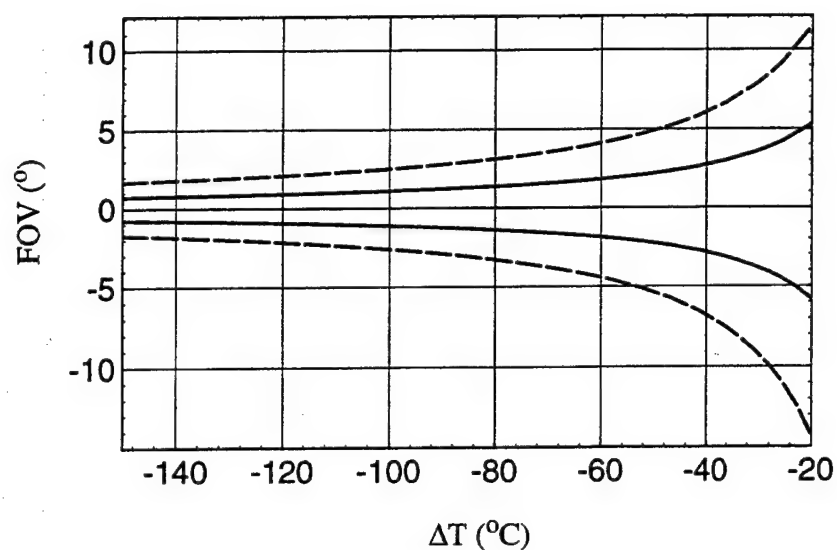


Figure 7.5: Field of view (FOV) (in degrees inside the crystal) as a function of temperature in the perpendicular geometry with use of LiNbO_3 . Solid curve: case (i); dashed curve: case (ii).

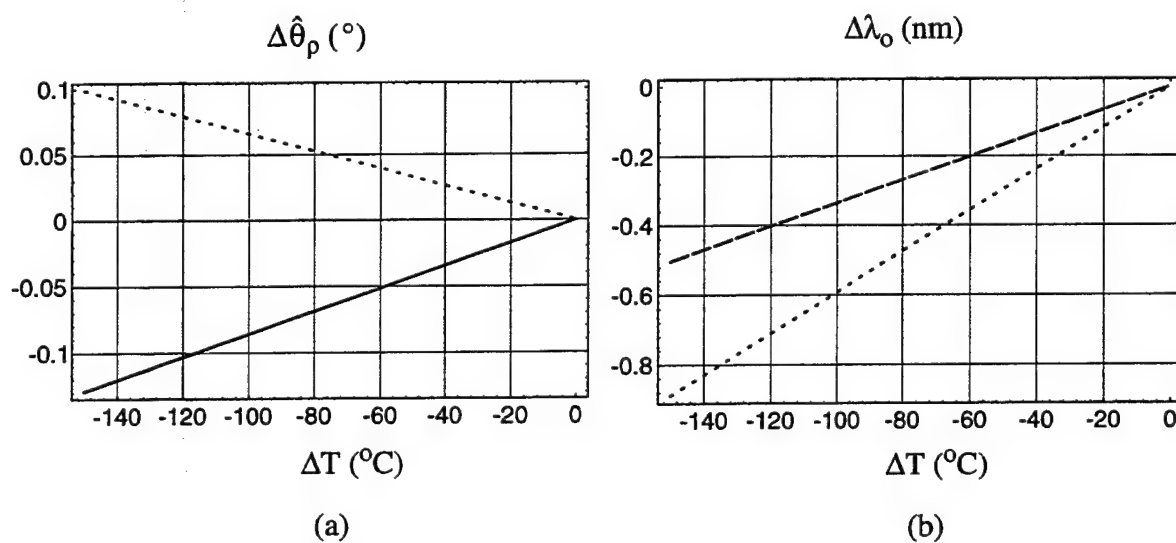


Figure 7.6: (a) Angular detuning (in degrees outside the crystal) and (b) wavelength detuning as a function of temperature. These are the detunings necessary to Bragg match the dc component of the image during readout. Solid curve: case (i); dashed curve: case (ii); and dotted line: case (iii).

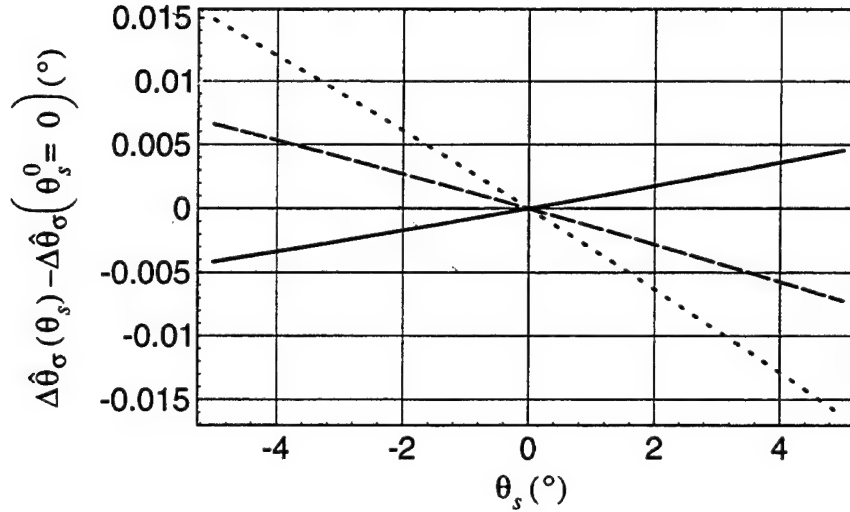


Figure 7.7: Relative angular shift of the diffracted beam $[\Delta\hat{\theta}_\sigma(\theta_s) - \Delta\hat{\theta}_\sigma(\theta_s^0)]$ (in degrees outside the crystal) as a function of θ_s for a $\Delta T = -150^\circ\text{C}$. Solid curve: case (i) $[\Delta\hat{\theta}_\sigma(\theta_s^0) = 0.05^\circ]$; dashed curve: case (ii) $[\Delta\hat{\theta}_\sigma(\theta_s^0) = -0.075^\circ]$; and dotted line: case (iii) $[\Delta\hat{\theta}_\sigma(\theta_s^0) = -0.17^\circ]$.

As shown by Eq. (6.11) the angular direction of the diffracted beam changes as a result of a temperature difference ΔT , and this shift depends on the signal angular extent θ_s as well. Therefore different parts of the image will be shifted by different amounts, resulting in image compression or dilatation. Figure 7.7 shows the relative change in angular shift compared with the shift of the central component (measured in degrees outside the crystal) as a function of θ_s for the cases (i), (ii), and (iii), assuming a $\Delta T = -150^\circ\text{C}$. In case (i) the shift results in a dilatation of the output image on the detector, and in cases (ii) and (iii) it results in a compression of the image on the output detector. Figure 7.7 shows that the image compression or dilatation is approximately equal to 0.2 - 0.3 %. This problem is of particular importance in a digital holographic data storage system where high accuracy is required to image the spatial light modulator onto the CCD array [67]. Indeed, for an input image consisting of 1024×1024 pixels, a deformation of 0.3 % represents several pixels, which is significant and cannot be neglected.

So far, the perpendicular geometry has been considered with $\theta_r = -90^\circ$. However

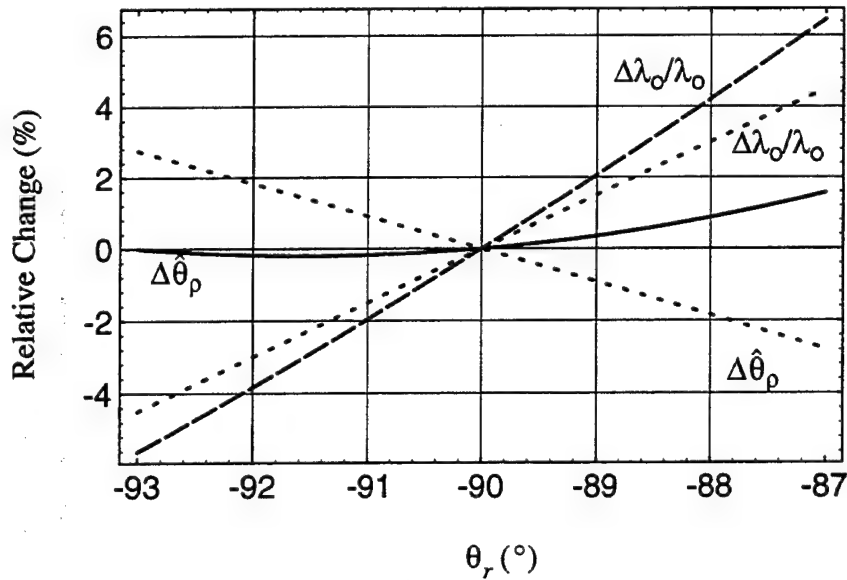


Figure 7.8: Relative detuning changes (%) as a function of the angle of the reference beam θ_r (in the perpendicular geometry and for a $\Delta T = -150^\circ\text{C}$). If angular multiplexing is used, each reference beam angle corresponds to an image number. Solid curve: case (i); dashed curve: case (ii); and dotted line: case (iii).

in a holographic data storage system that uses angular multiplexing, different pages are stored at different angles θ_r . In a typical setup, θ_r varies by a few degrees around the normally incident position. It is thus necessary to examine by how much the field of view and the different angular and wavelength detunings vary as a function of θ_r , i.e., as a function of page number in a data storage system. The relative changes in detuning (expressed in percent) are plotted in Fig. 7.8 and show that a variation of a few percent is possible between the two extreme pages stored in the crystal. These changes are significant enough that the Bragg condition needs to be readjusted for each of the retrieved pages of information. Note that the range of angles chosen in Fig. 7.8 for the reference beam angle corresponds to the range required for angularly multiplexing 1000 images in a 1-cm-thick crystal by placing reference beams at adjacent nulls.

Figures 7.9(a) and (b) represent the field of view in LiNbO_3 with a temperature difference of 150°C in the reflection, the perpendicular, and the transmission recording geometries. Figure 7.9(a) corresponds to the angular multiplexing case, where

only the readout angle is adjusted during reconstruction and Fig. 7.9(b) corresponds to the wavelength multiplexing case, where only the wavelength is adjusted.

In the angular multiplexing case it is clear that the reflection geometry is inappropriate because only an extremely small field of view can be reconstructed. However the smaller the reference angle (e.g., in the transmission geometry), the larger the reconstructed field of view, which shows that in terms of field of view, the transmission geometry is a better choice than the perpendicular one. Unfortunately, in the transmission geometry case, the total capacity is less and the cross talk is higher than in the perpendicular geometry.

In the wavelength multiplexing case the reflection geometry is the best choice because the reconstruction is almost perfect over the whole signal bandwidth, and it is also the optimum geometry in terms of wavelength selectivity [4] [52]. In this case the optimum in terms of field of view is also the optimum for achieving maximum capacity and minimum cross talk.

To get a better understanding of the consequences of temperature changes in a digital holographic data storage setup (we assume that we use angular multiplexing in the perpendicular geometry), it is necessary to relate the field of view to the number of pixels on the input spatial light modulator. This number will then give a better estimate of how much temperature differences limit the capacity per page. The maximum size D of the input image that can be fully reconstructed is given by $D \approx \bar{n} f \text{FOV}$ where f is the focal length of the Fourier lens and FOV is the field of view (inside the crystal) determined by the temperature difference applied to the crystal and by the writing configuration. For example, with $f = 3$ cm and $\text{FOV} = 4^\circ$, $D = 4.6$ mm. In comparison, the dimension of a typical spatial light modulator (SLM) of 1024×1024 pixels (of $18\text{-}\mu\text{m}$ size) is of the order of 20 mm.

Figure 7.10 shows the relationship between the field of view (expressed in degrees inside the crystal) and the number of pixels on the input SLM that are fully reconstructed. The field of view is plotted for three different focal lengths, f : $f = 3$ cm, $f = 5$ cm, and $f = 10$ cm. Figure 7.10 shows that if the 1024 pixels need to be reconstructed during readout and if a lens with $f = 10$ cm is used to store the information, the crystal needs to be able to reconstruct a total field of view of 5° , which limits the

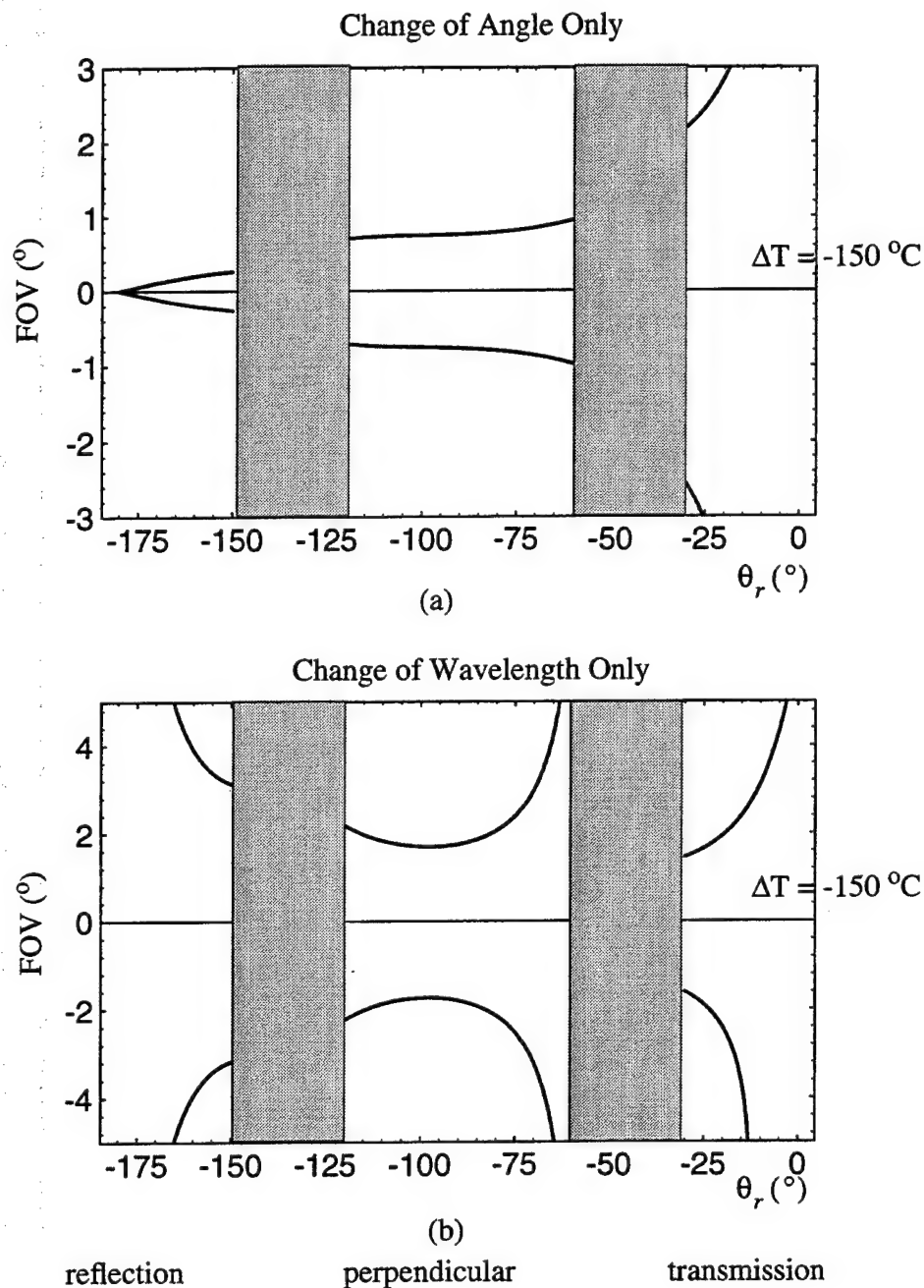


Figure 7.9: Field of view (in degrees inside the crystal) as a function of θ_r in the three recording geometries for a $\Delta T = -150^\circ\text{C}$. The shaded areas represent the forbidden regions resulting from the crystal boundary conditions and Snell's law. (a) Change in angle only (angular multiplexing), (b) change in wavelength only (wavelength multiplexing).

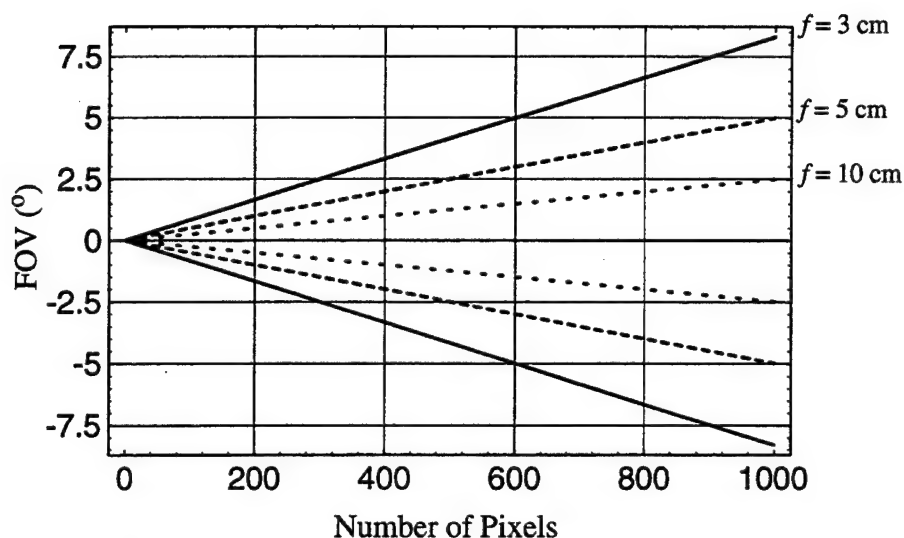


Figure 7.10: Field of view (in degrees inside the crystal) as a function of the number of SLM pixels that are fully reconstructed, for three different focal lengths, f .

temperature difference that can be applied to the crystal to a maximum value of 45 °C. If a temperature gradient of 150 °C is applied to the crystal [see Fig. 7.9(a)] in an angularly multiplexed storage system, a maximum field of view of approximately 1.5° can be fully reconstructed, which corresponds to ~ 300 pixels ($f = 10$ cm), one third of the total extent of the SLM.

7.4.4 Experimental Results

In this experiment the Fourier transform of a circular aperture of diameter $d = 2.5$ cm is stored and fixed in a LiNbO_3 crystal with use of the perpendicular geometry and a lens of focal length $f = 10$ cm. The image has a signal beam angular extent of 14° outside the crystal, i.e., 6.3° inside the crystal (the field of view is measured along the horizontal axis of the aperture). First the aperture is recorded at room temperature (25 °C). The crystal is then successively heated to 140 °C, cooled down to room temperature, and uniformly illuminated to fix and reveal the hologram (low-high-low process). Figure 7.11(a) shows the thermally fixed image on readout. In this case there is no temperature difference between the recording and the readout

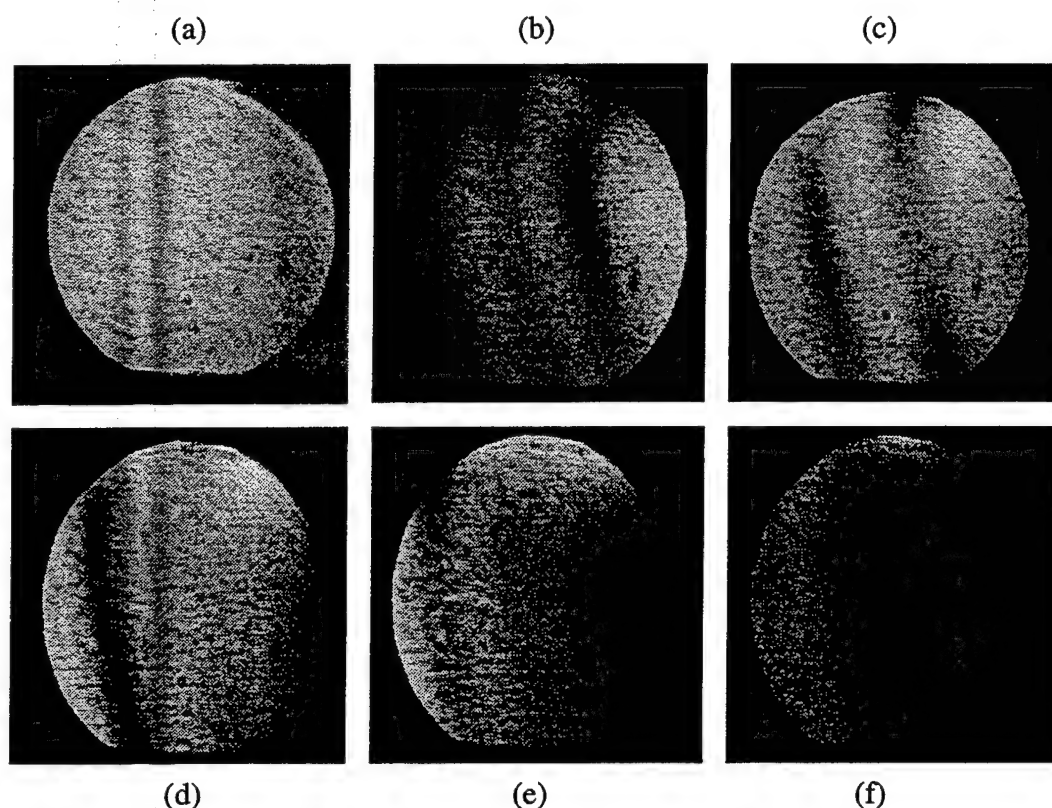


Figure 7.11: Circular aperture recorded in LiNbO_3 with the perpendicular geometry: (a) thermally fixed image with the low-high-low process, (b)-(f) fixed images with the high-low process, taken at five different readout angles ($\Delta T = -115^\circ\text{C}$).

conditions and no visible image deformation (as expected, the whole field of view is reconstructed).

Second, the other approach to achieve fixing is performed: the aperture is recorded at an elevated temperature (140°C), and then the crystal is cooled down and illuminated to reveal the fixed grating (high-low process). In this case there is a temperature difference of -115°C between the recording and the readout conditions. Figures 7.11(b)-(f) show the resulting diffracted signals taken at five slightly different readout angles (only the readout angle is adjusted to Bragg match the image; there is no wavelength detuning in this experiment). Figure 7.11(d) corresponds to the central image with the dc component exactly Bragg matched and clearly shows the different zeros of the transfer function. From this figure, it can be inferred that the field of view for a temperature difference of -115°C is approximately equal to 4° (inside the

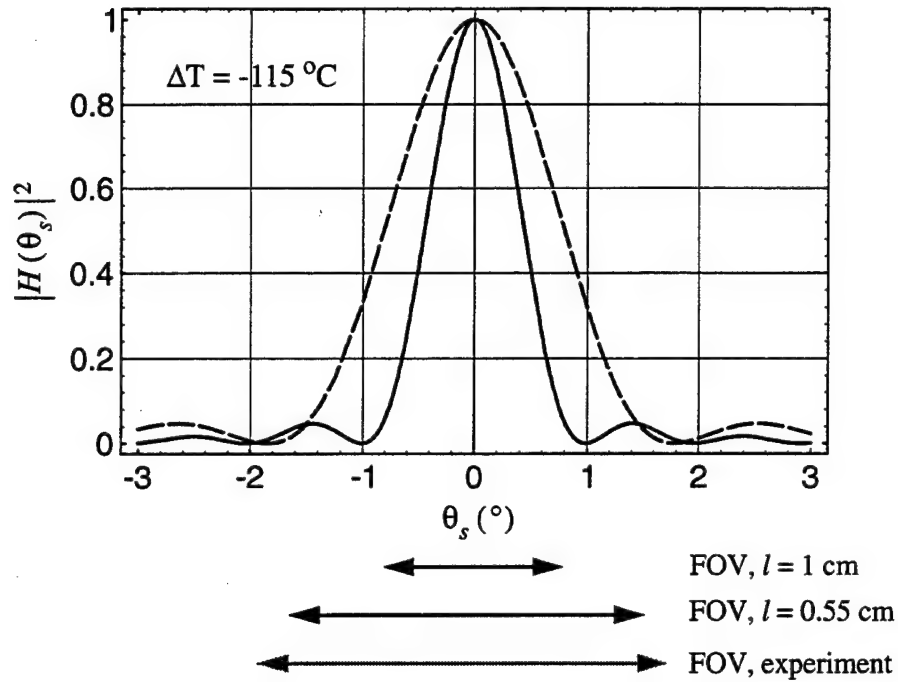


Figure 7.12: Transfer function corresponding to the experimental images of Fig. 7.11 ($\Delta T = -115^\circ\text{C}$). The experimental field of view is compared with the theoretical field of view computed given an interaction length $l = 1$ cm (solid curve) and $l = 0.55$ cm (dashed curve)

crystal). Figure 7.12 shows the corresponding transfer functions computed from the expression given by Eq. (7.2) and the parameters of Table 7.1. The theoretical field of view ($\sim 2^\circ$) shows good qualitative agreement with Fig. 7.11(d) although the experimental field of view ($\sim 4^\circ$) appears larger than the theoretical one ($\sim 2^\circ$). One of the reasons is that the interaction length of the fixed grating is less than the crystal length ($l = 1$ cm). This can be partly due to the fact that the illumination cannot be made perfectly uniform over the whole crystal. It could also be partly due to fringe bending and beam coupling. Figure 7.13 shows the experimentally measured angular selectivity of the different gratings, the unfixed, the fixed following the low-high-low process, and the fixed following the high-low process and compares these results with the theoretical curve for $l = 1$ cm. It shows that the interaction length of the grating inside the crystal is less than 1 cm. From these selectivity measurements the actual interaction length of the fixed grating can be estimated to be $l = 0.55$ cm. This result

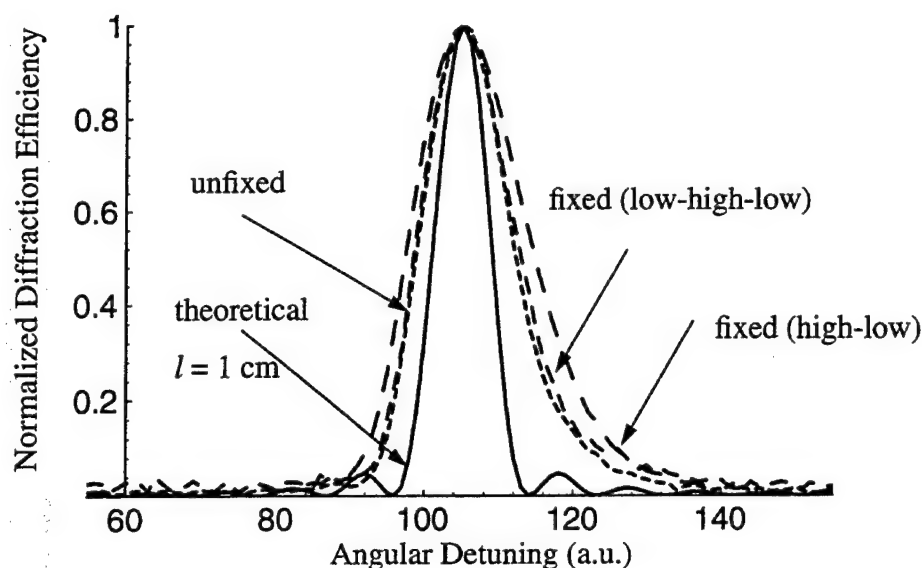


Figure 7.13: Angular selectivity: theoretical curve corresponding to $l = 1$ cm, and experimental curves corresponding to the unfixed grating, the fixed grating (low-high-low), and the fixed grating (high-low). The interaction length of the fixed grating can be estimated to be $l = 0.55$ cm.

is confirmed by the fact that the field of view corresponding to this interaction length shows better agreement with the observed value of 4° . Note that similar reduction in the grating interaction length because of the fixing process has been previously observed during attempts to build a wavelength filter containing a thermally fixed grating [68][69].

7.4.5 Conclusions

In this first application we study the effects that thermal fixing has in a digital holographic data storage system. One of the goals is to underscore and point out several trade-offs among efficiency, signal-to-noise ratio, and capacity to optimize a digital holographic data storage system that utilizes thermal fixing. When several pages of information (images) are multiplexed in a single crystal, it is well known that the diffraction efficiency of each page goes down as $1/N^2$ where N is the total number of pages multiplexed in a single location inside the crystal. Therefore it is highly desirable to store the smallest number of pages possible and pack as much

information as possible on a single page.

This study shows that because of a temperature change, the actual size D of the input image is limited to $D \sim \bar{n}f$ FOV, where f is the focal length of the Fourier lens and FOV is the field of view (inside the crystal) determined by the temperature difference applied to the crystal. Therefore it is necessary to maximize FOV to maximize D , D representing also the maximum number of pixels that can be perfectly reconstructed. In an imaging system the effects of temperature changes will similarly affect the resolution of the input images, i.e., the size and the spacing between the pixels on the SLM. The capacity per page and ultimately the total capacity of the data storage system will therefore be affected in a similar way by temperature differences. In both the Fourier and the imaging systems it is therefore necessary to maximize the reconstructed signal angular bandwidth, which can be done by adopting the low-high-low fixing process.

A recent study [70] showed that in the perpendicular and the reflection geometries, the gain in efficiency from using the high-low process compared with using the low-high-low process (η_{h-l}/η_{l-h-l}) is of the order of 1 to 2 for a usual LiNbO_3 crystal (material optimization is required to achieve this ratio). This gain in efficiency is relatively small compared with the price one has to pay in terms of image deformation, as shown by the experimental results and the theoretical transfer functions. Therefore in these geometries it is preferable to use the low-high-low process. However in the transmission geometry this gain factor η_{h-l}/η_{l-h-l} can be of the order of 10^2 - 10^3 , which shows that a substantial gain in diffraction efficiency and dynamic range can be achieved by use of the high-low process. Figure 7.9 also shows that distortions in the transmission geometry are relatively limited and that in practical situations and for typical temperature changes the field of view determined by a 1024×1024 -pixels SLM will be always fully reconstructed. Therefore in this geometry it is largely preferable to use the high-low process to achieve fixing of image-bearing holograms.

7.5 ECD Effect in Holographic Data Storage

7.5.1 Introduction

In this section we examine the operation of recording a hologram in a photorefractive crystal at a temperature slightly above the ferroelectric-paraelectric phase transition, or Curie point, so as to eliminate both beam fanning noise and beam coupling effects, while also employing electrically controlled diffraction to substantially enhance and adjust the diffraction efficiency of the stored holograms [56]. Above the Curie point defined by the Curie temperature T_c the crystal is in the paraelectric state and therefore, in the absence of an applied bias field, possesses no linear electro-optic effect. The lack of a linear electro-optic effect precludes first-order diffraction, thereby suppressing beam fanning and beam coupling. It is helpful in storage applications to eliminate beam coupling because, as we saw in earlier chapters, it acts to broaden the angular bandwidth of the holograms and can therefore diminish the overall storage capacity [71].

Operation above T_c also requires that an applied field be used during readout to electrically reveal the stored holograms [39]. The applied field induces a small-signal linear electro-optic component, thereby providing the necessary linear relationship between the photorefractive space-charge field and the refractive index modulation. When using this approach, field-induced changes in the average bulk refractive index also come into play since these changes alter the Bragg condition. For an image-bearing hologram, each angular component of the reconstructed signal wave is affected differently and is best described by means of a field-dependent transfer function, as defined earlier by Eq. (7.1).

Not only is electrically controlled diffraction (ECD) [39] an integral part of the scheme described here for holographic storage above T_c , it is also quite useful in its own right as a potentially important mechanism on which to base new holographic devices for applications such as dynamic wavelength filtering [72] and integrated crossbar switching [73]. In Chapter 9 we will describe in detail the properties of a dynamic multiple-wavelength filter based on a photorefractive stratified volume holographic optical element that uses the ECD effect to selectively address different wavelengths.

Material	T_c (°C)	Ref.
$\text{Sr}_{0.60}\text{Ba}_{0.40}\text{Nb}_2\text{O}_6$ (SBN:60)	78	Glass [74]
$\text{Sr}_{0.75}\text{Ba}_{0.25}\text{Nb}_2\text{O}_6$ (SBN:75)	44	Glass [74]
BaTiO_3	130	Klein [75]
$\text{KTa}_{0.70}\text{Nb}_{0.30}\text{O}_3$ (KTN)	-32	Levy [76]
$\text{Ba}_{2-x}\text{Sr}_x\text{K}_{1-y}\text{Na}_y\text{Nb}_5\text{O}_{15}$ (BSKNN)	80	Neurgaonkar [77]
PLZT 10/65/35	~ -20	Rupp [78]

Table 7.2: Ferroelectric photorefractive materials having phase transition temperatures within 100 °C of room temperature.

As shown in Table 7.2, there exists a number of ferroelectric photorefractive materials with a Curie temperature within 100 °C of room temperature [74] [75] [76] [77] [78]. Most notable are the tungsten bronzes – such as strontium barium niobate (SBN), lead barium niobate (PBN), and barium strontium potassium sodium niobate (BSKNN) – that can be grown over a wide compositional range, with the nominal phase transition temperature being dependent on the particular composition chosen. Previous studies of photorefractive recording in the vicinity of the ferroelectric phase transition have been carried out in SBN:75 [39], PLZT [78], and KTN [79]. By way of example, we focus on Ce-doped $\text{Sr}_{0.75}\text{Ba}_{0.25}\text{Nb}_2\text{O}_6$ (SBN:75) since it offers many interesting properties related to its near room-temperature diffuse phase transition, with T_c being distributed over a range of 35 - 45 °C [39].

7.5.2 Electric Field Enhancement

The ferroelectric phase transition of a crystal refers to the transformation of the crystal from a paraelectric state above T_c to a ferroelectric state below T_c . In the paraelectric state, the crystal is nonpolar and centrosymmetric, meaning that the material has no linear electro-optic effect; hence, no first-order diffraction can be observed from photorefractive holograms, although space-charge formation can still take place. In the ferroelectric state, the crystal acquires a spontaneous polarization in the form of ferroelectric domains. When a ferroelectric photorefractive crystal is uniformly poled to a single domain, it possesses a macroscopic linear electro-optic

effect and can record volume holograms in the usual manner. The minimum field necessary to pole the crystal is called the coercive field. The transition between the paraelectric and the ferroelectric states typically occurs at a critical temperature T_c , the Curie temperature, that is an intrinsic characteristic of the material [44].

When operating near the ferroelectric phase transition (i.e., around $T = T_c$), the material properties respond strongly to changes in electric field and become very sensitive to changes in other external variables such as temperature and pressure. Therefore, it is generally necessary to maintain fairly tight control over these parameters. The materials sensitivity to changes in the environment is governed by the nature of the phase transition. In a well-ordered crystalline lattice the transition is typically quite sharp, occurring over just a few degrees. In contrast, disordered solid-solution crystals, like many of the tungsten bronze materials, are characterized by local variations in composition which act to spread the transition over a much broader range of temperatures compared with an ideal crystal with a uniform composition. With regard to device applications, a diffuse phase transition is useful since it relaxes the degree to which the operating temperature and pressure must be maintained constant. Tungsten bronze materials such as SBN and PBN are also referred to as "relaxor ferroelectrics" because they exhibit strong dielectric dispersion near the phase transition [80].

As we said, in the vicinity of the ferroelectric-paraelectric phase transition, many of the crystal properties become strongly field-dependent and nonlinear. The fact that an applied field can, under these conditions, be used to control the hologram amplitude is most easily seen by considering the simplest nonlinear form, a purely quadratic electro-optic effect (characteristic of the paraelectric phase) in which $\Delta n(E_0) \propto E_{total}^2 = (E_{SC} + E_0)^2$, where E_{SC} is the photorefractive space-charge field defining the hologram and E_0 is a uniform applied field. By simply expanding the square, it is clear that the cross term $2E_{SC}E_0$ yields an index modulation proportional to E_{SC} with the amplitude being controlled by E_0 . Near the phase transition, the nonlinearity takes on a more general form, but the applied field can still be viewed as providing a bias to a linear regime. It can be shown [44] that $\Delta n(E_0) \propto E_{sc}f(E_0)$ where

$$f(E_0) = \frac{r(E_0)}{\epsilon(E_0)} \quad (7.9)$$

is an increasing function of E_0 , and where r is the electro-optic coefficient and ϵ is the dielectric constant. The field dependence of the dielectric constant must be taken into account since this determines the degree to which the space-charge field is screened by the lattice. The grating strength ν is then given by

$$\nu = \frac{\pi l \Delta n(E_0)}{\lambda_o \sqrt{\cos \theta_\rho \cos \theta_\sigma}} \quad (7.10)$$

where l is the crystal length, and $\theta_\rho, \theta_\sigma$ are the propagation angles (inside the crystal) of the readout and the diffracted beams, respectively. In conclusion, a hologram can still be recorded in the paraelectric state in the form of a space-charge pattern, but an applied field E_0 is needed to reveal the index grating $\Delta n(E_0)$ and to observe a diffracted signal.

7.5.3 Transfer Function

The transfer function is given by Eq. (7.1),

$$H(\theta_s) = \exp[-i\xi^0(\theta_s)] \frac{\sin \xi^0(\theta_s)}{\xi^0(\theta_s)} \quad (7.11)$$

where $\xi^0(\theta_s)$ is the detuning seen by the component at θ_s assuming that the component at θ_s^0 is exactly Bragg matched. The general expressions are given in an appendix to this chapter. Note that in the following experiments we consider only the transmission geometry and vary only the angle of the readout beam. Finally the image-bearing holograms are recorded using a telecentric imaging system.

Figures 7.14 and 7.15 show examples of transfer functions, $|H(\theta_s)|^2$, as a function of the signal beam angular extent θ_s (degrees inside the crystal) for the Ce-doped SBN:75 crystal used in the experiments described in the next section. The transfer functions are shown in case (i), in which only the readout angle is adjusted upon reconstruction. For a telecentric imaging system, the angular extent of an object is related to its spatial frequency f_o by

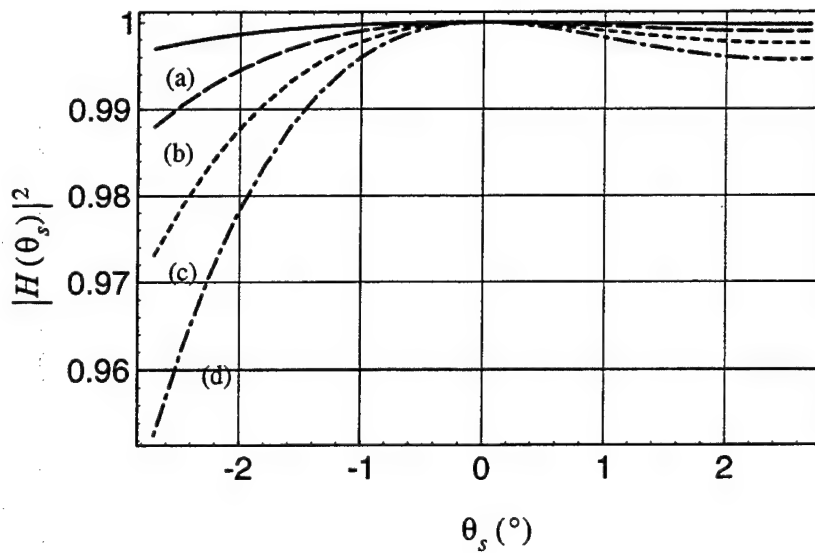


Figure 7.14: Transfer function as a function of the signal beam angular extent θ_s for $\theta_r = 5^\circ$ and $\theta_s^0 = 0^\circ$ at four different applied fields: (a) 1, (b) 2, (c) 3, and (d) 4 kV/cm ($l = 1$ cm, $\lambda_o = 514$ nm, extraordinary polarization).

$$\hat{\theta}_s = \lambda_o f_o \quad (7.12)$$

This indicates that an object with a resolution of 100 lp/mm has a total angular extent of $\pm 6^\circ$ outside the crystal, i.e., $\pm 2.7^\circ$ inside the crystal.

Figure 7.14 is computed for a reference beam angle $\theta_r = 5^\circ$ and a Bragg matched component $\theta_s^0 = 0^\circ$. Figure 7.15 is computed for a reference beam angle $\theta_r = 6.5^\circ$ and a Bragg matched component $\theta_s^0 = -6.5^\circ$. For a large angle difference between θ_r and θ_s^0 , substantial deformation occurs at the highest angular components of the input image. For a small difference between θ_r and θ_s^0 , very little distortion occurs during image retrieval. Note also that the transfer function, while being strongly dependent on the difference between θ_r and θ_s^0 , is also a non-symmetric function of the signal beam angular extent θ_s .

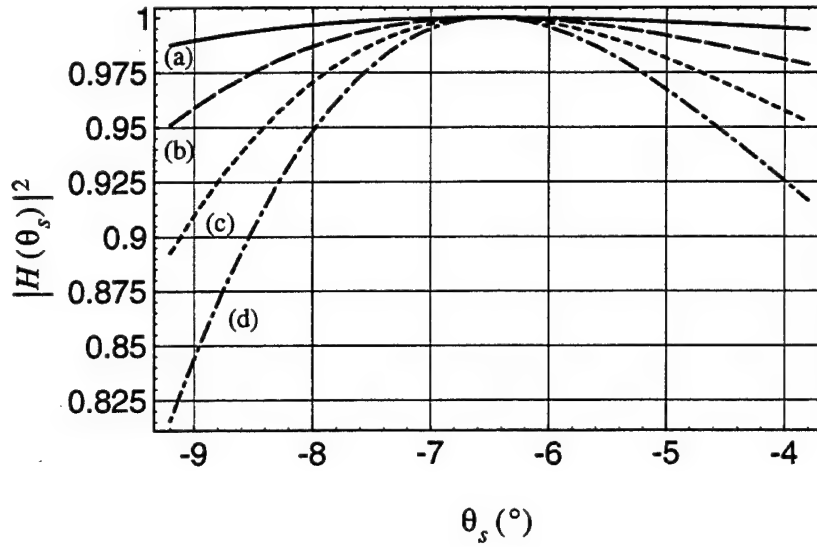


Figure 7.15: Transfer function as a function of the signal beam angular extent θ_s for $\theta_r = 6.5^\circ$ and $\theta_s^0 = -6.5^\circ$ at four different applied fields: (a) 1, (b) 2, (c) 3, and (d) 4 kV/cm ($l = 1$ cm, $\lambda_o = 514$ nm, extraordinary polarization).

7.5.4 Experimental Results

Angular Multiplexing of Plane Waves

In this experiment, we combine angular multiplexing and an applied field to store and efficiently retrieve multiple planar gratings in a Ce-doped SBN:75 crystal heated at 60°C . The temperature is maintained constant throughout the recording and the readout process. The recording intensities are $I_s = I_r = 5$ mW/cm². An asymmetric writing geometry where $\theta_s^0 = 0^\circ$ and $\theta_r = 12.5^\circ$ (30° outside the crystal) is used during the recording process. A sequential recording exposure schedule is considered to obtain equal diffraction efficiencies upon readout. The recording schedule [81] is determined from

$$t_m = \tau_r \ln \frac{(m-1)\beta + 1}{(m-1)\beta + 2} \quad (7.13)$$

with $\tau_r = 7$ s and $\beta = 0.75$. τ_r is the recording time constant, $\beta = 1 - \exp(-t_1/\tau_r)$, and t_m is the recording time of the m^{th} hologram. The multiplexed holograms are then read with a low intensity ($25 \mu\text{W}/\text{cm}^2$) readout beam so as not to erase the holograms.

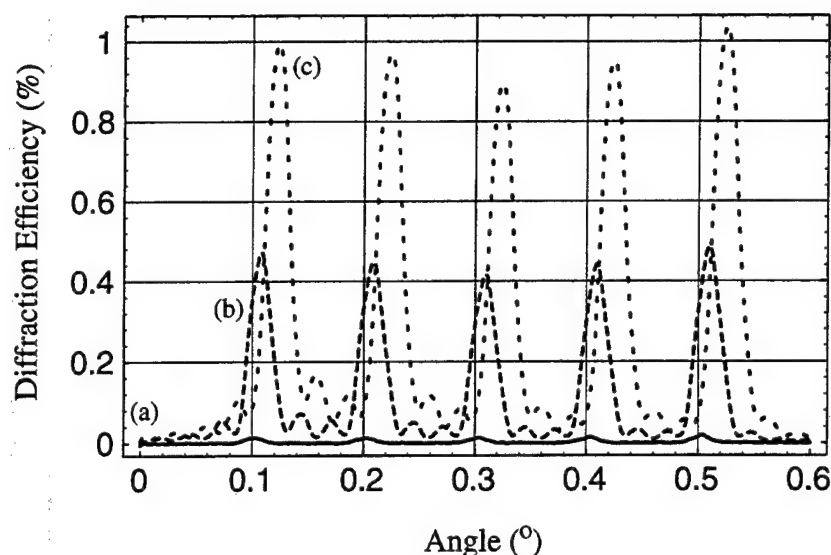


Figure 7.16: Diffraction efficiency of five angularly multiplexed planar holograms recorded in SBN:75 at $T = 60^\circ\text{C}$ ($\theta_r = 12.5^\circ$ and $\theta_s^0 = 0^\circ$). The holograms are successively read with three different applied fields: 0 kV/cm (a, solid), 2 kV/cm (b, dashed), and 4 kV/cm (c, dotted).

Figure 7.16 shows the diffraction efficiency as a function of angle, clearly illustrating the presence of the five holograms previously recorded in the crystal in a sequential way. It also shows how the field applied during readout drastically enhances the diffraction efficiency of all the holograms compared with the efficiency at no applied field, because of the strong ECD effect at $T = 60^\circ\text{C}$. The figure finally shows how the electric field changes the Bragg condition of each hologram, because an asymmetric writing geometry is used [see Eq. (6.51)].

Figure 7.17 shows the diffraction efficiency distribution of one hundred holograms stored in the same Ce-doped SBN:75 crystal under the same recording conditions as in Fig. 7.16. The following parameters are used for the recording schedule, $\tau_r = 25\text{ s}$ and $\beta = 0.05$. Figure 7.17 shows the relative uniformity of all the diffraction efficiencies, even after a field of 4 kV/cm is applied to the crystal to simultaneously reveal all the one hundred previously recorded holograms.

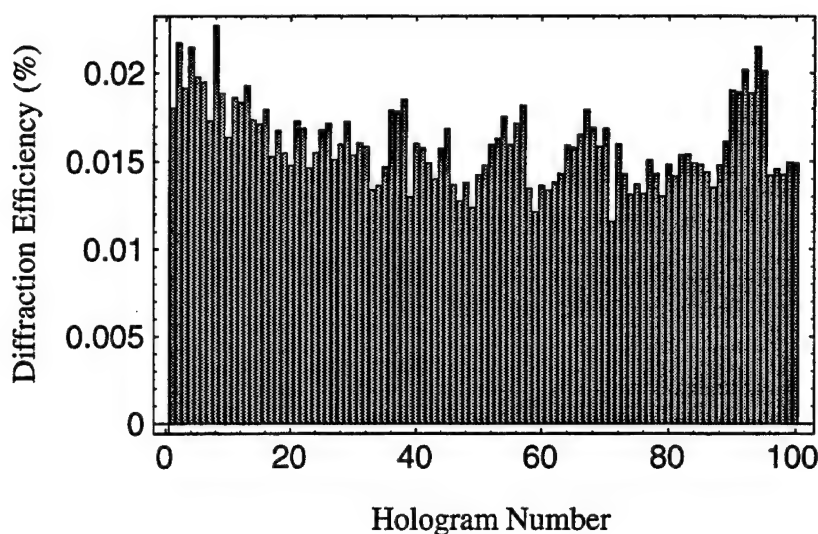


Figure 7.17: Distribution of the diffraction efficiencies of one hundred angularly multiplexed planar holograms recorded in SBN:75 at $T = 60^\circ\text{C}$ ($\theta_r = 12.5^\circ$ and $\theta_s = 0^\circ$). The holograms are read with an applied field of 4 kV/cm.

Storage Of High Resolution Images

Figure 7.18 shows three pictures of the Air-Force resolution test target (Group 6.2, i.e., a resolution of ~ 100 lp/mm). The image is recorded in the same Ce-doped SBN:75 crystal at $T = 60^\circ\text{C}$, as an image hologram using a telecentric imaging system. The magnification of the test target onto the crystal is 3.2, the writing intensities are $I_s = I_r = 5$ mW/cm² and a symmetric recording geometry is used with $\theta_s^0 = -6.5^\circ$ and $\theta_r = 6.5^\circ$ ($\pm 15^\circ$ outside the crystal); Fig. 7.18(a): original transmitted image through the crystal; Fig. 7.18(b): reconstructed image with no applied field, showing low diffraction efficiency; and Fig. 7.18(c): reconstructed image using a field of 2 kV/cm, showing no distortion compared with the original transmitted image and a greatly enhanced diffraction efficiency compared with the signal reconstructed with no field. Figure 7.15 represents the transfer function corresponding to this experiment. As mentioned earlier, 100 lp/mm corresponds to a total angular extent of 5.5° . The transfer function confirms the fact that, using this optical system, a resolution of 100 lp/mm can be effectively retrieved despite the presence of an applied field of 2 kV/cm.

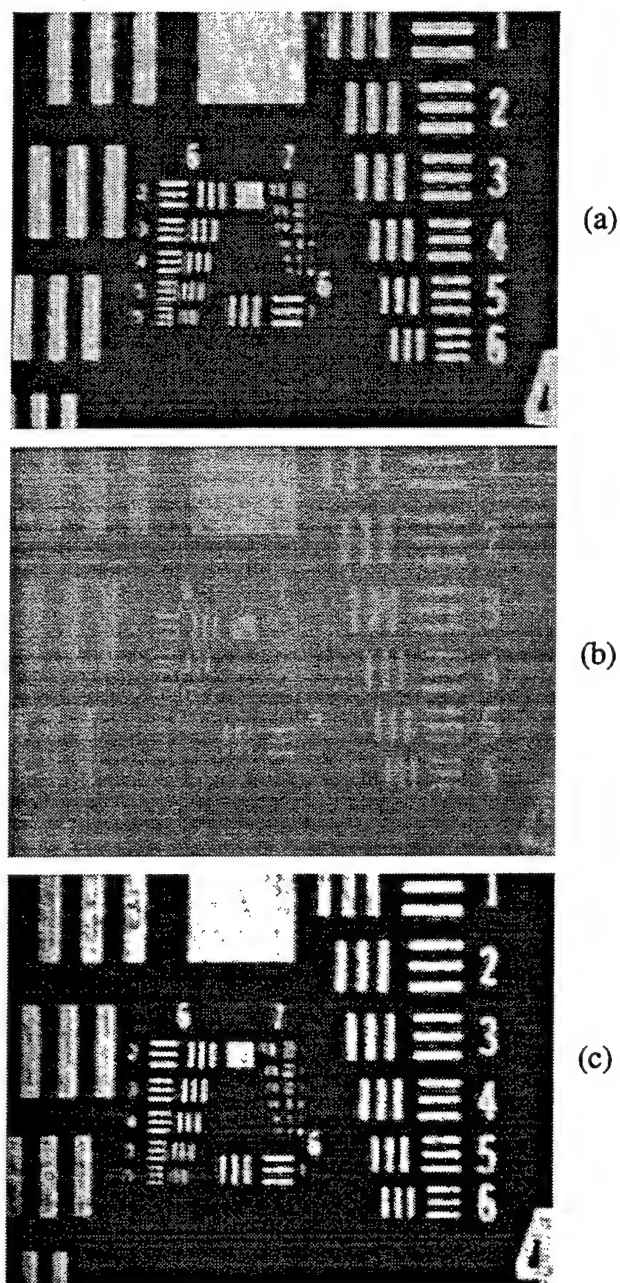


Figure 7.18: Air Force resolution test target stored in a Ce-doped SBN:75 crystal and reconstructed using the ECD effect: (a) original transmitted image; (b) reconstructed image at 0 kV/cm; and (c) reconstructed image at 2 kV/cm ($T = 60^\circ\text{C}$, $\theta_r = 6.5^\circ$ and $\theta_s^0 = -6.5^\circ$).

7.6 Conclusions

In Chapter 6 we studied the different effects that may induce changes in the Bragg condition in photorefractive crystals. The combined effect of angle, wavelength, index of refraction, and grating spacing changes were analyzed with temperature and electric field effects taken into consideration. These changes can be significant in many applications involving the use of photorefractive crystals and need to be carefully considered and studied to optimize diffraction efficiencies.

In this chapter, transfer functions are defined, computed and measured to describe and quantify the distortion that is due to Bragg detuning and that occurs during the readout of image-bearing holograms. We show that in certain cases, by adjusting the angle and the wavelength of the readout beam simultaneously, it is possible to compensate for these distortions. The knowledge of such transfer functions can also be potentially useful for design of suitable digital signal processing techniques that can compensate for such distortion if, for example, it is not possible to do it directly during the readout process. We have concentrated our study on applications in the field of holographic data storage, including the effect of thermal fixing in a digital holographic data storage system and the effect of electrically controlled diffraction for image enhancement. Finally I would like to thank J. F. Heanue and J. P. Wilde and acknowledge their help for mounting the experiments described in Sections 7.4 and 7.5, respectively and for storing and retrieving the images shown in Figs. 7.11 and 7.18.

7.7 Appendix to Chapter 7

In this appendix, we give the exact analytical expressions for the parameter $\xi^0(\theta_s)$ as well as the corresponding angle and wavelength detunings (in the three cases mentioned in the text). These expressions are functions of the recording geometry, the position of the reference beam, ΔT , ΔE_0 , and the different crystal parameters.

We start by defining several functions:

$$\mathcal{L} = \epsilon_c \cos^2(\theta_r - \beta) + \epsilon_a \sin^2(\theta_r - \beta) + \frac{\Delta n_\rho}{\bar{n}} \quad (7.14)$$

$$\begin{aligned} \mathcal{T} &= (\epsilon_a - \epsilon_c) \sin(\theta_r - \beta) \cos(\theta_r - \beta) - \frac{\Delta n_\rho}{\bar{n}} \tan \theta_r & \text{R, T} \\ &= (\epsilon_a - \epsilon_c) \sin(\theta_r - \beta) \cos(\theta_r - \beta) + \frac{\Delta n_\rho}{\bar{n}} \cot \theta_r & \text{P} \end{aligned} \quad (7.15)$$

where R denotes the reflection, T the transmission, and P the perpendicular geometry.

$$\begin{aligned} \partial \theta_\rho &= \frac{\cos \hat{\theta}_r}{\bar{n} \cos \theta_r} \Delta \hat{\theta}_\rho & \text{R, T} \\ &= \frac{\sin \hat{\theta}_r}{\bar{n} \sin \theta_r} \Delta \hat{\theta}_\rho & \text{P} \end{aligned} \quad (7.16)$$

$\partial \theta_\rho$ corresponds to the angular detuning of the readout beam that is due to the physical rotation outside the crystal ($\Delta \hat{\theta}_\rho$) but is expressed in terms of angles inside the crystal [see Eqs. (6.15) and (6.18)].

$$\mathcal{N}(\theta_s) = \frac{\Delta n_\rho - \Delta n_\sigma}{\bar{n}} \quad (7.17)$$

By use of these four definitions, the Bragg detuning parameter [Eq. (6.42)] can be expressed the following way

$$\xi(\theta_s) = \frac{\pi l \bar{n}}{\lambda_o \cos \theta_s} \left\{ \mathcal{N}(\theta_s) + \left(\mathcal{L} - \frac{\Delta \lambda_o}{\lambda_o} \right) [\cos(\theta_r - \theta_s) - 1] - (\mathcal{T} + \partial \theta_\rho) \sin(\theta_r - \theta_s) \right\} \quad (7.18)$$

The transfer function is given by

$$H(\theta_s) = \exp[-i\xi^0(\theta_s)] \frac{\sin \xi^0(\theta_s)}{\xi^0(\theta_s)} \quad (7.19)$$

where

case (i)

$$\xi^0(\theta_s) = \frac{\pi l \bar{n}}{\lambda_o \cos \theta_s \sin(\theta_r - \theta_s^0)} \left\{ \mathcal{N}(\theta_s) \sin(\theta_r - \theta_s^0) - \mathcal{N}(\theta_s^0) \sin(\theta_r - \theta_s) + \mathcal{L}[\sin(\theta_r - \theta_s) + \sin(\theta_s - \theta_s^0) + \sin(\theta_s^0 - \theta_r)] \right\} \quad (7.20)$$

$$\partial \theta_\rho = \frac{\mathcal{N}(\theta_s^0) + \mathcal{L}[\cos(\theta_r - \theta_s^0) - 1] - \mathcal{T} \sin(\theta_r - \theta_s^0)}{\sin(\theta_r - \theta_s^0)} \quad (7.21)$$

case (ii)

$$\xi^0(\theta_s) = \frac{\pi l \bar{n}}{\lambda_o \cos \theta_s [\cos(\theta_r - \theta_s^0) - 1]} \left\{ \mathcal{N}(\theta_s) [\cos(\theta_r - \theta_s^0) - 1] - \mathcal{N}(\theta_s^0) [\cos(\theta_r - \theta_s) - 1] + \mathcal{T} [\sin(\theta_r - \theta_s) + \sin(\theta_s - \theta_s^0) + \sin(\theta_s^0 - \theta_r)] \right\} \quad (7.22)$$

$$\frac{\Delta \lambda_o}{\lambda_o} = \frac{\mathcal{N}(\theta_s^0) + \mathcal{L}[\cos(\theta_r - \theta_s^0) - 1] - \mathcal{T} \sin(\theta_r - \theta_s^0)}{\cos(\theta_r - \theta_s^0) - 1} \quad (7.23)$$

case (iii)

$$\xi^0(\theta_s) = \frac{\pi l \bar{n}}{\lambda_o \cos \theta_s \sin(\theta_r - \theta_s^0)} \left\{ \mathcal{N}(\theta_s) \sin(\theta_r - \theta_s^0) - \mathcal{N}(\theta_s^0) \sin(\theta_r - \theta_s) + \frac{\sin(\theta_r - \theta_s) + \sin(\theta_s - \theta_s^0) + \sin(\theta_s^0 - \theta_r)}{\cos(\theta_r - \theta_s^0) - 1} \times \left[\sin(\theta_r - \theta_s^0) \frac{d\mathcal{N}}{d\theta_s} \Big|_o + \cos(\theta_r - \theta_s^0) \mathcal{N}(\theta_s^0) \right] \right\} \quad (7.24)$$

$$-\frac{\Delta\lambda_o}{\lambda_o} + \mathcal{L} = \frac{\sin(\theta_r - \theta_s^0) \frac{d\mathcal{N}}{d\theta_s} \Big|_o + \cos(\theta_r - \theta_s^0) \mathcal{N}(\theta_s^0)}{\cos(\theta_r - \theta_s^0) - 1} \quad (7.25)$$

$$\partial\theta_\rho + \mathcal{T} = \frac{d\mathcal{N}}{d\theta_s} \Big|_o + \frac{1 + \cos(\theta_r - \theta_s^0)}{\sin(\theta_r - \theta_s^0)} \mathcal{N}(\theta_s^0) \quad (7.26)$$

It is interesting to note that in case (iii), regardless of the geometry, the transfer function depends only on the index anisotropy ($\Delta n_\rho - \Delta n_\sigma$) and not on the crystal expansion. This is a consequence of the fact that it is possible to compensate for the anisotropic expansion by adjusting simultaneously the outside angle and the wavelength of the readout beam.

Part III

DIFFRACTION ANALYSIS OF STRUCTURES OF GRATINGS

Chapter 8

Structures of Thin Gratings

8.1 Introduction

Layered structures of gratings have been studied several times in the past. One of the first authors to study such structures and some of their applications was Yakimovitch [82], who showed how the diffraction efficiency and the angular selectivity of a system of three-dimensional holographic gratings in layers are determined by the total thickness of the structure and by the separation between the gratings. His approach was to solve the coupled-wave equations in each layer [4], implicitly assuming a structure of thick gratings. Zel'dovich and Yakovleva [83] and Zel'dovich *et al.* [84] studied in detail the characteristics of two-layer thin phase holograms and showed theoretically and experimentally how these systems can increase the diffraction efficiency and improve the selectivity compared with single thin phase holograms. The concept of stratified volume holographic optical element (SVHOE) was first introduced by Tanguay and Johnson [85][86]. A SVHOE consists of a succession of thin holographic recording layers separated by buffer layers. Nordin *et al.* [87] studied in detail the diffraction properties of SVHOE's by using a computational algorithm known as the optical beam-propagation method [88]. They also proposed several applications in the fields of optical processing and optical computing. One of the applications [89] that has been experimentally demonstrated consists of a multiple-beam-generation system in which the authors were able to divide an incoming beam of light into seven

beams of equal intensity by using an optimized two-layer SVHOE. This application underlines one of the major advantages of SVHOE's: by considering each layer as an independent degree of freedom and by being able to modify variables and parameters within each layer, SVHOE's can be exploited for new optical processing applications.

Different materials have been used in the fabrication of SVHOE's: (i) dichromated gelatin films [84], (ii) photoresist [86] [89], and (iii) photopolymers [90] [87]. All these materials require, to some extent, processing and complicated recording and development procedures.

We specifically concentrate on SVHOE's made of photorefractive films [91], although the general theory developed is also valid for SVHOE's made from other recording materials if the physical process responsible for the photorefractive effect is neglected. Photorefractive crystals are of growing interest currently because several methods, e.g., metalorganic chemical-vapor deposition (MOCVD) [92] and excimer-laser ablation [93], are being developed to grow them as thin films. Besides, photorefractive polymers [94] [22] and semiconductor quantum wells [95] are also being grown in the form of thin films having attractive photorefractive properties, which makes them suitable for the fabrication of artificially structured media, too. One of the main advantages of photorefractive materials compared with the materials previously used in the fabrication of SVHOE's is their interesting and unique properties in real-time optical processing and optical data storage [96][97].

In this chapter we first develop an analytical model to describe a structure of thin photorefractive films in a general holographic writing-reading configuration. The model is essentially an extension of the theory developed in Ref. [83] to an arbitrary number of thin holograms and includes the photorefractive effect. We extend the model, which gives a closed-form solution for the first-order diffraction efficiency of such structures, to a single thick photorefractive grating by taking the limit for an infinite number of thin films. This leads to a solution for the diffraction efficiency of a thick grating with a nonuniform amplitude and a nonuniform phase that agrees with the results that have been derived in Chapter 5 by using a coupled-wave approach. The analytical solutions for SVHOE's are then compared with the existing

numerical results for SVHOE's that can be found in Ref. [87]. Finally these structures are analyzed in the context of holographic multiplexing. More specifically, a new multiplexing scheme is proposed, with the application of an electric field to each layer, which permits the multiplexing of several holograms in the structure by means of the photorefractive phase shift. One general and important conclusion is that the maximum number of holograms that can be multiplexed in a photorefractive SVHOE is equal to the number of layers in the SVHOE. In Chapter 9 we will generalize the model developed in this chapter for a layered structure of thin gratings to take into account structures of thick gratings.

8.2 Analytical Analysis

8.2.1 General Configuration

Writing Geometry

Figure 8.1(a) describes the general writing geometry of a system containing a stack of N thin films separated by buffer layers. Incident upon the structure are the signal wave $A_s(\vec{r})$ and the reference wave $A_r(\vec{r})$. The two waves, assumed to be monochromatic plane waves, both at a frequency $\omega_o = ck_o = 2\pi\bar{n}c/\lambda_o$, write a thin phase hologram in each of the photorefractive films (if the signal beam carries an image, it is straightforward to decompose the image in its Fourier components and to treat each one of them as an independent plane wave).

The writing field incident on the structure can be written as

$$E(\vec{r}) = A_s(\vec{r}) + A_r(\vec{r}) = |A_s| \exp[-i(\phi_s + \vec{k}_s \cdot \vec{r})] + |A_r| \exp(-i\vec{k}_r \cdot \vec{r}) \quad (8.1)$$

where $|A_s|$ and $|A_r|$ are the real amplitudes of the signal and the reference waves, respectively, \vec{k}_s and \vec{k}_r are the corresponding wave vectors, and ϕ_s is an arbitrary constant phase in the signal beam. In the following calculations the vectors are decomposed into their transverse and longitudinal components, with the z axis being the propagation axis:

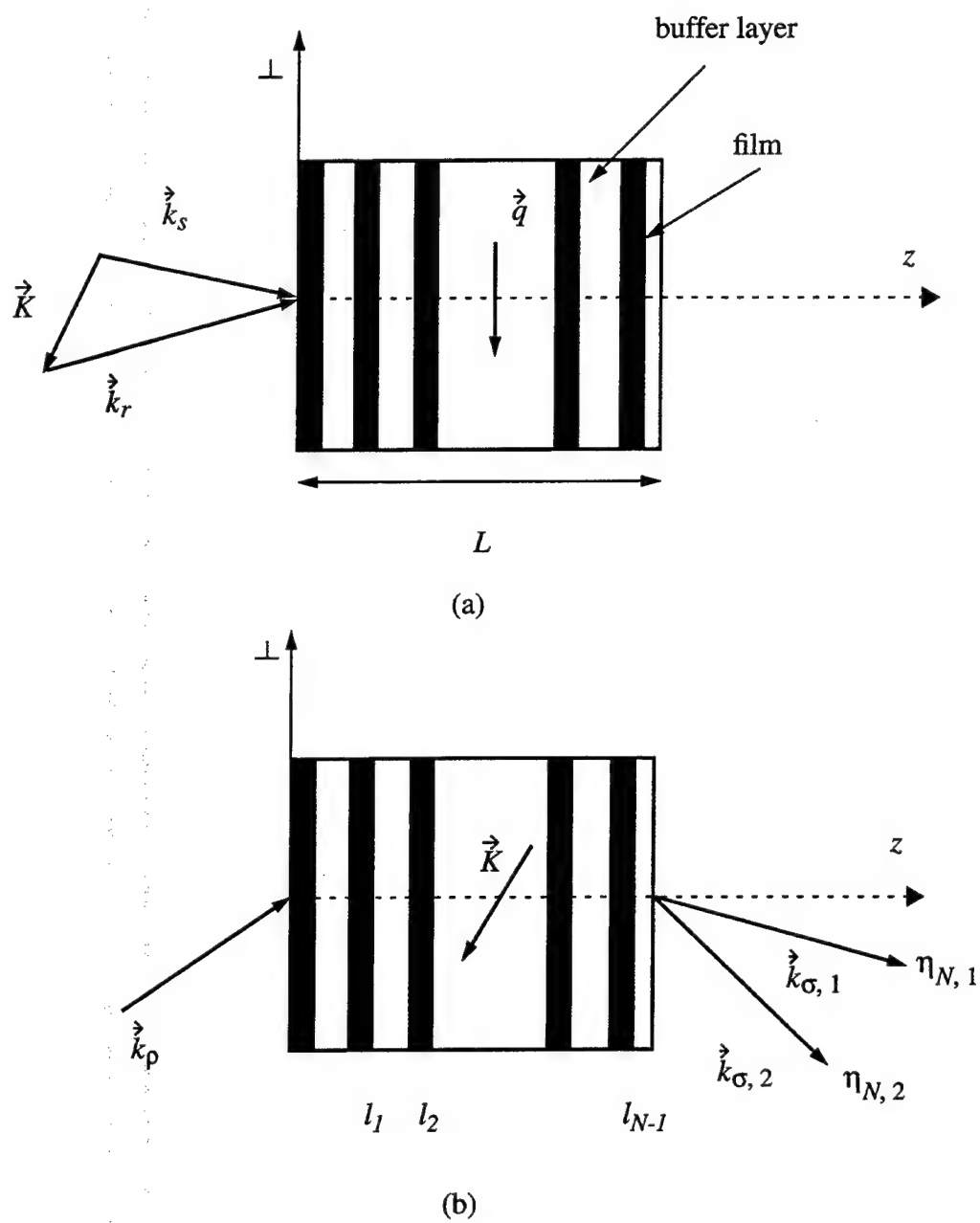


Figure 8.1: General configuration of a SVHOE: (a) writing geometry, (b) readout geometry.

$$\vec{k} = \vec{k}_\perp + \sqrt{|\vec{k}|^2 - \vec{k}_\perp^2} \hat{e}_z \quad (8.2)$$

$$\vec{r} = \vec{x} + z\hat{e}_z \quad (8.3)$$

In Chapter 2, we introduced the concept of amplitude grating in which the intensity modulates the absorption of the recording medium. In the case of photorefractive materials the hologram is modeled as a phase transparency because the incident intensity primarily modulates the index of refraction of the material. Each thin hologram is therefore represented by a transparency $t_j(\vec{x})$ describing, at steady state, the spatially modulated phase introduced by the photorefractive film located at $z = l_j$, when illuminated by the writing field:

$$t_j(\vec{x}) = \exp\left(-i\frac{2\pi}{\lambda_o} \int_{d_j} \Delta n_j(\vec{x}, z) dz\right) \quad \forall j \in [0, N-1] \quad (8.4)$$

with

$$\Delta n_j(\vec{x}, z) = -\frac{1}{2}\bar{n}^3 r_{eff} |E_{SC}|_j \cos(\phi_s + zK_z + \vec{q} \cdot \vec{x} + \phi_j) \quad (8.5)$$

where

$$\begin{aligned} \vec{q} &= \vec{k}_{s\perp} - \vec{k}_{r\perp} \\ K_z &= k_{sz} - k_{rz} \end{aligned} \quad (8.6)$$

are the perpendicular and the longitudinal components of the grating vector \vec{K} inside the structure, respectively; \bar{n} is the index of refraction; r_{eff} is the effective electro-optic coefficient; and d_j is the thickness of the film j . $|E_{SC}|_j$ is the magnitude of the space-charge field and ϕ_j is the photorefractive phase shift (ϕ_j could represent any arbitrarily imposed phase shift on the index grating). The magnitude of the space-charge field and the phase shift are assumed to be given by the results of the standard photorefractive band transport model [10][11], as described in Chapter 3:

$$|E_{SC}|_j \exp(i\phi_j) = -m \left[\frac{E_Q(E_0 + iE_D)}{E_Q + E_D - iE_0} \right]_j \quad (8.7)$$

where E_0 is the applied electric field; $m = 2|A_r||A_s|/(|A_r|^2 + |A_s|^2)$ is the modulation depth; $E_D = 2\pi k_B T/(e\Lambda)$ is the diffusion field and $E_Q = e\Lambda N_0^\circ(1 - N_0^\circ/N)/(2\pi\epsilon_0\epsilon)$ is the saturation field in film j . In the absence of an applied field $\phi_j = -\pi/2$ and in the presence of a field, ϕ_j can take any value between 0 and $-\pi$. Considering the thin-grating approximation and defining the grating strength by

$$\nu_j = \frac{\pi}{\lambda_0} d_j \bar{n}^3 r_{eff} |E_{SC}|_j \quad (8.8)$$

we can write the transmission function as

$$t_j(\vec{x}) = \exp[i\nu_j \cos(\phi_s + l_j K_z + \vec{q} \cdot \vec{x} + \phi_j)] \quad (8.9)$$

Use of this expression to describe the transparency of a thin phase hologram implicitly limits the theory to the paraxial region. Decomposing the transparency $t_j(\vec{x})$ into its Fourier components, we obtain

$$t_j(\vec{x}) = \sum_{a_j=-\infty}^{\infty} C_{a_j}^j \exp(-ia_j \vec{q} \cdot \vec{x}) \quad (8.10)$$

where the coefficients $C_{a_j}^j$ are given by

$$C_{a_j}^j = (-i)^{a_j} J_{a_j}(\nu_j) \exp[-ia_j(\phi_s + \phi_j + l_j K_z)] \quad (8.11)$$

where J_{a_j} is the Bessel function of order a_j .

Reading Geometry

Figure 8.1(b) describes the general reading geometry with the different diffracted orders and the readout field $A_\rho(\vec{r})$ at a frequency $\omega = \omega_0 + \Delta\omega$,

$$A_\rho(\vec{r}) = |A_\rho| \exp(-i\vec{k}_\rho \cdot \vec{r}) \quad (8.12)$$

where

$$\vec{k}_\rho = \vec{k}_{r\perp} + k_0 \vec{\Psi} + \sqrt{\frac{(\omega_0 + \Delta\omega)^2}{c^2} - (\vec{k}_{r\perp} + k_0 \vec{\Psi})^2} \hat{e}_z \quad (8.13)$$

is the wave vector and $|A_\rho|$ is the amplitude of the readout wave. The parameters $\vec{\Psi}$ and $\Delta\omega$ are introduced to describe the off-Bragg situation, i.e., when the readout wave vector \vec{k}_ρ does not satisfy the Bragg condition $\vec{k}_\rho = \vec{k}_r$. Within the paraxial approximation, the wave vectors of the different diffracted beams are given by

$$\vec{k}_{\sigma,Q} = \vec{k}_{\rho\perp} + Q\vec{q} + \sqrt{\frac{\omega^2}{c^2} - (\vec{k}_{\rho\perp} + Q\vec{q})^2} \hat{e}_z \quad (8.14)$$

where Q is the diffraction order.

8.2.2 Thin Hologram Condition

We assumed that the films in the SVHOE structure generate thin gratings when exposed to the spatially modulated incident light. This assumption can be verified by analysis of the value of the quality factor [3]

$$Q = 2\pi d \frac{\lambda_o}{\bar{n}\Lambda^2} \quad (8.15)$$

where d is the interaction length, i.e., the film thickness, and Λ the grating spacing. If $Q < 2\pi$, the hologram is said to be in the thin region (the Raman-Nath regime) and if $Q > 2\pi$, the hologram is said to be in the thick region (the Bragg regime). For the relatively small angles of incidence that satisfy the paraxial approximation, the grating spacing is usually several times larger than the wavelength (only the transmission geometry is of interest in this case). Therefore, for typical photorefractive materials, the thin hologram condition will be satisfied for thin films with thicknesses up to a few micrometers. As we stated in the introduction, such films have already been successfully grown [92] [93].

8.2.3 Propagation of the Readout Field

The electric field diffracted by the first transparency $t_0(\vec{x})$ can be written as

$$\begin{aligned} A_\sigma^{(1)}(\vec{x}) &= t_0(\vec{x}) A_\rho(\vec{x}, z=0) \\ &= \sum_{a_0=-\infty}^{\infty} |A_\rho| C_{a_0}^0 \exp \left[-i(a_0\vec{q} + \vec{k}_{r\perp} + k_o\vec{\Psi}) \cdot \vec{x} \right] \end{aligned} \quad (8.16)$$

which corresponds to a sum of plane waves. Between two transparencies, i.e., within a buffer layer, each wave propagates according to the free-space propagation of a plane wave:

$$U(\vec{k}; \vec{x}, z) = U(\vec{k}; \vec{x}, z_0) \exp \left[-i \sqrt{|\vec{k}|^2 - \vec{k}_\perp^2} (z - z_0) \right] \quad (8.17)$$

where $U(\vec{k}; \vec{x}, z)$ is a plane wave of wave vector \vec{k} . Continuing the propagation process through the whole structure and neglecting reflections at the different interfaces, we can write the field diffracted by the N holograms as

$$\begin{aligned} A_\sigma^{(N)}(\vec{x}) &= |A_\rho| e^{-i(\vec{k}_{r\perp} + k_o \vec{\Psi}) \cdot \vec{x}} \\ &\times \prod_{j=0}^{N-2} \left[\sum_{a_j=-\infty}^{\infty} C_{a_j}^j e^{-ia_j \vec{q} \cdot \vec{x}} e^{-i(l_{j+1}-l_j) \sqrt{\frac{\omega^2}{c^2} - (\vec{q} \sum_{k=0}^j a_k + \vec{k}_{r\perp} + k_o \vec{\Psi})^2}} \right] \\ &\times \sum_{a_{N-1}=-\infty}^{\infty} C_{a_{N-1}}^{N-1} e^{-ia_{N-1} \vec{q} \cdot \vec{x}} \end{aligned} \quad (8.18)$$

8.2.4 Diffraction Efficiency

The efficiency of the Q^{th} order diffracted wave is defined by

$$\eta_{N,Q} = \left| \frac{A_\sigma^{(N)}}{A_\rho(z=0)} \right|_{\sum_{j=0}^{N-1} a_j = Q}^2 \quad (8.19)$$

From Eq. (8.18) and with Eq. (8.11), we can write Eq. (8.19) as

$$\begin{aligned} \eta_{N,Q} &= \left| \sum_{a_0} \dots \sum_{a_{N-1}} \right. \\ &\times \prod_{j=0}^{N-1} J_{a_j}(\nu_j) e^{-ia_j(\phi_j + l_j K_z)} \prod_{j=0}^{N-2} e^{-i(l_{j+1}-l_j) \sqrt{\frac{\omega^2}{c^2} - (\vec{q} \sum_{k=0}^j a_k + \vec{k}_{r\perp} + k_o \vec{\Psi})^2}} \left. \right|^2 \end{aligned} \quad (8.20)$$

with the constraint

$$\sum_{j=0}^{N-1} a_j = Q \quad (8.21)$$

This is a useful formulation for the efficiencies of the different diffraction orders because it explicitly shows the dependence on all the individual parameters of each layer when an arbitrary grating vector \vec{K} is recorded in a SVHOE of N thin films and is then read by a readout beam that does not necessarily satisfy the Bragg condition. This is especially interesting in the design of complex structures in which each layer must be optimized separately.

First Order Diffraction Efficiency

We can explicitly calculate the first-order diffraction efficiency by making some further assumptions to obtain a simpler expression than Eq. (8.20). Without too much loss of generality, it is reasonable to consider all the films to be equidistant from each other; therefore if L is the total length of the SVHOE,

$$l_j = j \frac{L}{N-1} \quad \forall j \in [0, N-1] \quad (8.22)$$

Taking the first order $Q = 1$ implies that

$$\sum_{j=0}^{N-1} a_j = 1 \quad (8.23)$$

and, further assuming that all the grating strengths $\nu_j \ll 1$, which is always true for photorefractive thin gratings, we obtain

$$\prod_{j=0}^{N-1} J_{a_j}(\nu_j) \propto \prod_{j=0}^{N-1} \frac{\nu_j^{|a_j|}}{2^{|a_j|} |a_j|!} \quad (8.24)$$

Keeping the lowest-order terms implies that

$$\sum_{j=0}^{N-1} |a_j| = 1 \quad (8.25)$$

With this constraint [Eq. (8.25)] and the previous condition [Eq. (8.23)], only the terms in which one of the index a_j is equal to one and all the others are equal to zero must be kept in the multiple sum [Eq. (8.20)]. The expression for the first order diffraction efficiency [Eq. (8.20)] can then be simplified to yield

$$\eta_{N,1} = \frac{1}{4} \left| \sum_{j=0}^{N-1} \nu_j \exp(-i\phi_j) \exp \left(-i2j \frac{\xi(\vec{\Psi}, \Delta\omega)}{N-1} \right) \right|^2 \quad (8.26)$$

where

$$\begin{aligned} \xi(\vec{\Psi}, \Delta\omega) &= \frac{L}{2} \left[K_z + \sqrt{\frac{\omega^2}{c^2} - (\vec{k}_{r\perp} + k_o \vec{\Psi})^2} - \sqrt{\frac{\omega^2}{c^2} - (\vec{k}_{r\perp} + \vec{q} + k_o \vec{\Psi})^2} \right] \\ &= \frac{L}{2} (K_z + k_{pz} - k_{\sigma z}) = \frac{L}{2} \Delta k_z(\vec{\Psi}, \Delta\omega) \end{aligned} \quad (8.27)$$

is the Bragg detuning parameter, \vec{k}_ρ is the wave vector of the readout beam and \vec{k}_σ is the wave vector of the first-order diffracted beam.

It is easy to check that the function $\xi(\vec{\Psi}, \Delta\omega)$ defined by Eq. (8.27) is identical to zero when the wave vector of the reading beam satisfies the Bragg condition $\vec{k}_\rho = \vec{k}_r$. Figure 8.2 shows a two-dimensional k -space representation of the Bragg detuning parameter and of all the wave vectors incident upon and emerging from the structure.

Closed-Form Solution

If we further assume that there is no applied field and that all the films are made of the same material, i.e., for all the films $\phi_j = -\pi/2$ and $\nu_j = \nu$, Eq. (8.26) reduces to

$$\eta_{N,1} = \frac{\nu^2}{4} \left| \sum_{j=0}^{N-1} \exp \left[-i \frac{2j}{N-1} \xi(\vec{\Psi}, \Delta\omega) \right] \right|^2 = \frac{\nu^2 \sin^2 \left[\xi(\vec{\Psi}, \Delta\omega) \frac{N}{N-1} \right]}{4 \sin^2 \left[\xi(\vec{\Psi}, \Delta\omega) \frac{1}{N-1} \right]} \quad (8.28)$$

Figure 8.3(a) represents what physically happens when these approximations are considered: the diffracted field is the coherent sum of all the waves diffracted in the first order by the readout field at each thin grating. In this case, the representation of a SVHOE is analogous to the description of a Fabry-Perot etalon [98], for which the transmitted field can also be described as the coherent sum of waves with a constant dephasing term $\exp(i\delta)$ between them [see Fig. 8.3(b)].

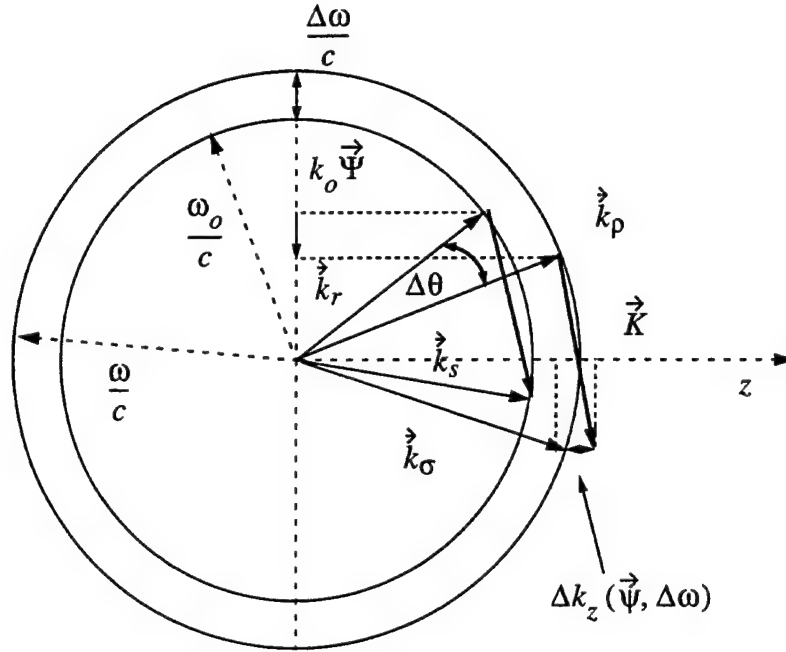


Figure 8.2: k -space diagram of the writing, the reading, and the diffracted wave vectors and the Bragg detuning parameter.

8.2.5 Limit for an Infinite Number of Holograms

It is interesting to take the limit of the previous results, Eqs. (8.26) and (8.28), for an infinite number of thin holograms, keeping the total distance L constant (i.e., the buffer layer thickness goes to zero):

$$\eta_{thick} = \lim_{N \rightarrow \infty} \eta_{N,1} \quad (8.29)$$

This equation yields the results for the equivalent thick grating, defined as the thick grating having a thickness equal to the total length L of the structure.

Nonuniform Grating

The successions $\phi_j = \phi(z_j)$ and $\nu_j = \nu(z_j)$ can be thought of as a description of nonuniform variations in the z direction of the phase and of the amplitude of a thick index grating. By taking the limit of Eq. (8.26) and by transforming the sum into an integral, we derive the following expression for the diffraction efficiency of a thick

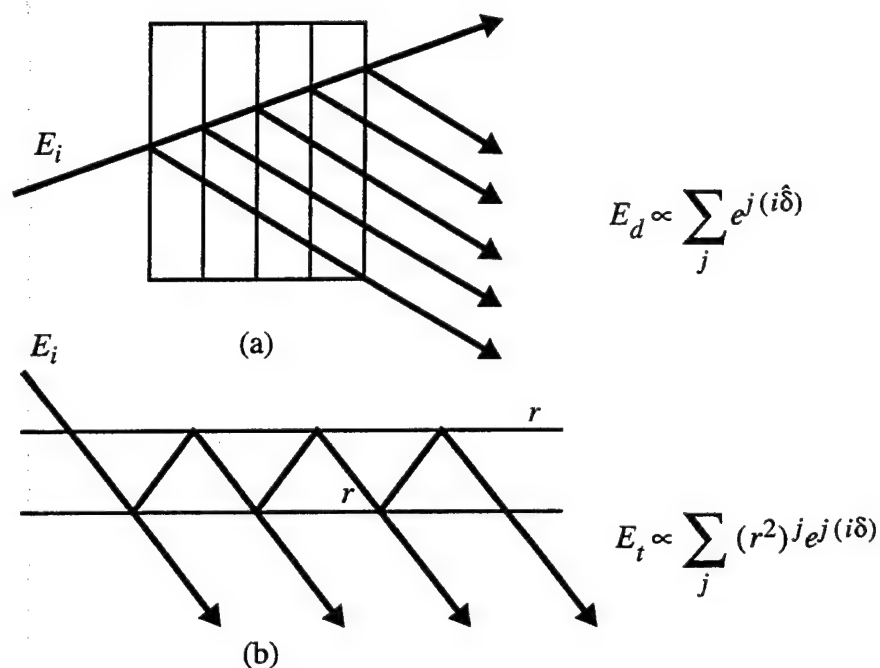


Figure 8.3: Comparison between a SVHOE (a) and a Fabry-Perot etalon (b). δ and $\hat{\delta}$ represent in both cases the phase retardation between adjacent beams. E_i is the incident field; E_d is the field diffracted by the SVHOE; E_t is the field transmitted by the etalon; and r is the reflectivity of the mirror.

nonuniform grating:

$$\eta_{thick} = \frac{\pi^2}{\lambda_o^2} \left| \int_0^L \Delta n(z) e^{-i\phi(z)} \exp \left[-i \frac{2\xi(\vec{\Psi}, \Delta\omega)}{L} z \right] dz \right|^2 \quad (8.30)$$

where the function $\phi(z)$ physically represents the shape of the fringes within the thick hologram. This formulation is interesting for two reasons. First, if we consider a large number of films to approximate a thick hologram and adjust the ϕ_j accordingly, any fringe shape $\phi(z)$ can be simulated. Then nonuniform gratings can occur in a thick medium when nonlinear two-wave mixing and fringe-bending effects are taken into account in the formation of a grating in a photorefractive crystal [28]. These effects have been studied in detail in Chapter 5 and indeed, Eq. (8.30) is identical to the result derived in Chapter 5, in which the diffraction properties of nonuniform gratings in photorefractive crystals are examined using a coupled-wave approach and Fourier transform arguments [Eq. (5.11)]. Note that this expression is only valid within the undepleted pump approximation (small ν).

Uniform Grating

If $\phi(z) = \text{constant}$ and $\nu(z) = \text{constant}$, we find from Eq. (8.30) or as the limit for $N \rightarrow \infty$ of Eq. (8.28) that

$$\eta_{thick} = \bar{\nu}^2 \frac{\sin^2 \xi(\vec{\Psi}, \Delta\omega)}{\xi^2(\vec{\Psi}, \Delta\omega)} \quad (8.31)$$

where

$$\bar{\nu} = \lim_{N \rightarrow \infty} \frac{\nu N}{2} = \frac{\pi \Delta n L}{\lambda_o} \quad (8.32)$$

is the grating strength as defined for a thick grating. It is denoted by $\bar{\nu}$ in this case to clearly differentiate it from the grating strength of the thin gratings denoted by ν . Note that the two equations are different by a factor of two. Equation (8.31) gives the well-known expression for the diffraction efficiency of a thick uniform hologram in the undepleted pump approximation.

In practice one is often concerned with the diffraction efficiency when the readout beam deviates only slightly from the Bragg condition. Expanding Eq. (8.27) to first order in $\vec{\Psi}$ and $\Delta\omega$ yields

$$\xi(\vec{\Psi}, \Delta\omega) = \frac{L}{2} \left(\frac{\vec{k}_{s\perp}}{k_{sz}} - \frac{\vec{k}_{r\perp}}{k_{rz}} \right) \cdot \vec{\Psi} k_o + \frac{L}{2} k_o \frac{\Delta\omega}{c} \left(\frac{1}{k_{rz}} - \frac{1}{k_{sz}} \right) \quad (8.33)$$

ξ is then proportional to the wavelength and the angle detuning of the readout beam. In a two-dimensional configuration in which all the wave vectors lie in the same plane of incidence (Fig. 8.2), relation (8.33) is equal to the Bragg detuning parameter of Kogelnik's coupled wave analysis of thick holograms [4]. Thus the general formula [Eq. (8.26)] for a structure containing N thin photorefractive films gives the expected expression for a thick-hologram diffraction efficiency when the limit for an infinite number of identical films is taken.

Figure 8.4 shows the diffraction efficiency [Eq. (8.28)], normalized to unity, as a function of the Bragg detuning parameter ξ for different numbers N of thin holograms in the structure and for the equivalent thick hologram. In this form these analytical results agree perfectly well with the numerical results of Johnson and Tanguay [86]. The selectivity behavior represented in Fig. 8.4 is a periodic function of the Bragg detuning parameter ξ . The period, i.e., the separation between the main diffraction peaks, is directly proportional to the number of films N (keeping L constant). Finally, the width of the main diffraction peak is determined by the total thickness L of the structure, regardless of the number of films and of the thicknesses of each one of them.

This diffraction-efficiency behavior demonstrates one reason for interest in these composite layered structures: they are able to duplicate, to some extent, the properties of a thick grating. But, more interestingly, these photorefractive structures permit new applications by precisely offering the possibility of modifying variables and parameters within the different layers as shown in the next section on holographic multiplexing and as demonstrated in one experimental application [89].

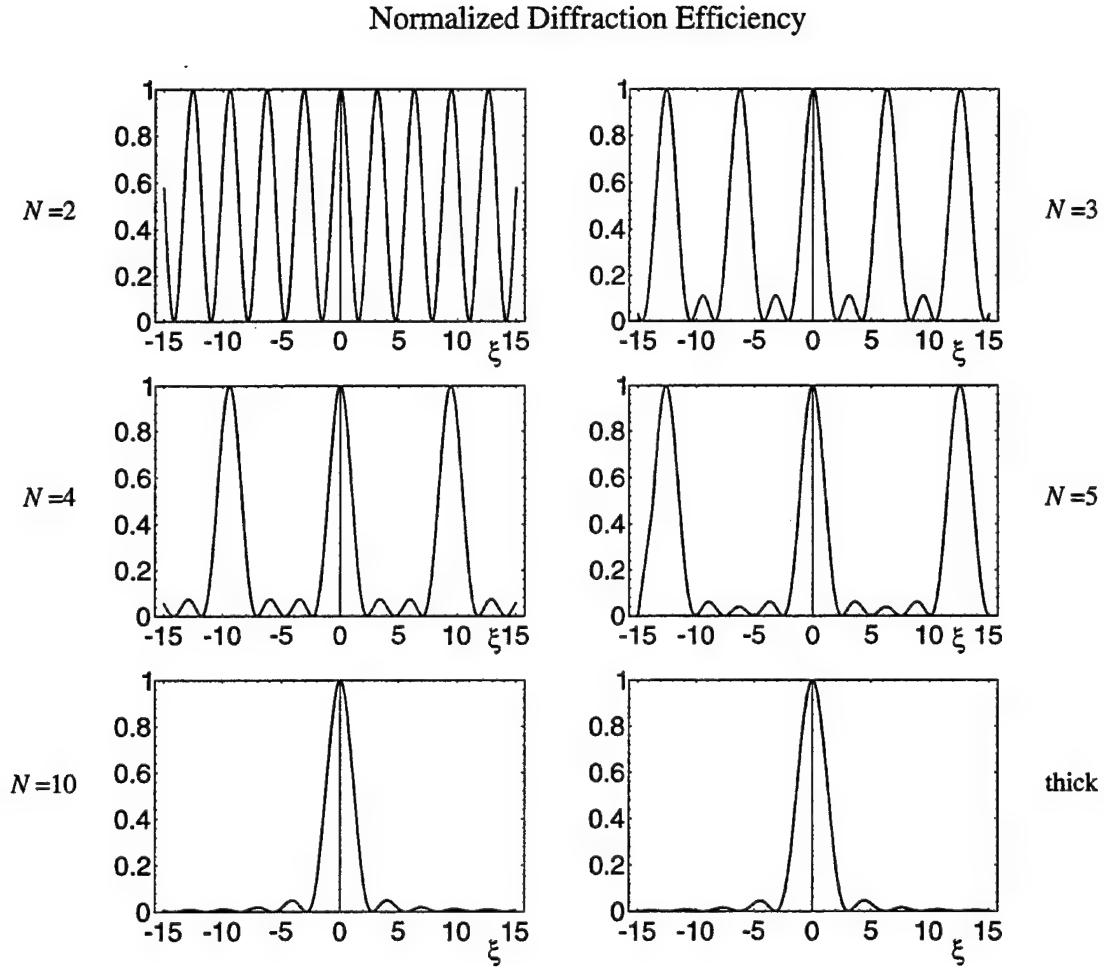


Figure 8.4: Normalized diffraction efficiency $\eta^{(norm)} = \frac{1}{N^2} \left\{ \frac{\sin^2[N\xi/(N-1)]}{\sin^2[\xi/(N-1)]} \right\}$ as a function of the Bragg detuning parameter ξ for SVHOE's of different number N of thin films and for the equivalent thick grating of length L .

8.2.6 Non-Photorefractive Films

Here we consider a structure of N identical films that are not necessarily photorefractive to check the validity of the theory in that case and compare it with some of the numerical results of Nordin *et al.* [87]. Equation (8.20) must be considered with no photorefractive phase shift ϕ_j and with $\nu_j = \nu$, where ν still represents the thin-grating strength but is no longer given by Eq. (8.8) and is no longer assumed to be much smaller than one. It is clear that the first part of the above analysis remains valid and that it is not limited to photorefractive SVHOE's.

It is interesting to examine, assuming that the Bragg condition is satisfied, the diffraction efficiency as a function of the grating strength. From Eq. (8.20) the following limits can be checked:

$$\begin{aligned}\lim_{N \rightarrow \infty} \eta_{N,1} &= \sin^2 \left(\pi \frac{\Delta n L}{\lambda_o} \right) \\ \lim_{N \rightarrow \infty} \eta_{N,Q} &= 0 \quad Q \neq 1\end{aligned}\tag{8.34}$$

which are the expected results for any thick grating [4].

Table 8.1 gives the maximum efficiency of the first diffraction order and the value of the grating strength ν at which the maximum occurs as a function of the number of films N . Provided that the correct grating strength ν can be achieved, a maximum diffraction efficiency close to 100% can be obtained with a relatively low number of films. It also shows how, when the number of films increases, all the diffracted energy progressively accumulates into the first order only at the expense of the higher orders. This behavior can be overcome by considering a structure of films where each film has a different property [89].

The convergence of the series [Eq. (8.20)] is quite rapid as long as the value of ν is not too large. The larger the value of ν , the larger the number of terms to be considered in the multiple sum to have a good approximation for the diffraction efficiency. In practice, with ν being of the order of one (e.g., for photographic films), it is sufficient to consider in the multiple sum [Eq. (8.20)] only the terms $a_j \in [-2, 2]$. In other words, a good approximation will be given when all the diffracted rays up to the orders ± 2 from all the different thin gratings are considered. The diffraction

N	Maximum Efficiency(%)	ν
1	33	1.84
2	68	1.30
3	87	1.00
4	92	0.76
5	95	0.62

Table 8.1: Maximum first-order diffraction efficiency as a function of N and corresponding grating strength.

efficiency [Eq. (8.20)] is also a periodic function of the grating spacing. However as $N \rightarrow \infty$ and $\nu < 0.5$, this dependence on the grating spacing disappears. This behavior is thus an interesting and unique feature of a stack of a low number of thin gratings, as pointed out in Ref. [87].

8.3 Holographic Multiplexing

In this section we analyze the possibilities of multiplexing several holograms in a structure of thin gratings. One important application of photorefractive materials in the form of bulk crystals, is holographic data storage. As mentioned in Chapter 7 several methods for multiplexing holograms in one crystal exist, with the most widely used being angular multiplexing [48], wavelength multiplexing [47], and phase encoding [51]. The main problem encountered in holographic multiplexing is the cross talk in the signal-to-noise-ratio (SNR) that results because when one hologram is being read, at the same time all the other holograms stored in the medium contribute to the diffracted signal because their diffraction efficiency is not uniformly identical to zero [13]. If M holograms are recorded in a SVHOE of N films, assuming an incoherent system and neglecting scattering from materials imperfections, the SNR for the hologram k can be estimated with

$$\text{SNR}^{(k)} = \frac{\eta_{N,1}^{(k)}(\xi = \xi_k)}{\sum_{\substack{j=1 \\ j \neq k}}^M \eta_{N,1}^{(j)}(\xi = \xi_k)} \quad (8.35)$$

where $\eta_{N,1}^{(j)}(\xi = \xi_k)$ is the diffraction efficiency of the hologram j when the Bragg condition for the hologram k is satisfied. Let us analyze how the multiplexing of M holograms in a SVHOE and in a thick crystal compare.

In a structure of N thin films it is not possible to record more than N holograms by angular or wavelength multiplexing while keeping a high SNR for each hologram. Indeed, as soon as $M > N$, the SNR [as given by Eq. (8.35)] abruptly decreases. This is because of the periodic nature of the diffraction efficiency (see Fig. 8.4) and because this period increases with the number of thin films, with the total length L remaining constant. Therefore a structure consisting of a low number of thin films is not suitable for storing a large number of holograms. But for applications involving a small number of multiplexed holograms such that $M \leq N$, the SNR of the structure is equal to the SNR of the equivalent thick crystal. As in angular or wavelength multiplexing in a thick crystal, the width of the main diffraction peak, i.e., the Bragg selectivity, is different for each recorded hologram, which is responsible for the intrinsic cross talk [13] (as opposed to the extrinsic cross talk which is mainly due to scattering and to imperfections in materials).

8.4 Phase Multiplexing

In this section we analyze the possibilities of multiplexing several holograms in a structure by taking advantage of the specific nature of a SVHOE, i.e., by changing the properties of each layer independently. As pointed out in the introduction to this chapter, this feature is one of the major reasons that makes these types of devices attractive and worth studying.

We propose a new technique for possibly recording several holograms in a stratified volume holographic optical element based on the freedom to adjust and to control externally the phase ϕ_j of each thin grating during the writing process (by applying

a different electric field, during recording, to each of the photorefractive thin films). Each hologram is then recorded with a different phase pattern (because of the photorefractive phase shift) across the structure of films (see Fig. 8.5), with the writing geometry remaining the same for all the recorded holograms. By this technique the maximum diffraction efficiency can be shifted along the Bragg detuning parameter axis, i.e., the Bragg condition can be controlled and can be changed independently for each hologram. Then each one of them can be selectively addressed during readout by satisfying its Bragg condition. The addressing can be done by a simple adjustment of the angle ($\Delta\theta_\rho$) or the wavelength ($\Delta\lambda_o$) of the readout beam. It is also possible to take advantage of the layered structure by introducing electro-optic but nonphotorefractive beam-steering devices, i.e., buffer layers that can change the amplitude and the direction of the readout wave vector when biased with an electric field in such a way that the Bragg condition for a given hologram is satisfied. This system has the advantages of having no moving parts and being completely electrically controlled and could easily be optimized to any given specifications.

The diffraction efficiency of the hologram k stored in the structure is given by

$$\eta_{N,1}^{(k)} = \frac{1}{4} \left| \sum_{j=0}^{N-1} \nu_{j,k} \exp(-i\phi_{j,k}) \exp\left(-i\frac{2j\xi}{N-1}\right) \right|^2 \quad (8.36)$$

where $\phi_{j,k}$ is the phase shift imposed on the thin grating of film j while hologram k is being recorded in the SVHOE. For the same reasons explained in the previous section, the maximum number of holograms that can be stored with a high SNR is theoretically limited to N .

8.4.1 Optimum Case

The ideal situation corresponds to the case in which, by some external means, the following conditions can be achieved:

$$\phi_{j,k} = jk\frac{2\pi}{N} \quad \text{and} \quad \nu_{j,k} = \nu_k \quad j, k \in [0, N-1] \quad (8.37)$$

It is easy to see that, with Eq. (8.37), the diffraction efficiency [Eq. (8.36)] can be written as

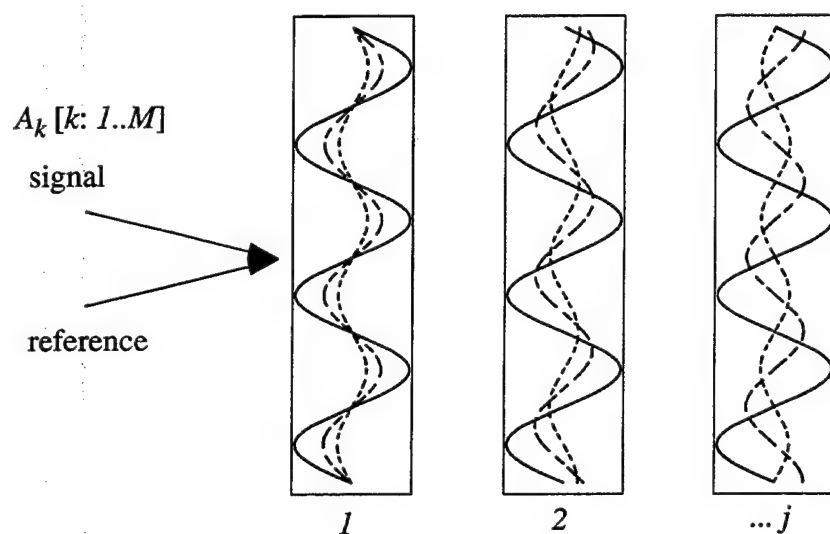


Figure 8.5: General concept of phase multiplexing in a SVHOE: the three types of curves (solid, short-dashed, and long dashed) represent three holograms stored in the structure with different amplitudes. Phase multiplexing is based on the fact that each hologram undergoes a different phase shift in each thin film layer.

	A_k^2	1	2	3	4	5	6	7	Film j
1	1	0	0	0	0	0	0	0	
2	$\frac{1}{7}$	0	$\frac{2\pi}{7}$	$\frac{4\pi}{7}$	$\frac{6\pi}{7}$	$-\frac{6\pi}{7}$	$-\frac{4\pi}{7}$	$-\frac{2\pi}{7}$	
3	$\frac{2}{7}$	0	$\frac{4\pi}{7}$	$-\frac{6\pi}{7}$	$-\frac{2\pi}{7}$	$\frac{2\pi}{7}$	$\frac{6\pi}{7}$	$-\frac{4\pi}{7}$	
4	$\frac{3}{7}$	0	$\frac{6\pi}{7}$	$-\frac{2\pi}{7}$	$\frac{4\pi}{7}$	$-\frac{4\pi}{7}$	$\frac{2\pi}{7}$	$-\frac{6\pi}{7}$	
5	$\frac{4}{7}$	0	$-\frac{6\pi}{7}$	$\frac{2\pi}{7}$	$-\frac{4\pi}{7}$	$\frac{4\pi}{7}$	$-\frac{2\pi}{7}$	$\frac{6\pi}{7}$	
6	$\frac{5}{7}$	0	$-\frac{4\pi}{7}$	$\frac{6\pi}{7}$	$\frac{2\pi}{7}$	$-\frac{2\pi}{7}$	$-\frac{6\pi}{7}$	$\frac{4\pi}{7}$	
7	$\frac{6}{7}$	0	$-\frac{2\pi}{7}$	$-\frac{4\pi}{7}$	$-\frac{6\pi}{7}$	$\frac{6\pi}{7}$	$\frac{4\pi}{7}$	$\frac{2\pi}{7}$	
Hologram k									

Table 8.2: Phase pattern $\phi_{j,k}$ across the structure for the optimum case and chosen intensities A_k^2 of each hologram.

$$\eta_{N,1}^{(k)} \propto A_k^2 \frac{\sin^2 \left(\xi \frac{N}{N-1} + \pi k \right)}{\sin^2 \left(\xi \frac{1}{N-1} + \frac{\pi k}{N} \right)} \quad (8.38)$$

This relation represents the identical diffraction-efficiency curve shifted by an amount $\xi = \pi k(N-1)/N$ for the hologram k . Table 8.2 shows the succession of phases across a SVHOE of $N = 7$ films of each of the seven holograms stored. Figure 8.6 shows the seven corresponding normalized diffraction efficiencies with the intensities A_k^2 given in Table 8.2. The values of these intensities are chosen to be different only for easy differentiation of each corresponding Bragg selectivity curve shown in Fig. 8.6. With this choice of phase [Eq. (8.37)], each efficiency is translated by an amount such that, where one hologram has its maximum diffraction efficiency, all the others have a zero diffraction efficiency. This situation is thus the optimum case because the SNR of each hologram, as defined by Eq. (8.35), will be infinite.

This process is analogous to angular multiplexing because imposing this phase scheme [Eq. (8.37)] is equivalent to forcing the grating fringes to slant at a given angle, different for each hologram. In angular multiplexing one achieves this effect by recording each hologram with a different angle for the reference beam. It is important

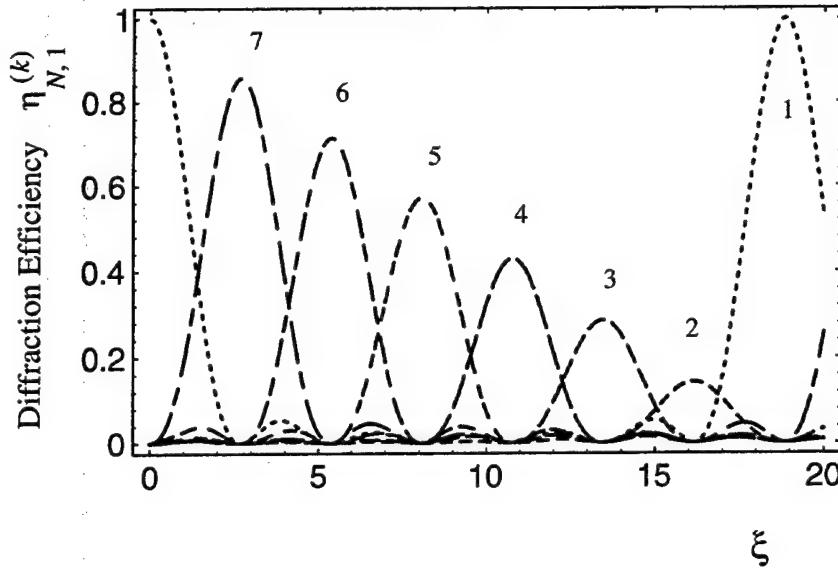


Figure 8.6: Normalized diffraction efficiencies of seven holograms recorded in a SVHOE of seven films: optimum case. The numbers correspond to the hologram numbers (k) in Table 8.2.

to note, though, that in the case of phase multiplexing, the writing geometry remains the same for all holograms.

8.4.2 Photorefractive Case

Unfortunately the optimum situation described in Table 8.2 cannot be achieved if only the photorefractive phase shift resulting from an applied electric field is considered. In this case, indeed, the phase shift can take only values between 0 and $-\pi$, half the full possible range of angles. From Eq. (8.7) the following expressions for the magnitude of the space-charge field and the photorefractive phase shift are derived (see also Chapter 3):

$$|E_{SC}|_{j,k} = m \sqrt{\frac{E_Q^2(E_{0j,k}^2 + E_D^2)}{(E_Q + E_D)^2 + E_{0j,k}^2}} \quad (8.39)$$

$$\phi_{j,k} = \phi_{PR}(E_{0,j,k}) = -\arctan \frac{E_D}{E_{0,j,k}} \left(1 + \frac{E_D}{E_Q} + \frac{E_{0,j,k}^2}{E_D E_Q} \right) \quad (8.40)$$

where $E_{0,j,k}$ is the electric field applied to film j during the recording of hologram k . A structure of N identical films is otherwise considered. The diffraction efficiency [Eq. (8.36)] can then be written as

$$\eta_{N,1}^{(k)} \propto A_k^2 \left| \sum_{j=0}^{N-1} \sqrt{\frac{E_Q^2 (E_{0,j,k}^2 + E_D^2)}{(E_Q + E_D)^2 + E_{0,j,k}^2}} e^{-i\phi_{PR}(E_{0,j,k})} \exp \left(-i \frac{2j\xi}{N-1} \right) \right|^2 \quad (8.41)$$

The optimizing problem addressed here is then to find a sequence of fields $E_{0,j,k}$ to maximize the SNR of each hologram. The SNR, which we compute by using Eq. (8.41) in Eq. (8.35), therefore becomes a direct function of the different applied electric fields $E_{0,j,k}$.

Table 8.3 gives one qualitative example of a field pattern $E_{0,j,k}$ and Fig. 8.7 shows the corresponding normalized diffraction efficiencies for four holograms stored in a structure of seven thin films made of SBN. It shows how the Bragg condition of four holograms recorded with the same writing geometry can be made different only by application of different electric fields to the successive layers of the SVHOE. The numerical values used to compute the diffraction efficiencies are: $N_0^\circ = 1.5 \cdot 10^{23} \text{m}^{-3}$, $N = 10^{25} \text{m}^{-3}$, $\epsilon = 880$, and $\lambda_o = 514 \text{ nm}$ as well as a grating spacing $\Lambda = 15 \mu\text{m}$. Because this situation is not optimum (compared with Table 8.2), the total number of holograms that can be stored in the structure with a high SNR will have to be less than the number of films N . With only the photorefractive phase shift, half the full range of phases is available, and as a general rule the maximum number of holograms that can be stored will be equal to $N/2$ if N is even or $(N+1)/2$ if N is odd.

8.5 Conclusions

We have developed an analytical formalism to describe, in an arbitrary recording and reading geometry, the diffraction properties of stratified volume holographic optical elements made of photorefractive thin films. The model is shown to be valid for

	A_k^2	1	2	3	4	5	6	7	Film j
1	1	7	7	7	7	7	7	7	
2	1	7	-7	7	-7	7	-7	7	
3	1	6	6	-9	-9	-9	6	6	
4	1	5	-9	-5	5	-5	-9	5	
Hologram k									

Table 8.3: Field pattern $E_{0,j,k}$ ($\frac{kV}{cm}$) across the structure for the photorefractive case and chosen intensities A_k^2 of each hologram.

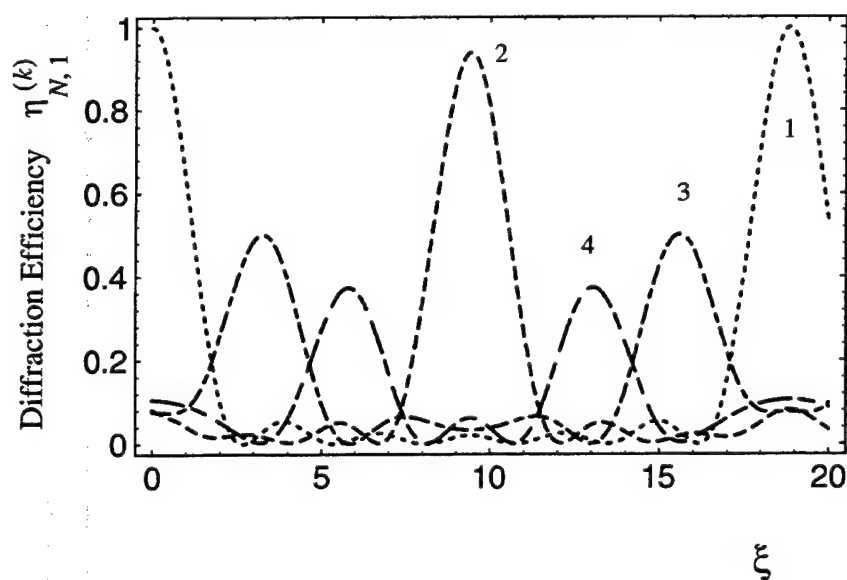


Figure 8.7: Normalized diffraction efficiencies of four holograms recorded in a SVHOE of seven films: photorefractive case. The numbers correspond to the hologram numbers (k) in Table 8.3.

SVHOE's made of any type of recording material. This model leads to a simple closed-form formulation for the first-order diffraction efficiency [Eq. (8.28)] that agrees with the numerical results of Nordin *et al.* [87]. We then considered the limiting case of a SVHOE, a thick photorefractive crystal, and found an expression for the diffraction efficiency of a thick index grating, nonuniform in phase and in amplitude that confirms the results derived in Chapter 5 using a coupled-wave approach.

Finally, SVHOE's made of photorefractive thin films have been analyzed in the context of holographic multiplexing. We have proposed a new principle for multiplexing several holograms in a SVHOE that uses the freedom to adjust the phase of each thin grating of the structure by applying an electric field to the different layers during recording. We have also shown how the finite number of films limits the maximum number of holograms that can be recorded in a SVHOE.

In the next chapter we extend the analytical formalism developed in this chapter to study the diffraction properties of layered structures of thick holograms. We show that, to first order, the formulation for the diffraction efficiency is identical to the one derived in this chapter for layered structures of thin gratings. Finally, we study in detail the properties of one application of a photorefractive SVHOE: a dynamic multiple-wavelength filter.

Chapter 9

Structures of Thick Gratings

9.1 Introduction

In this chapter, we generalize the concept of photorefractive SVHOE introduced in Chapter 8 to include structures of thick gratings that can then be used in the transmission geometry as well as in the reflection geometry. By using thick gratings instead of thin gratings, we can also obtain higher diffraction efficiencies. One of the goals of this theoretical analysis is to obtain a closed-form expression for the diffraction efficiency of such structures and to compare it with the expression obtained in Chapter 8 for structures made of thin gratings. The theory is developed to account for such cases in which photorefractive SVHOE's are made of several different kinds of materials or cases in which for example gratings with different grating spacings are written in successive layers. Constructing a comprehensive analytical model describing the properties of photorefractive SVHOE's is useful in guiding their development, because it offers a simple framework to manipulate the different diffraction parameters for optimal performance.

To compute the diffraction efficiency describing the Bragg selectivity, one solves the coupled-wave equations in each grating layer [4] and then combines these solutions to find the general solution for the whole structure, taking into account wave propagation in the buffer layers. This analytical development is a generalization of the theory developed by Yakimovich in Ref. [82], so we can obtain an explicit closed-form

solution for SVHOE's made of an arbitrary number of layers, having each different properties. We consider the transmission and the reflection geometry and show that in both cases the diffraction efficiency can formally be written in a similar manner.

The theory developed in this chapter is especially important for describing applications that use photorefractive films fabricated from photopolymer materials. Photopolymers tend to grow as films having thicknesses in the range 10 - 100 μm , for which the thin grating approximation is usually not valid. However, the thickness of these films is such that, in the context of holographic storage, it is difficult to use them individually. Therefore, as first demonstrated by Nordin and Tanguay [99] and more recently by Stankus *et al.* [90], these materials are excellent candidates for grating layer components of photorefractive SVHOE's.

One application of these layered structures consists of a multiple-layer optical memory. Basic proof-of-principle devices that use this idea have already been proposed and demonstrated [100] [101]. The theory developed in this chapter helps one to a better understanding of the properties of these memory devices and to an accurate estimation of their cross talk and signal-to-noise characteristics. Finally, a novel optical application, a dynamic multiple-wavelength filter, is proposed and analyzed. It consists of a photorefractive SVHOE in the reflection geometry that makes use of the electrically controlled diffraction (ECD) effect [39] (see explanation in Chapter 7) to change individually the properties of each thick grating layer. We show how this device can be used to filter dynamically one or several wavelengths by selectively applying different electric fields to the grating layers of the photorefractive SVHOE. Such a device might be useful in the context of wavelength division multiplexing (WDM).

For simplicity, we consider the unslanted grating configuration in which the read-out and the diffracted beams are symmetric with respect to the z axis. Two types of geometries are considered: the transmission geometry in which the two recording beams are copropagating and the reflection geometry in which these two beams are counterpropagating. In most of the holographic applications (filtering, storage, etc.), a large Bragg selectivity is desirable. This is the reason why angular selectivity is used in the transmission geometry whereas wavelength selectivity is used in the reflection

geometry [4].

We assume that the gratings inside the thick grating layers are uniform in amplitude and in phase. In photorefractive crystals, it means that beam coupling and wave mixing [28] are neglected during grating formation. A detailed description of the diffraction properties of nonuniform gratings can be found in Chapter 5.

9.2 Transmission Geometry

In the symmetric configuration, as shown in Fig. 9.1, the grating vector is perpendicular to the propagation axis, i.e., $K_z = 0$ and $K_\perp = -2k \sin \theta_B$, where θ_B is, by definition, the Bragg angle and $k = 2\pi/\lambda$ where $\lambda = \lambda_o/\bar{n}$. If we assume that the angle θ_p of the readout beam varies in the plane of incidence and that the readout wavelength λ is the same as the wavelength used during recording, the Bragg detuning parameter is given by

$$\xi = \frac{\pi l}{\lambda} \left\{ \cos \theta_R - \sqrt{1 - (\sin \theta_R - 2 \sin \theta_B)^2} \right\} \quad (9.1)$$

For arbitrary boundary conditions at the front face of the crystal ($z = 0$), the solutions to the coupled-wave equations [Eq. (2.18)] at the exit face of the crystal ($z = l$) are expressed in the following way,

$$\begin{pmatrix} A_p(l) \\ A_\sigma(l) \end{pmatrix} = M^{tr}(l) \begin{pmatrix} A_p(0) \\ A_\sigma(0) \end{pmatrix} \quad (9.2)$$

where $M^{tr}(l)$ is the matrix describing the diffraction from a uniform grating of length l in the transmission geometry. Figure 9.2 represents the succession of grating layers and buffer layers forming the SVHOE. Each layer is described by a matrix relating its input field to its output field.

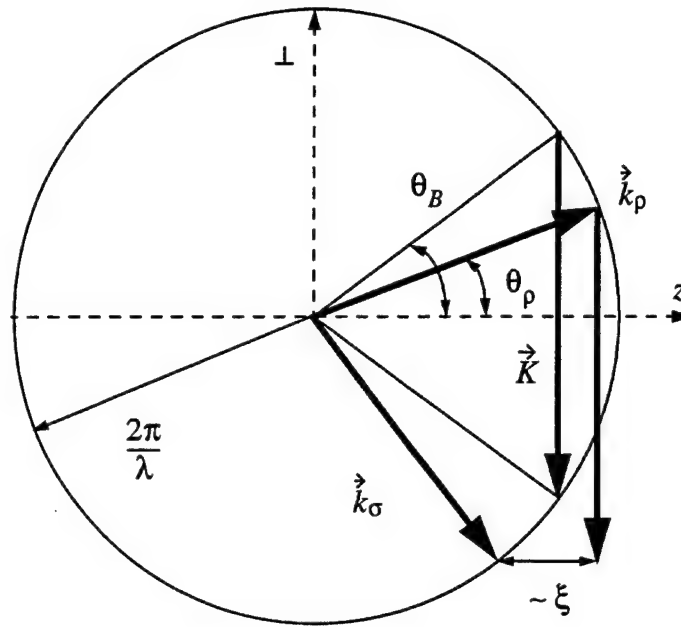


Figure 9.1: k -vector diagram in the symmetric configuration using the transmission geometry.

9.2.1 Layer Matrices

Grating Layer Matrix

The grating layer matrix defined by Eq. (9.2) has been explicitly computed in Chapter 2 [Eq. (2.24)] and is given by

$$M^{tr}(l) = \exp(i\xi) \times \begin{pmatrix} -i\xi \frac{\sin \sqrt{\xi^2 + \nu^2}}{\sqrt{\xi^2 + \nu^2}} + \cos \sqrt{\xi^2 + \nu^2} & -i\nu \exp(i\phi) \frac{\sin \sqrt{\xi^2 + \nu^2}}{\sqrt{\xi^2 + \nu^2}} \\ -i\nu \exp(-i\phi) \frac{\sin \sqrt{\xi^2 + \nu^2}}{\sqrt{\xi^2 + \nu^2}} & i\xi \frac{\sin \sqrt{\xi^2 + \nu^2}}{\sqrt{\xi^2 + \nu^2}} + \cos \sqrt{\xi^2 + \nu^2} \end{pmatrix} \quad (9.3)$$

where $\nu = \kappa l / \cos \theta_\rho$ is the grating strength, $\kappa = \pi \Delta n / \lambda_o$, and ϕ is the phase of the grating.

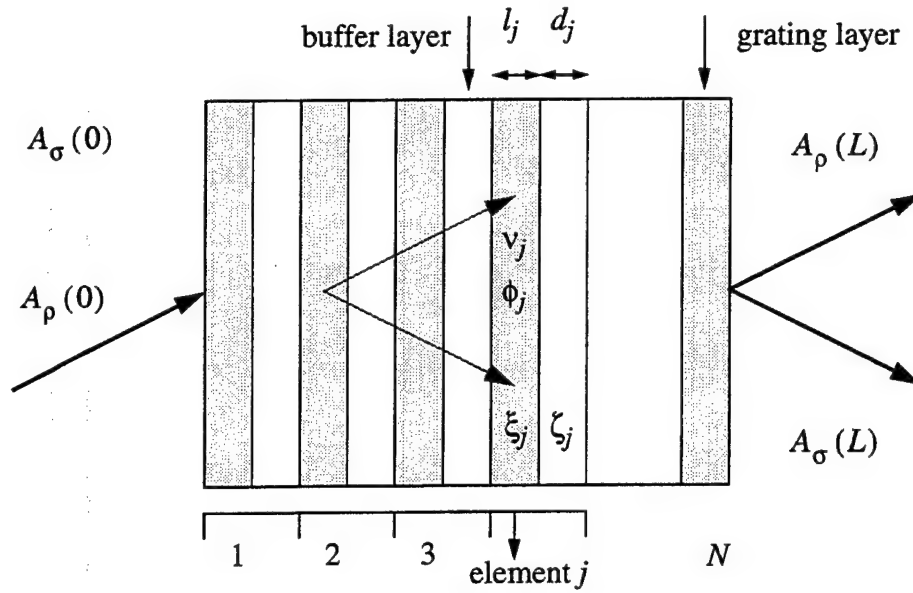


Figure 9.2: Photorefractive SVHOE of N grating layers in the transmission geometry. ν_j is the grating strength; ϕ_j is the grating phase; l_j and d_j are the thicknesses and ξ_j and ζ_j are the Bragg detuning parameters of the grating layers and the buffer layers, respectively.

Buffer Layer Matrix

The propagation of the transmitted and the diffracted beams over the length d of a buffer layer between two successive grating layers is taken into account by the introduction of a buffer layer matrix defined by

$$\begin{pmatrix} A_\rho(d) \\ A_\sigma(d) \end{pmatrix} = M^{bu}(d) \begin{pmatrix} A_\rho(0) \\ A_\sigma(0) \end{pmatrix} \quad (9.4)$$

where

$$M^{bu}(d) = \begin{pmatrix} \exp(-ik_{Rz}^{bu}d) & 0 \\ 0 & \exp(-ik_{Sz}^{bu}d) \end{pmatrix} \quad (9.5)$$

In a buffer layer we define a detuning parameter ζ :

$$\zeta = \frac{d}{2}(k_{Rz}^{bu} - k_{Sz}^{bu}) \quad (9.6)$$

where *bu* denotes the buffer layer. Therefore,

$$M^{bu}(d) = \exp(-ik_{sz}^{bu}d) \exp(-i\zeta) \begin{pmatrix} \exp(-i\zeta) & 0 \\ 0 & \exp(i\zeta) \end{pmatrix} \quad (9.7)$$

We assume that the buffer layers have a similar index of refraction to that of the grating layers and we thus neglect the multiple reflections at the different interfaces.

Element Matrix

The matrix of one element *j*, consisting of a grating layer of thickness *l_j* followed by a buffer layer of length *d_j*, is the product of the two matrices:

$$M_j^{el} = M_j^{bu}(d_j) M_j^{tr}(l_j) \quad (9.8)$$

Structure Matrix

The complete stratified element consists of a succession of *N* grating layers and (*N*−1) intermediate buffer layers as shown in Fig. 9.2. The grating layer properties, namely the grating strength [$\nu_j = \pi \Delta n_j l_j / (\lambda_o \cos \theta_\rho)$] and the grating phase (ϕ_j), as well as the Bragg detuning parameters ξ_j and ζ_j are allowed to be different from one layer to another. Cases in which, for example, holograms with different grating periods are written in different layers can then be considered with a composite detuning parameter,

$$\xi_j = \frac{\pi l_j}{\lambda} \left\{ \cos \theta_\rho - \sqrt{1 - (\sin \theta_\rho - 2 \sin \theta_{Bj})^2} \right\} \quad (9.9)$$

where θ_{Bj} is the Bragg angle in the grating layer *j*. The total length *L* of the structure is given by

$$L = \sum_{j=1}^N l_j + \sum_{j=1}^{N-1} d_j \quad (9.10)$$

The structure matrix is defined such that

$$\begin{pmatrix} A_\rho(L) \\ A_\sigma(L) \end{pmatrix} = M^{st} \begin{pmatrix} A_\rho(0) \\ A_\sigma(0) \end{pmatrix} \quad (9.11)$$

and is given by the product of all the different layer matrices:

$$M^{st} = M_N^{tr}(l_N) \prod_{j=N-1}^1 M_j^{el} \quad (9.12)$$

9.2.2 Closed-Form Solutions

Structure of Different Layers

To obtain an analytical expression for M^{st} and a closed-form solution for the diffraction efficiency, we assume that the grating strengths ν_j are small compared with unity (this is equivalent to assuming the undepleted pump approximation throughout the structure). However, there is no restriction on the magnitude of the Bragg detuning parameter ξ_j , which is usually much larger than the grating strength. If we develop the grating layer matrices $M_j^{tr}(l_j)$ [Eq. (9.3)] to first order in ν_j , the following expression is found:

$$M_j^{tr}(l_j) = \exp(i\xi_j) \begin{pmatrix} \exp(-i\xi_j) & -i\nu_j \frac{\sin \xi_j}{\xi_j} \exp(i\phi_j) \\ -i\nu_j \frac{\sin \xi_j}{\xi_j} \exp(-i\phi_j) & \exp(i\xi_j) \end{pmatrix} \quad (9.13)$$

The element matrix is then given by

$$\begin{aligned} M_j^{el} &= \exp(-ik_{S_{zj}}^{bu} d_j) \exp[i(\xi_j - \zeta_j)] \\ &\times \begin{pmatrix} \exp[-i(\xi_j + \zeta_j)] & -i\nu_j \frac{\sin \xi_j}{\xi_j} \exp[-i(\zeta_j - \phi_j)] \\ -i\nu_j \frac{\sin \xi_j}{\xi_j} \exp[i(\zeta_j - \phi_j)] & \exp[i(\xi_j + \zeta_j)] \end{pmatrix} \end{aligned} \quad (9.14)$$

If we keep only the first order terms in ν_j in the product defining the structure matrix [Eq. (9.12)], M^{st} is given by

$$M^{st} = \exp \left(-i \sum_{j=1}^{N-1} k_{szj}^{bu} d_j \right) \exp \left(-i \sum_{j=1}^{N-1} \zeta_j \right) \exp \left(i \sum_{j=1}^N \xi_j \right) \times$$

$$\begin{pmatrix} \exp \left(-i \sum_{j=1}^N \xi_j - i \sum_{j=1}^{N-1} \zeta_j \right) & -i \exp \left(-i \sum_{k=1}^N \xi_k - i \sum_{k=1}^{N-1} \zeta_k \right) \sum_{j=1}^N \nu_j \\ \frac{\sin \xi_j}{\xi_j} e^{i(\xi_j + \phi_j)} \exp \left[2i \sum_{k=1}^{j-1} (\xi_k + \zeta_k) \right] & \\ -i \exp \left(i \sum_{k=1}^N \xi_k + i \sum_{k=1}^{N-1} \zeta_k \right) \sum_{j=1}^N \nu_j & \exp \left(i \sum_{j=1}^N \xi_j + i \sum_{j=1}^{N-1} \zeta_j \right) \\ \frac{\sin \xi_j}{\xi_j} e^{-i(\xi_j + \phi_j)} \exp \left[-2i \sum_{k=1}^{j-1} (\xi_k + \zeta_k) \right] & \end{pmatrix} \quad (9.15)$$

For the boundary conditions associated with the usual diffraction problem, $A_\rho(0) = 1$ and $A_\sigma(0) = 0$, the diffraction efficiency is given by

$$\eta = |A_\sigma(L)|^2$$

$$= \left| \sum_{j=1}^N \nu_j \exp(-i\phi_j) \frac{\sin \xi_j}{\xi_j} \exp(-i\xi_j) \exp \left[-2i \sum_{k=1}^{j-1} (\xi_k + \zeta_k) \right] \right|^2 \quad (9.16)$$

The solution [Eq. (9.16)] can be further simplified if the same grating is written in each layer and if the layers lengths are assumed equal, i.e., $\xi_j = \xi$ and $\zeta_j = \xi d/l$. In this case, the diffraction efficiency reduces to

$$\eta = \left(\frac{\sin \xi}{\xi} \right)^2 \left| \sum_{j=1}^N \nu_j \exp(-i\phi_j) \exp \left[-2i(j-1)\xi \left(1 + \frac{d}{l} \right) \right] \right|^2 \quad (9.17)$$

If we take $l = 0$ in Eq. (9.17), the expression reduces to the expression obtained in Chapter 8 for the diffraction efficiency of a structure of thin holograms [Eq. (8.26)],

$$\eta^{thin} = \left| \sum_{j=1}^N \nu_j \exp(-i\phi_j) \exp[-2i(j-1)\zeta] \right|^2 \quad (9.18)$$

by noting that the factor $1/4$ in Eq. (8.26) comes from the different definition of the grating strength ν adopted in Chapter 8 and Chapter 9 (it is different by a factor of 2 between thin and thick gratings). The modulation factor in front of the absolute value in Eq. (9.17), $\text{sinc}^2 \zeta$, represents the Bragg selectivity of a single thick hologram in the structure. In the case of a structure of thin holograms, this factor is equal to unity because thin holograms do not exhibit any Bragg selectivity behavior. Therefore the diffraction efficiency of a structure of thick gratings is essentially the same as the diffraction efficiency of a structure of thin gratings except that it is modulated by the selectivity of a single layer.

Structure of Identical Layers

If a structure of grating layers with identical properties is considered, the exact solution for the diffraction efficiency can be derived without the assumption of the undepleted pump approximation. In this case, the element matrix, which is the same for all the elements of the structure, can be written as

$$M^{el} = \exp(-ik_{sz}d) \exp \left[i\zeta \left(1 - \frac{d}{l} \right) \right] \times \begin{pmatrix} \left(-i\zeta \frac{\sin \sqrt{\xi^2 + \nu^2}}{\sqrt{\xi^2 + \nu^2}} + \cos \sqrt{\xi^2 + \nu^2} \right) e^{-i\zeta \frac{d}{l}} & -i\nu e^{i\phi} \frac{\sin \sqrt{\xi^2 + \nu^2}}{\sqrt{\xi^2 + \nu^2}} e^{-i\zeta \frac{d}{l}} \\ -i\nu e^{-i\phi} \frac{\sin \sqrt{\xi^2 + \nu^2}}{\sqrt{\xi^2 + \nu^2}} e^{i\zeta \frac{d}{l}} & \left(i\zeta \frac{\sin \sqrt{\xi^2 + \nu^2}}{\sqrt{\xi^2 + \nu^2}} + \cos \sqrt{\xi^2 + \nu^2} \right) e^{i\zeta \frac{d}{l}} \end{pmatrix} \quad (9.19)$$

The structure matrix is given by

$$M^{st} = M^{tr}(l) (M^{el})^{N-1} \quad (9.20)$$

The diffraction efficiency can then be calculated by use of the Chebyshev identity: if a matrix \mathcal{M}

$$\mathcal{M} = \begin{pmatrix} A & B \\ C & D \end{pmatrix} \quad (9.21)$$

is unimodular ($AD - BC = 1$), \mathcal{M}^N is given by

$$\mathcal{M}^N = \begin{pmatrix} A & B \\ C & D \end{pmatrix}^N = \begin{pmatrix} AU_{N-1} - U_{N-2} & BU_{N-1} \\ CU_{N-1} & DU_{N-1} - U_{N-2} \end{pmatrix} \quad (9.22)$$

where

$$\begin{aligned} U_N &= \frac{\sin(N+1)y}{\sin y} \\ y &= \arccos\left(\frac{A+D}{2}\right) \end{aligned} \quad (9.23)$$

It is easy to check that, because of energy conservation, the element matrix given by Eq. (9.19) is unimodular. The diffraction efficiency is then given by

$$\eta = \nu^2 \frac{\sin^2 \sqrt{\nu^2 + \xi^2}}{\nu^2 + \xi^2} \left(\frac{\sin^2 \left[N \arccos \left(\cos \sqrt{\nu^2 + \xi^2} \cos \xi \frac{d}{l} - \xi \frac{\sin \sqrt{\nu^2 + \xi^2}}{\sqrt{\nu^2 + \xi^2}} \sin \xi \frac{d}{l} \right) \right]}{\sin^2 \left[\arccos \left(\cos \sqrt{\nu^2 + \xi^2} \cos \xi \frac{d}{l} - \xi \frac{\sin \sqrt{\nu^2 + \xi^2}}{\sqrt{\nu^2 + \xi^2}} \sin \xi \frac{d}{l} \right) \right]} \right) \quad (9.24)$$

For small grating strengths, i.e., to first order in ν ,

$$y = \arccos \left(\cos \xi \cos \xi \frac{d}{l} - \sin \xi \sin \xi \frac{d}{l} \right) = \xi \left(1 + \frac{d}{l} \right) \quad (9.25)$$

and the diffraction efficiency [Eq. (9.24)] reduces to

$$\eta = \nu^2 \left(\frac{\sin \xi}{\xi} \right)^2 \frac{\sin^2 \left[N \xi \left(1 + \frac{d}{l} \right) \right]}{\sin^2 \left[\xi \left(1 + \frac{d}{l} \right) \right]} \quad (9.26)$$

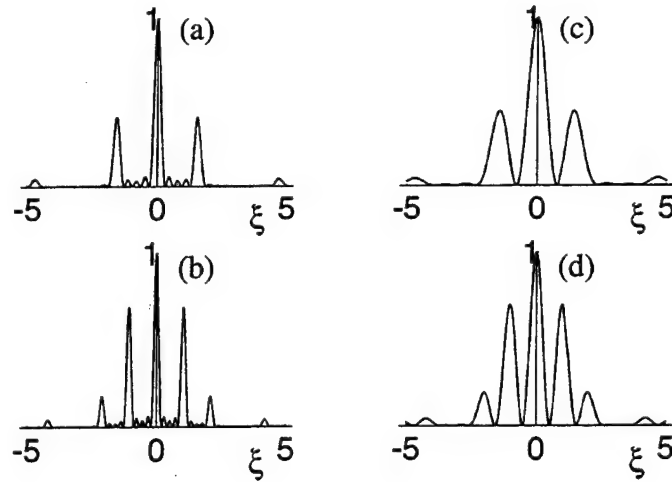


Figure 9.3: Normalized diffraction efficiency η^{norm} as a function of the Bragg detuning parameter ξ for a SVHOE of N identical grating layers in the transmission geometry: (a) $\frac{d}{l} = 1$, $N = 5$, and $L/l = 9$, (b) $\frac{d}{l} = 2$, $N = 5$, and $L/l = 13$, (c) $\frac{d}{l} = 1$, $N = 2$, and $L/l = 3$, (d) $\frac{d}{l} = 2$, $N = 2$, and $L/l = 4$.

We can also derive this simple expression from Eq. (9.17), by explicitly computing the absolute value of the finite sum for grating layers with identical properties ($\nu_j = \nu$, $\phi_j = \phi$). The normalized (to unity) diffraction efficiency is given by

$$\eta^{norm} = \frac{1}{N^2} \left(\frac{\sin \xi}{\xi} \right)^2 \frac{\sin^2 \left[N \xi \left(1 + \frac{d}{l} \right) \right]}{\sin^2 \left[\xi \left(1 + \frac{d}{l} \right) \right]} \quad (9.27)$$

Figure 9.3 represents the normalized diffraction efficiency η^{norm} describing the selectivity behavior [Eq. (9.27)] of a structure of thick gratings for two values of the ratio d/l and N . One distance can be chosen as unit, in this case l because ξ is proportional to l . The normalized length of the structure is then given by $L/l = (N-1)(1+d/l)+1$. Figure 9.4 represents the diffraction efficiency for two cases that have the same total length $L/l = 13$. From Figs. 9.3 and 9.4, it is interesting to note the presence of three inverse length scales: the inverse of the total length of the structure, $1/L$, which determines the width of each narrow selectivity peak; the inverse of the thickness of the

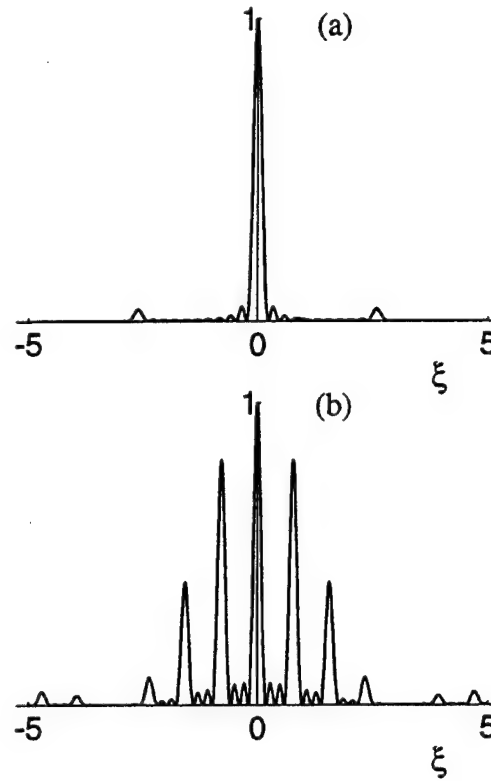


Figure 9.4: Normalized diffraction efficiency η^{norm} as a function of the Bragg detuning parameter ξ for a SVHOE of N identical grating layers in the transmission geometry (constant total length L): (a) $\frac{d}{l} = 0.2$, $N = 11$, and $L/l = 13$, (b) $\frac{d}{l} = 3$, $N = 4$, and $L/l = 13$.

grating, $1/l$, which determines the width of the overall envelope of the diffraction efficiency; and the inverse of the thickness of the buffer layer, $1/d$, which determines the separation between two main narrow peaks. Figures 9.3 and 9.4 and Eq. (9.26) agree perfectly well with the experimental selectivity measurements and the conclusions as described in Refs. [90] and [99].

9.3 Reflection Geometry

In the symmetric configuration, as shown in Fig. 9.5, the perpendicular component and the longitudinal component of the grating vector are given by $K_{\perp} = 0$ and $K_z = -2k_B \cos \theta_B = -4\pi \cos \theta_B / \lambda_B$, where θ_B is, by definition, the Bragg angle and λ_B is the writing wavelength (i.e., the Bragg wavelength). If we assume that only the

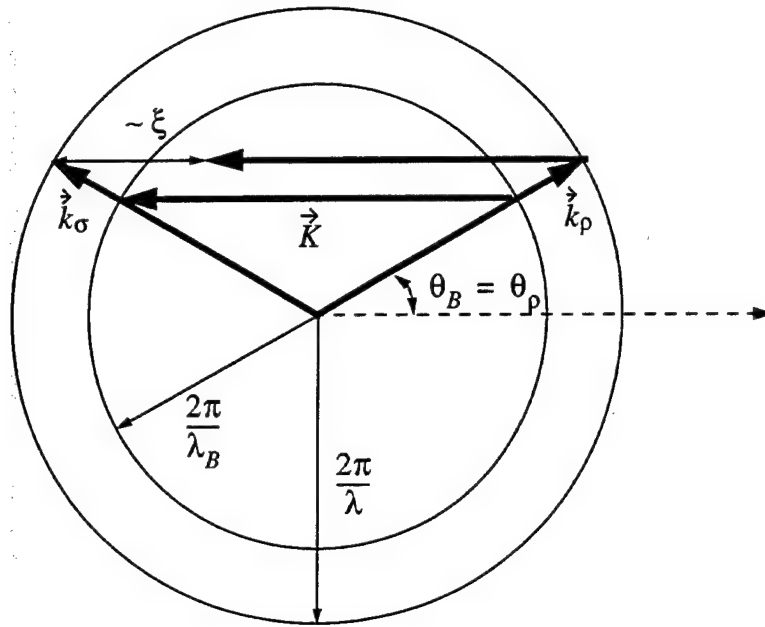


Figure 9.5: k -vector diagram in the symmetric configuration using the reflection geometry.

wavelength λ of the readout beam varies, the Bragg detuning parameter is given by

$$\xi = 2\pi l \cos \theta_B \left(\frac{1}{\lambda} - \frac{1}{\lambda_B} \right) \quad (9.28)$$

For arbitrary boundary conditions $A_\rho(0)$ and $A_\sigma(l)$, the solutions to the coupled-wave equations [Eq. (2.18)] are expressed in the following way:

$$\begin{pmatrix} A_\rho(l) \\ A_\sigma(0) \end{pmatrix} = M^{re}(l) \begin{pmatrix} A_\rho(0) \\ A_\sigma(l) \end{pmatrix} \quad (9.29)$$

where $M^{re}(l)$ is the matrix describing the diffraction from a uniform grating of length l in the reflection geometry. Figure 9.6 represents the succession of grating and buffer layers forming the SVHOE in the reflection geometry.

9.3.1 Layer Matrices

Grating Layer Matrix

In the reflection geometry, the grating matrix defined by Eq. (9.29) has been explicitly derived in Chapter 2 [Eq. (2.31)] and it is given by

$$M^{re}(l) = \frac{1}{\sqrt{\nu^2 - \xi^2} \cosh \sqrt{\nu^2 - \xi^2} + i\xi \sinh \sqrt{\nu^2 - \xi^2}} \times \begin{pmatrix} \exp(i\xi)\sqrt{\nu^2 - \xi^2} & i\nu \exp(i\phi) \sinh \sqrt{\nu^2 - \xi^2} \\ i\nu \exp(-i\phi) \sinh \sqrt{\nu^2 - \xi^2} & \exp(-i\xi)\sqrt{\nu^2 - \xi^2} \end{pmatrix} \quad (9.30)$$

Buffer Layer Matrix

The buffer layer matrix is now defined as follows because the beams are counterpropagating:

$$\begin{pmatrix} A_\rho(d) \\ A_\sigma(0) \end{pmatrix} = M^{bu}(d) \begin{pmatrix} A_\rho(0) \\ A_\sigma(d) \end{pmatrix} \quad (9.31)$$

where

$$M^{bu}(d) = \begin{pmatrix} \exp(-ik_{Rz}^{bu}d) & 0 \\ 0 & \exp(ik_{Sz}^{bu}d) \end{pmatrix} \quad (9.32)$$

Defining $\zeta = 2\pi d \cos \theta_B / \lambda$, we obtain

$$M^{bu}(d) = \begin{pmatrix} \exp(-i\zeta) & 0 \\ 0 & \exp(-i\zeta) \end{pmatrix} \quad (9.33)$$

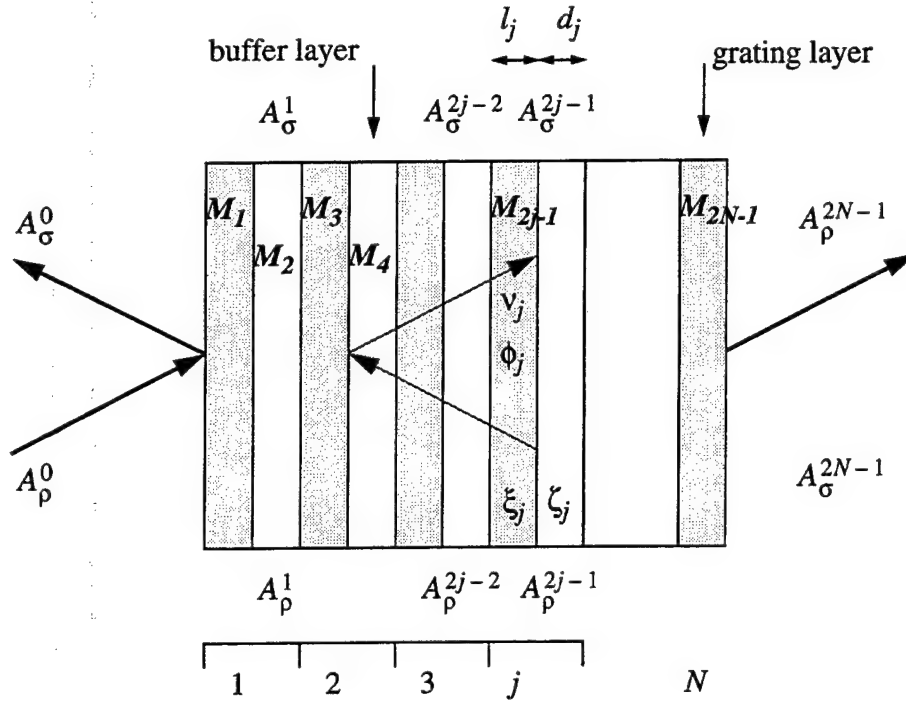


Figure 9.6: Photorefractive SVHOE of N grating layers in the reflection geometry. ν_j is the grating strength; ϕ_j is the grating phase; l_j and d_j are the thicknesses and ξ_j and ζ_j are the Bragg detuning parameters of the grating layers and the buffer layers, respectively; M_j is the layer matrix.

Structure Matrix

Figure 9.6 represents an example of a layered structure of thick gratings in the reflection geometry. Because the beams are counterpropagating, the structure matrix cannot simply be represented by the product of the different element matrices as in the transmission case. For a structure containing N grating layers and $N - 1$ buffer layers, one needs to solve a system of $2(2N - 1)$ equations to find the expression for the diffracted beam exiting the structure:

$$\begin{pmatrix} A_\rho^k \\ A_\sigma^{k-1} \end{pmatrix} = M_k \begin{pmatrix} A_\rho^{k-1} \\ A_\sigma^k \end{pmatrix} \quad k \in [1, 2N - 1] \quad (9.34)$$

where M_k represents either the buffer layer matrix or the grating layer matrix, depending on the layer considered,

$$\begin{aligned} M_{2j-1} &= M_j^{re}(l_j) & j \in [1, N] \\ M_{2j} &= M_j^{bu}(d_j) & j \in [1, N-1] \end{aligned} \quad (9.35)$$

A_ρ^k and A_σ^k are the values of the transmitted and the diffracted beam at the different interfaces, A_ρ^0 and A_σ^{2N-1} are the known boundary conditions and A_σ^0 is the diffracted wave exiting the structure.

As an example, the next equation, derived from Eq. (9.34), represents the linear system of algebraic equations corresponding to a three-grating-layer system ($N = 3$) (this equation can easily be generalized to an arbitrary number of layers):

$$\mathcal{M} \begin{pmatrix} A_\rho^1 \\ A_\sigma^0 \\ A_\rho^2 \\ A_\sigma^1 \\ A_\rho^3 \\ A_\sigma^2 \\ A_\rho^4 \\ A_\sigma^3 \\ A_\rho^5 \\ A_\sigma^4 \end{pmatrix} = \begin{pmatrix} M_1^{[1,1]} A_\rho^0 \\ M_1^{[2,1]} A_\rho^0 \\ 0 \\ 0 \\ 0 \\ 0 \\ 0 \\ 0 \\ M_5^{[1,2]} A_\sigma^5 \\ M_5^{[2,2]} A_\sigma^5 \end{pmatrix} \quad (9.36)$$

where $M_k^{[p,q]}$ is the (p, q) element of the matrix M_k defined by Eq. (9.35) and \mathcal{M} is the structure matrix given by

$\mathcal{M} =$

$$\begin{pmatrix} 1 & 0 & 0 & -M_1^{[1,2]} & 0 & 0 & 0 & 0 & 0 & 0 \\ 0 & 1 & 0 & -M_1^{[2,2]} & 0 & 0 & 0 & 0 & 0 & 0 \\ -M_2^{[1,1]} & 0 & 1 & 0 & 0 & -M_2^{[1,2]} & 0 & 0 & 0 & 0 \\ -M_2^{[2,1]} & 0 & 0 & 1 & 0 & -M_2^{[2,2]} & 0 & 0 & 0 & 0 \\ 0 & 0 & -M_3^{[1,1]} & 0 & 1 & 0 & 0 & -M_3^{[1,2]} & 0 & 0 \\ 0 & 0 & -M_3^{[2,1]} & 0 & 0 & 1 & 0 & -M_3^{[2,2]} & 0 & 0 \\ 0 & 0 & 0 & 0 & -M_4^{[1,1]} & 0 & 1 & 0 & 0 & -M_4^{[1,2]} \\ 0 & 0 & 0 & 0 & -M_4^{[2,1]} & 0 & 0 & 1 & 0 & -M_4^{[2,2]} \\ 0 & 0 & 0 & 0 & 0 & 0 & -M_5^{[1,1]} & 0 & 1 & 0 \\ 0 & 0 & 0 & 0 & 0 & 0 & -M_5^{[2,1]} & 0 & 0 & 1 \end{pmatrix} \quad (9.37)$$

9.3.2 Closed-Form Solutions

In the reflection geometry, a general expression of the form of Eq. (9.24) could not be derived because, without the assumption of the undepleted pump approximation, the diffraction problem to be solved is more complex than it is in the transmission geometry. It is however possible to solve Eq. (9.36) for an arbitrary number of layers and to find an analytical solution for the diffraction efficiency if only the first order terms in ν_j are considered (there is no restriction on the magnitude of ξ_j). To first order in ν_j , the grating layer matrix is given by

$$M_j^{re}(l_j) = \begin{pmatrix} 1 & i\nu_j \exp[-i(\xi_j - \phi_j)] \frac{\sin \xi_j}{\xi_j} \\ i\nu_j \exp[-i(\xi_j + \phi_j)] \frac{\sin \xi_j}{\xi_j} & \exp(-2i\xi_j) \end{pmatrix} \quad j \in [1, N] \quad (9.38)$$

By generalizing Eq. (9.36) to an arbitrary number of layers and by solving it with the boundary conditions $A_\rho^0 = 1$ and $A_\sigma^{2N-1} = 0$, we derive the following expression for the diffraction efficiency:

$$\begin{aligned}\eta &= |A_\sigma^0|^2 \\ &= \left| \sum_{j=1}^N \nu_j \exp(-i\phi_j) \frac{\sin \xi_j}{\xi_j} \exp(-i\xi_j) \exp \left[-2i \sum_{k=1}^{j-1} (\xi_k + \zeta_k) \right] \right|^2\end{aligned}\quad (9.39)$$

This expression is formally identical to the expression obtained for the diffraction efficiency of a structure of thick holograms in the transmission geometry [Eq. (9.16)]. However, in this case, the detuning parameters are given by

$$\begin{aligned}\xi_k &= 2\pi l_k \cos \theta_B \left(\frac{1}{\lambda} - \frac{1}{\lambda_B^k} \right) \\ \zeta_k &= \frac{2\pi d_k}{\lambda} \cos \theta_B\end{aligned}\quad (9.40)$$

where λ_B^k is the writing wavelength in the grating layer k and λ is the readout wavelength. The physical meaning of Eqs. (9.16) and (9.39) is that the diffracted intensity is the coherent sum of all the N first-order diffracted signals from each of the N grating layers. A similar argument was used to explain the diffraction efficiency of a structure of thin gratings and the analogy with a Fabry-Perot etalon. If the same grating is written in all the layers, i.e., if $\lambda_B^k = \lambda_B$, and if the layers lengths are assumed equal ($l_k = l$, $d_k = d$), the diffraction efficiency given by Eq. (9.39) simplifies to

$$\eta = \left(\frac{\sin \xi}{\xi} \right)^2 \left| \sum_{j=1}^N \nu_j \exp(-i\phi_j) \exp[-i(j-1)\delta\varphi] \exp \left[-2i(j-1)\xi \left(1 + \frac{d}{l} \right) \right] \right|^2 \quad (9.41)$$

where

$$\delta\varphi = \frac{4\pi d}{\lambda_B} \cos \theta_B \quad (9.42)$$

The expression for the diffraction efficiency in the reflection geometry [Eq. (9.41)] is similar to the expression for the transmission geometry [Eq. (9.17)], except for the phase factor $\exp[-i(j-1)\delta\varphi]$. This term is due to the fact that there is a phase

difference between the N different diffracted beams $\sigma^{(k)}$ forming the diffracted signal $A_\sigma(0)$: because of the propagation in the buffer layers, two beams $\sigma^{(k)}$ and $\sigma^{(l)}$, diffracting from the grating layers k and l , respectively, will have a phase difference given by $(k-l)\delta\varphi$ after propagation in the structure, even when the Bragg condition ($\xi = 0$) is satisfied (see Fig. 9.7). This term does not appear in the transmission-geometry case, because there is no such phase difference between two beams $\sigma^{(k)}$ and $\sigma^{(l)}$ when the Bragg condition is satisfied, i.e., when $\xi = 0$.

If a structure of identical gratings is considered ($\nu_j = \nu$, $\phi_j = \phi$), the sum in Eq. (9.41) can be evaluated to yield

$$\eta = \nu^2 \left(\frac{\sin \xi}{\xi} \right)^2 \frac{\sin^2 \left\{ N \left[\xi \left(1 + \frac{d}{l} \right) + \frac{2\pi d}{\lambda_B} \cos \theta_B \right] \right\}}{\sin^2 \left[\xi \left(1 + \frac{d}{l} \right) + \frac{2\pi d}{\lambda_B} \cos \theta_B \right]} \quad (9.43)$$

The selectivity behavior in the reflection geometry is thus analogous to that in the transmission case (see Figs. 9.3 and 9.4), except for the fact that the maximum diffraction efficiency can be shifted along the Bragg detuning parameter (ξ) axis.

The detuning shift is a unique feature of a stratified medium used in the reflection geometry and is inherent to the fact that the beams must propagate through buffer layers. This phenomenon, through which one can shift the Bragg peaks by, for example, changing the properties of the buffer layers only, without affecting the grating itself, offers opportunities for novel applications involving the use of photorefractive SVHOE's (e.g., dynamic beam-steering devices). Figure 9.8 shows the relative wavelength shift $\Delta\lambda/\lambda|_{shift}$ of the maximum diffraction efficiency as a function of the buffer layer thickness for a given grating layer thickness.

Equations (9.26) and (9.43), however, reduce to the diffraction efficiency of a single thick grating of thickness Nl when the limit $d \rightarrow 0$ is taken.

$$\eta = (N\nu)^2 \left(\frac{\sin N\xi}{N\xi} \right)^2 \quad (9.44)$$

This expression is valid in the transmission geometry as well as in the reflection geometry, provided the undepleted pump approximation is assumed [4].

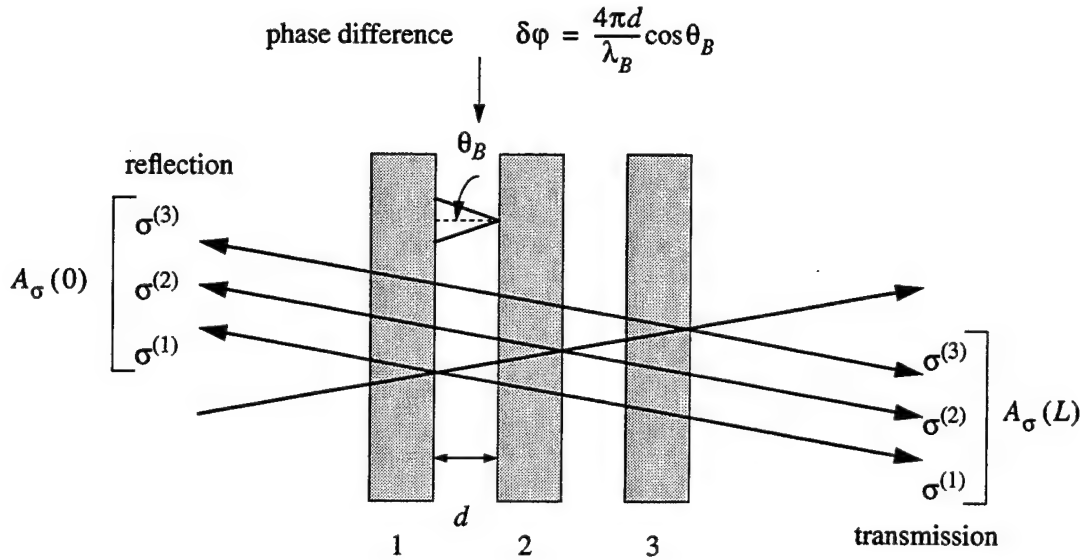


Figure 9.7: Illustration of the phase shift $\delta\phi$ that arises between the beams $\sigma^{(k)}$ in the reflection geometry as a result of the propagation in the buffer layers. In the transmission geometry, such phase shift does not exist.

9.4 Dynamic Multiple-Wavelength Filter

Wavelength filters with narrow spectral bandwidths are widely used in such applications as spectroscopy, astronomy, and optical communication. One way of achieving a narrow-band filter is to use the principle of volume holography in a thick grating [63][68] [69][102]. Because of its Bragg selectivity a thick grating acts as a filter and by using the reflection geometry, which exhibits the highest wavelength selectivity, one can achieve subnanometer spectral resolution. Extending this idea, we propose a novel device, a dynamic multiple-wavelength filter: it is based on a photorefractive SVHOE in which planar holograms with different grating spacings (i.e., central Bragg wavelengths) are recorded in different grating layers and then fixed. Figure 9.9 represents schematically such a device in the perfectly counterpropagating geometry ($\cos \theta_B = 1$). Therefore each layer k will selectively respond at one given wavelength, the Bragg wavelength λ_B^k , with a bandwidth $\Delta\lambda^k$ given by [69]

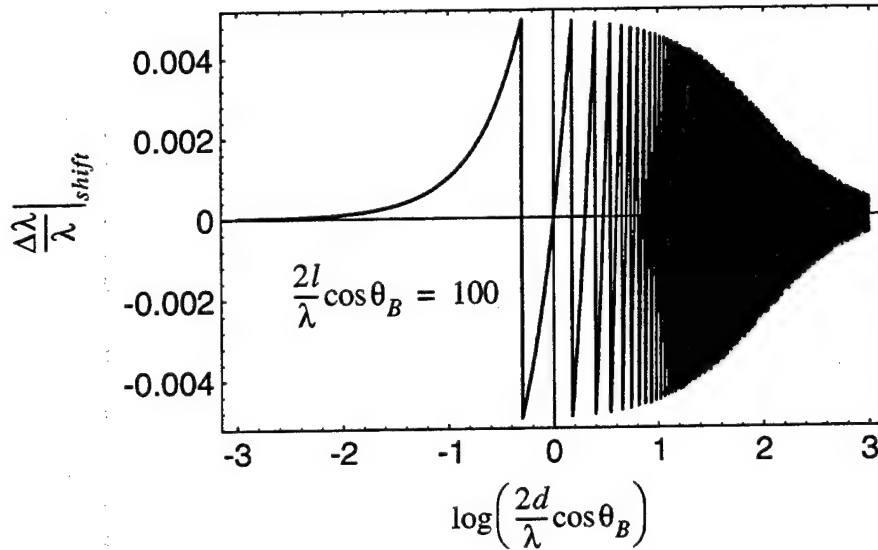


Figure 9.8: Wavelength shift $\Delta\lambda/\lambda|_{shift}$ of the maximum diffraction efficiency as a function of buffer layer thickness d for a photorefractive SVHOE in the reflection geometry.

$$\Delta\lambda^k = \frac{(\lambda_B^k)^2}{l_k} \quad (9.45)$$

One can then use the electrically controlled diffraction (ECD) effect [44] during the filtering process to control independently the diffraction efficiency of each single thick grating layer. The ECD effect is present in some photorefractive materials (like SBN) operating near the ferroelectric-paraelectric phase transition. In the vicinity of this phase transition, the electro-optic coefficient and the dielectric constant are strongly dependent on the applied field. As shown in Ref. [44] and in Chapter 7, this combined field dependence allows the grating amplitude and ultimately the diffraction efficiency to be electrically controlled and enhanced. Through this effect, a single grating efficiency can be enhanced from almost 0% in the absence of a field to 70% in the presence of a field of a few kilovolts per centimeter. Therefore, by application of a field E_0^k to the grating of a layer k , its amplitude $\nu_k = \nu_k(E_0^k)$ can be electrically controlled, i.e., the grating layer k can alternately be switched “on” and “off”.

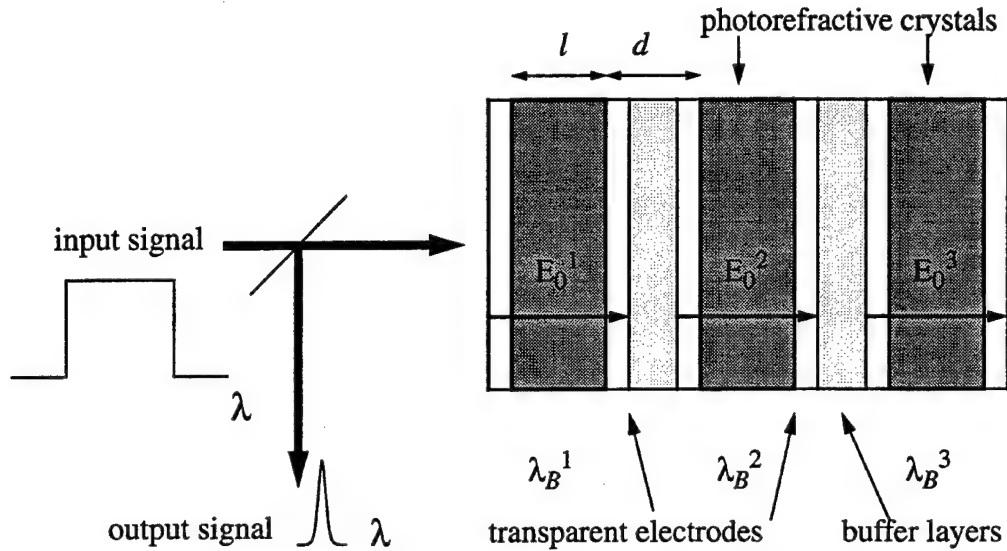


Figure 9.9: Schematic representation of a dynamic multiple-wavelength filter, with the photorefractive layers (of thickness l), the buffer layers (of thickness d), and the transparent electrodes.

The dynamic multiple-wavelength filter is thus a device that can be electrically switched to filter one or several wavelengths at a time from a broad-band input signal. Figure 9.9 represents the general configuration of a dynamic multiple-wavelength filter consisting of a photorefractive SVHOE with its grating layers, buffer layers and transparent electrodes used in the reflection geometry. By use of the electrically controlled diffraction effect, one can selectively activate one or several holograms within the structure, making it possible to filter selectively one or several wavelengths from an incoming incident light with a broad wavelength spectrum.

Because of the nature of a SVHOE, there is interference between the different grating layers as described by the theory developed in the previous sections. As seen in Figs. 9.3 and 9.4, this interference is maximum when the same grating is written in all the layers ($\lambda_B^k = \lambda_B, \forall k$) because in this case the diffraction efficiency is expressed by a coherent sum [Eq. (9.41)]. As we shall show, this interference decreases with an increase in the separation between Bragg wavelengths λ_B^k and with a decrease in the length of the buffer layer d . This effect introduces a minimum separation between two

wavelengths λ_B^k in the dynamic multiple-wavelength filter for some maximum allowed interference cross talk. It is easy to show that the separation between two successive Bragg wavelengths, $\lambda_B^{k+1} - \lambda_B^k$, must satisfy the following approximate relation for the interference terms between two successive layers to be less than a small number ϵ :

$$|\lambda_B^{k+1} - \lambda_B^k| \geq \frac{1}{\pi\epsilon} \Delta\lambda^k \quad (9.46)$$

Figure 9.10 shows the Bragg selectivity responses as a function of wavelength of a two-layer system if the separations between the two writing wavelengths are given by

$$\lambda_B^2 - \lambda_B^1 = j\Delta\lambda^1 \quad j = 1, 2, 3, 4 \quad (9.47)$$

with $\lambda_B^1 = 223.5$ nm (corresponding to 514 nm outside the crystal with $\bar{n} = 2.3$, $d = 100$ μm , $l_1 = l_2 = 100$ μm). It clearly illustrates the strong interference present in the wavelength selectivity responses when two writing wavelengths λ_B^k are only a few $\Delta\lambda^k$ apart. If the peak wavelengths λ_B^k are separated such that the cross talk between layers is negligible ($\epsilon \ll 1$), the interference terms between grating layers can be neglected and the diffraction efficiency of the device reduces to the incoherent sum

$$\eta = \sum_{j=1}^N \nu_j^2 \frac{\sin^2 \xi_j}{\xi_j^2} \quad (9.48)$$

This shows that the diffraction efficiency around each Bragg wavelength λ_B^k varies like $\nu_k^2(E_0^k)$. Such a device can be useful for wavelength division multiplexing (WDM). Typical requirements for WDM are channels bandwidths of about 1 nm separated by a few nanometers. A bandwidth of 1 nm can be achieved with a grating layer thickness of 50 μm (at $\lambda_o = 514$ nm). Several of these layers can then be stacked together to form a SVHOE multiple-wavelength filter with the desired performance for WDM.

Figure 9.11 represents the normalized output spectral distribution of a dynamic multiple-wavelength filter when different grating layers are successively turned "on" and "off", assuming that light with a constant spectral distribution is incident on the device. This figure is computed with the use of Eq. (9.39) for a structure of three layers

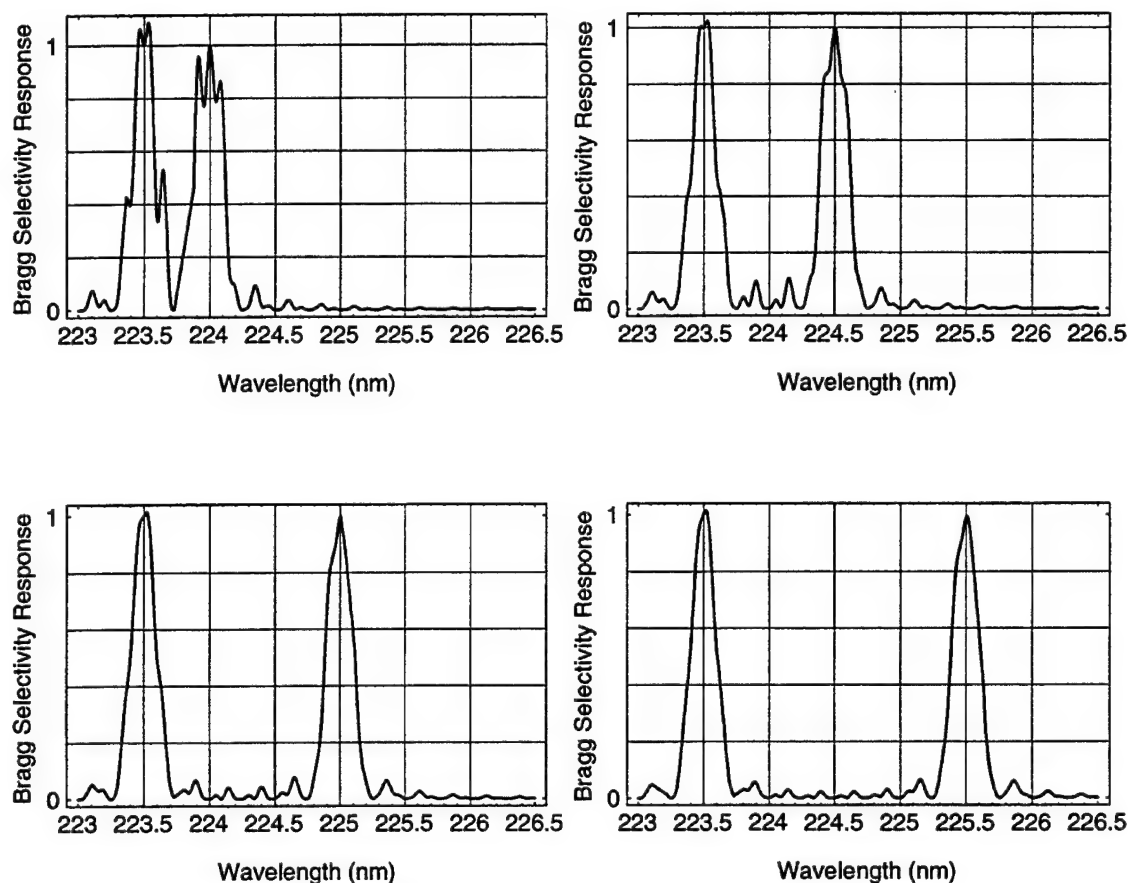


Figure 9.10: Bragg selectivity (wavelength) responses as a function of wavelength for a two-layer system illustrating the interference when the two Bragg wavelengths λ_B^1 and λ_B^2 are close to each other: $\lambda_B^2 = \lambda_B^1 + j\Delta\lambda^1$ ($l_1 = l_2 = 100 \mu\text{m}$, $d = 100 \mu\text{m}$, $\lambda_B^1 = 223.5 \text{ nm}$): (a) $j = 1$, (b) $j = 2$, (c) $j = 3$, and (d) $j = 4$.

with widely spaced Bragg wavelengths λ_B^k [such that Eq. (9.48) is actually valid]. It is further assumed that a field E_0^k applied to the photorefractive material of a grating layer k increases the grating amplitude by a factor of 10, i.e., $\nu_k(E_0^k) = 10\nu_k(0)$.

When a field is applied to a photorefractive crystal, it also induces a change in the Bragg condition due to the electro-optic effect and the piezoelectric effect. This will introduce a shift between the writing wavelength (λ_B^k) and the reflected wavelength. This shift is given by [68]

$$\frac{\Delta\lambda_B^{k(det)}}{\lambda_B^k} = \left(\frac{n^2}{2} r_{13} E_0^k + d_{33} E_0^k \right) \quad (9.49)$$

where r_{13} is the electro-optic coefficient, d_{33} is the piezoelectric coefficient and E_0^k is the field applied to the layer k during the filtering process. In Eq. (9.49), we assume that the electric field E_0^k is applied along the c axis of the photorefractive crystal. If this is not the case, the detuning has a more complex expression, as described in Ref. [45]. For a given applied field this detuning is constant and can therefore be compensated for during writing in order to yield the desired central filtering wavelength.

An additional possible application of photorefractive SVHOE's that use the same configuration as in Fig. 9.9, consists of a multiple-layer optical memory: any multiplexing technique can be used to store several holograms in one grating layer, and one can then use the ECD effect to achieve spatial multiplexing of these holograms within a single layer of the whole structure. The reflection geometry is especially interesting, as the Bragg detuning that is due to a given applied electric field or wavelength change is the largest in this case and therefore allows a high number of holograms to be recorded in one grating layer. Elementary layered optical memory devices based on this idea have been proposed and successfully demonstrated [100] [101], although they were not using the ECD effect. The capacity and the performance of these elementary memory devices could potentially be improved by the introduction of the ECD effect. The theory developed in this paper is then an important step to a better understanding of these devices and also to improvement of their performance.

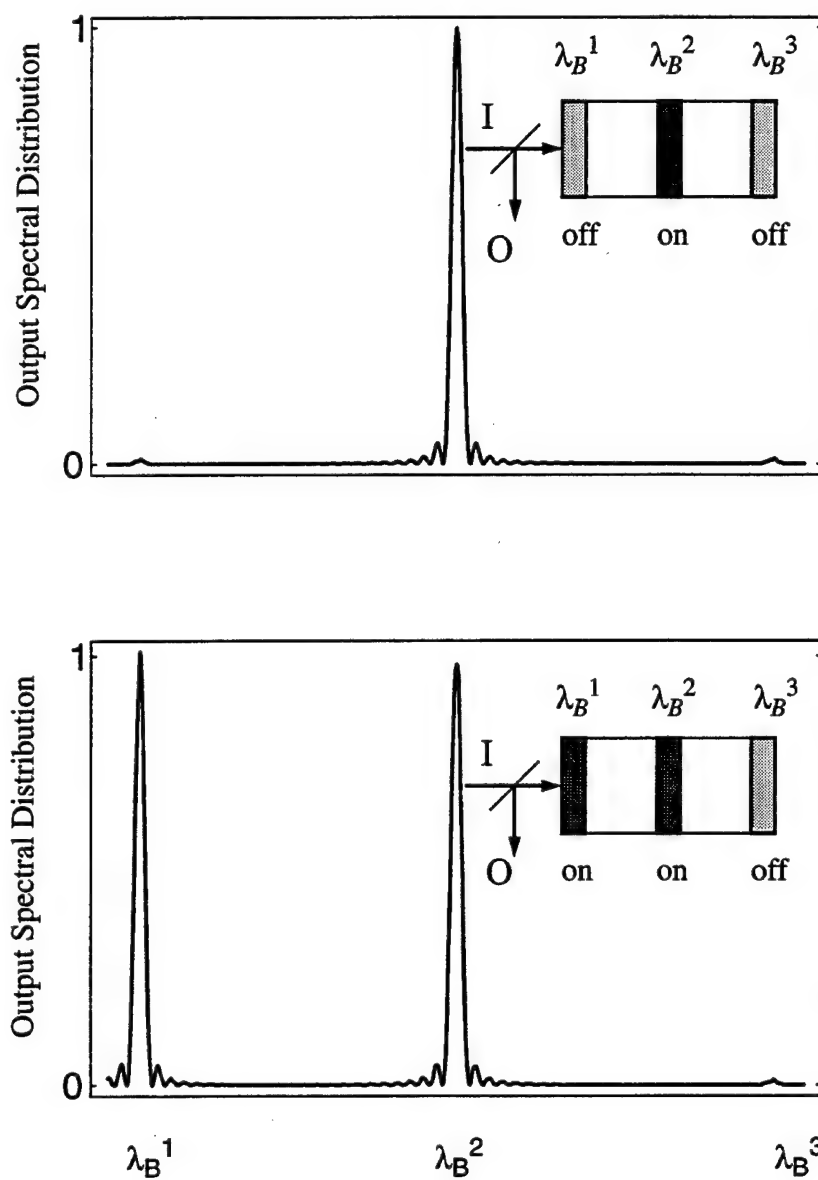


Figure 9.11: Output spectral distribution of a dynamic multiple-wavelength filter: (a) layers 1 and 3 turned off and layer 2 turned on, (b) layers 1 and 2 turned on and layer 3 turned off.

9.5 Conclusions

We have developed in this last chapter a theory to analyze the diffraction properties of layered structures of thick photorefractive gratings in the transmission and in the reflection geometries. A closed-form solution for the diffraction efficiency is found in both cases. The theory accounts for cases in which holograms with different grating spacings are written in different recording layers and cases in which the different grating and buffer layers have different properties (composite structures). Finally, the performance of a novel optical device, a dynamic multiple-wavelength filter, based on the properties of photorefractive SVHOE's, is described and analyzed.

Chapter 10

Conclusions and Future Research

After reviewing the fundamental principles of volume holography and the photorefractive effect in the first part of this thesis, we have studied, in the second part, grating formation in photorefractive crystals and analyzed the diffraction properties of the resulting holograms. We have shown that in the presence of an applied field, amplitude and phase coupling can considerably alter the grating formation process, resulting in a grating that is strongly nonuniform in amplitude and in phase, although it is recorded using plane waves. We have experimentally demonstrated the presence of phase coupling by measuring the diffraction properties of these nonuniform gratings. Indeed phase coupling results in fringe bending, i.e., a rotation of the fringes inside the crystal, that can be measured by analyzing the angular selectivity of the nonuniform grating and the shift in Bragg condition.

We have then generalized the concept of shift in the Bragg condition to encompass a series of effects that are encountered in photorefractive applications. We have first developed a general formalism to describe Bragg detuning that is due to the following effects: electro-optic effect, piezoelectric effect, anisotropic expansion, index of refraction changes, and polarization changes. We have then verified this model by explicitly measuring changes in Bragg condition in strontium barium niobate (SBN:60 and SBN:75) that are due to electric field effects and polarization effects.

However in most of the photorefractive applications, particularly in holographic data storage, image-bearing holograms are stored in the crystals. In the presence of

Bragg detuning, image-bearing holograms can be severely distorted when one tries to retrieve the information previously stored in the crystal. To analyze this problem we have first defined detuning-based transfer functions in a general way and then used this theory to consider two cases that are of practical interest.

The first case deals with thermal fixing in a digital holographic data storage system. The fixing of information stored in photorefractive crystals can be achieved by heating the crystal during or after the recording process. We have analyzed these two methods to achieve thermal fixing: the first method, in which there is a temperature difference between recording and readout, is called the high-low process, and the second method, in which no net temperature difference is present between recording and readout, is called the low-high-low process. We have finally considered the trade-offs regarding image deformation and diffraction efficiency between these two fixing methods in the different typical recording geometries.

The second case deals with the electrically controlled diffraction effect in strontium barium niobate in which, by application of an electric field during readout, it is possible to dynamically control and enhance diffraction efficiencies. We have experimentally shown that electrically controlled diffraction can be successfully implemented in a holographic data storage system: we have stored and retrieved with an applied field of a few kilovolts per centimeter multiple planar holograms recorded using angular multiplexing as well as high-resolution image-bearing holograms without image field loss.

In the third part of this thesis, we have concentrated on a theoretical study of the diffraction properties of stratified volume holographic optical elements. We have developed a general analytical formalism to study the diffraction properties of structures of thin as well as thick gratings. Finally, we have described a novel optical device, a dynamic multiple-wavelength filter, with potential applications in the fields of spectroscopy, optical communication and wavelength division multiplexing.

In the future, more work needs to be done in the field of thermal fixing, first to have a better understanding of the physical processes underlying the fixing mechanism, and then to fully integrate thermal fixing in a high-capacity digital holographic data storage system. At the same time more work can be done to try to improve

and optimize the different photorefractive materials used as recording media for holographic storage.

Future work can also be done to grow and characterize stratified volume holographic optical elements. Because of their versatility, SVHOE's can be used as composite structures of photorefractives with enhanced properties or as engineered materials with potential applications in the fields of wavelength filtering, beam steering or wave guiding.

Appendix A

List of Publications

A.1 Papers

- R. De Vré, M. Jeganathan, J. P. Wilde and L. Hesselink. "Effect of applied fields on the Bragg condition and the diffraction efficiency in photorefractive crystals". *Opt. Lett.*, **19**:910 (1994).
- R. De Vré and L. Hesselink. "Analysis of photorefractive stratified volume holographic optical elements". *J. Opt. Soc. Am. B*, **11**:1800 (1994).
- R. De Vré, M. Jeganathan, J. P. Wilde and L. Hesselink. "Effect of applied electric fields on the writing and readout of photorefractive gratings". *J. Opt. Soc. Am. B*, **12**:600 (1995).
- R. De Vré, M. Jeganathan and L. Hesselink. "Diffraction properties of a reflection photorefractive hologram: comments". *Appl. Opt.*, **34**:2590 (1995).
- R. De Vré and L. Hesselink. "Diffraction analysis of layered structures of photorefractive gratings". *J. Opt. Soc. Am. A*, **13**:285 (1996).
- R. De Vré, J. F. Heanue, K. Gürkan and L. Hesselink. "Transfer functions based on Bragg detuning effects for image-bearing holograms recorded in photorefractive crystals". *J. Opt. Soc. Am. A*, **13**:(in press) (1996).

- J. P. Wilde, R. De Vré and L. Hesselink. "Holographic storage near the ferroelectric phase transition". Manuscript in preparation.

A.2 Presentations

- J. P. Wilde, R. De Vré, M. Jeganathan and L. Hesselink. "Electric field control of image-bearing volume holograms stored in photorefractive media". In Technical Digest Series, Volume 8, p. 98. CLEO 94, 1994 (Anaheim, California) Paper CTuK26.
- R. De Vré, M. Jeganathan and L. Hesselink. "Diffraction properties of gratings written with amplitude and phase coupling in photorefractive crystals". OSA Annual Meeting/ ILS-X, 1994 (Dallas, Texas) Paper MDD3.
- R. De Vré and L. Hesselink. "Diffraction analysis of structures of switchable photorefractive gratings". Photorefractive materials, effects and devices, 1995 (Estes Park, Colorado) Paper WDD12.
- R. De Vré, J. F. Heanue, K. Gürkan and L. Hesselink. "Bragg detuning effects in photorefractive crystals". Photorefractive materials, effects and devices, 1995 (Estes Park, Colorado) Paper WDD13.
- R. De Vré, J. F. Heanue, K. Gürkan and L. Hesselink. "Bragg detuning effects in photorefractive crystals". OSA Annual Meeting/ILS-X, 1995 (Portland, Oregon) Paper ThWW3.
- J. F. Heanue, K. Gürkan, M. C. Bashaw, R. De Vré and L. Hesselink. "Thermal fixing in digital holographic data storage". OSA Annual Meeting/ILS-X, 1995 (Portland, Oregon) Paper MB2.

Bibliography

- [1] D. Gabor. A new microscope principle. *Nature*, **161**:777, (1948).
- [2] J. W. Goodman. *Introduction to Fourier Optics*. McGraw-Hill, 1968.
- [3] H. J. Eichler. *Laser-induced dynamic gratings*. Springer-Verlag, Berlin, 1986.
- [4] H. Kogelnik. Coupled wave theory for thick hologram gratings. *The Bell System Technical Journal*, **48**:2909–2947, (1969).
- [5] N. V. Kukhtarev, V. B. Markov, S. G. Odulov, M. S. Soskin, and V. L. Vinetskii. Holographic storage in electrooptic crystals. *Ferroelectrics*, **22**:949–960, (1979).
- [6] J. T. Sheridan. A comparison of diffraction theories for off-Bragg replay. *Journal of Modern Optics*, **39**:1709–1718, (1992).
- [7] M. C. Bashaw, J. F. Heanue, A. Aharoni, J. F. Walkup, and L. Hesselink. Cross talk considerations for angular and phase-encoded multiplexing in volume holography. *J. Opt. Soc. Am. B*, **11**:1820–1836, (1994).
- [8] A. Ashkin, G. D. Boyd, J. M. Dziedzic, R. G. Smith, A. A. Ballman, and K. Nassau. *Appl. Phys. Lett.*, **9**:72, (1966).
- [9] G. H. Brown. *Photochromism*. Wiley, New York, 1971.
- [10] N. V. Kukhtarev. Kinetics of hologram recording and erasure in electrooptic crystals. *Pis'ma Zh. Tekh. Fiz.*, **2**:1114, (1976). [English Transl.: Sov. Tech. Phys. Lett **2**, 438-440 (1976)].

- [11] A. G. Glass. The photorefractive effect. *Opt. Eng.*, **17**:470–479, (1978).
- [12] T. J. Hall, R. Jaura, L. M. Connors, and P. D. Foot. The photorefractive effect - a review. *Prog. Quant. Electr.*, **10**:77–146, (1985).
- [13] L. Hesselink and M. C. Bashaw. Optical memories implemented with photorefractive media. *Optical and Quantum Electron.*, **25**:S611–S661, (1993).
- [14] P. Günter and J.-P. Huignard, editors. *Photorefractive materials and their applications*, volume I and II. Springer-Verlag, Berlin, 1989.
- [15] P. Yeh. *Introduction to photorefractive nonlinear optics*. Wiley, New York, 1993.
- [16] M. Cronin-Golomb, B. Fischer, J. O. White, and A. Yariv. Theory and applications of four-wave mixing in photorefractive media. *IEEE J. Quantum Electron.*, **20**:12–30, (1984).
- [17] D. Z. Anderson and J. Feinberg. Optical novelty filters. *IEEE J. Quantum Electron.*, **25**:635–647, (1989).
- [18] P. P. Banerjee, J.-J. Liu, and R. M. Misra. Optical limiting based on deterministic beam fanning in photorefractive materials. *International Journal of Nonlinear Optical Physics*, **2**:631–642, (1993).
- [19] J. F. Heanue, M. C. Bashaw, and L. Hesselink. Volume holographic storage and retrieval of digital data. *Science*, **265**:749–752, (1994).
- [20] J. O. White and A. Yariv. Real-time processing via four-wave mixing in a photorefractive medium. *Appl. Phys. Lett.*, **37**:5–7, (1980).
- [21] C. Uhrich. *Submicron defect detection in periodic structures using photorefractive holography*. PhD thesis, Stanford University, (1992).
- [22] S. Ducharme, J. C. Scott, R. J. Twieg, and W. E. Moerner. Observation of the photorefractive effect in a polymer. *Phys. Rev. Lett.*, **66**:1846–1849, (1991).

- [23] M. Jeganathan. *Transients due to two-wave mixing in photorefractive media*. PhD thesis, Stanford University, (1995).
- [24] M. C. Bashaw, M. Jeganathan, and L. Hesselink. Theory of two-center transport in photorefractive media for low-intensity, continuous-wave illumination in the quasi-steady-state limit. *J. Opt. Soc. Am. B*, **11**:1743–1757, (1994).
- [25] M. D. Ewbank, R. R. Neurgaonkar, W. K. Cory, and J. Feinberg. Photorefractive properties of strontium barium niobate. *J. Appl. Phys.*, **62**:374–380, (1987).
- [26] A. Yariv and P. Yeh. *Optical waves in crystals*. John Wiley and Sons, 1984.
- [27] S. Ducharme, J. Feinberg, and R. R. Neurgaonkar. Electrooptic and Piezoelectric measurements in photorefractive barium titanate and strontium barium niobate. *IEEE J. Quantum Electron.*, **23**:2116–2121, (1987).
- [28] P. Yeh. Two-wave mixing in nonlinear media. *IEEE J. Quantum Electron.*, **25**:484–519, (1989).
- [29] T. Kubota. The bending of interference fringes inside a hologram. *Optica Acta*, **26**:731–743, (1979).
- [30] R. N. Bracewell. *The Fourier transform and its applications*. McGraw-Hill, 1986.
- [31] J. H. Hong and R. Saxena. Diffraction efficiency of volume holograms written by coupled beams. *Opt. Lett.*, **16**:180–182, (1991).
- [32] R. Hofmeister, A. Yariv, and S. Yagi. Spectral response of fixed photorefractive grating interference filters. *J. Opt. Soc. Am. A*, **11**:1342–1351, (1994).
- [33] M. P. Petrov, S. I. Stepanov, and A. A. Kamshilin. Light diffraction from the volume holograms in electrooptic birefringent crystals. *Optics Commun.*, **29**:44–48, (1979).
- [34] K. R. Sangameswara. *Thermal expansion of crystals*. Pergamon Press, 1979.

- [35] R. De Vré, M. Jeganathan, J. P. Wilde, and L. Hesselink. Effect of applied electric fields on the writing and readout of photorefractive gratings. *J. Opt. Soc. Am. B*, **12**:600-614, (1995).
- [36] J. M. Heaton, P. A. Mills, E. G. S. Paige, L. Solymar, and T. Wilson. Diffraction efficiency and angular selectivity of volume phase holograms recorded in photorefractive materials. *Optica Acta*, **31**:885-901, (1984).
- [37] S. Tao, D. R. Selviah, and J. E. Midwinter. Optimum replay angle for maximum diffraction efficiency of holographic gratings in Fe:LiNbO₃ crystals. *Topical meeting on photorefractive materials, effects and devices*, August 1993, Kiev, Ukraine. Paper FRG11/1(4).
- [38] S. Tao, Z. H. Song, and D. R. Selviah. Bragg-shifting of holographic gratings in photorefractive Fe:LiNbO₃ crystals. *Optics Commun.*, **108**:144-152, (1994).
- [39] J. P. Wilde and L. Hesselink. Electric-field-controlled diffraction in photorefractive strontium barium niobate. *Opt. Lett.*, **17**:853-855, (1992).
- [40] P. Günter and M. Zgonik. Clamped-unclamped electro-optic coefficient dilemma in photorefractive phenomena. *Opt. Lett.*, **16**:1826-1828, (1991).
- [41] G. Pauliat, P. Mathey, and G. Roosen. Influence of piezoelectricity on the photorefractive effect. *J. Opt. Soc. Am. B*, **8**:1942-1946, (1991).
- [42] A. A. Izvanov, A. E. Mandel, N. D. Khat'kov, and S. M. Shandarov. Influence of the piezoelectric effect on hologram writing and reconstruction in photorefractive crystals. *Optoelectronics, instrumentation, and data processing*, **2**:80-84, (1986).
- [43] S. I. Stepanov, A. A. Kamshilin, and M. P. Petrov. Electrically controlled optical diffraction by volume holograms in electrooptic crystals. *Pis'ma Zh. Tekh. Fiz.*, **3**:89-93, (1977). [English Transl.: *Sov. Tech. Phys. Lett* **3**, 36-38 (1977)].

- [44] J. P. Wilde. *Growth and characterization of strontium barium niobate crystals for multiplex photorefractive holography*. PhD thesis, Stanford University, (1992).
- [45] A. Kewitsch, M. Segev, A. Yariv, and R. R. Neurgaonkar. Electric-field multiplexing/demultiplexing of volume holograms in photorefractive media. *Opt. Lett.*, **18**:534–536, (1993).
- [46] A. S. Bhalla, R. Guo, L. E. Cross, G. Burns, F. H. Dacol, and R. R. Neurgaonkar. Measurements of strain and the optical indices in the ferroelectric $\text{Ba}_{0.4}\text{Sr}_{0.6}\text{Nb}_2\text{O}_6$: Polarization effects. *Phys. Rev. B*, **36**:2030–2035, (1987).
- [47] K. Curtis, C. Gu, and D. Psaltis. Cross talk in wavelength-multiplexed holographic memories. *Opt. Lett.*, **18**:1001–1003, (1993).
- [48] F. H. Mok. Angle-multiplexed storage of 5000 holograms in Lithium Niobate. *Opt. Lett.*, **18**:915–917, (1993).
- [49] G. W. Burr, F. H. Mok, and D. Psaltis. Storage of 10000 holograms in $\text{LiNbO}_3\text{:Fe}$. In *Technical Digest Series*, volume 8, page 9, (1994). CLEO 94, paper CMB7.
- [50] C. Denz, G. Pauliat, G. Roosen, and T. Tschudi. Volume hologram multiplexing using a deterministic phase encoding method. *Opt. Commun.*, **85**:171–176, (1991).
- [51] C. Denz, G. Pauliat, G. Roosen, and T. Tschudi. Potentialities and limitations of hologram multiplexing by using the phase-encoding technique. *Appl. Opt.*, **31**:5700–5705, (1992).
- [52] G. A. Rakuljic, V. Leyva, and A. Yariv. Optical data storage by using orthogonal wavelength-multiplexed volume holograms. *Opt. Lett.*, **17**:1471–1473, (1992).

- [53] J. F. Heanue, M. C. Bashaw, and L. Hesselink. Sparse selection of reference beams for wavelength- and angular-multiplexed volume holography. *J. Opt. Soc. Am. A*, **12**:1671-1676, (1995).
- [54] K. Curtis, A. Pu, and D. Psaltis. Method for holographic storage using peristrophic multiplexing. *Opt. Lett.*, **19**:993-995, (1994).
- [55] J. J. Amodei and D. L. Staebler. Holographic pattern fixing in electro-optic crystals. *Appl. Phys. Lett.*, **18**:540-542, (1971).
- [56] J. P. Wilde, R. De Vré, M. Jeganathan, and L. Hesselink. Electric field control of image-bearing volume holograms stored in photorefractive media. In *Technical Digest Series*, volume **8**, pages 98-99, (1994). CLEO 94, paper CTuK26.
- [57] Yu. L. Korzinin and V. I. Sukhanov. Diffraction of light by 3-D holograms with a continuous spectrum of spatial frequencies. System of equations for coupled waves. *Opt. Spectrosc.*, **56**:467-469, (1984).
- [58] Yu. L. Korzinin and V. I. Sukhanov. Diffraction of light by 3-D holograms with a continuous spectrum of spatial frequencies. *Opt. Spectrosc.*, **56**:572-574, (1984).
- [59] Yu. L. Korzinin and V. I. Sukhanov. Diffraction efficiency of a 3-D hologram of a diffuse object. *Opt. Spectrosc.*, **58**:86-88, (1985).
- [60] D. L. Staebler and J. J. Amodei. Thermally fixed holograms in LiNbO₃. *Ferroelectrics*, **3**:107-113, (1972).
- [61] M. Carrascosa and F. Agulló-López. Theoretical modeling of the fixing and developing of holographic gratings in LiNbO₃. *J. Opt. Soc. Am. B*, **7**:2317-2322, (1990).
- [62] A. Yariv, S. Orlov, G. Rakuljic, and V. Leyva. Holographic fixing, readout, and storage dynamics in photorefractive materials. *Opt. Lett.*, **20**:1334-1336, (1995).

- [63] R. Müller, M. T. Santos, L. Arizmendi, and J. M. Cabrera. A narrow-band interference filter with photorefractive LiNbO_3 . *J. Phys. D: Appl. Phys.*, **27**:241–246, (1994).
- [64] J. F. Heanue, K. Gürkan, M. C. Bashaw, R. De Vré, and L. Hesselink. Thermal fixing in digital holographic data storage. OSA annual meeting, Portland, OR, 1995. Paper MB2.
- [65] D. L. Staebler, W. J. Burke, W. Phillips, and J. J. Amodei. Multiple storage and erasure of fixed holograms in Fe-doped LiNbO_3 . *Appl. Phys. Lett.*, **26**:182–184, (1975).
- [66] Properties of lithium niobate. *INSPEC, EMIS Datareviews Series*, **5**, (1989).
- [67] J. F. Heanue, M. C. Bashaw, and L. Hesselink. Volume holographic storage and retrieval of digital information. In *Technical Digest Series*, volume **15**, page 27, (1995). CLEO 95, paper CMF5.
- [68] R. Müller, J. V. Alvarez-Bravo, L. Arizmendi, and J. M. Cabrera. Tuning of photorefractive interference filters LiNbO_3 . *J. Phys. D: Appl. Phys.*, **27**:1628–1632, (1994).
- [69] G. A. Rakuljic and V. Leyva. Volume holographic narrow-band optical filter. *Opt. Lett.*, **18**:459–461, (1993).
- [70] J. F. Heanue. *Volume holographic storage of digital data implemented in photorefractive media*. PhD thesis, Stanford University, (1995).
- [71] R. De Vré, M. Jeganathan, J. P. Wilde, and L. Hesselink. Effect of applied fields on the Bragg condition and the diffraction efficiency in photorefractive crystals. *Opt. Lett.*, **19**:910–912, (1994).
- [72] R. De Vré and L. Hesselink. Diffraction analysis of layered structures of photorefractive gratings. *J. Opt. Soc. Am. A*, **13**:285–295, (1996).

- [73] J. P. Wilde, R. McRuer, L. Hesselink, and J. Goodman. Dynamic holographic interconnections using photorefractive crystals. *Proceedings of the SPIE*, **752**:200–208, (1987). Digital Optical Computing. Held: Los Angeles, CA, USA, 13–14 Jan. 1987.
- [74] A. M. Glass. Investigation of the electrical properties of $\text{Sr}_{1-x}\text{Ba}_x\text{Nb}_2\text{O}_6$ with special reference to pyroelectric detection. *J. Appl. Phys.*, **40**:4699, (1969).
- [75] M. B. Klein. Photorefractive properties of BaTiO_3 . In *Photorefractive Materials and Their Applications I*, ed. by P. Gunter and J. P. Huignard (Springer-Verlag, Berlin, 1988), chap. 7.
- [76] V. Leyva, A. Agranat, and A. Yariv. Determination of the physical parameters controlling the photorefractive effect in $\text{KTa}_{1-x}\text{Nb}_x\text{O}_3\text{:Cu,V}$. *J. Opt. Soc. Am. B*, **8**:701–707, (1991).
- [77] R. R. Neurgaonkar, W. K. Cory, J. R. Oliver, W. W. Clark III, G. L. Wood, M. J. Miller, and E. J. Sharp. Growth and ferroelectric properties of tungsten bronze BSKNN single crystals. *J. Cryst. Growth*, **84**:629–637, (1987).
- [78] R. A. Rupp, A. E. Krumins, and K. Kerperin. Dielectric, electrooptic, and holographic properties close to the diffuse phase transition of PLZT 10/65/35. *Phys. Stat. Sol. A*, **113**:637–651, (1989).
- [79] A. Agranat, V. Leyva, and A. Yariv. Voltage-controlled photorefractive effect in paraelectric $\text{KTa}_{1-x}\text{Nb}_x\text{O}_3\text{:Cu,V}$. *Opt. Lett.*, **14**:1017–1019, (1989).
- [80] L. E. Cross. Relaxor ferroelectrics: an overview. *Ferroelectrics*, **151**:305–320, (1994).
- [81] E. S. Maniloff and K. M. Johnson. Maximized photorefractive holographic storage. *J. Appl. Phys.*, **70**:4702–4707, (1991).
- [82] A. P. Yakimovich. Multilayer three-dimensional holographic gratings. *Opt. Spectrosc.*, **49**:85–88, (1980).

- [83] B. Ya. Zel'dovich and T. V. Yakovleva. Theory of a two-layer hologram. *Sov. J. Quantum Electron.*, **14**:323–328, (1984).
- [84] B. Ya. Zel'dovich, D. I. Mirovitskii, N. V. Rostovtseva, and O. B. Serov. Characteristic of two-layer phase holograms. *Sov. J. Quantum Electron.*, **14**:364–369, (1984).
- [85] A. R. Tanguay and R. V. Johnson. Stratified volume holographic optical elements. *J. Opt. Soc. Am. A*, **3**(13):P53, (1986).
- [86] R. V. Johnson and A. R. Tanguay. Stratified volume holographic optical elements. *Opt. Lett.*, **13**:189–191, (1988).
- [87] G. P. Nordin, R. V. Johnson, and A. R. Tanguay. Diffraction properties of stratified volume holographic optical elements. *J. Opt. Soc. Am. A*, **9**:2206–2217, (1992).
- [88] R. V. Johnson and A. R. Tanguay. Optical beam propagation method for birefringent phase grating diffraction. *Opt. Eng.*, **25**:235–249, (1986).
- [89] A. Granger, L. Song, and R. A. Lessard. Multiple beam generation using a stratified volume holographic grating. *Appl. Opt.*, **32**:2534–2537, (1993).
- [90] J. J. Stankus, S. M. Silence, W. E. Moerner, and G. C. Bjorklund. Electric-field switchable stratified volume holograms in photorefractive polymers. *Opt. Lett.*, **19**:1480–1482, (1994).
- [91] R. De Vré and L. Hesselink. Analysis of photorefractive stratified volume optical holographic optical elements. *J. Opt. Soc. Am. B*, **11**:1800–1808, (1994).
- [92] Z. Lu, R. S. Feigelson, R. K. Route, R. Hiskes, S. A. DiCarolis, and R. D. Jacowitz. Solid source MOCVD for the epitaxial growth of thin oxide films. *J. Crystal Growth*, **128**:788–792, (1992).
- [93] K. E. Youden, R. W. Eason, M. C. Gower, and N. A. Vainos. Epitaxial growth of $\text{Bi}_{12}\text{GeO}_{20}$ thin-film optical waveguides using excimer laser ablation. *Appl. Phys. Lett.*, **59**:1929–1932, (1991).

- [94] M. Liphardt, A. Goonesekera, B. E. Jones, S. Ducharme, J. M. Takacs, and L. Zhang. High-performance photorefractive polymers. *Science*, **263**:367–369, (1994).
- [95] Q. Wang, R. M. Brubaker, and D. D. Nolte. Photorefractive quantum wells: transverse Franz-Keldysh geometry. *J. Opt. Soc. Am. B*, **9**:1626–1641, (1992).
- [96] P. Günter and J.-P. Huignard, editors. *Photorefractive materials and their applications*, volume I. Springer-Verlag, Berlin, 1989. Chap. 2 , p. 46 .
- [97] P. Günter and J.-P. Huignard, editors. *Photorefractive materials and their applications*, volume II. Springer-Verlag, Berlin, 1989. Chap. 6 , p. 205 .
- [98] M. Born and E. Wolf. *Principles of optics*. Pergamom Press, sixth edition, 1985.
- [99] G. P. Nordin and A. R. Tanguay. Photopolymer-based stratified volume holographic optical element. *Opt. Lett.*, **17**:1709–1711, (1992).
- [100] J. B. Thaxter and M. Kestigan. Unique properties of SBN and their use in layered optical memory. *Appl. Opt.*, **13**:913–924, (1974).
- [101] T. Yasuhira, Y. Mitsuhashi, T. Morikawa, J. Shimada, and T. Kamijo. Electrically accessible Lippmann hologram memory. *Appl. Opt.*, **16**:2532–2534, (1977).
- [102] V. Leyva, G. A. Rakuljic, and B. O'Conner. Narrow bandwidth volume holographic optical filter operating at the Kr transition at 1547.82 nm. *Appl. Phys. Lett.*, **65**:1079–1081, (1994).